High temperature quantum transport in graphene/hexagonal-boron nitride heterostructures

A Thesis submitted to Lancaster University for the degree of Doctor of Philosophy in the Faculty of Sciences and Engineering

2017

R. Krishna Kumar

Department of Physics

`

Contents

`

`

Abstract

The past decade has seen a new paradigm in solid state physics, where a new class of layered crystals can be thinned down to a monolayer and exhibit drastic changes in their electronic and optical properties in comparison to their bulk counterpart. Graphene was the first, and certainly most outstanding, of this set of so called two-dimensional (2D) materials. Aside from its obvious appeal which earnt its discovery the 2010 Nobel Prize, the electronic properties of graphene are truly unique. Perhaps the most familiar is its linear electron dispersion which hosts quasi-particles that obey the Dirac equation. This has enabled the study of a plethora of transport phenomena, as well as the realisation of novel device architectures that will be used in the next generation electronics.

In general, experimental signatures of electron transport are most prominent at liquid helium temperatures when lattice vibrations are weak, for example in quantum hall physics. In this Thesis, we explore the regime of intermediate temperatures where the physics of interest is strongest between 100 and 300 K. Equipped with the state of the art high quality graphene samples, we demonstrate novel electron transport unique to graphene.

The experimental work consists of two themes. In the first work, we study hydrodynamic electron flow in graphene encapsulated with hexagonal boron nitride devices. At elevated temperatures, electron-electron collisions become significant, and the electron viscosity starts to influence the steady state current distribution in a variety of surprising ways. In the first work, we perform transport experiments on standard graphene hall bars in a unique measurement geometry which allows the detection of negative non-local voltages intrinsic to viscous flow. In another experiment, we study viscous electron flow through graphene nano-constrictions/classical point contacts. Here, we observed anomalous temperature dependence in the conductance measured across the constriction. Specifically, the conductance increases with increasing temperature and even exceeded the semi-classical limit which is expected for single-particle ballistic transport. The underlying mechanism originates from electron-electron collisions, which, counter-intuitively, act to enhance current flow.

In the second work, we slightly change our experimental system by studying magneto transport in a graphene/hexagonal boron nitride superlattice. Owed to the large periodicity of the superlattice unit cell, these devices have allowed experimental observation of the long sought Hofstadter butterfly, which addresses the electronic dispersion of electrons in a periodic potential and magnetic field.

`

Here, we again go to elevated temperatures, where all the spectral gaps related to Hofstadter butterflies are completely smeared, and instead find a new type of quantum oscillation. These new oscillations are periodic in 1/B with a frequency corresponding to one flux quantum piercing the superlattice unit cell. Whilst these oscillations are related to Hofstadter physics, they are in fact more primal in origin. The most fascinating feature is their robustness with respect to increasing temperature. The oscillations are easily observable at room temperature in fields as low as 3 T and still remained prominent at 373 K, the boiling point of water

`

Copyright Statement

`

Declaration

No portion of the work referred to in this thesis has been submitted in support of an application for another degree or qualification of this or any other university or other institute of learning.

`

Acknowledgements

First of all, I would like to thank my PhD supervisor Dr. Leonid Ponomarenko. I am truly lucky to have had the chance to work with him over the years. For one, he has spent an incredible amount of time training me and teaching me. Only through his close guidance have I been able to develop my research skills to such a high level, in particular with regard to electrical measurements. His matiliculous eye and attention to detail has resulted in a number of pioneering works on graphene, especially in the case of this Thesis. Without him I honestly cannot say whether we would have accomplished so much. I now understand that he is truly the master of graphene transport in Manchester. Leonid, you are the hero here.

Secondly I have to thank Professor Irina Grigorieva at the University of Manchester. She was the one who liaised with everyone and arranged for me to work closely with the Condensed Matter Physics group even though I am a Lancaster student.

I also have to thank Professor Andre Geim for allowing me to occupy one of his cryostats and perform my transport experiments. I am truly grateful that he has allowed me to work in his group as if I was part of it. More importantly, I must thank him for his supervision and guidance over the years. His constant drive and energy to push research has resulted in a number of exciting publications which I have been actively part of during my PhD. Although those periods of writing were indeed stressful at times, when it came to experiments he was always ready to listen and give me freedom to play. I thank him for “adopting” me in to the Condensed Matter Physics group at the University of Manchester.

As for my colleagues, my dear friend Dr. Denis Bandurin deserves a huge acknowledgement. We were both carrying out our PhD’s at the same time in electron transport. Over the years we have been working closely on a number of different projects. Of particular importance is our work on electron hydrodynamics, which we were both extremely excited about. Only though working together were we able to push our research to publication level. The numerous discussions we had helped to convince ourselves of the physics behind our work, and have led to even more ideas for future experiments. He is certainly one of the smartest guys I have met and I am very grateful to have been working so closely with him.

Of course, I have to thank many people in the Condensed Matter Physics group at the University of Manchester. Everyone here shares the same drive. You can find people here any time of the day and any day of the week, working with such focus that inevitably results in high-quality research. Aside

`

from this, the knowledge sharing and collaborations that go on within the group make it an ideal environment for working as a PhD student. A special mention goes to my colleagues and friends; Artem Mischenko (a super intelligent but extremely humble guy), Davit Ghazarant, Katya Khestanova, Qian Yang, Colin Woods, Geliang Yu and Jack (Mengjian Zhu,).

I cannot forget the fabrication team here in Manchester who have made all my transport experiments possible by providing me with the highest quality graphene devices around; Yang Cao and Moshe Ben-Shalom are amongst the best at fabricating 2D heterostructures in the world. I am very lucky to have access to those high quality samples where we found lots of new physics. A special mention goes to my dear friend and colleague Greg Auton, another guy with the skills in fabricating such high-quality devices. His endless optimism and kindness pretty much kick started my PhD. In the early days when I was starting out, I had burnt one of my first devices, and consequently was finding it difficult to convince others to make new ones! Greg, without hesitation, provided me with high quality graphene sample, which was in fact the very first device used to study electron hydrodynamics. Over the years we have worked together on many different experiments, and I am very grateful for him investing his fabrication time in all our projects.

I certainly have to thank one of my collaborators and now good friend, Professor Marco Polini. He is now a big guy in graphene research, but is still one of the most approachable relaxed guys I have met. I am grateful for his patience in explaining complicated theoretical concepts at an experimental level.

A big thanks goes to Mark and Paul, our cryogenic experts over here in the University of Manchester. Both these guys are kings. Mark, thank you for your experience and smooth running of the helium liquefier over the years. Paul, I admire your passion and drive, digging in to our research and coming to seminars to learn more. I think this attitude is exactly what the group needs. Keep at it!

Of course I have to thank my family. My parents, for one, always supporting me and helping me through stressful times (thanks Mum and Dad for bringing me such awesome food when you come to visit). My brother, Dr Ravinash Krishna Kumar, now a chemist working as a post-doctoral researcher in Oxford University, has helped me a lot with my writing skills over the years; for that I am truly grateful. My girlfriend Claire, for her endless patience and understanding of my obsession with science! Thank you for supporting me during the most stressful parts of my PhD. I love you dearly. Pretty much the whole Ganasalingam (my grandfather) family deserves acknowledgement. I am very lucky to have such a big supportive family.

R. Krishna Kumar

`

P.S. a very special shout out goes to my Manchester Reggae Society family. My friends Senan Robinson, Cai Niclas Wyn, Sean Caio, Thomas Catherall, Marley Round, Claire Andrews, Sophie Ayres, Megan Barker, Molly Hall, Harry Cadisch, , Christian Berger, Dale Haworth, Dan Eye, Tiffany Cathcart, Zain Ismail, Femi da Costa Greaves, Martin Griffin, Lamia Kholoud and the Reggae Thursday team. Sound system culture for me has really been a family affair, and I am grateful to have been part of it during my time in Manchester.

`

Chapter 1 - Introduction

The vast and increasingly growing electronics industry is at the forefront of technological applications that impact society. The rapid progress in the performance of such devices, for example the transistor, has stemmed from the fundamental study of electron transport in solid state crystals. Moreover, the operation of nearly all electronic devices can be understood from the band theory of electrons in crystals. After fundamental understanding of the individual crystals electronic properties is discerned, different crystals can then be assembled to make artificial structures with unique electronic properties that are not found intrinsically in any material. For example, a two-dimensional electron gas (2DEG) can be formed at the interface of two doped semiconductor crystals[1]. This cleverly designed electronic system can be extremely clean, hosting a rich variety of solid state physics such as the quantum hall effect[2], coloumb drag[3,4] and exciton physics[4] to name a few.

Recently a new branch of materials, termed Van der Waals crystals, have gained increasing interest for electronic and opto-electronic applications. Often these crystals can be thinned down to one atomic layer, and are therefore referred to as 2D materials because the crystal periodicity exists only in two dimensions. Furthermore, the family of 2D materials covers nearly every type of solid-state system including metals[5], semi-conductors[6], insulators[7] and even superconductors[8]. The bench mark for VdW crystals and 2D materials is their strict layer dependent electronic and optical properties. For example in graphene, atomically thin graphite, the monolayer and bilayer have very different electronic properties. Remarkably, the difference in only one atomic layer results in graphene electrons having a zero effective mass[9]. In another example, molybdenum disulphide (MoS_2) shows a direct – indirect bandgap transition upon decreasing the number of atomic layers[6]. Following the framework of GaAs and silicon based heterostructures; 2D crystals with different electronic properties can also be assembled to make novel materials. However, the different crystal layers within such devices are bonded only by Van der Waals interaction and therefore are usually referred to as Van der Waals heterostructures[10]. In these structures, we have atomic control of the layer thickness for each material, allowing the possibility to create artificial crystals not found in nature, that have unique electronic properties which can be exploited for devices. A prime example is the vertical tunnelling field effect transistor reported by the University of Manchester in 2010[11]. Again, the realisation of such devices stems from fundamental understanding of the electronic behaviour of individual layered crystals.

Since its discovery in 2004, the electronic properties of graphene have been studied extensively. This has been owed to its unique crystal symmetry which harbours massless Dirac fermions, an

`

elementary particle which has been long-sought in particle physics. For example, the anomalous integer quantum hall effect[5], zeroth landau level[12,13] and Klein tunnelling[14] are a few examples unique to graphene. Nearly fifteen years on, and we are still finding new physics in graphene. This is owed to the advance in sample preparation and improved fabrication of high quality devices. In this thesis, we study transport phenomena in such high quality devices, focussing on transport behaviour at elevated temperatures. As a result, we have found a number of exotic transport phenomena unique to graphene.

In Chapter 2, we provide a brief history on the development of graphene devices over the past fifteen years. Here, we introduce the basic electronic properties of graphene and describe different transport experiments that have been performed. In particular, we focus on the evolution of high quality graphene samples and the physics which can be found there.

In Chapter 3, we describe the theoretical concepts related to hydrodynamic electron flow. This section focuses on electron-electron interactions in graphene, where electron transport is dominated by like-particle collisions and current flow is governed by the Navier-Stokes equation. This section contains the background for the experimental work presented in Chapters 6 and 7.

In Chapter 4, we revisit the foundations of solid state physics and the band theory of electrons in periodic potentials. First, we cover Bloch's theorem, a huge milestone which describes the peculiar nature of quantum mechanics. Second, we look at Bloch electrons in magnetic fields. Third, we combine the two effects and introduce the even more peculiar behaviour of Bloch electrons in magnetic fields and periodic potentials. Here, we introduce the concept of zero effective magnetic field, where electrons expel the magnetic field when the cyclotron radius becomes commensurable with the spacing of the periodic potential. This chapter is essentially theoretical support for the experimental work which will be presented in Chapter 8.

In Chapter 5, we outline experimental techniques and fabrication procedures which have been used for all of the experimental work in this Thesis.

In Chapter 6, we demonstrate one of the first experimental signatures of hydrodynamic electron flow in graphene/hexagonal boron nitride (hBN) heterostructures.

In Chapter 7, we build on Chapter 6 and perform experiments on graphene nano-constrictions/classical point contacts and perform experiments at the cross-over of the ballistic to hydrodynamic regime. Here, we demonstrate the transport becomes super-ballistic in the hydrodynamic regime, and the conductivity exceeds the semi-classical limit allowed for single-particle ballistic transport.

`

In Chapter 8, we switch our experimental system to a graphene/hBN superlattice, and study transport at non-cryogenic temperatures. Here, we find magneto quantum oscillations, which are un-related to any previously observed oscillatory phenomena and have rather unique properties.

Finally, in chapter 9 we provide a brief summary and outlook on future experiments related to Chapters 6-8.

`

Chapter 2 - Electron transport in graphene/hexagonal-boron nitride heterostructures

Here we introduce our experimental system; graphene encapsulated with hexagonal-boron nitride. These devices have gained extensive research efforts over the past decade due to the extremely high-quality and cleanliness of the graphene channel. This chapter is structured as a time line, where we show the evolution of graphene devices and the development of electron transport studies that accompanied this. First, we cover the basic electronic properties of graphene and hexagonal boron-nitride. Second, we introduce two familiar and well-studied transport regimes which are both accessible in graphene; the diffusive and ballistic regime. Here we introduce a variety of concepts and experiments which are already well known to the 2DEG) community and are often referred to in this Thesis.

`

2.1 The Electronic properties of Graphene and hexagonal boron-nitride

Graphene

Graphene is a rather unique electronic system. Intrinsically, it is a zero-gap semiconductor which hosts quasi-particles that follow linear energy dispersion as described by the Dirac equation and move relativistically with a zero effective mass. Furthermore, the band structure in graphene is electron-hole symmetric about the crossing of the conduction and valence band, also known as Dirac points. This symmetry allows electron and hole excitations to be described by the same Dirac equation, resulting in such exotic phenomena as Klein Tunnelling[14].

The unique electronic properties of graphene are owed to its distinct crystal symmetries. In a graphene lattice, the "s" and "p" atomic orbitals for each carbon atom hybridise to form three sp^2 orbitals and one spare p_z orbital (Fig. 1a). The sp^2 orbitals make in-plane covalent bonds, called σ bonds, with three neighbouring carbon atoms, forming a hexagonal lattice structure (Fig. 1b). The remaining P_z electrons form an additional π bond (Fig. 1b) with neighbouring atoms. Notably, it is these π electrons that are responsible for the extraordinary electronic properties in graphene. The resulting honeycomb lattice (Fig. 1c) contains two carbon atoms per unit cell with a lattice constant $a \approx 2.42$ A. The corresponding Bravais lattice is described by two interpenetrating triangular sub-lattices (A and B in Fig. 1c) that are occupied by two in-equivalent carbon atoms.

As for the band structure, quantum mechanical hopping between the crystal sublattices produce two overlapping energy bands that intersect forming a zero gapped linear dispersion (Fig. 1d). This result was first derived analytically in a tight binding approach by Wallace[15] in 1947 by considering electrons in the π bonds of the graphene lattice, hopping between neighbouring lattice sites. The resulting band structure of the full calculation is shown in Fig. 1d. The conduction and valence bands cross at six special points in the corners of the Brillouin zone, forming gapless Dirac cones. However, only two Dirac cones are non-equivalent. This means that graphenes' band structure hosts two indistinguishable Dirac points, which are referred to as the K and $K^{'}$ points. This symmetry creates a 4-fold degeneracy in the density of states (two valley and two spin degeneracies).

`

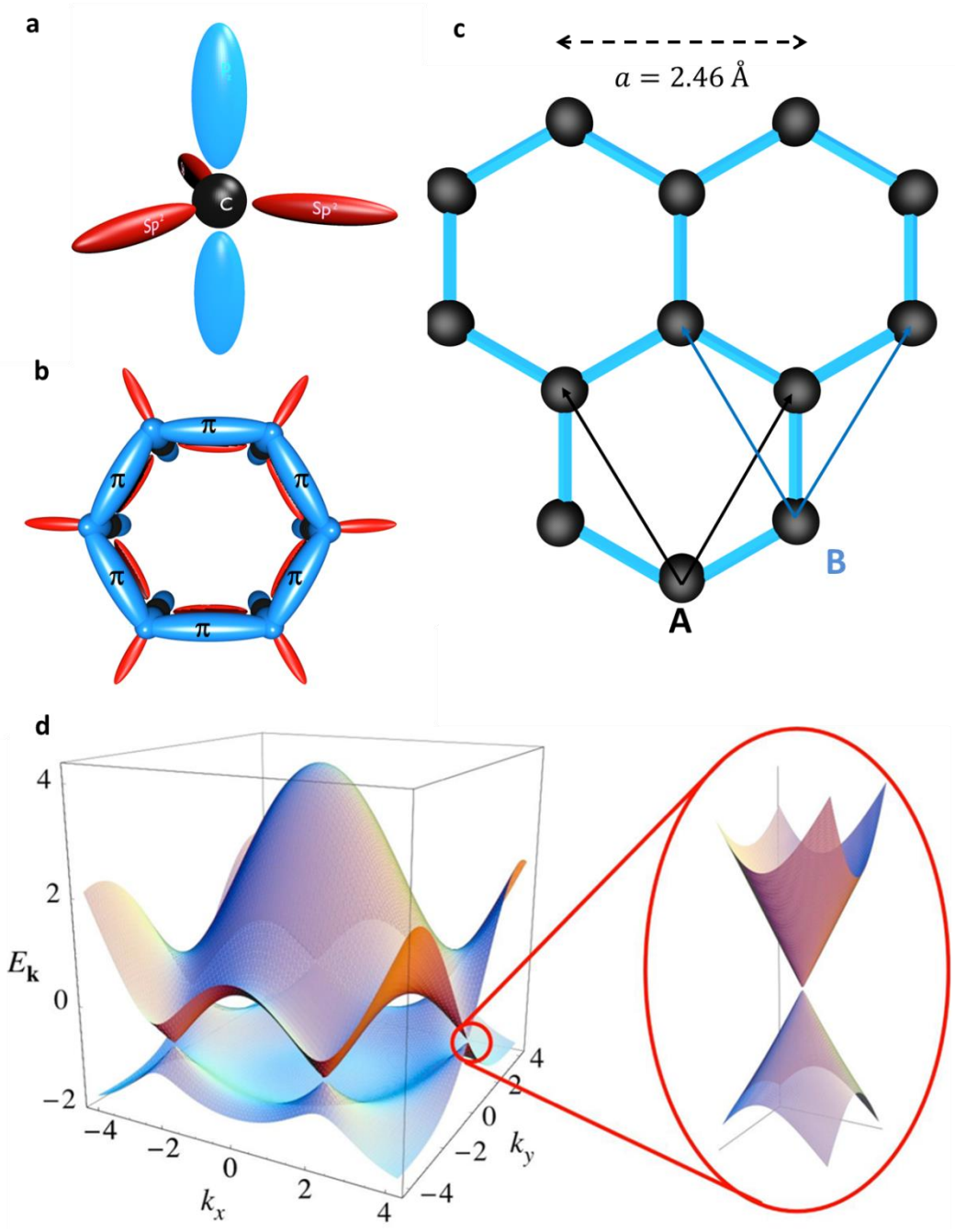

Figure. 1 crystal structure of graphene. **a,** An illustration of Sp^2 hybridisation in carbon atoms. **b,** demonstration of how Sp^2 bonding leads to a hexagonal structure. **c**, The hexagonal crystal structure of graphene is built from two interpenetrating triangular Bravais lattices called the A and B sublattice. The sublattice vectors are drawn as black and blue arrows for the A and B sublattice respectively. **d,** This three-dimensional plot shows the full calculation of the band structure of graphene within the 1st Broullin zone[9]. The low energy dispersion is magnified (red circle) and shows how Dirac points form from the two overlapping sublattice bands.

`

Intrinsically the Fermi-level sits exactly at the Dirac point where the density of states (DOS) is zero. However, by electrostatic gating graphene devices we can dope charge carriers and study electron transport of relativistic Dirac quasi-particles. To demonstrate the most basic electronic properties of graphene, we will look at experimental data measured with the first graphene devices[16]. Figure 2a shows a schematic of the device architecture; a graphene flake is placed on to a silicon dioxide (SiO_2)/silicon (Si) substrate and is contacted by gold. The SiO_2 and Si act as a dielectric and gate electrode respectively, which allows electrostatic doping of the graphene channel by applying a gate voltage, V_G (Fig. 2b). Figure 2c plots the longitudinal resistivity ρ_{xx} as a function of back gate voltage V_G. At V_G = 0 V, a sharp peak in the resistance is observed, corresponding to the Fermi-level sitting at the Dirac point where the DOS is at a minimum. At finite V_G, the DOS increases and the resistance drops quickly as the Fermi-level is moved away from the Dirac point, irrespective of the polarity of V_G, reflecting the electron-hole symmetry in graphenes' Dirac spectrum. These devices showed remarkably high quality, with a carrier mobility $\mu \approx 15{,}000$ cm^2/Vs at T = 4.5 K, despite transport being dominated by extrinsic effects such as scattering from defects and impurities[16]. Notably, the most detrimental source of extrinsic scattering occurs with charge impurities and surface phonons at the SiO_2/graphene interface[17]. As discussed in an experimental work featuring in Nature Nanotechnology[18], the intrinsic mobility of graphene is nearly two orders of magnitude larger than that obtained for graphene on SiO_2. In the following chapters, we describe the current methods for fabricating high-quality graphene samples with carrier mobility's approaching this intrinsic limit.

`

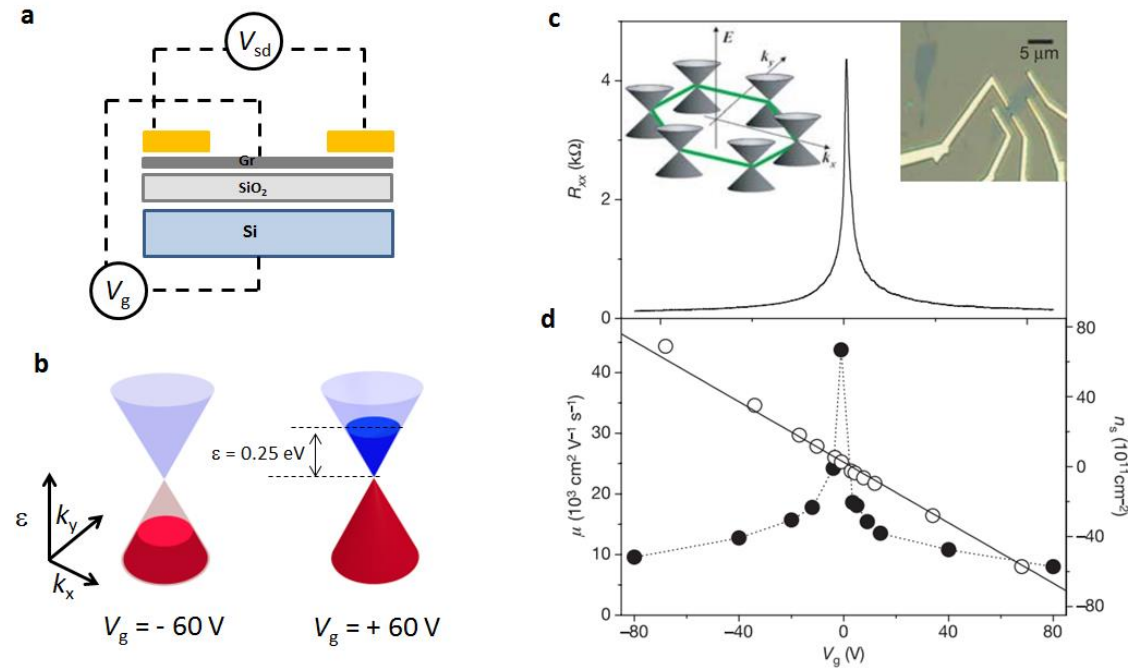

Figure. 2 Basic operation of a graphene on SiO_2 FET. **a,** device schematic of a graphene FET. Current is passed through the graphene layer between two gold electrodes by applying some voltage V_{sd}. A gate voltage (V_G) is applied between the graphene and silicon substrate to dope the channel. **b**, Schematic of the Fermi-level filling in Dirac cones in the presence of an applied gate. Negative V_G (left panel) dopes graphene with holes, and positive (right panel) with electrons. **c,** resistivity as a function of V_g for a graphene FET at T = 4.2 K. **d,** mobility (left axes) calculated from resistivity data in **c**. The carrier density (n_s) as a function of V_G is plotted on the right axes. Data in **c** and **d** is taken from ref (16).

Hexagonal Boron Nitride

Since the discovery of graphene, a number of other 2D crystals with different electronic properties followed. Amongst all of them, hexagonal boron nitride (hBN) is perhaps the most complimentary to graphene and has become a crucial ingredient for building high quality, clean heterostructures based on graphene and other 2D materials. Here we briefly discuss the main properties and applications of hBN.

Similar to graphene, hBN is a layered structure built of atomic planes that have a hexagonal crystal lattice. However, instead of carbon, hBN hosts two distinguishable atoms per unit cell; boron and nitrogen (Fig. 3a). Although boron and nitrogen are adjacent to carbon in the periodic table, hBN has

drastically different electronic properties to graphene. In contrast to graphene, the sublattice symmetry within the hexagonal lattice is broken, since the atoms occupying the A (boron) and B (nitrogen) sub lattice are in-equivalent (see red and blue circles Fig. 3a). Consequently, hBN is a wide band gap (5.97 eV) insulator. It does however have a very similar lattice constant (Fig. 3a) to graphene, differing only by 1.8 %. Because of the small lattice mismatch between graphene and hBN, atomically thin heterolayers can be stacked on top of one another with little influence from strain. Furthermore, the interfaces between heterolayers can be smooth, free of defects and are atomically flat, creating an ideal interface. Owed to its atomic flatness and electrical inertness, hBN is often used as an ideal substrate for making graphene devices, removing the detrimental effects of surface roughness. Graphene on hBN field effect transistors were first fabricated by the Columbia group in 2010[19], exhibiting far superior mobility ($\mu \approx 50{,}000$ cm^2/Vs) and homogeneity to graphene on SiO_2[5]. A device schematic is drawn in Fig. 3b demonstrating how a graphene (blue lattice) on hBN (green substrate) heterostructure is etched in to a hall bar device.

To measure the quality of the graphene/hBN interface, the experimentalists measured surface roughness by atomic force microscopy (AFM). Figure 3c shows a histogram of surface roughness of different substrates[19]. We can see that the roughness for graphene on hBN (blue squares) is almost equivalent to the bare hBN (red circles), suggesting graphene forms an atomically flat interface with hBN. In contrast, the graphene on SiO_2 devices (black triangles) exhibit nearly three times more surface roughness. A further engineering step was employed by the Manchester group in 2011[20] to improve the quality of graphene devices even further. They placed a second hBN layer on top of the graphene to encapsulate it (Fig. 3d), protecting it from both substrate roughness and ambient conditions. These devices exhibited even higher carrier mobility than graphene on hBN, approaching the intrinsic limit ($\mu \approx 500{,}000$ cm^2/Vs at low temperatures) which corresponds to a mean free path of a few microns. Encapsulating graphene with hBN has pushed the operation of graphene based devices in to the ballistic transport regime, where the electron mean free path is comparable to the dimensions of the channel.

`

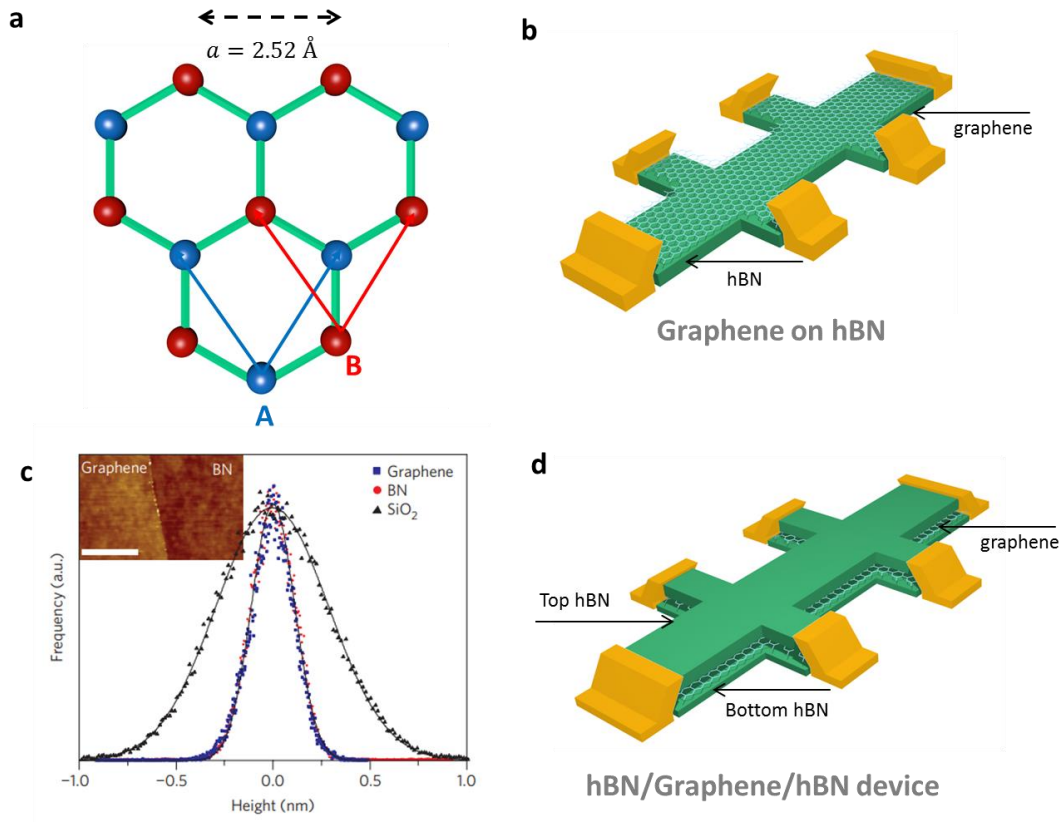

Figure 3 Hexagonal boron nitride in graphene heterostructures a, The crystal lattice of hBN. The blue circles are nitrogen atoms whilst the red are boron atoms. **b,** device schematic of graphene devices supported by an hBN substrate, the yellow shapes are gold electrical contacts. **c** a histogram of surface roughness for different graphene devices[21]. The micrograph shows an AFM image of graphene on hBN (left panel) and bare hBN (right panel), the two are almost indistinguishable. Scale bar: 0.5 μm.

2.2 Quasi-ballistic, Drude-like transport in Graphene

At non-cryogenic temperatures, transport in bulk metals and semi-conductors is diffusive, where carriers scatter very frequently with impurities and phonons (lattice vibrations). When a potential difference is applied, the electrons gain some "average" velocity in the direction of the resulting E-field and "diffuse" slowly down the potential.

The diffusive regime is best described by the Drude model, which applies the simple kinetic theory of classical gas particles to electrons in crystals. In brief, when an electric field is applied to a crystal, electrons are accelerated following straight trajectories unperturbed by external forces. Their momentum increases until they scatter with lattice vibrations or impurities where they suffer momentum loss. In other words, electron momentum changes, on average, over the time scale, τ,

`

defined by the rate of elastic and inelastic collisions. The electrons therefore move with an "average" velocity, known as the drift velocity that is determined by solving the equations of motion for a charged particle in an electric field. Knowing this, the current density is then determined by the following equation known as Ohms law

$$J = \sigma E\ ,\ \sigma = \frac{ne^2\tau}{m^*} = ne\mu \tag{1}$$

where the conductivity, σ, is governed by the time between scattering events, τ, the electron density, *n*, and the effective mass of an electron in a crystal, m^*. For the case of massless Dirac fermions in graphene, m^* is replaced by the cyclotron mass m_c[22]. Equation (S1) is essentially a modified version of Ohms first law, which states that the current *I* flowing through a conductor is proportional to the voltage drop *V* across it.

$$V = IR, \quad R = \frac{L}{AW\sigma} \quad , \quad R = G^{-1} \tag{2}$$

Where the resistance *R* (reciprocal of conductance G^{-1}) depends both on the geometry (*L* is the length, *W* is the width and *A* is the cross-sectional area of a three dimensional sample) and material properties (σ). The conductivity is often recast in terms of electron mobility, μ, according to equation (1). In our graphene samples, we measure conductivity and carrier density (by Hall Effect measurements), which allows us to determine μ . Figure 4a plots resistivity for one of our graphene devices at 100 K. The corresponding mobility is plotted in Fig. 4b for a few different temperatures. The mobility is around 300,000 cm^2/Vs at 50 K, exhibits little temperature dependence and persists to about 100,000 cm^2/Vs at room temperature. Knowing the effective mass, $m_c = \hbar\sqrt{n\pi}/v_f$, and the Fermi-velocity, v_F, of graphene, we can also estimate the mean free path between collisions,

$$l_{mfp} = \frac{\mu\hbar}{e}\sqrt{n\pi} \tag{3}$$

where $\hbar$ is a reduced plank constant, and $\sqrt{n\pi}$ is the Fermi wave vector, k_F, in graphene. At low temperatures the mobility translates in to a mean free between 1-4 μm (Fig. 4c). Notably, this is roughly equal to the size of our samples, where our devices typically have a width between 1 and 4 μm. This means that the dominant scattering process for electrons in our graphene samples is with device edges. There are no defects or impurities in the graphene channel and the electrons travel ballistically until they scatter at device boundaries. We refer to such behaviour as the ballistic regime of electron transport, where the electron mean free path is larger than the conducting channel. Although the Drude model is usually only applied for diffusive electron flow, it has much more elementary significance. The scattering time, τ, which is found in equation S1, describes all

`

momentum non-conserving collisions. Even in the ballistic regime, we can define some scattering time τ, and measure a Drude-like conductivity. The only difference compared with the diffusive regime is that τ is much larger and the scattering have a different microscopic mechanism. Of course there are also a number of different ballistic phenomena that occur, but these require different device geometries and equations for their modelling.

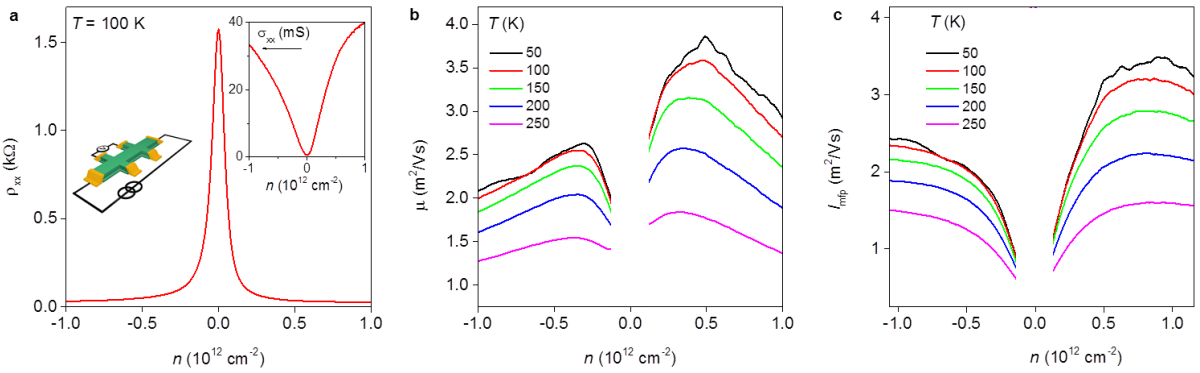

Figure 4|Mobility in typical encapsulated graphene devices. a, longitudinal resistivity as a function of carrier density *n* measured at *T* = 100 K. The measurement geometry is sketched in the micrograph. Inset: corresponding conductivity $\sigma_{xx} = 1/\rho_{xx}$. **b,** Mobility μ as a function of carrier density *n* plotted for a few different temperatures *T*. **c,** The corresponding mean free path (l_{mfp}).

2.3 Ballistic transport in Graphene

Landauer/Sharvin conductance

In the previous chapter, we used the Drude model (1) to determine the mobility of our graphene samples and we extracted a mean free path corresponding to the width, *w,* of our sample. According to equation (2), if we decrease the length of our sample, *L,* the resistance tends to zero and the measured conductance *G* would tend to infinity. Experimentally however, when *L* is decreased below the mean free path, *G* starts to saturate and is limited by the width of the channel. This is because in the ballistic regime carriers do not scatter or thermalize in the conductor, and instead *G* depends only on the number of one-dimensional electron modes that can fit in the channel. Moreover, quantum mechanics tells us that each mode carries a conductance value of e^2/h. This is the minimum possible value for conductance in any metal. These qualitative statements are underlined in the derivation of the Landauer formula[23,24] where the conductance is calculated by considering the transmission of one-dimensional (1D) electron modes between electrical contacts through an ideal conductor (Fig. 5a). From this, we arrive at the following solution.

`

$$G_b = N \frac{e^2}{h} M \quad (4)$$

Where G_b is the ballistic conductance, *N* is the degeneracy for each mode and *M* is the number of 1D conducting modes. In very narrow channels, where the width *w* is comparable to the Fermi wavelength (λ_F) the conductance becomes quantized and increases in steps of integer values of e^2/h as the Fermi-level increases and more modes are populated. Consequently, a set of plateaus are observed at intervals Ne^2/h in G_b as the Fermi-level or *w* increases. This size quantization was first observed in GaAs-AlGaAs heterostructures (Fig. 5b), where quantum point contacts with narrow channels was made by depleting specific regions of the 2DEG using split gates[24]. In the case of $w >> \lambda_F$, we can still use the formalism of 1D propagating modes, which is determined by calculating the number of stationary states in a box of size *w*. We then find $M = k_F W/\pi$ and obtains the ballistic conductance for wide channels

$$G_b = \frac{Ne^2}{h}\frac{2W}{\lambda_F} \quad (5)$$

where λ_F in graphene is $2\pi/\sqrt{n\pi}$ and the factor of 4 accounts for spin and valley degeneracy. We note that equation (5) is exactly the Sharvin formula, which can also be obtained in a semi-classical approximation by considering the angular distribution of electrons in a 2DEG passing through a small aperture or constriction[25]. Equation (5) is essentially the macroscopic version of equation (4), where the width of the channel is much larger than the Fermi-wavelength.

For graphene devices, it is rather difficult to approach the limit of equation (4), because of the difficulty in defining narrow channels. The split-gate technique used for 2DEG devices does not work because of Klein tunnelling[14]. Instead, point contacts in graphene can be defined by etching constriction geometries in to heterostructures[26] (Fig. 5c), or by current annealing suspended graphene samples[27]. Previous works demonstrated quantisation of Dirac electrons (equation 4) in such devices at low temperatures[27,26] (Fig. 5d). In this work, we study electron transport through wide point contacts where $w >> \lambda_F$ and the conductance is described by equation (5). In this chapter we have not mentioned anything about scattering; the equations derived are based on electrons propagating without loss of momentum. In this thesis, we study the effects of electron-electron scattering in the ballistic conductor (see Chapter 5).

`

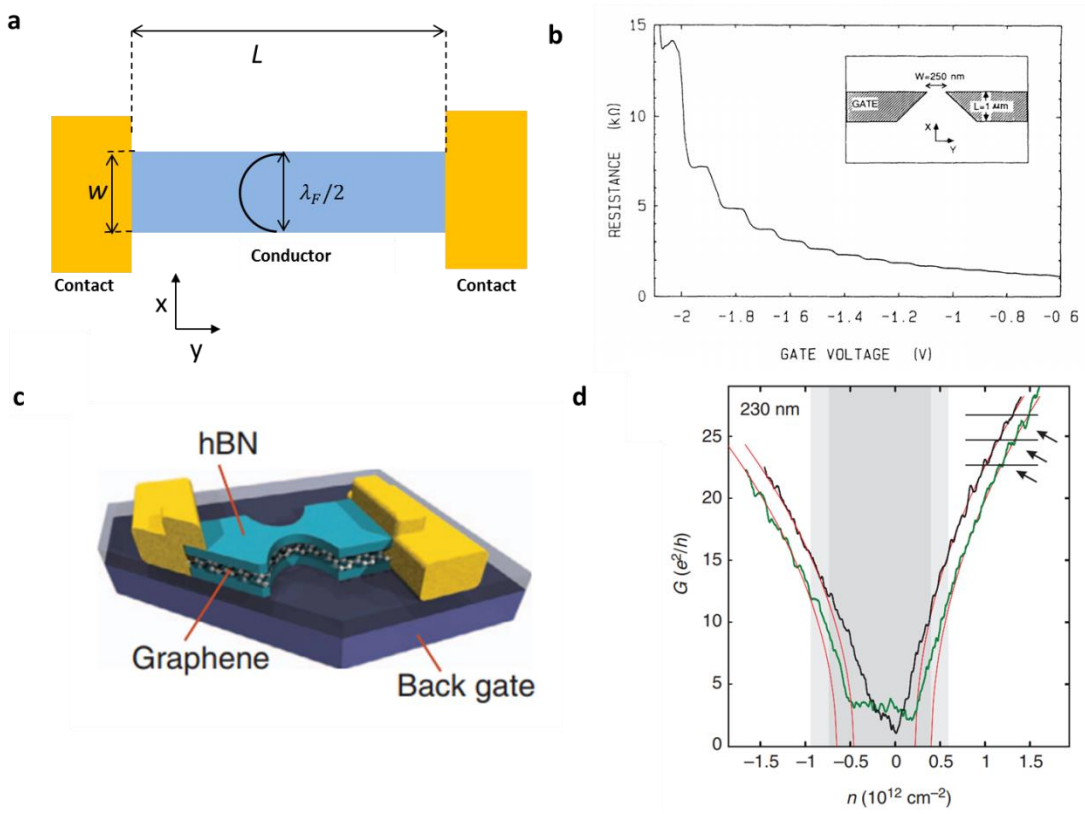

Figure 5| Ballistic conductance in narrow channels. a, a schematic demonstrating the quantisation of electron wave functions in a narrow channel. The ideal conductor (blue rectangle) allows only electrons which occupy stationary modes (with respect to the y direction). **b,** resistance through a split-gate quantum point contact[28] as a function of gate voltage measured at 2.5 K. Clear plateaus can be seen corresponding to integer values of $2e^2/h$. This is due to the narrowing of the channel when voltage is applied to the split gates. **c,** device schematic of a graphene point contact taken from the work of Ref. 26. **d**, measured conductance[26] through such a device as a function of carrier density *n* (Fermi energy) at $T = 2$ K. Kink like features occur in intervals of $4e^2/h$ due to quantisation.

Bend resistance and Magnetic focussing

In the ballistic regime, the steady-state current distribution can look very different to that in the case of diffusive flow, where electrons follow random paths due to frequent scattering and drift slowly in the direction of the applied electric field. This is because electrons injected from the current source contact follow their initial trajectory for long distances without scattering. In the case of a small drive current, the carriers propagate in all directions out of the source contact unperturbed by the force due to the applied electric field, because the kinetic energy of carriers is far larger than the potential energy produced by the field. Consequently, carriers fly everywhere and collect in different regions of the device, producing a build-up of charge that creates peculiar potential distributions in the

`

sample. In general, the standard longitudinal geometry employed for measuring conductivity is insensitive to the ballistic nature of electrons. However, special geometries are employed to study these electron trajectories. Below we summarise a few experiments that confirm the ballistic nature of graphene's charge carriers.

First, let us take a look at the so-called bend geometry. Figure 6a sketches a device schematic and measurement scheme. The hBN/graphene/hBN heterostructure (green region) is patterned in to a cross. Current is passed between contacts 1 (high) and 2 (low), and the voltage is measured between contacts 3 (high) and 4 (low). In a diffusive flow, charge carriers follow the electric field lines that bend around the cross as they diffuse slowly to the drain contact 2. In this regime we measure a positive resistance. In contrast, ballistic electrons injected at contact 1 shoot straight across the device area collecting instead at contact 4 (Fig. 6a). Charge carriers build up at contact 4 which, in this configuration, creates a negative potential distribution due to the absence of charge carriers at contact 3. Typically the measured voltage is normalised by the source current such that the phenomena is referred to as "negative bend resistance". A demonstration of such an experiment was made by the Manchester group in 2011[20] where a strong negative bend resistance (Fig. 6b) was found to persist up to room temperature, demonstrating the robust, ballistic nature of electrons in graphene.

In a second experiment, one can study transverse magnetic focussing. Here, a non-local geometry is employed (see Fig. 6c.). By applying weak magnetic fields, B, we can bend trajectories of ballistic electrons and guide them towards the voltage probes. Similar to the bend resistance experiment, carriers collect at the voltage probes, provided the mean free path is larger than the cyclotron trajectory required to "focus" those electrons, and we measure a positive potential drop between contacts 3 and 4. Again, the potential difference arises due to the absence of carriers at contact 4. More importantly, we only detect electrons that have a cyclotron radius commensurable with the distance between the current injector and voltage probe. Therefore, as we sweep B, we measure a set of peaks which reflect this commensurate condition. Figure 6d shows a map of the measured resistance (V_c/I_i) as a function of B and n, for a magnetic focussing experiment made in graphene by researchers at MIT[29]. For a fixed n, we can resolve three peaks which seem to occur periodically with the applied B. To explain these features, the micrographs above the panel sketch trajectories for which those peaks correspond to. The blue arrow indicates trajectories which are directly focused in to the voltage probes. In contrast, the red and yellow arrows point to those which have undergone one or two reflections at the boundary respectively. In graphene devices, magnetic focussing has

`

been demonstrated over distances as large as 6 μm[30]. These ballistic experiments demonstrate the high quality of encapsulated graphene samples.

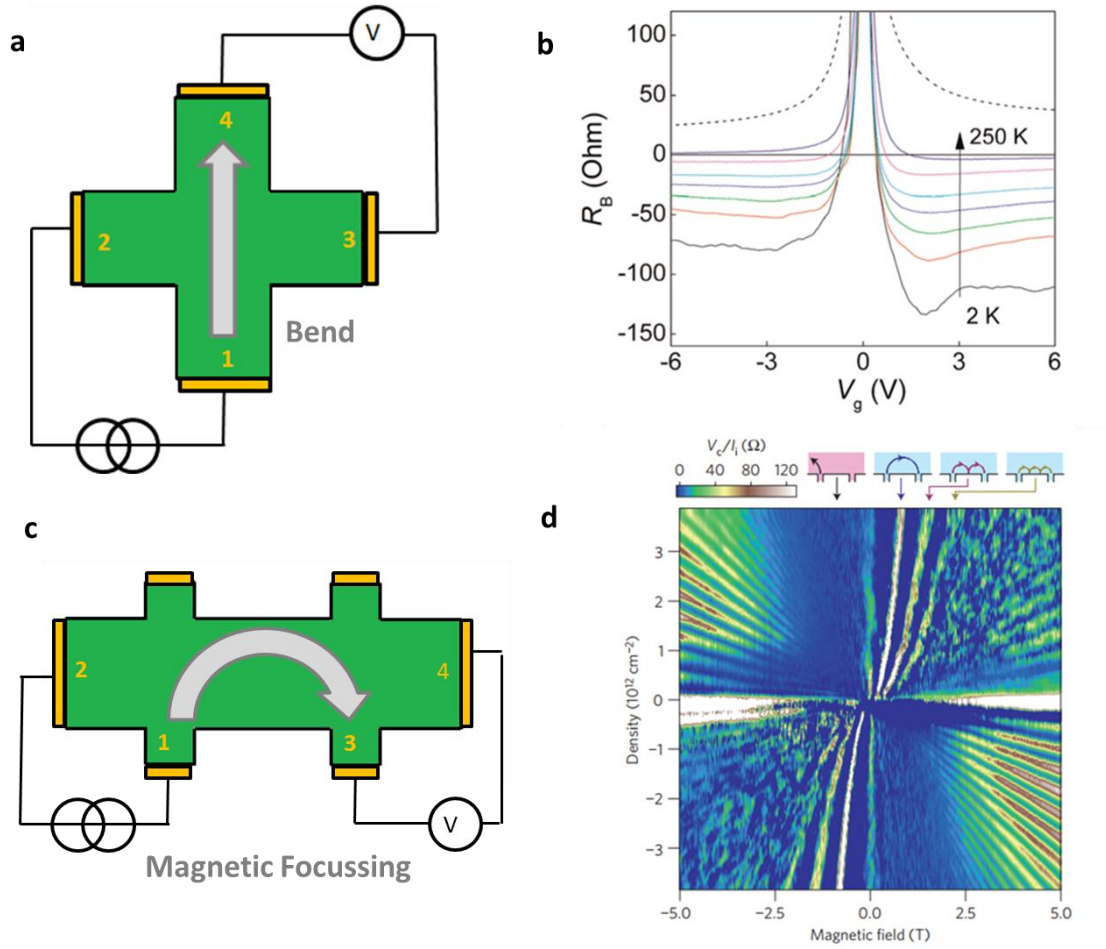

Figure| 6 Ballistic experiments in graphene/hBN heterostrucutres. a, Device schematic of a graphene device shaped in to a cross for bend resistance experiments. Current is passed from 1-2 and voltage is measured from 3-4. **b,** bend resistance R_B as a function of back gate voltage V_g for temperatures between 2 K (black curve) and 250 K (purple curve). Black dotted line is the Drude-like contribution expected for diffusive flow. Data is taken from (ref. 20) **c,** Device schematic for magnetic focussing measurements in a graphene hall bar. Contacts numbered the same as in **a**. **d**, maps of the measured resistance, *V*/I, as a function of magnetic field (x-axis) and carrier density (y-axis). Data is taken from (ref. 29).

`

2.4 Electron-phonon scattering in graphene

In conventional III-V heterostructures, the carrier mobility of high quality samples is around 10,000,000 cm^2/Vs at liquid helium T[31] (an order of magnitude larger than typical graphene/hBN heterostructures). However, their mobility degrades quickly upon increasing T due to the activation of polar optical phonon modes which scatter in-elastically with charge carriers[32]. These types of phonons are only found in polar crystals, when the two atoms in the unit cell have some differing charge, and limit the intrinsic room temperature mobility to around 2000 cm^2/Vs.

In contrast, high-quality graphene devices have room temperature mobility of around 100,000 cm^2/Vs, with the possibility of observing ballistic phenomena even at 250 K (Fig. 6b). This is because the unit-cell of graphene contains two equivalent carbon atoms, which have no inherent polarization (Fig. 1a) such that polar optical phonons do not exist. Therefore, only acoustic phonon modes limit the intrinsic mobility of graphene[33]. As we show in the next chapter, the reduced electron-phonon interaction of graphene allows us to study a peculiar transport regime which is dominated instead by electron-electron interactions.

`

Chapter 3 – Hydrodynamic electron transport in graphene

In the previous chapter, we discussed the ballistic and diffusive transport regimes of graphene. In conventional GaAs 2DEG systems, electron transport is qualitatively similar. Electrons are ballistic at liquid helium temperatures, where one can observe also size quantisation/magnetic focussing etc., but transition to a diffusive regime upon increasing *T* due to increased scattering with phonons. In graphene however, electron-phonon scattering is rather weak and we can see ballistic phenomena all the way up to room temperature (Fig. 6b), whilst optical phonons in GaAlAs heterostructures kill ballistics by about 30 K. Because of this, electron-electron collisions play a dominant role in graphene at high temperatures. In this section we introduce the idea of hydrodynamic electron flow, where electrons experience frequent e-e collisions and move collectively like a fluid. We show that in this regime, electron viscosity strongly influences electron transport in graphene and leads to a number of astonishing phenomena.

`

3.1 Hydrodynamics

Hydrodynamics is a macroscopic theory that describes the transport of fluids; a system of particles that undergo frequent collisions with each other. The collisions are so frequent that the particles making up a fluid element are always in equilibrium, such that they move collectively when perturbed by an external force. This collective behaviour results in a number of peculiar flow patterns, where different parts of the fluid propagate at different speeds as momentum loss diffuses slowly through it. A classic example of this is presented in Fig. 7a, which shows the two dimensional Poiseuille flow of a viscous fluid (blue area) in a pipe. The blues arrows represent the magnitude of flow velocity at different points in the fluid along the y-direction. A longer arrow indicates larger velocity. We can see that the fluid moves slower at the edges of the pipe and fastest in the middle. This is because the outer layers of the fluid suffer momentum loss at the edges, whereas the central layers are shielded by the outer layers and can move more easily. In other words, the momentum loss diffuses very slowly through the fluid, such that the inner layers essentially do not feel the frictional drag of the walls. The parameter which describes momentum transfer is called the kinematic viscosity, ν, which essentially describes the internal friction of the fluid. If ν was infinitely large, the momentum loss diffuses through the whole fluid and every point in the fluid would propagate at the same speed (Fig. 7b).

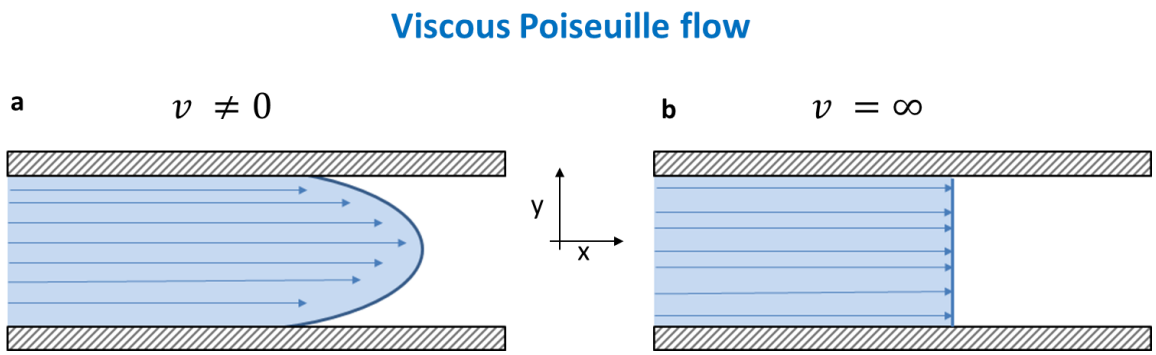

Figure 7| Viscous Poiseuille flow of water flowing in a pipe. The diagrams sketches a fluid (blue region) flowing in pipe (the walls are sketched by grey patterned rectangles) for one with a finite viscosity (**a**) and infinite viscosity (**b**). The dark blue lines and long blue arrows represent the flow pattern and velocity distribution respectively.

The theory of hydrodynamics has been around for nearly two centuries, where the equations of motion governing fluid flow were first derived by Euler in 1755 to describe ideal classical fluids[34]. The problem involves solving partial differential equations for some thermodynamic parameters of the system at any point in space or time. For example, the velocity field *v*(x,y,z,t) could be determined,

`

which tells us the velocity of a fluid element (an infinitely small region of the fluid) at any spatial co-ordinate for a given time. The starting point for hydrodynamics originates from two equations, the continuity equation (conservation of mass) and Euler r's equation (conservation of momentum).

$$\frac{\delta\rho}{\delta t} + \nabla \cdot \mathrm{j} = 0 \qquad \text{Continuity equation (6)}$$

$$\frac{\delta \mathrm{v}}{\delta t} + (\mathrm{v} \cdot \nabla)\mathrm{v} + \frac{1}{\rho}\nabla \mathrm{p} = 0 \qquad \text{Euler's fluid equation (7)}$$

Where *p*, ρ, *v*, and *t* are pressure, density, velocity and time respectively, and j = ρ*v* is the mass flux density. These equations describe idealised fluids, sometimes called perfect fluids, which exhibit no shear stress, viscosity or heat conduction[34]. Shortly after this, Navier, Poisson, Saint-Venant and Stokes derived an alternative form of Euler's fluid equation to account for energy dissipation within the fluid

$$\rho\left[\frac{\delta \mathrm{v}}{\delta t} + (\mathrm{v} \cdot \nabla)\mathrm{v}\right] + \nabla \mathrm{p} - \eta \Delta \mathrm{v} + \left(\xi + \frac{1}{3}\eta\right)\nabla(\nabla \cdot \mathrm{v}) = 0 \qquad \text{Navier-Stokes equation (8)}$$

where $\eta = \nu\rho$ is the dynamic/shear viscosity and ξ is the bulk viscosity, which describes the resistance of the fluid to compression. By solving this equation we could obtain the flow behaviour illustrated in Fig. 7.

3.2 Hydrodynamics in the electron liquid

Two hundred years on and the hydrodynamic theory is now being used to study viscous flows of strongly interacting quantum fluids. For example, the shear viscosity of quantum liquids[35] like He^3 and He^4, cold atom gases[36] and quark-gluon plasmas[37] have been measured only very recently. However, only a few theoretical efforts and experimental techniques have been proposed[38] to measure viscosity of a two-dimensional electron liquid. This is in part is due to the lack of hydrodynamic behaviour in any 2DEG system.

Hydrodynamic electron flow refers to a transport regime where electron-electron collisions are so frequent that macroscopic variables like velocity are governed by equation's (7) and (8). This idea was first put forward by Gurzhi in the 1960's[39,40] where he proposed a transport regime in metals dominated by e-e collisions (Poiseuille flow). He suggested that the resistivity of a metallic system should change non-monotonically upon increasing temperature due to the interplay of different scattering mechanisms, including a dominant presence of e-e collisions. His result is summarised in Fig. 8a, which plots *T* dependence of longitudinal resistance *R* (T) for a metallic system. Upon increasing temperature, the resistance first drops due to a decrease in the electron viscosity as e-e

`

collisions increase. Then at some characteristic temperature T_3, the resistance starts to grow (the usual behaviour expected for a metal) as electron-phonon scattering starts to overwhelm the system. This effect of course requires the correct system parameters, i.e one where e-e collisions are dominant.

As for experiment, in typical metals and semi-conductors e-e collisions are hidden by the dominance of other scattering mechanisms such as impurities or lattice vibrations, preventing the establishment of local equilibrium required for hydrodynamic flow. We need a system where electron-electron collisions are dominant, and the e-e mean free path l_{ee} is the smallest length scale in the problem. i.e

$$l_{ee} \ll W \ll l_{mfp} \tag{9}$$

Where l_{mfp} is the electron mean free path with respect to momentum non-conserving collisions (scattering with impurities, device edges and phonons) as defined in equation (3), and *W* is the characteristic size of the sample. Unfortunately, even in high mobility systems like (Al,Ga)As 2DEG, it is not possible to reach the hydrodynamic regime because of competing length scales. At low temperature, $l_{mfp} \gg W$ due to the high purity of the 2DEG and frozen phonons. However, l_{ee} is also much larger than *W* because of Pauli-blocking[41] (see next section). Upon increasing temperature, both l_{ee} and l_{mfp} start to decrease. However, l_{mfp} drops at a much faster rate because of low-energy optical phonons which are easily activated in polar materials . In other words, electrons scatter more frequently with optical phonons rather than each other[41]. Consequently, the system transitions from the ballistic (Chapter 2.2) to the diffusive regime without ever seeing the hydrodynamic regime.

Because of the demanding system requirements, there has been only one experimental investigation on hydrodynamic transport in (AlGa)As heterostructures[42]. In this experiment, the authors perform measurements of the longitudinal resistivity and heat the electron gas by applying a large DC current (Fig. 8b). This allowed them to raise the electron temperature (shorten l_{ee}) without heating the lattice and thus avoid activation of optical phonons. They measure non-monotonic changes in the differential resistance which they attribute to a transition between ballistic (when l_{ee} > W) and viscous (when l_{ee} < W) flow regimes upon increasing the electron temperature. Figure 8c shows the measured data taken from ref. 30. At *T* = 2.5 K (bottom curve), *dV*/d*I* starts to decrease at around 10 μA as the system transitions to the Poiseuille flow regime where increasing temperature decreases electron viscosity. At larger drive current (around 50 μA), *dV*/d*I* starts to grow because the

`

lattice becomes hot. Since the observed non-monotonicity was originally described by Gurzhi[39] , it became known as the Gurzhi effect.

However, non-linearity is rather difficult to interpret, and Gurzhi himself criticised the experiment a few years later claiming the interpretation was wrong[43]. A simpler, more insightful experiment would be to study a viscous electron system in a linear response regime (small drive currents). To do this, high mobility clean systems are not enough. We also require non-polar systems where the electron-phonon coupling is very weak. Indeed, graphene demonstrates experimentally that it has weak electron-phonon coupling as indicated by its intrinsically high room temperature mobility. We therefore might expect to find viscous flow in graphene samples, although it is likely to exist at elevated temperatures when l_{ee} is sufficiently small and equation (9) is satisfied.

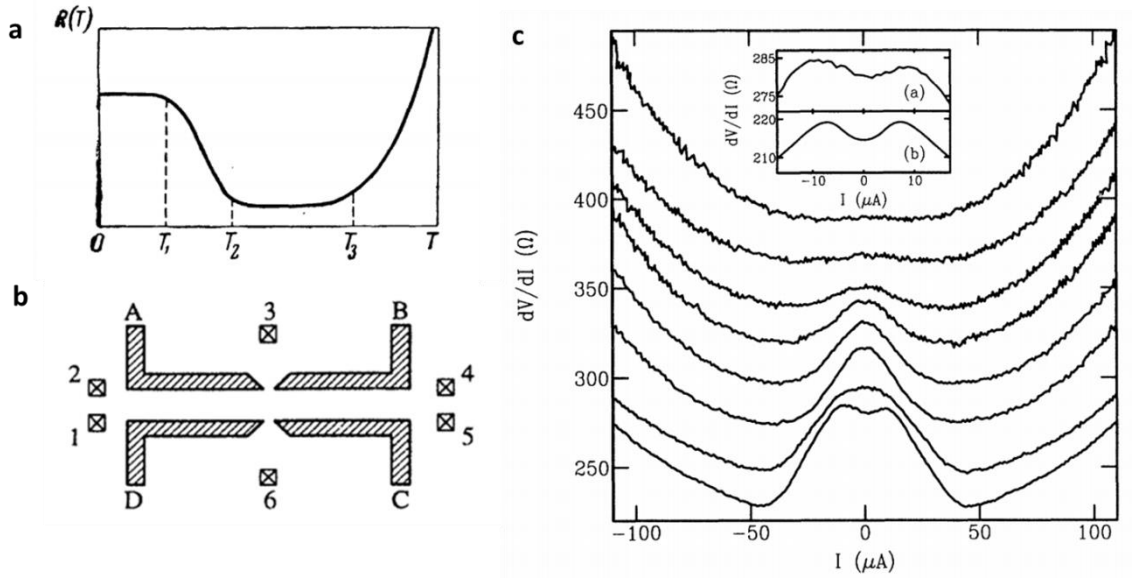

Figure 8| Hydrodynamic electron flow in high mobility samples. a, the proposed temperature dependence of resistance *R*(T) in a metallic conductor with dominant e-e collisions (ref. 39). **b,** Device schematic for the experiment of ref. 42. The patterned rectangles indicate top gates which define the conducting channel. A large drive current is passed between contacts 1 and 5 and the differential resistance *dV/dI* is measured between contacts 2 and 4. **c,** experimental data of ref. 42. The graph plots *dV/dI* (*I*), where *I* is the large DC heating current. The different traces correspond to different *T* ranging from 2.5 K (bottom) to 24.7 K (top).

`

3.3 Electron-electron scattering in graphene

Here, we address the issue of scattering lengths and show that equation (9) is easily satisfied in graphene/hBN heterostructures. As demonstrated in Chapter 2.3, our graphene devices are ballistic throughout the channel. There are no impurities and the only scattering occurs with device edges. It is clear then that at low temperature's (T = 5 K) $l_{mfp} \gg W$. Upon increasing temperature, l_{mfp} shortens as electrons start scattering with the newly activated phonons. In graphene, scattering with phonons is weak due to the non-polar nature of the crystal and only acoustic phonons influence transport. For acoustic phonons in graphene[33], the electron-phonon scattering length $l_{ep} \sim 1/T$.

As for the electron-electron scattering length, l_{ee} at low temperature it is also large. This is because the Pauli Exclusion Principle imposes there must be available states for electrons to scatter within, and the numbers of available states are small due to the restricted phase space. This is illustrated in Fig. 9a, which sketches a 2D Fermi-surface in momentum space at 0 K, where the blue line represents the Fermi level, E_F. Because all states below E_F are occupied, and momentum conservation restricts electrons from scattering in to states above E_F, there are no available states for electrons to scatter in to.

Upon increasing T, the Fermi-surface becomes smeared on the order of K_BT (Fig. 9b) and the number of empty states increases (white circles). As for electron-electron collisions, only electrons with energies within K_BT of the Fermi-energy E_F can scatter. The probability to find an electron within this region (shaded red circle in Fig. 9b) is proportional to K_bT/E_F. Since two electrons are involved in one scattering event, the e-e scattering rate is proportional to $(K_bT/E_F)^2$. From this simple argument, we infer that $l_{ee} \sim 1/T^2$. We note however, that the $1/T^2$ behaviour is only valid in the Fermi-liquid regime, when $K_bT << E_F$.

`

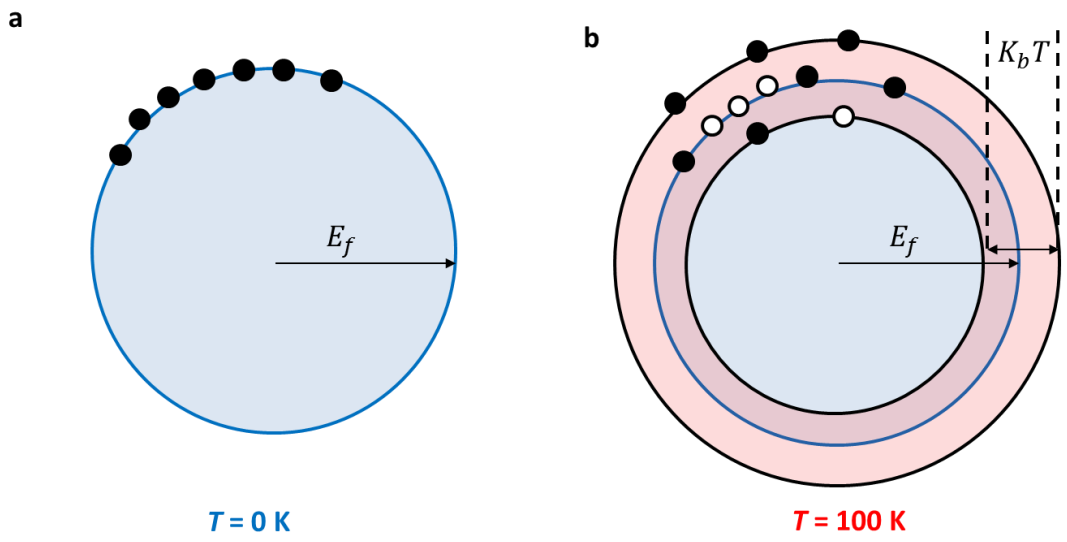

Figure 9| available states for e-e collisions. a, An illustration of electron occupation in the 2D *k*-space at *T* = 0 K. The occupied electron states are represented by the blue shaded circle, with the Fermi-level indicated by the dark blue circumference. The black circles illustrate filled states (electrons). **b,** The same picture at *T* > 0 K. Now the Fermi-surface becomes smeared and there become available states (white circles indicating holes) within a small region (shaded red area) of the Fermi-surface.

Since l_{ee} decays quicker than l_{ep} there should be a temperature range where equation (9) is satisfied. As for experiment, we know that $l_{mfp} > W$ (at least 1 um in our devices) all the way up to room temperature (Fig. 4b). Furthermore, full many-body calculations of the e-e scattering length have been performed in a doped graphene sheet[44], demonstrating that l_{ee} drops below 0.3 um at 200 K (Fig. 10). Therefore, in a first approximation, we expect hydrodynamic flow to on-set around 150-200 K.

`

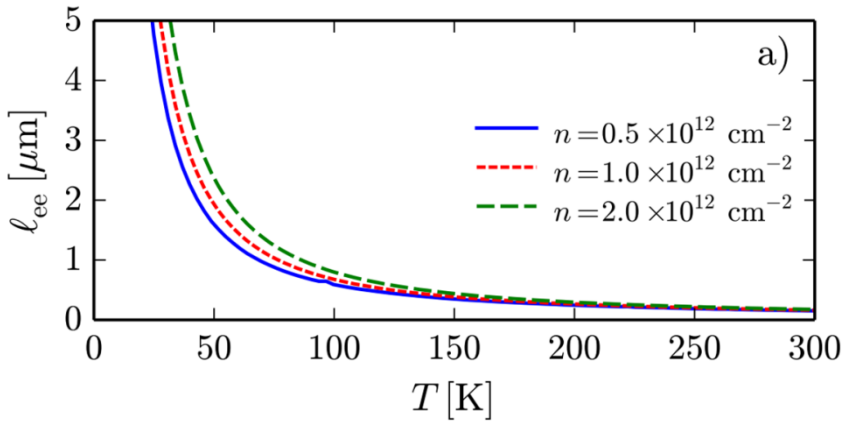

Figure 10| e-e scattering length in doped graphene. Many-body calculations of $l_{ee}(T)$ in graphene, given for a few different carrier densities (ref. 42).

3.4 Viscous electron flow in graphene

In Chapters 5 and 6, we study hydrodynamic electron transport in graphene. To start with, we derive a set of equations which describe hydrodynamic flow of an incompressible viscous electron fluid, under steady-state conditions in the linear response regime. These assumptions greatly simplify the hydrodynamic transport equations in (5) and (6), since all time-derivatives are equal to zero. Instead, we find transport of the two-dimensional electron liquid (2DEL) is described by[45]

$$\nabla \cdot J(\mathrm{r}) = 0 \tag{9}$$

$$\frac{ne}{m_C} \nabla \phi + v\nabla^2 J(\mathrm{r}) = \frac{J(r)}{\tau} \tag{10}$$

where ϕ is the applied potential, n is electron density, m_C is the cyclotron mass of Dirac fermions, and $\tau \equiv l_{\mathrm{MFP}}/\mathrm{v}_F$ is the electron scattering time with momentum non-conserving collisions. Equation (9) is merely the continuity equation for steady-state flow of an incompressible fluid, whilst equation (10) is the Navier-Stokes equation for the viscous 2DEL. The force terms appearing in (10) are the electric field ($\nabla \phi$), the force due to shear viscosity (expressed here as kinematic viscosity v) and a friction term that represents all momentum non-conserving collisions. By solving equations (1) and (4), we can determine the electrical potential ϕ and current density J for any device geometry provided the current source and drain are defined by the appropriate boundary conditions. Finally, we note that equation (10) describes also the transition between viscous and diffusive flow. In the limit of v and τ tends to zero (high temperature regime), the viscous term vanishes and equation (10) takes the usual form of Ohms law (equation 1) which was derived in chapter 1.2.

`

Viscous Poiseuille flow of the electron liquid

In our graphene devices, we can drive current in many different ways. To start with, let us look at the simplest longitudinal geometry where current is driven through the length of a hall bar, resembling fluid flow in a pipe (Fig. 7). If one solves equations (9) and (10) for a given ν, and small τ (and assume for example non-slip boundary conditions), we find a current distribution identical to Poiseuille flow, where the current density is largest in the middle of the channel and zero at the edges. In transport experiments, the benchmark for detecting viscous Poiseuille flow is through measuring the anomalous temperature dependence in the resistivity predicted by Gurzhi[39] . Again, the resistivity of a metal in the viscous regime decreases upon increasing temperature due to a decrease in viscosity. This experimental signature (originally proposed by Gurzhi in his 1963 paper) has remained elusive. Even in high-quality graphene devices, where the viscous regime should be accessible, the resistivity increases monotonically and no sign of Poiseuille like flow can be found. A simple explanation is that the Drude-like resistivity is still large in a standard longitudinal geometry. To amplify the effects of electron viscosity, we can engineer geometries which generate inhomogeneous current distributions. In Chapter 7, we study electron transport through graphene constrictions. Here, we measure the anomalous temperature dependent resistivity predicted by Gurzhi nearly 50 years ago

Viscous electron whirlpools

Instead of longitudinal measurement geometries, non-local geometries can also be used, where current is injected across the width of a hall bar and the voltage drop is measured at a distance where Ohmic flow is negligible. It has been shown that the steady-state current distribution of viscous flow in a non-local geometry hosts vortices/current whirlpools[45,46]. Moreover, these vortices are accompanied by a negative potential region which is found close to the current injector (Fig. 10b). In Chapter 6 we perform transport measurements in a graphene hall bar and employ a unique non-local geometry to search for these negative voltage regions intrinsic to viscous flow.

`

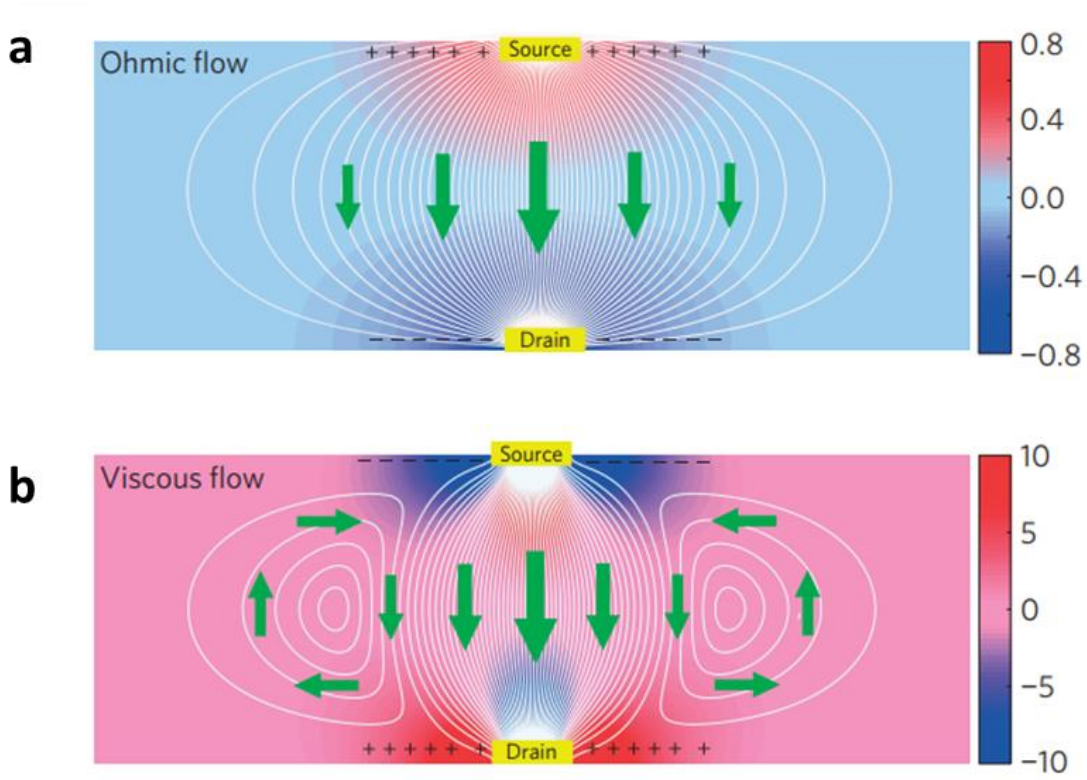

Figure 10| Current vortices in a graphene strip. a, current flow and potential map of a graphene strip in a diffusive regime, where electrical current is injected at the top (Source) and drained at the bottom (Drain). Current (green arrows) flow down the potential as expected. **b,** the current and potential distribution in the viscous regime, obtained by solving equation (10). In the centre of the graphene strip, current flows down the potential. However, adjacent to this, current vortices are formed and strong negative potential regions are found close to the source. The two figures are taken from ref. (44).

`

Chapter 4- Electron transport in a periodic potential and magnetic field

In this chapter, we take a step back and re-visit the fundamentals of solid state physics. We forget about many-body interactions and think simply about single-particle transport. With this in mind, we consider perhaps the most naïve possible question one can ask; how do electrons propagate over such large distances without bumping in to atoms which make up the lattice? To answer this, we have to turn to quantum mechanics and appeal to the wave behaviour of electrons. Taking the problem further, we might wonder how electrons conduct in the presence of a perpendicular magnetic field. Scientists forge whole careers studying electron transport in high-magnetic fields, paying close attention to the quantum Hall effect and exotic many-body states which exist in this regime. This field started with the discovery of Shubnikov de-Haas oscillations in 1930[47], where the conductivity oscillates upon increasing magnetic field *B*. Since then, the Shubnikov de-Haas effect has proven itself an essential tool in probing the fundamental properties of a solid state crystal. In general, there are only a handful of different types of quantum oscillations, and it is not very often new fundamental transport phenomena are discovered. In fact, it has been nearly 30 years since Aharanov Bohm oscillations were discovered, and no new magneto-oscillatory phenomena have been reported since then. In Chapter 7, we report on a completely novel type of quantum oscillation that we observed in graphene/hexagonal-boron nitride superlattices[48]. In the proceeding sub-sections, we introduce the basic theoretical concepts required to understand the physical origin of these novel oscillations.

`

4.1 Nearly free electrons in crystals – Bloch electrons

Shortcomings of the Drude-Sommerfeld model

In Chapter 1, we explained how the Drude expression for conductivity is useful for estimating τ, the average time electrons can propagate before suffering momentum loss. We should note however, that the Drude model is a classical theory, and therefore is not suitable for describing the quantum mechanical nature of electrons. Some further limitations stem from the following assumptions which are made; electrons scatter only through collisions with ion cores and in-between collisions do not feel the potential of the crystal lattice, that is, they are free electrons which behave like an ideal gas. The latter posed a huge discrepancy between experiment and theory, because the electrons were assumed to have a thermal velocity $v \sim T^{1/2}$, which implied a mean free path of a few Angstroms, the distance between atoms in the lattice[49]. A number of other experimental signatures proved this value to be far too small. For example, the resistivity was found to depend strongly on the density of impurities within a sample, even though the spacing between impurities was far larger than the distance between atoms. The mean free path inferred from this empirical experiment is actually an order of magnitude larger than the spacing between atoms. It was then quite a mystery how electrons could avoid atoms for such large distances.

A vast improvement on the transport theory was made when Sommerfeld used a quantum mechanical treatment, combining the classical Drude model with quantum mechanical Fermi-Dirac statistics. Similar to Drude, Sommerfeld considered electrons as free particles. He then proceeded by solving the Schrödinger equation for free particles in a box of volume V, which described the free electrons in a crystal sample of volume V.

$$\frac{-h^2\nabla^2}{2m_e}\psi(r) = E\psi(r) \tag{12}$$

By choosing appropriate boundary conditions (Born-Von Karman), he found the following solution

$$\psi_r\,(r) = \frac{1}{\sqrt{V}}e^{ik.r} \tag{13}$$

This means the electrons behave as plane waves carrying a momentum *k,* that is quantised and takes discrete values which satisfy the Born-Von Karman boundary conditions. This treatment allows us to calculate the density of states (DOS) which in turn can accurately predict many different thermodynamic properties[49]. In addition, the Fermi velocity, v_F, was defined (an order of magnitude larger than the thermal velocities assumed in the Drude model) and gave much more reasonable

`

values of the mean free path l. However, the Sommerfeld model still could not explain the microscopic origin of insulating and metallic like behaviour in different crystals. Not to mention there was still no physical insight in to how electrons propagate over such large distance without bumping in to the ion cores (in the Sommerfeld model, the potential of the ion cores were ignored). To understand these things, we have to consider the effects of the periodic potential of the lattice.

Bloch's Theoreom

Now we turn on the effects of the crystal lattice, which is described by a periodic potential

$$U(r) = U(r + R) \tag{14}$$

Where R corresponds to one crystal lattice vector. We then proceed by solving the Schrödinger equation which now includes the positive periodic potential

$$\frac{-h^2\nabla^2}{2m_e}\psi(r) + U(r)\psi(r) = E\psi(r) \tag{15}$$

Remarkably, Bloch found the following solution

$$\psi_k(r) = e^{ik.r}u_k(r) \tag{16}$$

Where $u_k(r) = u_k(r + R)$ is a function which has the periodicity of the lattice (for a detailed derivation see Ref. 34 Chapter 17). The wave function is simply a plane wave modulated by some periodic function. In other words, the electrons behave as "nearly free" particles, propagating as plane waves without scattering. The term "nearly free" refers to the fact that electrons travelling in the crystal move slower than in free space because they now feel the lattice potential. This is quantified by ascribing an "effective" mass (m^*) to the electrons. Regardless of their speed, Bloch's proof shows that electrons can move without scattering (at T = 0 K and in ideal, defect free crystals) even in the presence of the positively charged atomic centres. The physical reason stems from the fact that the electron wave functions exhibit translational symmetry around the crystal lattice. This means that the wave function of an electron in some state *k* is the same when you move one lattice vector in real space, differing only by a phase factor i.e

$$\psi_k\,(r + R) = e^{ik\cdot R}\psi_k(r) \tag{17}$$

Where *r* is the position and *R* is the distance corresponding to one lattice vector. Figure 11 illustrates the electron wavefunction in a periodic potential. This means the electron wavefunction is essentially delocalised around the whole crystal lattice, which is why it can move such large distance and explains the relatively large conductivity of metals.

`

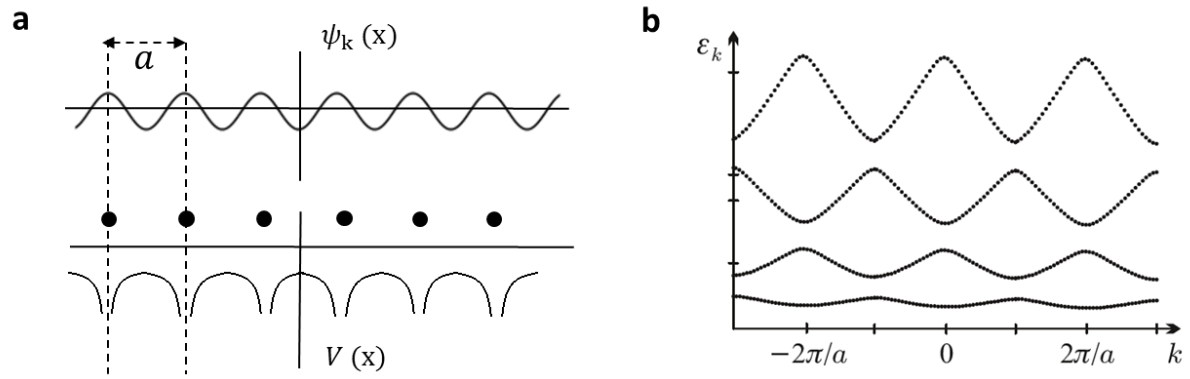

Figure 11| Bloch electrons in crystals. a, The electron wavefunction $\psi_k(x)$ (top panel) in a one-dimensional periodic potential *V*(x) (bottom panel) is plotted. Note the wavefunction shares the same periodicity as the periodic potential. **b,** The energy dispersion $\varepsilon_k(k)$ for Bloch states[49]. Here, four energy bands are present which are periodic over the reciprocal lattice vector $G = 2\pi/a$. Illustration is taken from ref. 49.

Finally, we note one more essential property of Bloch electrons, that is, Bloch states differing by one reciprocal lattice vector are identical.

$$\psi_{k+G}\,(r) = \psi_k(r) \tag{18}$$

Where *G* is one reciprocal lattice vector. Accordingly, the energies of both Bloch states in equation (18) are identical. This means that the electronic dispersion is periodic with the reciprocal lattice (Fig. 11 b) and therefore the full energy spectrum is described by electron states within the first Brillouin zone only.

To calculate those energies, we then proceed by solving the Schrödinger equation, which however is recast in the form of a Fourier expansion of the periodic structure, and is known instead as the central equation. The resulting solution gives a set of bands separated by gaps which describes all the possible allowed electronic states of the Bloch wave functions (Fig. 11b). The solution found in (17) finally answers our question raised at the beginning of Chapter 3. Because of the wave nature of electrons, they can travel for large distances in a periodic potential without scattering, so long as there are no impurities or thermal vibrations in the lattice. Electrons behave like this provided their wave function retains its translational symmetry with respect to the crystal lattice.

`

4.2 Electrons in magnetic fields – Landau quantization

If we apply a perpendicular magnetic field to a 2DEG, the charge carriers experience some Lorentz Force and follow curved trajectories. If the *B* field is strong enough, such that electrons can complete closed orbits without scattering, they become localised on their orbital centres. This cyclotron motion breaks translational symmetry of the electron wave function with respect to the crystal lattice, and it is much harder now for electrons to move within the crystal. Indeed, the classical equations of motion which describe electrons in magnetic fields are governed by the cyclotron radius r_c and cyclotron frequency ω_c.

$$r_c = \frac{mv}{eB} \qquad\qquad \omega_c = \frac{eB}{m} \tag{19}$$

Where *v* is velocity, B is the applied magnetic field, and *m* is the electron mass. Now, as *B* increases and r_c becomes increasingly small, quantum mechanics tells us of there are only discrete values of energy ($\hbar\omega_c$) and radi r_c which the electron can have. To determine these values, a full quantum mechanical treatment is required which involves solving the Schrödinger equation for a free electron in magnetic field.

$$\frac{-1}{2m_e}\left(\frac{\hbar}{i}\nabla + eA\right)\psi(r) = \varepsilon\psi(r) \tag{20}$$

Here, we have chosen the magnetic field, *B*, along the z direction, such that the magnetic potential *A* = (0, 0, Bz). After some maths[49], we find that equation (12) simplifies to the problem of a linear harmonic oscillator that is localised about some centre co-ordinate x_0.

$$-\frac{\hbar}{2m_e}^2 \frac{d^2\psi(x)}{dx^2} + \frac{1}{2}m_e{\omega_c}^2(x - x_0)^2\,\psi(x) = (\varepsilon - \frac{\hbar^3{k_z}^2}{2m_e})\psi(x) \tag{21}$$

Where the wavefunction and energy ε_n for the n^{th} level is given by

$$\psi_n(x) \sim \frac{1}{\sqrt{l_0 2^n n!}}\,H_n\,(\frac{x-x_0}{l_0})e^{-(x-x_0)^2/2{l_0}^2} \tag{22}$$

and

$$\varepsilon_n = \left(n + \frac{1}{2}\right)\hbar\omega_c \tag{23}$$

respectively, where $l_0 = \sqrt{\frac{\hbar}{eB}}$ is the quantum magnetic length, and H_n is the n^{th} Hermite polynomial. The quantised energy levels in (23) are referred to as Landau Levels. Although equation (22) is rather complicated, we notice two important properties of the electron wave function

`

(equation 22). First, it is localised about a centre co-ordinate, x_0, in contrast to the zero magnetic field case (17). Second, the energy (ε_n) is independent of that centre co-ordinate.

Now consider the electrons are placed inside a box with dimensions (L_x, $L_{y,}$) which represents the size of the unit cell. This will allow us to calculate the density of states and dispersion of Landau levels. Because the energy is independent on the centre or orbit, the Landau Levels become highly degenerate. It turns out, the degeneracy *N* for each Landau Level of energy ε_n is simply equal to the number of flux quanta which can fit inside the unit cell (L_x, L_y).

$$N = \frac{\phi}{\phi_0} \tag{24}$$

Where $\phi = BL_xL_y$ the total flux piercing the unit-cell in a crystal, and $\phi_0 = e/h$ is the flux quantum. This means that each state contributes one flux quantum. Furthermore, as *B* increases the energy levels become more degenerate and condense on to fewer and fewer Landau Levels. This is illustrated in Fig. 12 which plots the evolution of Energy-levels in a 2DEG with increasing *B*.

Now we turn to the case of Bloch electrons. If the cyclotron radius is much larger than the size of the unit cell, we can simply replace *m* with the effective mass, *m** (or cyclotron mass m_c for graphene) and apply the same equations which we just derived. This is known as the effective mass approximation.

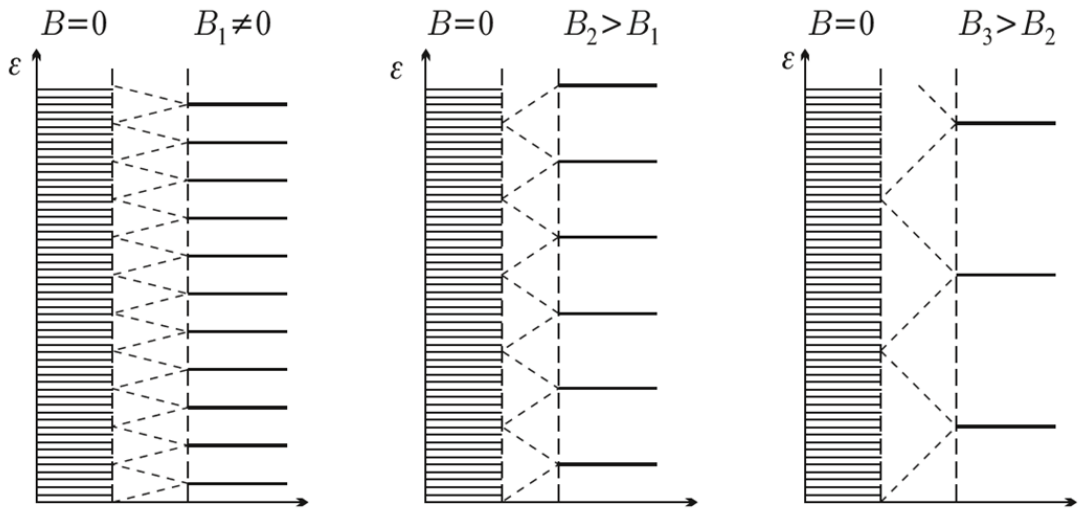

Figure 12| Energy dispersion of a 2DEG in magnetic field. The energy dispersion *E* is plotted for zero magnetic field and three finite values. As *B* is increased, the spacing between Landau levels increases (equation (23)), and the degeneracy also increases (equation (24). Illustration is taken from ref. 47

`

4.3 Shubnikov de-Haas oscillations

Landau quantisation happens in all metals under sufficiently high magnetic fields. It requires the coherence of electron trajectories around closed orbits, that is, the electron mean free path is larger than the circumference of the orbit. If this holds, the continuous Bloch bands, found in zero magnetic fields, turn in to a series of highly degenerate Landau Levels (Fig. 12). If we pay attention to the Fermi-level, we find that upon increasing magnetic field, it continuously changes between sitting at a Landau Level and sitting in a gap. Naturally, this causes oscillations in the conductivity/resistivity of the material upon increasing *B.* Specifically, the conductivity oscillates periodically with 1/B. The phenomena, known as Shubnikov de-Haas oscillations[47], are extremely sensitive to the characteristic properties of the charge carriers. For example, the oscillation frequency depends only on the carrier density. Figure 13a shows Shubnikov de-Haas oscillations measured in a WSe_2 field-effect transistor[50] for different gate voltages, V_G. We can see that the frequency chances upon increasing V_G (carrier density). We note however, that usually liquid helium temperatures are required to observe Shubnikov de-Haas oscillations, since the amplitude decays quickly with temperature due to the de-coherence of cyclotron orbits (Fig. 13b).

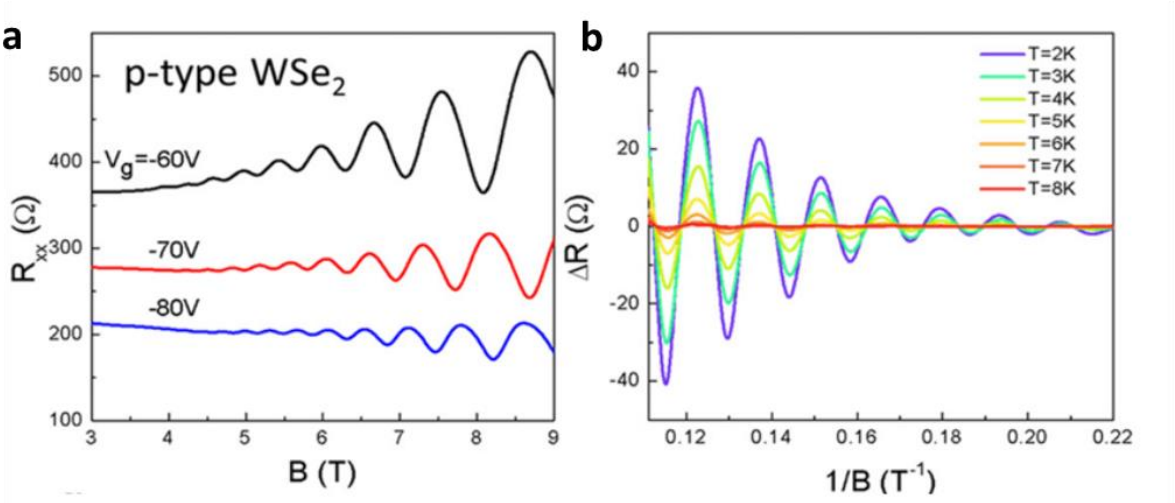

Figure 13| Shubnikov de-Haas oscillations in a WSe_2 field-effect transistor. a, the resistance as function of magnetic field at T = 2 K measured in WSe_2 for a few different carrier densities (gate voltage, V_g). **b**, Temperature dependence of the magnetoresistance after subtraction of a smooth background (ΔR). We can see that Shubnikov de-Haas oscillations are already supressed around T = 8 K. Experimental data of **a** and **b** is taken from ref. 50.

`

4.4 Magnetic translation group

To describe the following concepts, Figure 14 illustrates the evolution of electron motion and energy dispersion upon increasing magnetic field, *B*. In zero magnetic fields, the electron wavefunction in a periodic lattice is delocalised around the whole crystal; it is in a Bloch state and propagates freely around the lattice following straight trajectories (Fig. 14a). In finite *B*, electrons develop cyclotron motion and become localised on their centre of orbits (Fig. 14b). In graphene, the cyclotron radius corresponding to this motion, r_c , is described by

$$r_c = \frac{\hbar\sqrt{n\pi}}{eB} \tag{25}$$

Where *n* is the electron/hole carrier density, and *B* is magnetic field. As *B* increases and r_c becomes small, the energy dispersion is modified and becomes quantised according to the Landau Level description derived in Chapter 3.2. This formalism however is only valid in the limit when r_c is much larger than the lattice spacing *a*. In this case, the energy levels are highly degenerate with respect to the centre of orbit x_0. However, if r_c is made significantly small such that it becomes comparable to the distance between atoms in the lattice (period of the potential), the physics is quite different. Now, the cyclotron motion has different energies depending on its position in the unit cell, and consequently the orbital degeneracy becomes lifted. As for the dispersion relation, the discrete Landau Levels become broadened and resemble something that looks more like continuous bands (Fig. 14c). This effect is known as Harper broadening[51]. Furthermore, for particular values of magnetic field, the cyclotron radius becomes commensurable with the lattice spacing (Fig. 14c) and translational symmetry is restored in the Hamiltonian. Because of this, the electron wave functions in a magnetic field take the form of de-localised Bloch states (Fig. 14d). In other words, the electrons start moving straight again as if they experience effectively zero magnetic field (Fig. 14 a). This result was first derived by Zak[52] in 1963 in his theoretical paper entitled “Magnetic translation group”.

Here, he found that translational symmetry of the electron wavefunction occurs for many different special values of magnetic field where

$$\frac{\phi}{\phi_0} = \frac{p}{q} \tag{26}$$

Where *p* and *q* are integers and are interpreted as the number of flux quantum p piercing a newly defined super unit cell which is *q* times larger than the lattice. That is to say, a super cell can be defined which is *q* times larger than the unit cell of the crystal lattice.

`

For example $\phi/\phi_0 = 1/3$ corresponds to the condition that 1 flux quantum pierces a supercell which is three times that of the crystal unit cell (Fig. 15a). Notably, at these special values, the electrons feel effectively zero magnetic field and follow straight trajectories again. We also note that despite ϕ/ϕ_0 appearing both in equation (5) and equation (6), the magnetic translation group has nothing to do with Landau quantization. It describes only the translational symmetry of electron wave functions in magnetic fields.

Hofstadter's Butterfly

Following the work by Zak, Douglass Hofstadter in 1973 again addressed the problem of electrons in crystals when r_c is comparable to a. In this work[53], he extended the ideas of Harper broadening and performed numerical calculations of the full magneto-energy dispersion, for electrons in a square lattice. With the result, he plotted the available states as a function of energy and magnetic field, which produced an intriguing picture known as the "Hofstadter butterfly" (Fig. 15b). It showed a self-similar, fractal structure where the dispersion was identical at B = 0 T as B when $\phi/\phi_0 = 1$. The recursive nature originates actually from the magnetic translation group which was first derived by Zak. The difference being that Hofstadter's complicated energy spectrum includes the effects of Landau quantisation, that is, the regime where electron orbits are quantised. Hofstadter's work was easy to understand via the figures he made, such that physicists sought to find first the Hofstadter butterfly in solid-state crystals, whilst forgetting the earlier work of Zak. In fact, the magnetic translation group has more fundamental significance than Hofstadter's butterfly. It is the pre-cursor to understanding Hofstadter's work and, as we show in Chapter 7, significantly affects electron transport over a much wider parameter space.

To end this section, let us note that the physics described here is not attainable in any normal solid-state crystal. In typical crystals, the lattice spacing is only a few Angstroms, and extraordinarily high magnetic fields are required to shrink the cyclotron radius by this much. In graphene for example, where a = 2.42 A, magnetic fields of 10,000 T are required to reach the condition $\phi/\phi_0 = 1$. However, thanks to the advancement in fabrication of graphene/hBN heterostructures, we can make aritifical lattices with a far larger unit cell, pushing electron transport in magnetic fields in to the regime described here.

`

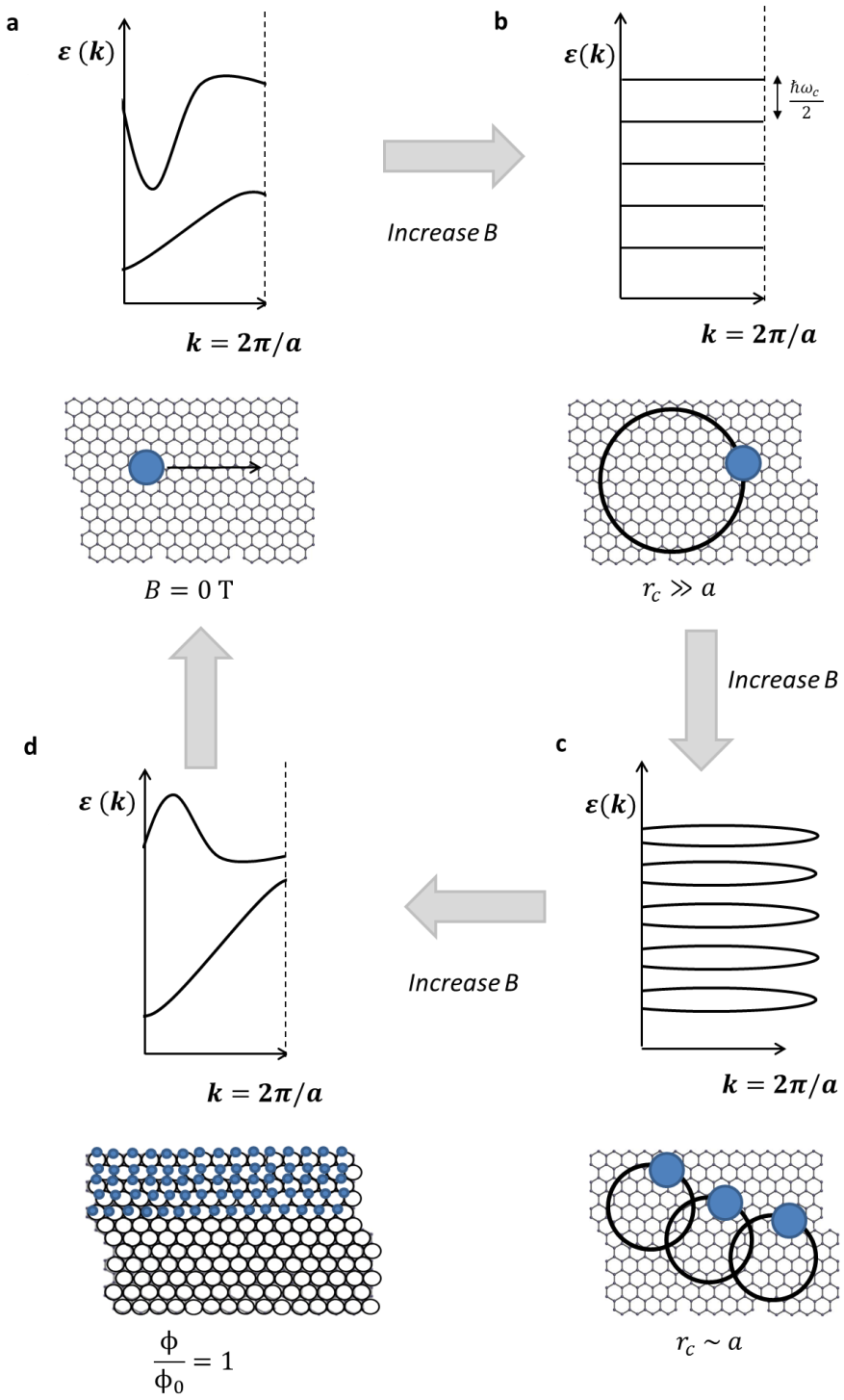

Figure 14| Magnetic translation group. **a,** The energy dispersion (top panel) and electron trajectories (bottom panel) in zero magnetic field. The blue circle and black line shows the electron and its trajectory respectively. **b,** The same as in **a** in the presence of a quantising magnetic field *B*. **c**, same as **a,b** when r_c becomes comparable to the lattice spacing, *a*. **d**, the magnetic translation group is shown, i.e when one flux quantum pierces the unit cell.

`

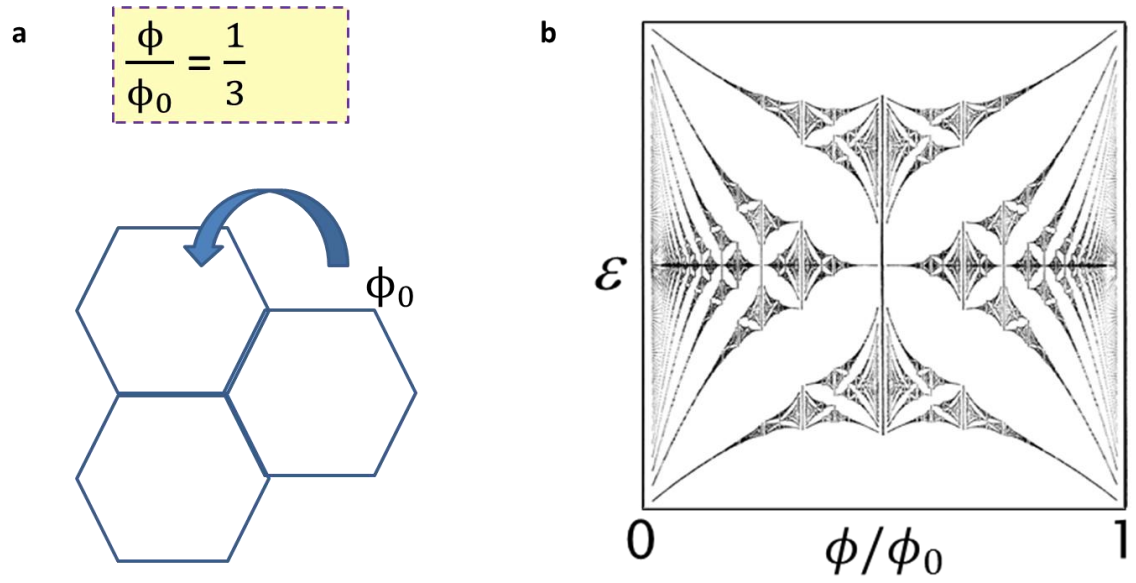

Figure 15| Magnetic supercells and Hofstadter's butterfly. a, The condition $\phi/\phi_0 = 1/3$ corresponds to one flux quantum piercing (blue arrow) a new unit cell which is three times larger than the base unit cell. The three hexagons sketch the size of the "supercell". **b,** The allowed energy levels (black regions) as a function of energy ε and magnetic field in units ϕ/ϕ_0 which were calculated by Hofstadter[53].

4.5 Graphene/hBN superlattice

In chapters 1 and 2, we described one of our experimental systems, an ultra-clean graphene channel formed by encapsulation between two hBN layers. In these samples, the effects of the underlying potential due to Van der Waals interaction between graphene and hBN are negligible. This is because the individual layers are usually stacked in a random manor without paying attention to the relative crystallographic directions of each material. If however, graphene is positioned on top of hBN in such a way that there is only a small misalignment angle θ between their crystallographic axes, the situation is quite different. In this case, beating of the two crystal periodicities produces a Moiré pattern (Fig. 16 a), which creates an additional periodic potential on the nm scale. This Moiré potential strongly modifies the electronic spectrum in graphene and is therefore referred to as a superlattice. Specifically, the additional periodic potential imposes zone folding of graphene's energy dispersion in to a smaller superlattice Brillouin zone, which creates a number of interesting features such as Van Hove singularities and secondary Dirac points (inset in the top panel of Fig. 16c). The secondary Dirac points were first observed in scanning tunnelling microscopy experiments at energies around 0.3 eV away from the main Dirac point[54]. If the crystal layers are close to perfect alignment, the superlattice period is about 14 nm (Fig. 16b) and the secondary Dirac points occur at

`

energies around 0.2 eV from the main Dirac point in graphene. Such energies are easily accessible by electrostatic gating, and, shortly after STM experiments, signatures of the graphene/hBN superlattice were measured in transport[55,48].

Figure 16c shows typical gate dependences of the resistivity ρ_{xx} and hall resistance R_{xy} in a graphene/hBN superlattice measured by the Manchester group in 2013[48]. At zero doping, a sharp peak in resistivity is observed corresponding to the main Dirac point. At large *n*, neighbouring satellite peaks in resistivity are observed for holes and electrons, at equal distances from charge neutrality point. These sharp peaks in resistivity occur when the Fermi energy moves through the secondary Dirac points. Notably, the secondary Dirac point is much more pronounced for holes than electrons. Further evidence for the presence of secondary Dirac points is found also when measuring the hall resistance R_{xy}, because the sign of R_{xy} reflects the type of majority charge carrier in the conducting channel. In graphene, R_{xy} diverges as the Fermi-level moves closer to the Dirac point and exhibits a sign reversal when moving through it, corresponding to a change in carrier type (electrons or holes). In the graphene/hBN superlattice, this feature is mimicked around the secondary Dirac points (bottom panel of Fig. 16c). We note however that R_{xy} changes in a non-trivial manor when tuning the Fermi-energy, changing three times in total as we move away from the main Dirac point (for both holes and electrons). This is due to the presence of Van Hove singularities in the density of states[56].

The underlying Moiré potential can also strongly influence the zero energy dispersion (charge neutrality point). This is because the superlattice potential breaks inversion symmetry within graphene's A-B sub-lattice, creating a global band gap at the Dirac point[56] . Aside from technological interest (for year's research efforts have focussed on trying to induce a band gap in graphene to operate as a transistor device), the band gap opening also has fundamental, topological implications. For example, this creates Berry curvature hot spots close to the Dirac point, allowing the study of topological currents[57] in graphene which has in turn sparked a new field in the electronics industry coined "valleytronics".

In this Thesis, we are concerned with the magneto transport properties of the graphene/hBN superlattice. This type of experiment has gained intense interest over the past few years because the superlattices' energy spectrum hosts the long sought Hofstadter butterfly described in Chapter 3.5. This physics becomes accessible because of the large lattice spacing in graphene/hBN superlattices; For a superlattice with a = 14 nm, we only need B = 26 T to reach the condition $\phi/\phi_0 = 1$. In 2013, Hofstadter butterflies were observed in graphene/hBN superlattices[48,55]. Figure 16d plots conductivity as a function of magnetic field and carrier density (energy) at T = 2 K. For comparison,

`

Fig. 16e shows theoretical calculations of the Hofstadter butterfly spectrum in graphene/hBN superlattices, where black regions show states and white spaces show gaps. In experiment, we can see the conductivity accurately maps out gaps and states where it is minimum (white) and maximum (black), respectively.

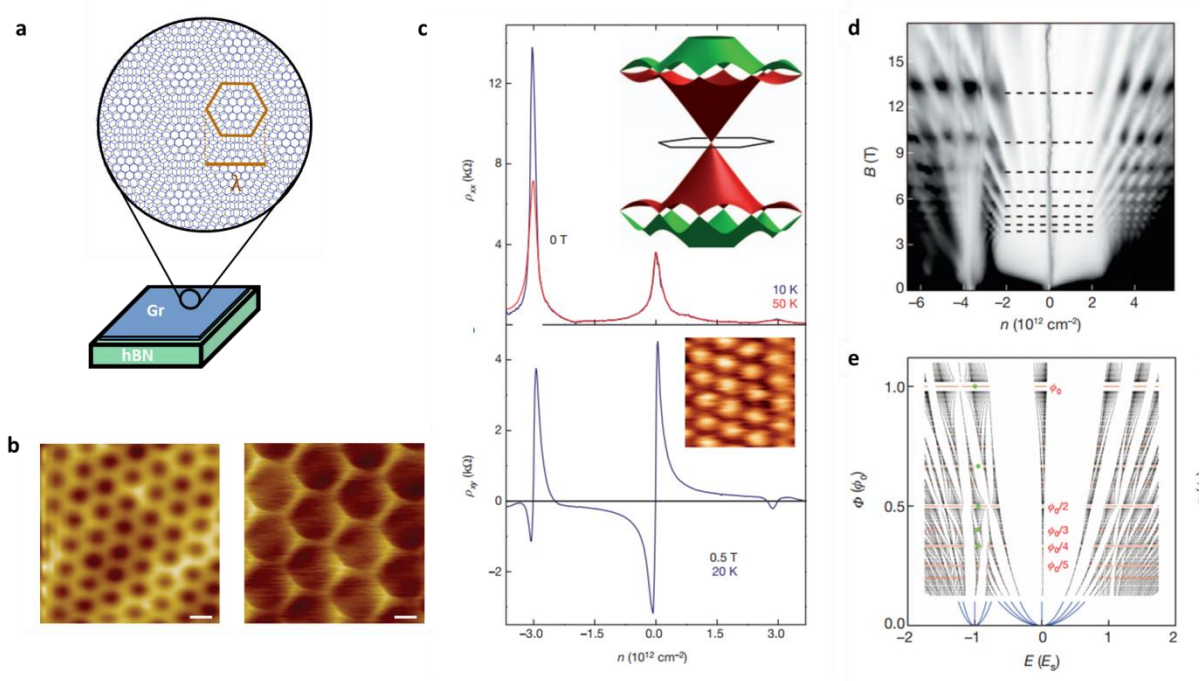

Figure 16| Graphene/hexagonal boron nitride superlattices. a, Schematic of a graphene on hBN heterostructure. The magnified region shows the Moiré pattern produced with a wavelength λ when the crystal layers are aligned to within a few degrees. **b**, STM images[54] of heterostructures with different alignment angle that produce superlattices with $\lambda = 6$ and 11 nm respectively (left to right). Scale bar: 5nm. **c,** longitudinal resistivity (ρ_{xx}) and hall resistance (ρ_{xy}) as a function of carrier density *n*. **d**, longitudinal conductivity σ_{xx} (*B*,*n*) for the same device as in **c**. Grey scale: white, 0 kΩ; black, 8,5 kΩ. **e**, The energy dispersion calculated for graphene/hBN superlattices as a function of energy and *B*. The black regions are available states whilst the white regions show gaps in the energy spectrum. Data from **c –e** is taken from ref. 48.

`

Chapter 5 – Experimental techniques

In this chapter, we will introduce the experimental set-up and measurement techniques which have been employed in this Thesis. First we provide a detailed recipe for fabricating graphene/hBN heterostructures. Then we describe the measurement techniques and equipment used for performing transport experiments.

`

5.1 Device fabrication

Mechanical exfoliation/identifying materials

To date, the highest quality 2D materials are obtained by mechanical exfoliation, which was first established upon its discovery in 2004[58]. This method involves peeling few layers from bulk crystals using scotch tape, and therefore become known as the "scotch tape method". It works rather well for Van der Walls crystals because the inter-atomic layers are bonded only by Van der Waals forces, such that they cleave preferentially along their in-place crystallographic axes. This allows us to isolate crystals down to the monolayer.

Figure 17 illustrates the method used for isolating few layer crystals like graphene and hexagonal boron nitride. First, the bulk crystal is sandwiched within a piece of scotch tape (Fig. 17a). The crystal is then cleaved in half by pulling the scotch tape apart, creating two crystals of half the thickness. This process is repeated multiple times to continuously thin the crystallites. Assuming a bulk graphite crystal contains 10,000 atomic layers, and the crystal indeed cleaves in half after every peel, the crystal thins by a factor of 2^n where n is the number of peels made. In practice, the crystal cleaves a number of different ways and in fact we only have to repeat the process maybe 3 or 4 times to get down to the monolayer graphene. The exfoliated flakes which are attached to the scotch tape are then pressed on to a SiO_2 on Si substrate (Fig. 17b). The substrate at this point contains a mixture of different flakes of varying thickness and areas, where monolayer flakes however are minority. Under an optical microscope, we then have to search for the monolayers. Although only one atom thick, graphene still modulates the optical path length of light. Therefore when placed on a suitable substrate (300 nm thick SiO_2), it can be identified by the colour contrast it produces with respect to the empty substrate. Whilst the empty substrate appears blue-violet, thin graphitic films appear blue (far right panel in Fig. 17c). However, it takes a trained eye to identify a monolayer quickly and correctly.

For the un-trained eye, atomic force microscopy (AFM) is sometimes employed to measure the thickness of individual flakes, although the procedure is exhausting. Instead, Raman spectroscopy can be employed to identify the thickness of different crystals[59]. Figure 17d and e show the Raman spectra for thin graphite layers of varying thickness down to the monolayer. There are two main Raman active modes in graphene, the G and 2D peak which occur at wavenumbers 1580 cm^{-1} and 2700 cm^{-1} respectively (Fig 17d). One can see that the position and width of the so-called 2D peak changes drastically upon increasing the number of layers, becoming wider and shifting to higher energies for the case of graphite. Remarkably, the difference is significant even between 1 and 2

`

layers (Fig. 17e) and reflects the subtle changes in the phonon dispersion between monolayer and bilayer graphene. By a combination of optical spectroscopy, AFM and Raman spectroscopy, we can reliably isolate monolayer graphene.

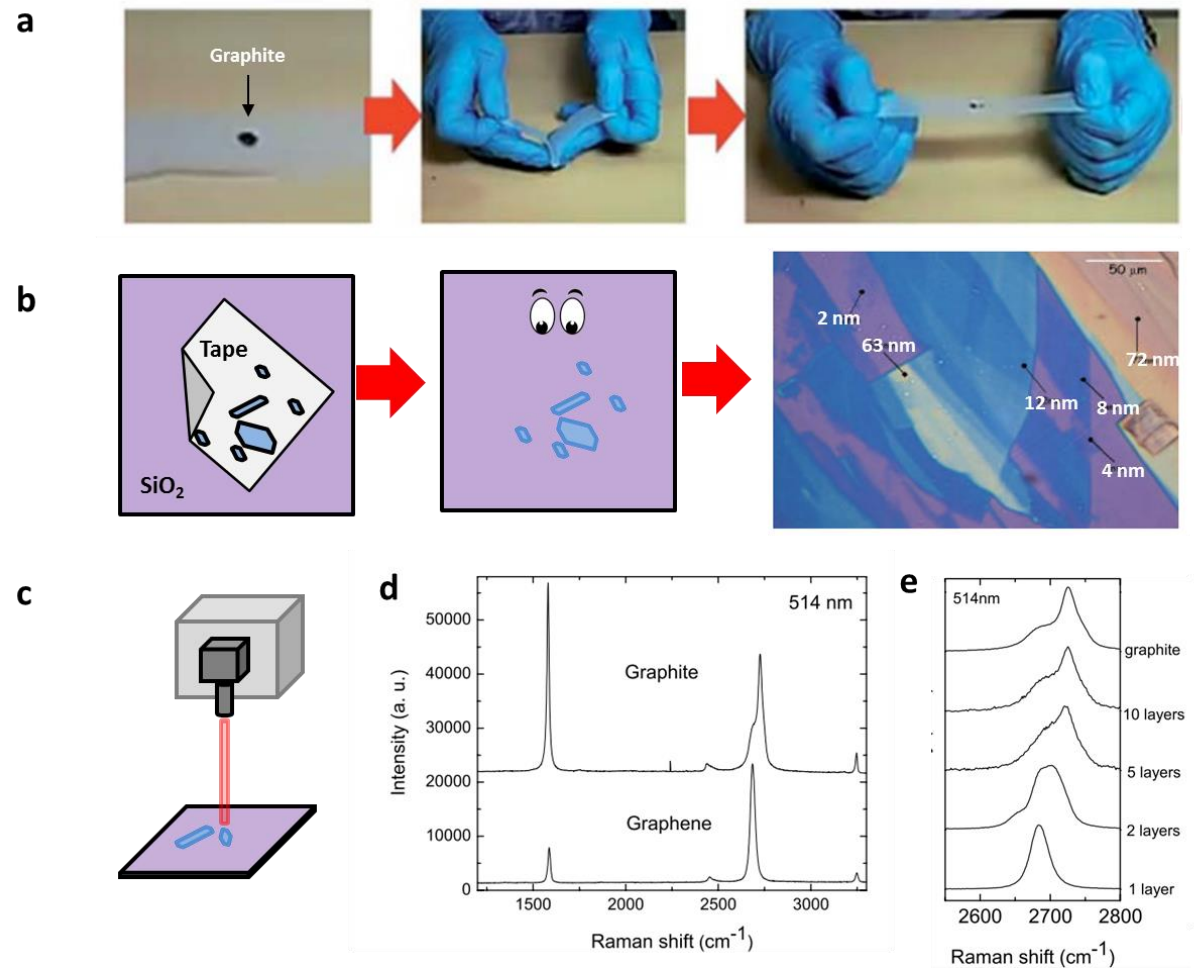

Figure 17| a, photographs demonstrating the mechanical exfoliation method (right to left panel)[60]. **b**, Schematic of graphene flakes being pressed on to SiO_2. The far right panel is an optical image of the resulting flakes whose thickness is labelled in nm[58]. **c**, schematic of Raman spectroscopy experiment. **d** Raman spectroscopy data taken from ref. 59 compares spectra of bulk graphite and monolayer graphene. **e,** data of ref. 59 shows the change in Raman spectrum for crystals of different thickness.

Van der Waals heterostructures – Stamp Transfer Method

After identifying the required flakes, they are assembled on top of one another to make the desired heterostructure. Over the past 15 years there have been a few different techniques developed for this. In the early days, a number or processing steps were employed to isolate graphene layers and transfer them on to suitable substrates. This often involved processing the flakes in solvents and/or

`

manipulating them with a polymer membrane. Inevitably, the graphene flakes become contaminated with polymer and degrade the quality of the resulting heterostructure. In this Thesis, we employ a technique known as the “stamp transfer” method.

First, we fabricate the “stamp”, which is essentially a polymer membrane held in a frame which is used to pick-up and drop individual crystals to assemble the heterostructure. For this, a multi-layer (Fig. 18a) of PMMA (1 μm) and PMGI (500 nm) is spin coated on to a SiO_2/Si Wafer. Then, a small circle is cut through the structure with tweezers, which defines the desired size and area of the “stamp” (Fig. 18b). A solvent (MF-319) is then pipetted in to the cut which dissolves the underlying PGMI but leaves the PMMA stamp un-touched (Fig. 18b). The processed polymer heterostructure is then placed gently in water where the PMMA stamp detaches itself from the excess area and is left floating on the water (Fig. 18c). The circular membrane is then fished out with a 2mm washer where it remains suspended in the aperture (Fig. 18c). This forms the stamp.

Then we proceed by assembling the heterostructure. To avoid contamination of the graphene channel with PMMA, we first pick up the desired hexagonal boron nitride crystal by gently pressing the stamp down onto the flake (Fig. 18d). The crystal then bonds to the membrane by Van der Waals interaction and is removed from the SiO_2 substrate where it was first exfoliated. This first boron nitride flake forms the top of the heterostructure. We then repeat the process and pick up a graphene flake with the top boron nitride/polymer membrane stamp (Fig. 18e). Since the graphene adheres to the boron-nitride and not the polymer, it is not contaminated. Finally we pick up the bottom boron-nitride crystal such that the polymer stamp now holds the hBN/graphene/hBN heterostructure (Fig. 18f). The stamp is then pressed on to a fresh Si/SiO_2 wafer (either 90 nm or 290 nm SiO_2) (Fig. 18g-h) which transfers the entire heterostructure to the wafer (Fig. 18i) where it is ready for further processing.

`

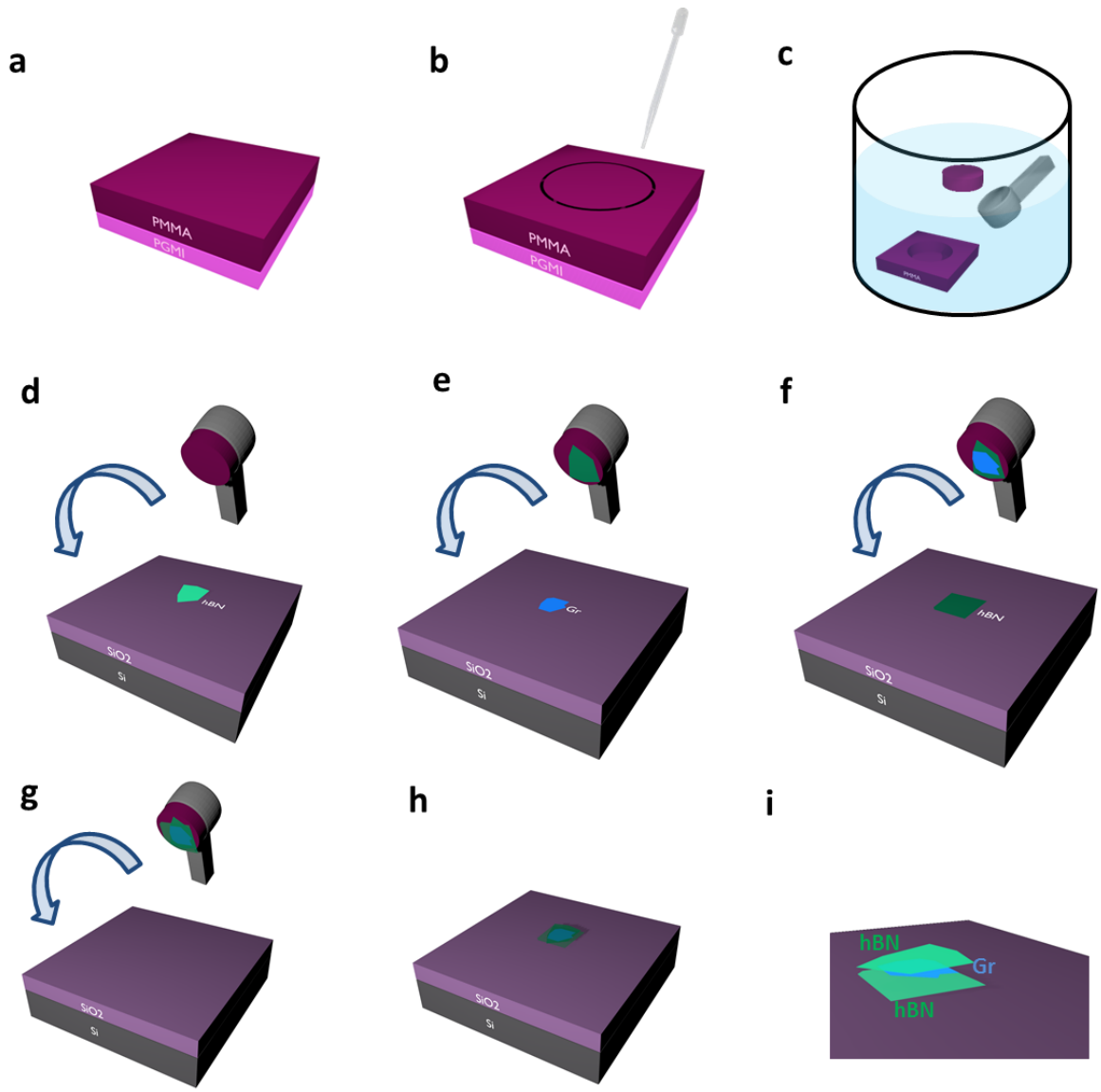

Figure 18| Stamp transfer method. The procedure is illustrated chronologically in the schematics above. **a-c,** The PMMA stamp is first made. Here, the light pink, and dark purple regions represent the PGMI and PMMA respectively. The light blue shading and the grey spoon in **c** represents the water solution and washer respectively. **d-f,** The stamp is then used to assemble the heterostructure. Here, the black and violet shades depict the Si and SiO_2 substrate respectively, whilst the green and blue objects represent graphene and hexagonal boron-nitride crystals respectively. **g-I,** The whole heterostructure is then stamped on to a fresh Si wafer ready for lithography.

`

Lithography

The next step involves etching the heterostructure (Fig. 19a) in to a functioning device, for example in to hall bar geometry. However, before etching the hall bar shape, we first etch contact regions leading up to the hall bar; the reason will become clear shortly. Before etching we first need to define an etch mask. We proceed then by spin coating photo resist over the desired heterostructure (Fig. 19b). Electron beam lithography is then used to pattern the etch mask (Fig. 18c), defining regions where gold contacts will be deposited. After this, reactive ion etching is employed to create trenches in the heterostructure (Fig. 19d). Then, the etch mask is used again to deposit gold in to the trenches (Fig. 19e). This method ensures that no polymer touches the graphene channel, preserving its cleanliness whilst making a high-quality low resistance contact. Notably, the gold contact graphene only at the edges and is usually referred to as a one-dimensional (1D) contact[61]. Finally, we make another etch mask, with a fresh layer of photoresist and another round of electron beam lithography, which this time defines the channel/hall bar shape (Fig. 19g). The result is a high-quality graphene/hBN heterostructure. The schematics in Fig. 19a-h are simplified for illustrative purposes. The heterostrucutre actually has an edge profile which looks like that in Fig. 19i due to etching procedure[61].

`

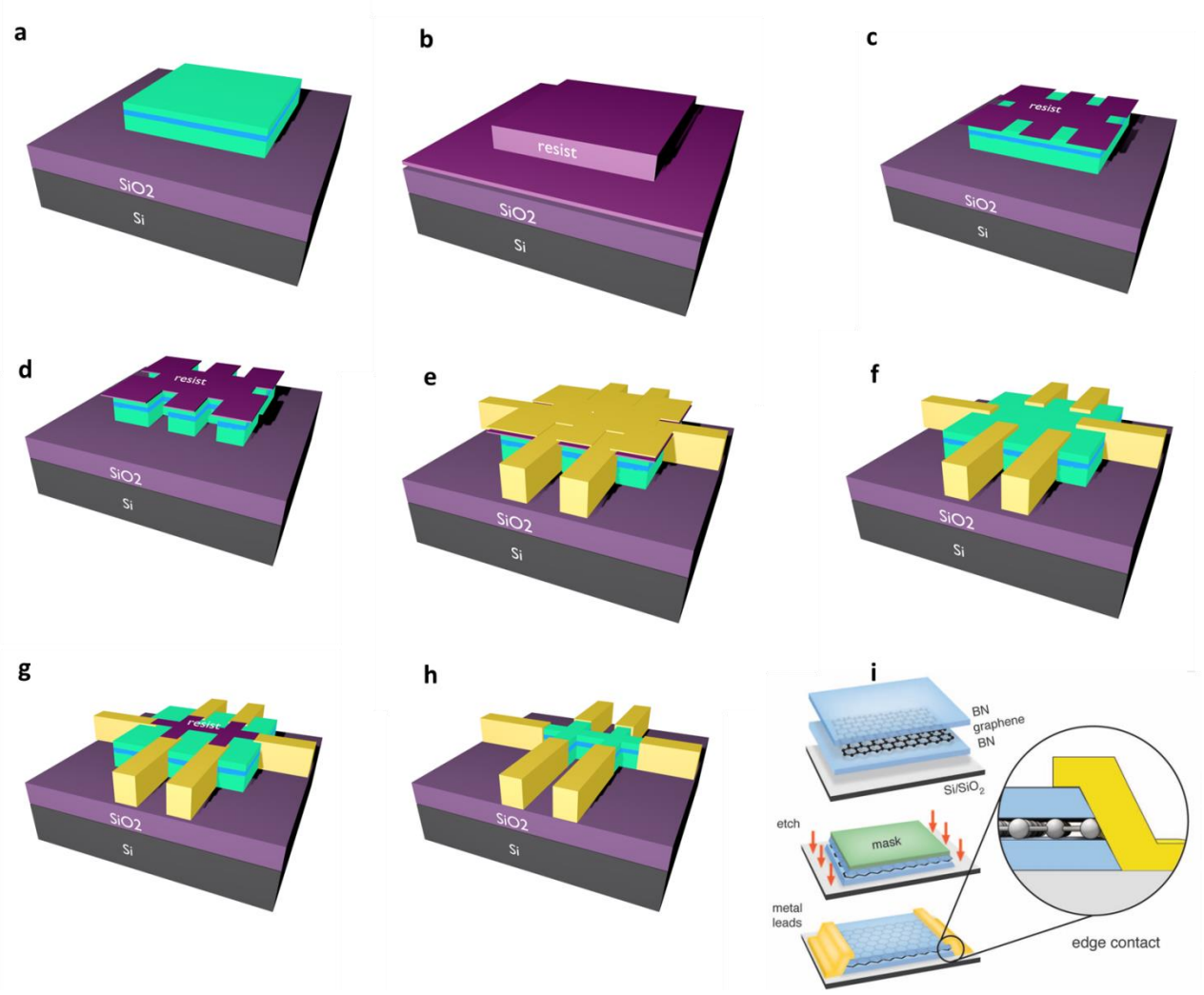

Figure 19| Electron beam lithography on graphene/hBN heterostructures. The procedure is illustrated chronologically in the schematics above from. **a-c,** An etch mask is first patterned on to the heterostructure by electron beam lithography. Dark grey; silicon. Violet; silicon dioxide. Green; hexagonal boron-nitride. Blue; graphene. Dark purple; photoresist. **d**, the mask is first used to etch away regions of the heterostructure. **e,** Gold (yellow regions) is then evaporated onto the heterostructure. **f**, Subsequent lift-off unveil electrical leads which contact the graphene only at the edges. **g-h**, the same etching procedure (**a-d)** is then used to define the mesa, **h**. **I** an illustration of the one-dimensional contact which forms in graphene heterostructures[61].

`

5.2 Transport Measurements

Cryostat

Most transport experiments have been performed in a He^4 flow cryostat. The Cryostat consists of a variable temperature insert (VTI) mounted in to a 120 L cryogenic Dewar. The Dewar is filled with liquid helium prior to experiments, and can remain cold for up to three weeks if not in use. Fig. 20a-b shows a photo of our cryostat with a schematic showing the inside. The VTI and helium bath are connected by a small capillary with a valve (usually called needle valve) that controls the flow of liquid helium in to the VTI (Fig. 20b). Usually, the temperature in the VTI is above the boiling point of liquid helium (1.2 K). Therefore, when liquid helium flows there it evaporates immediately. To remove the helium gas, a separate line is pumped to maintain a constant pressure within the VTI. The removed gas goes straight to a recovery line for recycling. The VTI also has as a temperature sensor and heater, which is used for temperature stabilisation and heating the system up to 400 K if required.

In addition to temperature control, our cryostats have built in superconducting magnets which allow us to apply magnetic fields of up to 15 T. For this, a superconducting coil is wrapped around the VTI, but sits in the helium bath where it remains cold because it is thermally isolated. So long as there is liquid helium in the bath, the magnet stays superconducting even if the VTI is heated to 400 K. The superconducting magnetic is powered by an Oxford Instruments IPS – 120.

Electrical Measurements

In the entirety of this Thesis, we have been performing transport measurements on graphene devices described in Chapter 4.1. The majority of measurements have been performed in AC using standard lock-in amplifier techniques. For this, we supply a constant AC current to the device under test (DUT), and measure the voltage drop across it. The Lock-in amplifiers' however only source voltage. Therefore, a constant current is sourced from a lock-in amplifier by placing a large resistor (usually 10 MΩ) in series with the device under test (DUT). In this configuration, the majority of the supplied voltage drops across the fixed resistor, such that any small changes in the DUTs' resistance does not significantly influence the sourced current. Usually we measure with 2 or 3 lock-in amplifiers simultaneously. As for the frequency response, we measure below 30 Hz to remove the risk of any coupling to parasitic capacitance in the device. This might arise from devices with a high contact resistance, which is owed to bad quality contacts made during fabrication.

`

In most experiments we measure in the linear response regime, with a current source of around 0.1 to 1 μA. In some cases, we study non-linear effects (high current regime) by performing differential resistance measurements. This technique employs a small AC excitation current (around 0.1 uA) in conjunction with a large DC current (up to 1 mA). The measurement scheme is sketched in Fig. 20c. The technique allows us to measure the local gradient of an I-V curve (Fig. 20d). For sourcing DC current and measuring DC voltage, we use a Keithley 2614 B source meter and a Keithley 2182A respectively.

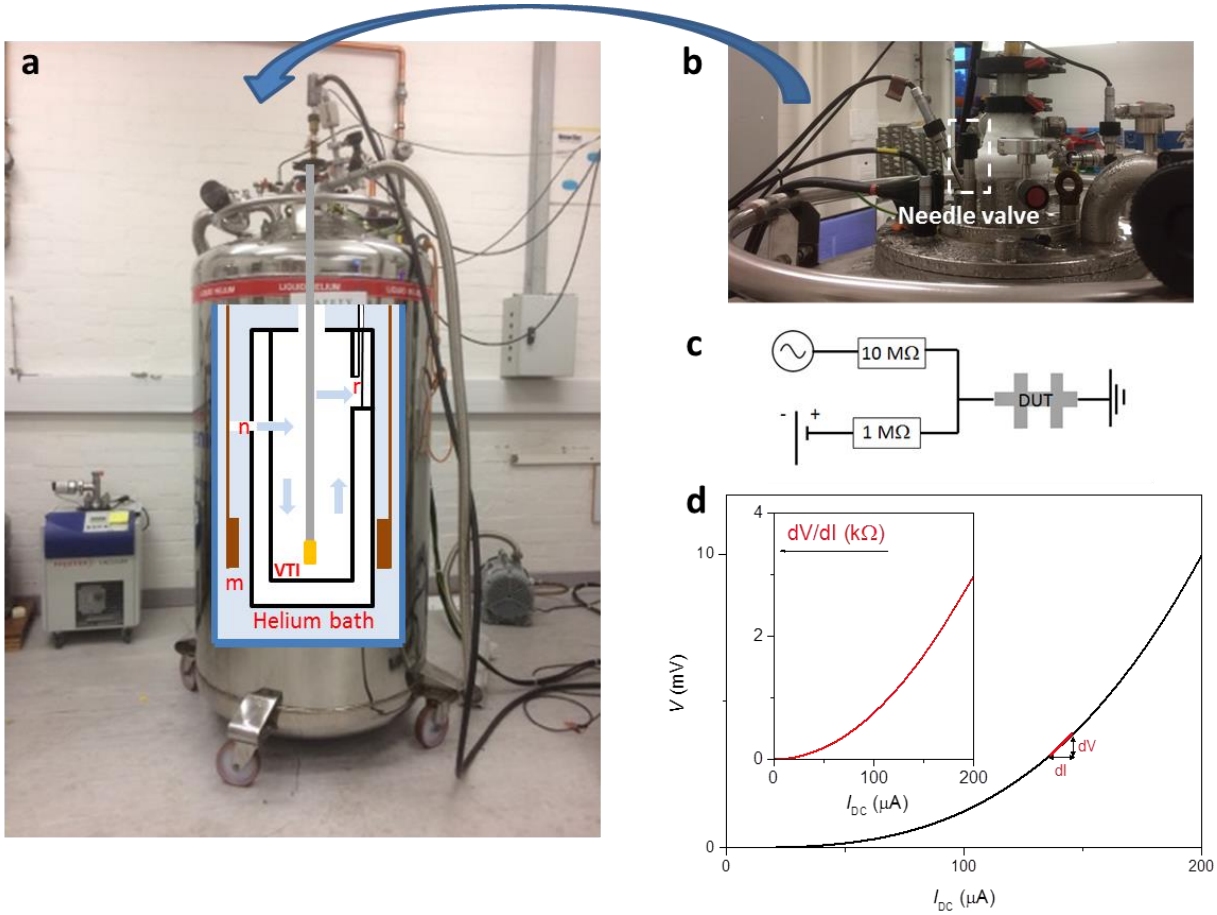

Figure 20| Electrical measurements. a, A device schematic of our Cryostat. The labels *m*, *n* and *r* represent the magnet, needle valve and recovery line respectively. **b,** a zoomed image of the top of our cryostat. **c**, a circuit diagram demonstrating differential resistance measurements. **d**, an example measurement for **c.** The voltage drop across a non-linear DUT (measured with a nano-voltmeter) as a function of current. Inset: the differential resistance that would be measured with a lock-in amplifier for the same DUT.

`

Chapter 6 – Viscous electron whirlpools

Paper Title: Negative local resistance caused by viscous electron backflow

Journal Reference: Science 351, 1055–1058 (2016)

DOI: 10.1126/science.aad0201

My contribution: In this work I performed transport experiments on graphene/hBN devices. I also contributed to the design of experiment, analysis and interpretation of data. I measured electron whirlpools in two devices employed in the paper, and studied more advanced device geometries which provided essential understanding for the underlying physics (see devices with "cuts" in Supplementary Section).

Full Author List: D. A. Bandurin, I. Torre, **R. Krishna Kumar**, M. Ben Shalom, A. Tomadin, A. Principi, G. H. Auton, E. Khestanova, K. S. Novoselov, I. V. Grigorieva, L. A. Ponomarenko, A. K. Geim, M. Polini

Author contributions: D.A.B, R.KK and L.A.P performed transport experiments and the design of experiments. L. A.P, M.P and A.K.G supervised the project. Devices were fabricated by M.B.S, G.H.A and E.K. Theoretical support was provided by I.T, A.T, A.P and M.P. The manuscript was written by M.P, A.K.G, L.A.P, D.A.B and R.K.K. Experimental support was given by I.V.G and K.S.N.

In this chapter, we present the first experimental work on hydrodynamic electron transport since Molenkamp's' experiment in (Al,Ga)As heterostructures performed over twenty years ago. Here, we study transport in graphene devices of the highest quality (by encapsulation with hexagonal boron-nitride) in the high temperature regime where electron-electron collisions are rather frequent. Our collaborators performed numerical simulations of viscous electron flow in graphene, and demonstrated that current vortices/whirlpools can form in regions of the device where there is no applied electric field. Accompanying these vortices is a negative potential distribution which is strongest close to the current injection point.

For observing these whirlpools, we study electron transport in a customised geometry which we call the "vicinity geometry". The device is essentially a hall bar with narrow and closely spaced side contacts, whilst the measurement geometry is one that maximises the contribution from viscous flow. We observe a negative resistance in the "vicinity geometry" which we attribute to the presence of viscous whirlpools. From the theory, we used our experimental data to extract electron viscosity. Remarkably, the electron viscosity was found to be 50 x more viscous than honey, in agreement with independent many-body calculations.

REPORTS

ELECTRON TRANSPORT

Negative local resistance caused by viscous electron backflow in graphene

D. A. Bandurin,[1] I. Torre,[2] R. Krishna Kumar,[1,3] M. Ben Shalom,[1,4] A. Tomadin,[5] A. Principi,[6] G. H. Auton,[4] E. Khestanova,[1,4] K. S. Novoselov,[4] I. V. Grigorieva,[1] L. A. Ponomarenko,[1,3] A. K. Geim,[1]* M. Polini[7]*

Graphene hosts a unique electron system in which electron-phonon scattering is extremely weak but electron-electron collisions are sufficiently frequent to provide local equilibrium above the temperature of liquid nitrogen. Under these conditions, electrons can behave as a viscous liquid and exhibit hydrodynamic phenomena similar to classical liquids. Here we report strong evidence for this transport regime. We found that doped graphene exhibits an anomalous (negative) voltage drop near current-injection contacts, which is attributed to the formation of submicrometer-size whirlpools in the electron flow. The viscosity of graphene's electron liquid is found to be ~0.1 square meters per second, an order of magnitude higher than that of honey, in agreement with many-body theory. Our work demonstrates the possibility of studying electron hydrodynamics using high-quality graphene.

The collective behavior of many-particle systems that undergo frequent interparticle collisions has been studied for more than two centuries and is routinely described by the theory of hydrodynamics (*1*, *2*). The theory relies only on the conservation of mass, momentum, and energy and is highly successful in explaining the response of classical gases and liquids to external perturbations that vary slowly in space and time. More recently, it has been shown that hydrodynamics can also be applied to strongly interacting quantum systems, including ultrahot nuclear matter and ultracold atomic Fermi gases in the unitarity limit (*3*–*6*). In principle, the hydrodynamic approach can also be used to describe many-electron phenomena in condensed matter physics (*7*–*13*). The theory becomes applicable if electron-electron scattering provides the shortest spatial scale in the problem, so that $\ell_{ee} \ll W, \ell$, where ℓ_{ee} is the electron-electron scattering length, W is the characteristic sample size, $\ell \equiv v_F\tau$ is the mean free path, v_F is the Fermi velocity, and τ is the mean free time with respect to momentum-nonconserving collisions, such as those involving impurities and phonons. The above inequalities are difficult to meet experimentally. At low temperatures (T), ℓ_{ee} varies approximately $\propto T^{-2}$, reaching a micrometer scale at liquid helium T (*14*), which necessitates the use of ultraclean systems to satisfy $\ell_{ee} \ll \ell$. At higher T, electron-phonon scattering rapidly reduces ℓ. However, for two-dimensional (2D) systems in which acoustic phonon scattering dominates, ℓ decays only $\propto T^{-1}$, slower than ℓ_{ee}, which should in principle allow the hydrodynamic description to apply over a certain temperature range, until other phonon-mediated processes become important. So far, there has been little evidence for hydrodynamic electron transport. An exception is an early work on 2D electron gases in ballistic devices ($\ell \sim W$) made from GaAlAs heterostructures (*15*). These devices exhibited nonmonotonic changes in differential resistance as a function of a large applied current I, which was used to increase the electron temperature (making ℓ_{ee} short) while the lattice temperature remained low (allowing long ℓ). The nonmonotonic behavior was attributed to the Gurzhi effect, a transition between Knudsen ($\ell_{ee} \gg \ell$) and viscous electron flows (*7*, *15*). Another possible hint about electron hydrodynamics comes from an explanation (*16*) of the Coulomb drag measured between two graphene sheets at the charge neutrality point (CNP) (*17*).

Here we address electron hydrodynamics by using a special measurement geometry (Fig. 1) that amplifies the effects of the shear viscosity ν and, at the same time, minimizes a contribution from ballistic effects that can occur not only in the Knudsen regime but also in viscous flows in graphene. A viscous flow can lead to vortices appearing in the spatial distribution of the steady-state current (Fig. 1, A and B). Such "electron whirlpools" have a spatial scale $D_\nu = \sqrt{\nu\tau}$, which depends on electron-electron scattering through ν and on the electron system's quality through τ (*18*). To detect the whirlpools, electrical probes should be placed at a distance comparable to D_ν. By using single- and bi-layer graphene (SLG and BLG, respectively) encapsulated between boron nitride crystals (*19*–*21*), we were able to reach a D_ν of 0.3 to 0.4 μm thanks to the high viscosity of graphene's Fermi liquid and its high carrier

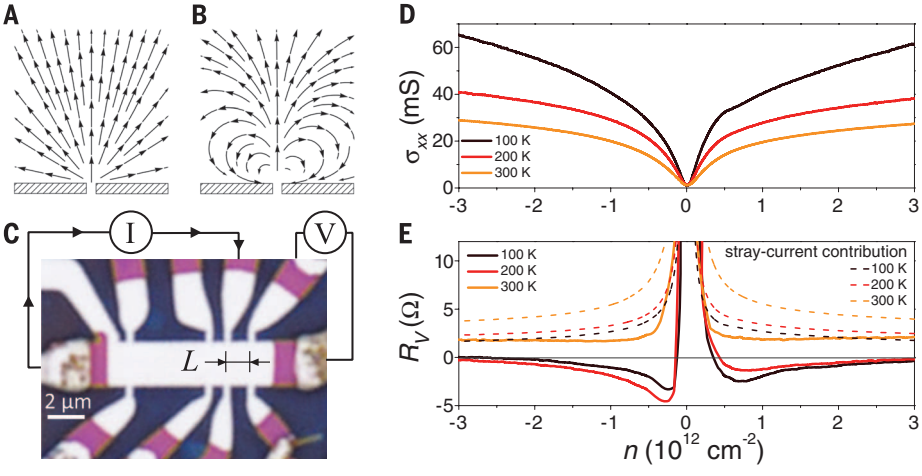

Fig. 1. Viscous backflow in doped graphene. (**A** and **B**) The calculated steady-state distribution of a current injected through a narrow slit for (A) a classical conducting medium with zero ν and (B) a viscous Fermi liquid. (**C**) Optical micrograph of one of our SLG devices. The schematic explains the measurement geometry for vicinity resistance. The top gate electrode appears in white and the mesa, which is etched in encapsulated graphene and not covered with a metal, appears in purple. Mixed colors at the periphery are areas of metallic contacts on top of the mesa. (**D** and **E**) Longitudinal conductivity σ_{xx} and R_V as a function of n, induced by applying gate voltage. The dashed curves in (E) show the contribution expected from classical stray currents in this geometry (*18*). I = 0.3 μA; L = 1 μm; W = 2.5 μm.

[1]School of Physics and Astronomy, University of Manchester, Oxford Road, Manchester M13 9PL, UK. [2]National Enterprise for nanoScience and nanoTechnology, Scuola Normale Superiore, I-56126 Pisa, Italy. [3]Department of Physics, Lancaster University, Lancaster LA14YB, UK. [4]National Graphene Institute, University of Manchester, Manchester M13 9PL, UK. [5]National Enterprise for nanoScience and nanoTechnology, Istituto Nanoscienze-Consiglio Nazionale delle Ricerche and Scuola Normale Superiore, I-56126 Pisa, Italy. [6]Institute for Molecules and Materials, Radboud University, NL-6525 AJ Nijmegen, Netherlands. [7]Istituto Italiano di Tecnologia, Graphene Labs, Via Morego 30, I-16163 Genova, Italy.
*Corresponding author. E-mail: geim@man.ac.uk (A.K.G.); marco.polini@iit.it (M.P.)

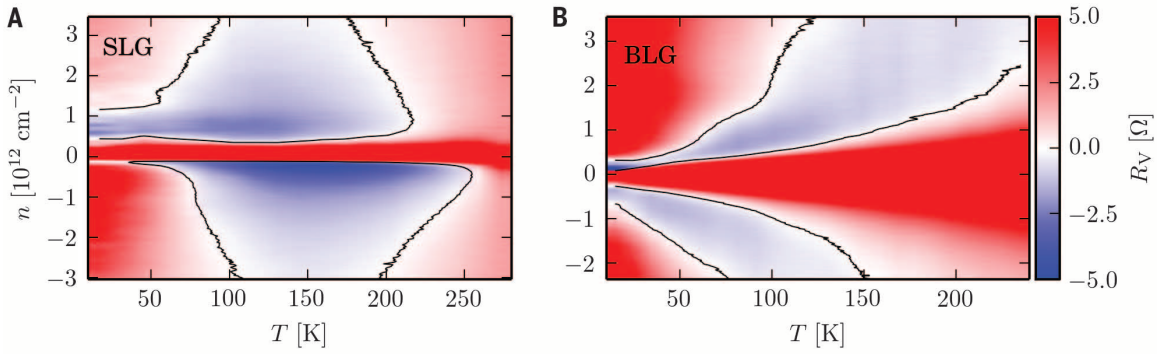

Fig. 2. Vicinity resistance maps. (**A** and **B**) $R_v(n,T)$ for SLG and BLG, respectively. The black curves indicate zero R_v. For each n away from the CNP, there is a wide range of T over which R_v is negative. For the SLG device, W = 2.5 μm and L = 1 μm; for the BLG device, W = 2.3 μm and L = 1.3 μm. All measurements for BLG presented in this work were taken with zero displacement between the graphene layers (*18*).

mobility μ, even at high T. Such a large D_v, which is unique to graphene, nevertheless necessitates submicron resolution to probe the electron backflow. To this end, we fabricated multiterminal Hall bars with narrow (~0.3 μm) and closely spaced (~1 μm) voltage probes (Fig. 1C and fig. S1). Details of the device fabrication are given in (*18*).

All our devices were first characterized in the standard geometry by applying I along the main channel and using side probes for voltage measurements. The typical behavior of longitudinal conductivity σ_{xx} at a few characteristic values of T is shown in Fig. 1D. At liquid helium T, the devices exhibited μ ~ 10 to 50 $m^2 V^{-1} s^{-1}$ for carrier concentrations n over a wide range of the order of 10^{12} cm^{-2}, and μ remained above 5 $m^2 V^{-1} s^{-1}$ up to room T (fig. S2). Such values of μ allow ballistic transport with $\ell > 1$ μm at $T < 300$ K. At $T \geq 150$ K, ℓ_{ee} decreases to 0.1 to 0.3 μm over the same range of n (figs. S3 and S4) (*22, 23*). This allows the essential condition for electron hydrodynamics ($\ell_{ee} \ll W, \ell$) to be satisfied within this temperature range. If one uses the conventional longitudinal geometry of electrical measurements, viscosity has little effect on σ_{xx} (figs. S5 to S7), essentially because the flow in this geometry is uniform, whereas the total momentum of the moving Fermi liquid is conserved in electron-electron collisions (*18*). The only evidence for hydrodynamics that we could find in the longitudinal geometry was the Gurzhi effect that appeared as a function of the electron temperature, which is controlled by applying large I, similar to the observations in (*15*) (fig. S8).

To look for hydrodynamic effects, we used the geometry shown in Fig. 1C. In this setup, I is injected through a narrow constriction into the graphene bulk, and the voltage drop V_v is measured at the nearby side contacts located at the distance L ~ 1 μm away from the injection point. These can be considered as nonlocal measurements, although the stray currents are not exponentially small (dashed curves in Fig. 1E). To distinguish from the proper nonlocal geometry (*24*), we refer to the linear-response signal measured in our geometry as vicinity resistance, $R_v = V_v/I$. The idea is that, in the case of a viscous flow, whirlpools emerge as shown in Fig. 1B, and their appearance can then be detected as sign reversals of V_v, which is positive for the conventional current flow (Fig. 1A) and negative for viscous backflow (Fig. 1B). Figure 1E shows examples of R_v for the same SLG device as in Fig. 1D, and other SLG and BLG devices exhibited similar behavior (*18*). Away from the CNP, R_v is negative over a wide range of intermediate T, despite an expected substantial offset due to stray currents. Figure 2 details our observations further by showing maps of $R_v(n,T)$ for SLG and BLG. The two Fermi liquids exhibited somewhat different behavior, reflecting their different electronic spectra, but R_v was negative over a large range of n and T for both. Two more R_v maps are provided in fig. S9. In total, seven multiterminal devices with W ranging from 1.5 to 4 μm were investigated, showing vicinity behavior that was highly reproducible both for different contacts on the same device and for different devices, independently of their W, although we note that the backflow was more pronounced for devices with the highest μ and lowest charge inhomogeneity.

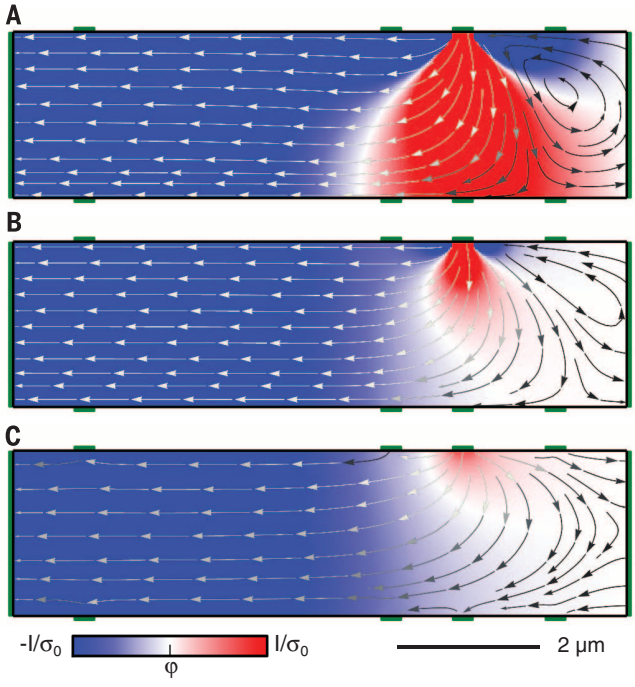

Fig. 3. Whirlpools in electron flow. (**A** to **C**) Calculated **J**(**r**) and φ(**r**) for a geometry similar to that shown in Fig. 1C, with the green bars indicating voltage contacts. D_v = 2.3, 0.7, and 0 μm for (A), (B), and (C), respectively. Vortices are evident in the top right corners of (A) and (B), where the current flow is in the direction opposite to that in (C), which shows the case of zero viscosity. In each panel, the current streamlines also change from white to black to indicate that the current density |**J**(**r**)| is lower to the right of the injecting contact.

The same anomalous vicinity response was also evident when we followed the method of (*15*) and used the current I to increase the electron temperature. In this case, V_v changed its sign as a function of I from positive to negative to positive again, reproducing the behavior of R_v with increasing T of the cryostat (fig. S10). Comparing figs. S8 and S10, it is clear that the vicinity geometry strongly favors the observation of hydrodynamic effects: The measured vicinity voltage changed its sign, whereas in the standard geometry, the same viscosity led only to relatively small changes in dV/dI. We also found that the magnitude of negative R_v decayed rapidly with L (fig. S11), in agreement with the finite size of electron whirlpools.

Negative resistances can in principle arise from other effects, such as single-electron ballistic transport ($\ell_{ee} \gg \ell$) or quantum interference (*18, 20, 24*). The latter contribution is easily ruled out, because quantum corrections rapidly wash out at $T > 20$ K and have a random sign that rapidly oscillates as a function of magnetic field. Also, our numerical simulations using the Landauer-Büttiker formalism and the realistic device geometry showed

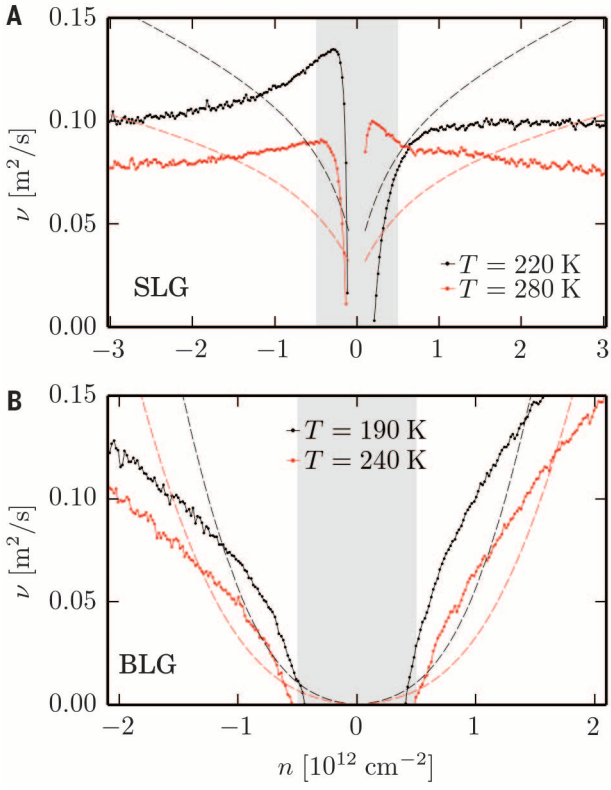

Fig. 4. Viscosity of the Fermi liquids in graphene. (**A** and **B**) Solid curves show values of ν for SLG and BLG, respectively. Dashed curves represent calculations based on many-body diagrammatic perturbation theory (no fitting parameters). The gray shaded areas indicate regions around the CNP where our hydrodynamic model is not applicable (*18*).

that no negative resistance could be expected for the vicinity configuration in zero magnetic field (*19*, *21*). Nonetheless, we carefully considered the possibility of any accidental spillover of single-electron ballistic effects into the vicinity geometry of our experiment. The dependences of the negative vicinity signal on T, n, I, and the device geometry allowed us to unambiguously rule out any such contribution (*18*). For example, the single-electron ballistic phenomena should become more pronounced for longer ℓ (that is, with decreasing T or electron temperature and with increasing n), in contrast to the nonmonotonic behavior of V_v.

Turning to theory, we can show that negative R_v arises naturally from whirlpools that appear in a viscous Fermi liquid near current-injecting contacts. As discussed in (*18*), electron transport for sufficiently short ℓ_{ee} can be described by the hydrodynamic equations

$$\nabla\cdot\mathbf{J}(\mathbf{r}) = 0 \qquad (1)$$

and

$$\frac{\sigma_0}{e}\nabla\phi(\mathbf{r}) + D_v^2\nabla^2\mathbf{J}(\mathbf{r}) - \mathbf{J}(\mathbf{r}) = 0 \qquad (2)$$

where $\mathbf{J}(\mathbf{r})$ is the (linearized) particle current density, and $\varphi(\mathbf{r})$ is the electric potential in the 2D plane. If $D_v \to 0$, Eq. 2 yields Ohm's law $-e\mathbf{J}(\mathbf{r}) = \sigma_0\mathbf{E}(\mathbf{r})$ with a Drude-like conductivity $\sigma_0 \equiv ne^2\tau/m$, where $-e$ and m are the electron charge and the effective mass, respectively (**E,** electric field). The three terms in Eq. 2 describe (i) the electric force generated by the steady-state charge distribution in response to the applied current I, (ii) the viscous force (*1*, *2*), and (iii) friction caused by momentum-nonconserving processes that are parameterized by the scattering time $\tau(n,T)$.

Equations 1 and 2 can be solved numerically (*18*), and Fig. 3 shows examples of spatial distributions of $\varphi(\mathbf{r})$ and $\mathbf{J}(\mathbf{r})$. For experimentally relevant values of D_v, a vortex appears in the vicinity of the current-injecting contact. This is accompanied by the sign reversal of $\varphi(\mathbf{r})$ at the vicinity contact on the right of the injector, which is positive in Fig. 3C (no viscosity) but becomes negative in Fig. 3, A and B. Our calculations for this geometry show that R_v is negative for $D_v \gtrsim 0.4\,\mu m$ (*18*). Because both τ and ν decrease with increasing T, D_v also decreases, and stray currents start to dominate the vicinity response at high T. This explains why R_v in Figs. 1 and 2 becomes positive close to room T, even though our hydrodynamic description has no high-temperature cutoff (*18*). Despite positive R_v values, the viscous contribution remains considerable near room T (Fig. 1D and fig. S12). At low T, the electron system approaches the Knudsen regime, and our hydrodynamic description becomes inapplicable because $\ell_{ee} \sim \ell$ (*18*). In the latter regime, the whirlpools should disappear and R_v should become positive (fig. S13), in agreement with the experiment and our numerical simulations based on the Landauer-Büttiker formalism.

The numerical results in Fig. 3 can be understood if we rewrite Eqs. 1 and 2 as

$$\mathbf{J}(\mathbf{r}) = \frac{\sigma_0}{e}\nabla\phi(\mathbf{r}) - nD_v^2\nabla\times\omega(\mathbf{r}) \qquad (3)$$

where $\omega(\mathbf{r}) \equiv n^{-1}\nabla\times\mathbf{J}(\mathbf{r}) = \omega(\mathbf{r})\hat{\mathbf{z}}$ is the vorticity ($\hat{\mathbf{z}}$ is the unit vector perpendicular to the graphene plane) (*2*). Taking the curl of Eq. 3, the vorticity satisfies the equation $\omega(\mathbf{r}) = D_v^2\nabla^2\omega(\mathbf{r})$, where D_v plays the role of a diffusion constant. The current I injects vorticity at the source contact, which then exponentially decays over the length scale D_v. For $\nu = 0.1\ m^2\ s^{-1}$ [as estimated in (*25*)] and $\tau = 1.5$ ps (fig. S2), we find that $D_v \approx 0.4\,\mu m$, in qualitative agreement with the measurements in fig. S11.

Lastly, we can combine the measurements of R_v and resistivity ρ_{xx} with the solution of Eqs. 1 and 2 in Fig. 3 to extract the kinematic viscosity for SLG and BLG. Because the observed Gurzhi effect in ρ_{xx} is small at low currents (fig. S6), we can use $\rho_{xx} = 1/\sigma_0 = m/(ne^2\tau)$ to determine $\tau(n,T)$ (*18*). Furthermore, for the experimentally relevant values of D_v, we find that R_v is a quadratic function of D_v

$$R_V = (b + aD_v^2)\sigma_0^{-1} \qquad (4)$$

where a and b are numerical coefficients dependent only on the measurement geometry and boundary conditions, and b describes the contribution from stray currents (fig. S14). For the specific device in Fig. 3, we determined that $a = -0.29\ \mu m^{-2}$ and $b = 0.056$, and this allows us to estimate $D_v(n,T)$ from measurements of R_v. For the known τ and D_v, we find that $\nu(n,T) = D_v^2/\tau$. The applicability limits of this analysis are discussed in (*18*), and the results are plotted in Fig. 4 for one of our devices. The figure shows that, at carrier concentrations of ~10^{12} cm^{-2}, the Fermi liquids in both SLG and BLG are highly viscous, with $\nu \approx 0.1\ m^2\ s^{-1}$. In comparison, liquid honey has typical viscosities of ~0.002 to 0.005 $m^2\ s^{-1}$.

Figure 4 also shows the results of fully independent microscopic calculations of $\nu(n,T)$, which were carried out by extending the many-body theory of (*25*) to the case of 2D electron liquids hosted by encapsulated SLG and BLG. Within the range of applicability of our analysis in Fig. 4 ($n \sim 10^{12}$ cm^{-2}), the agreement in absolute values of the electron viscosity is good, especially taking into account that no fitting parameters were used in the calculations. Because the strong inequality $\ell_{ee} \gg \ell$ required by the hydrodynamic theory cannot be reached even for graphene, it would be unreasonable to expect better agreement (*18*). In addition, our analysis does not apply near the CNP, because the theory neglects contributions from thermally excited carriers, spatial charge inhomogeneity, and coupling between charge and energy flows, which can play a substantial role at low doping (*16*, *18*). Further work is needed to understand electron hydrodynamics in the intermediate regime $\ell \gtrsim \ell_{ee}$ and, for example, to explain ballistic transport ($\ell > W$) in graphene at high T in terms of suitably modified hydrodynamic theory. The naive single-particle description that is routinely used for graphene's ballistic phenomena even above 200 K (*19*, *21*) cannot be justified; a more complete theory is needed to describe the injection of a collimated electron beam into a strongly interacting 2D liquid. As for experimental approaches, the highly viscous Fermi liquids in graphene and their accessibility offer a promising opportunity to use various scanning probes for visualization and further understanding of electron hydrodynamics.

REFERENCES AND NOTES

1. L. D. Landau, E. M. Lifshitz, *Fluid Mechanics* (Pergamon Press, 1987).
2. G. K. Batchelor, *An Introduction to Fluid Dynamics* (Cambridge Univ. Press, 1967).
3. B. V. Jacak, B. Müller, *Science* **337**, 310–314 (2012).
4. C. Cao *et al*., *Science* **331**, 58–61 (2011).
5. E. Elliott, J. A. Joseph, J. E. Thomas, *Phys. Rev. Lett.* **113**, 020406 (2014).
6. T. Schäfer, D. Teaney, *Rep. Prog. Phys.* **72**, 126001 (2009).
7. R. N. Gurzhi, *Sov. Phys. Usp.* **11**, 255–270 (1968).
8. A. O. Govorov, J. J. Heremans, *Phys. Rev. Lett.* **92**, 026803 (2004).
9. R. Bistritzer, A. H. MacDonald, *Phys. Rev. B* **80**, 085109 (2009).
10. M. Müller, J. Schmalian, L. Fritz, *Phys. Rev. Lett.* **103**, 025301 (2009).
11. A. V. Andreev, S. A. Kivelson, B. Spivak, *Phys. Rev. Lett.* **106**, 256804 (2011).
12. A. Tomadin, G. Vignale, M. Polini, *Phys. Rev. Lett.* **113**, 235901 (2014).
13. B. N. Narozhny, I. V. Gornyi, M. Titov, M. Schütt, A. D. Mirlin, *Phys. Rev. B* **91**, 035414 (2015).
14. G. F. Giuliani, G. Vignale, *Quantum Theory of the Electron Liquid* (Cambridge Univ. Press, 2005).
15. M. J. M. de Jong, L. W. Molenkamp, *Phys. Rev. B* **51**, 13389–13402 (1995).
16. J. C. W. Song, L. S. Levitov, *Phys. Rev. Lett.* **109**, 236602 (2012).
17. R. V. Gorbachev *et al*., *Nat. Phys.* **8**, 896–901 (2012).
18. Supplementary materials are available on *Science* Online.
19. A. S. Mayorov *et al*., *Nano Lett.* **11**, 2396–2399 (2011).
20. L. Wang *et al*., *Science* **342**, 614–617 (2013).
21. T. Taychatanapat, K. Watanabe, T. Taniguchi, P. Jarillo-Herrero, *Nat. Phys.* **9**, 225–229 (2013).
22. Q. Li, S. Das Sarma, *Phys. Rev. B* **87**, 085406 (2013).
23. M. Polini, G. Vignale, http://arxiv.org/abs/1404.5728 (2014).
24. D. A. Abanin *et al*., *Science* **332**, 328–330 (2011).
25. A. Principi, G. Vignale, M. Carrega, M. Polini, http://arxiv.org/abs/1506.06030 (2015).

ACKNOWLEDGMENTS

This work was supported by the European Research Council, the Royal Society, Lloyd's Register Foundation, the Graphene Flagship, and the Italian Ministry of Education, University and Research through the program Progetti Premiali 2012 (project ABNANOTECH). D.A.B. and I.V.G. acknowledge support from the Marie Curie program SPINOGRAPH (Spintronics in Graphene). A.P. received support from the Nederlandse Wetenschappelijk Organisatie. R.K.K. received support from the Engineering and Physical Sciences Research Council.

SUPPLEMENTARY MATERIALS

www.sciencemag.org/content/351/6277/1055/suppl/DC1
Supplementary Text
Figs. S1 to S14
References (*26*–*37*)

14 July 2015; accepted 23 December 2015
Published online 11 February 2016
10.1126/science.aad0201

ELECTRON TRANSPORT

Observation of the Dirac fluid and the breakdown of the Wiedemann-Franz law in graphene

Jesse Crossno,[1,2] Jing K. Shi,[1] Ke Wang,[1] Xiaomeng Liu,[1] Achim Harzheim,[1] Andrew Lucas,[1] Subir Sachdev,[1,3] Philip Kim,[1,2]* Takashi Taniguchi,[4] Kenji Watanabe,[4] Thomas A. Ohki,[5] Kin Chung Fong[5]*

Interactions between particles in quantum many-body systems can lead to collective behavior described by hydrodynamics. One such system is the electron-hole plasma in graphene near the charge-neutrality point, which can form a strongly coupled Dirac fluid. This charge-neutral plasma of quasi-relativistic fermions is expected to exhibit a substantial enhancement of the thermal conductivity, thanks to decoupling of charge and heat currents within hydrodynamics. Employing high-sensitivity Johnson noise thermometry, we report an order of magnitude increase in the thermal conductivity and the breakdown of the Wiedemann-Franz law in the thermally populated charge-neutral plasma in graphene. This result is a signature of the Dirac fluid and constitutes direct evidence of collective motion in a quantum electronic fluid.

Understanding the dynamics of many interacting particles is a formidable task in physics. For electronic transport in matter, strong interactions can lead to a breakdown of the Fermi liquid (FL) paradigm of coherent quasi-particles scattering off of impurities. In such situations, provided that certain conditions are met, the complex microscopic dynamics can be coarse-grained to a hydrodynamic description of momentum, energy, and charge transport on long length and time scales (*1*). Hydrodynamics has been successfully applied to a diverse array of interacting quantum systems, from high-mobility electrons in conductors (*2*) to cold atoms (*3*) and quark-gluon plasmas (*4*). Hydrodynamic effects are expected to greatly modify transport coefficients compared with their FL counterparts, as has been argued for strongly interacting massless Dirac fermions in graphene at the charge-neutrality point (CNP) (*5*–*8*).

Many-body physics in graphene is interesting because of electron-hole symmetry and a linear dispersion relation at the CNP (*9*, *10*). Together with the vanishing Fermi surface, the ultra-relativistic spectrum leads to ineffective screening (*11*) and the formation of a strongly interacting quasi-relativistic electron-hole plasma known as a Dirac fluid (DF) (*12*). The DF shares many features with quantum critical systems (*13*): most importantly, the electron-electron scattering time is fast (*14*–*17*) and well suited to a hydrodynamic description. Because of the quasi-relativistic nature of the DF, this hydrodynamic limit is described by equations (*18*) quite different from those applicable to its nonrelativistic counterparts. A number of unusual properties have been predicted, including nearly perfect (inviscid) flow (*19*) and a diverging thermal conductivity, which results in the breakdown of the Wiedemann-Franz (WF) law at finite temperature (*5*, *6*).

Away from the CNP, graphene has a sharp Fermi surface, and the standard FL phenomenology holds. By tuning the chemical potential, we are able to measure thermal and electrical conductivity in both the DF and the FL in the same sample. In a FL, the relaxation of heat and charge currents is closely related, as they are carried by the same quasi-particles. The WF law (*20*) states that the electronic contribution to a metal's thermal conductivity κ_e is proportional to its electrical conductivity σ and temperature T, such that the Lorenz ratio $\mathcal{L}$ satisfies

$$\mathcal{L} \equiv \frac{\kappa_e}{\sigma T} = \frac{\pi^2}{3}\left(\frac{k_B}{e}\right)^2 \equiv \mathcal{L}_0 \qquad (1)$$

where e is the electron charge, k_B is the Boltzmann constant, and $\mathcal{L}_0$ is the Sommerfeld value derived from FL theory. $\mathcal{L}_0$ depends only on fundamental constants, not specific details of the system such as carrier density or effective mass. As a robust prediction of FL theory, the WF law has been verified in numerous metals (*20*). At high temperatures, the WF law can be violated due to inelastic electron-phonon scattering or bipolar diffusion in semiconductors, even when electron-electron interactions are negligible (*21*). In recent years, several nontrivial violations of the WF law—all of which are related to the emergence of non-FL behavior—have been reported in strongly interacting systems such as Luttinger liquids (*22*), metallic ferromagnets (*23*), heavy fermion metals (*24*), and underdoped cuprates (*25*).

Owing to the strong Coulomb interactions between thermally excited charge carriers, the WF law is expected to be violated at the CNP in a DF. An electric field drives electrons and holes in opposite directions; collisions between them introduce a frictional dissipation, resulting in a finite conductivity even in the absence of disorder (*26*). In contrast, a temperature gradient causes electrons and holes to move in the same direction,

[1]Department of Physics, Harvard University, Cambridge, MA 02138, USA. [2]John A. Paulson School of Engineering and Applied Sciences, Harvard University, Cambridge, MA 02138, USA. [3]Perimeter Institute for Theoretical Physics, Waterloo, Ontario N2L 2Y5, Canada. [4]National Institute for Materials Science, Namiki 1-1, Tsukuba, Ibaraki 305-0044, Japan. [5]Quantum Information Processing Group, Raytheon BBN Technologies, Cambridge, MA 02138, USA.
***Corresponding author. E-mail: pkim@physics.harvard.edu (P.K.); kc.fong@bbn.com (K.C.F.)**

Science

Negative local resistance caused by viscous electron backflow in graphene

D. A. Bandurin, I. Torre, R. Krishna Kumar, M. Ben Shalom, A. Tomadin, A. Principi, G. H. Auton, E. Khestanova, K. S. Novoselov, I. V. Grigorieva, L. A. Ponomarenko, A. K. Geim and M. Polini

Science **351** (6277), 1055-1058.
DOI: 10.1126/science.aad0201originally published online February 11, 2016

Electrons that flow like a fluid

Electrons inside a conductor are often described as flowing in response to an electric field. This flow rarely resembles anything like the familiar flow of water through a pipe, but three groups describe counterexamples (see the Perspective by Zaanen). Moll *et al.* found that the viscosity of the electron fluid in thin wires of $PdCoO_2$ had a major effect on the flow, much like what happens in regular fluids. Bandurin *et al.* found evidence in graphene of electron whirlpools similar to those formed by viscous fluid flowing through a small opening. Finally, Crossno *et al.* observed a huge increase of thermal transport in graphene, a signature of so-called Dirac fluids.

Science, this issue p. 1061, 1055, 1058; see also p. 1026

Supplementary Material

Negative local resistance due to viscous electron backflow in graphene

D. A. Bandurin[1], I. Torre[2,3], R. Krishna Kumar[1,4], M. Ben Shalom[1,5], A. Tomadin[6], A. Principi[7], G. H. Auton[5], E. Khestanova[1,5], K. S. Novoselov[5], I. V. Grigorieva[1], L. A. Ponomarenko[1,4], A. K. Geim[1], M. Polini[3]

#1 Device fabrication

Our devices were made from single- and bi-layer graphene encapsulated between relatively thick (~ 50 nm) crystals of hexagonal boron nitride (hBN). The crystals' transfers were carried out using the dry-peel technique described previously (*20,26*). The heterostructures were assembled on top of an oxidized Si wafer (300 nm of SiO_2) which served as a back gate, and then annealed at $300°C$ in Ar-H_2 atmosphere for 3 hours. After this, a PMMA mask was fabricated on top of the hBN-graphene-hBN stack by electron-beam lithography. This mask was used to define contact areas to graphene, which was done by dry etching with fast selective removal of hBN (*27*). Metallic contacts (usually, 5 nm of Ta followed by 50 nm Nb) were then deposited onto exposed graphene edges that were a few nm wide. Such quasi-one-dimensional contacts to graphene (*27*) had notably lower contact resistance than those reported previously without the use of selective hBN etching (*20*). As the next step, another round of electron-beam lithography was used to prepare a thin metallic mask (≈ 40 nm Al) which defined a multiterminal Hall bar. Subsequent plasma etching translated the shape of the metallic mask into encapsulated graphene (see *figs*. *S1A-B* and Fig. 1C of the main text). The Al mask could also serve as a top gate, in which case Al was wet-etched near the Nb/Ta leads to remove the electrical contact to graphene. All our bilayer graphene (BLG) devices were prepared with such a top gate, which allowed us to control not only the carrier concentration but also the displacement field between the two layers. Also, for single-layer graphene (SLG) we usually (but not always) made both top and bottom gates for the sake of fabrication procedures, even though the two gates fulfilled essentially the same function.

The studied Hall bars were 1.5 to 4 μm in width W and up to 20 μm in length (larger W were avoided as we previously found them to suffer from charge inhomogeneity induced by contamination bubbles and associated strain; ref. *28*). The devices were carefully characterized and, in addition to Fig. 1D of the main text, an example of typical behavior of $\rho_{xx}(n)$ is shown in *fig. S1C*. All the studied devices, independently of their width or length, were found to exhibit negative vicinity resistance over the described range of temperatures below room T and over a wide range of $n \sim 10^{12}$ cm^{-2}. *Fig. S1D* shows another example of this behavior, which is rather similar to that in Fig. 1E of the main text.

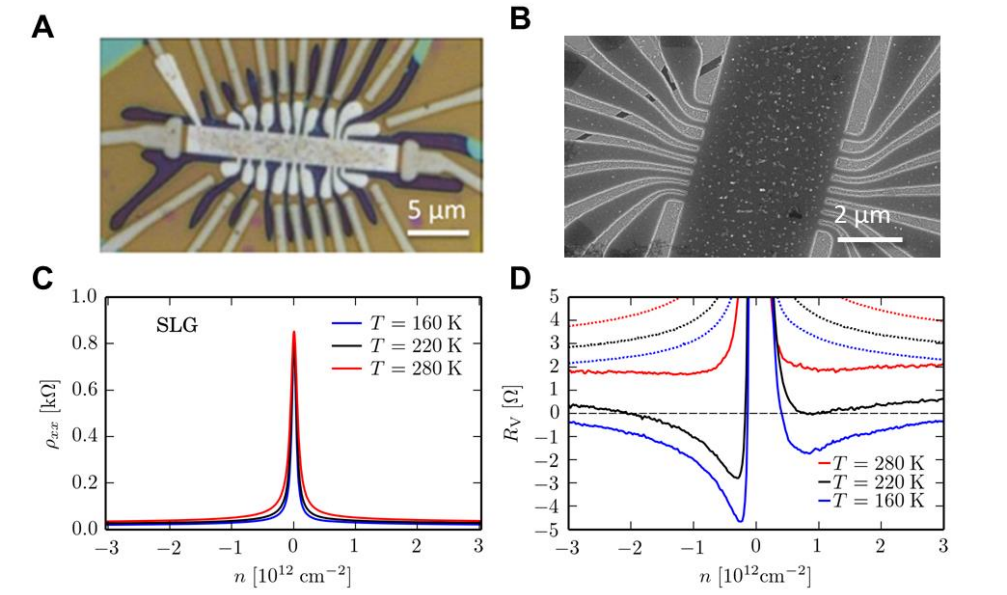

Fig. S1. Further examples of the studied graphene devices and their behavior. (**A**) Optical micrograph for an encapsulated SLG device. The bright white area is the top gate and the graphene Hall bar repeats its shape. Numerous metallic leads terminated with quasi-one-dimensional contacts to graphene are seen in a duller white color. Other colors on the photo appeared due to different etching depths of the hBN-graphene-hBN stack. (**B**) Electron micrograph of yet another SLG device. Resistivity (**C**) and vicinity resistance (**D**) for the device shown in (A). For resistivity measurements, we always used voltage probes separated by a distance larger than the main channel width. In (C), voltage probes were 8 μm away from each other. The vicinity probe used in (D) was 1 μm away from the current injecting lead. Positive and negative sign of n correspond to gate-induced electrons and holes, respectively. The dashed curves in (D) show the expected 'classical' contribution $b\rho_{xx}$ which arises due to stray currents. For this particular device, we find $b \approx 0.1$ using numerical simulations of the device geometry as described in the main text and the supplementary section on numerical simulation.

#2 Mobility and scattering times

Our longitudinal measurements allowed us to determine $\mu(n,T)$ and $\tau(n,T)$ using the standard relation, $\sigma_{xx} = ne\mu = ne^2\tau/m$. Results are shown in *fig. S2* for both SLG and BLG. The plotted behavior is universal, that is, it changes little between different devices because, for the shown T range of interest, electron transport was limited by electron-phonon scattering. One can see that away from the charge neutrality point (CNP), τ depends weakly on n for both SLG and BLG. Typical times are of about 1-2 ps. As for $\mu(n,T)$, its behavior as a function of n is notably different in the two graphene systems because of different energy dependences of their effective

masses. For BLG, which has a nearly parabolic spectrum, we can for simplicity use the constant $m = 0.03m_0$ where m_0 is the free electron mass. This yields that μ is simply proportional to τ. For SLG, the effective (or cyclotron) mass is given by $m \propto \sqrt{n}$, leading to μ varying approximately as $n^{-1/2}$ (*fig. S2B*).

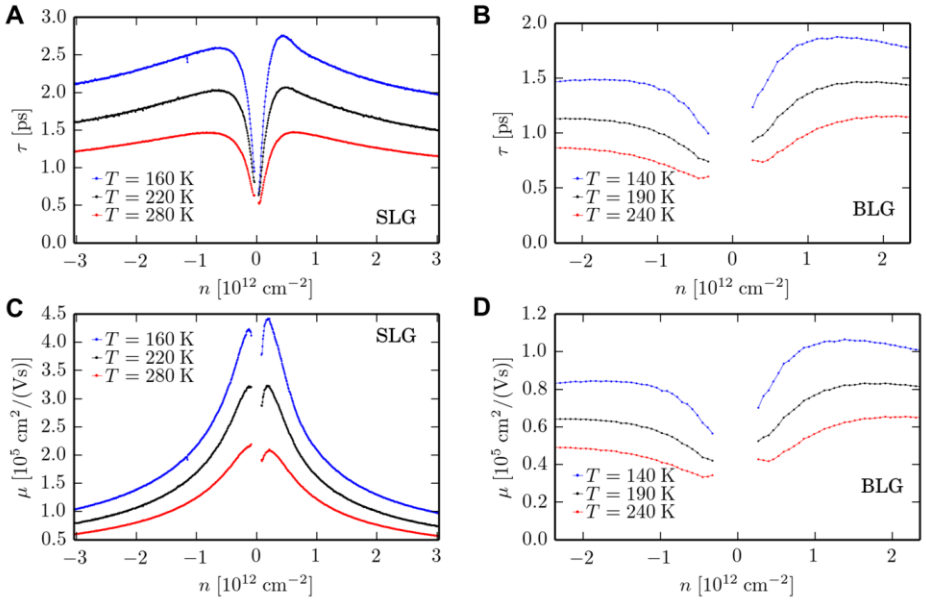

Fig. S2. Phonon-limited transport in graphene. (**A,B**) Mean free times and mobilities in encapsulated SLG, respectively. (**C,D**) Same for encapsulated BLG. The plots are for the T range in which hydrodynamics effects were found strongest.

#3 Microscopic calculations of the electron-electron mean free path

In this Section we briefly summarize the results of many-body diagrammatic perturbation theory calculations of the electron-electron scattering length ℓ_{ee}. Results in this Section refer to SLG, in the region of parameter space relevant for our experiments.

We calculated $\ell_{\mathrm{ee}} = v_{\mathrm{F}}\tau_{\mathrm{ee}}$ from the imaginary part of the retarded quasiparticle self-energy $\Sigma_\lambda(k,\omega)$, evaluated at the Fermi surface. For an electron doped system we find $\hbar/\tau_{\mathrm{ee}} = -2\,\Im m[\Sigma_{\lambda=+1}(k_{\mathrm{F}},0)]$. Here, v_{F} is the (bare) Fermi velocity (which is equal to the Dirac velocity v_{D} in SLG and $\hbar k_{\mathrm{F}}/m$ in BLG), $\lambda = \pm 1$ is a conduction/valence band index, and τ_{ee} is the quasiparticle lifetime due to e-e scattering (*14*). The quantity $\Sigma_\lambda(k,\omega)$ can be calculated by using the G_0W approximation (*23*) with a dynamically screened interaction $W_{\boldsymbol{k},\omega}$ evaluated at the level of the random phase approximation (RPA) (*14*).

In the case of SLG, the imaginary part of the quasiparticle self-energy is given by the following expression (*23*)

$$\Im m[\Sigma_\lambda(k,\omega)] = -\sum_{\lambda'=\pm 1}\int \frac{d^2\boldsymbol{q}}{(2\pi)^2}\Im m\left[W_{\boldsymbol{q},\omega-\xi_{\lambda',\boldsymbol{k}+\boldsymbol{q}}}\right]F_{\lambda\lambda'}[n_{\mathrm{B}}\left(\hbar\omega-\xi_{\lambda',\boldsymbol{k}+\boldsymbol{q}}\right)+n_{\mathrm{F}}\left(-\xi_{\lambda',\boldsymbol{k}+\boldsymbol{q}}\right)]$$

where $F_{\lambda\lambda'} = \left[1+\lambda\lambda'\cos\left(\theta_{\boldsymbol{k},\boldsymbol{k}+\boldsymbol{q}}\right)\right]/2$ is the chirality factor, $\xi_{\lambda,\boldsymbol{k}} = \lambda\hbar v_{\mathrm{F}}k-\mu$ is the Dirac band energy measured with respect to the chemical potential μ, $W_{\boldsymbol{q},\omega} = v_q/\varepsilon(q,\omega) \equiv v_q/\left[1-v_q\chi_0(q,\omega)\right]$ the RPA dynamically screened interaction, and $n_{\mathrm{B/F}}(x) \equiv 1/[\exp(\beta x)\mp 1]$ are the Bose/Fermi statistical factors with $\beta = 1/(k_{\mathrm{B}}T)$. In the above expressions, v_q is a suitably-chosen effective Coulomb interaction (see below), and $\chi_0(q,\omega)$ is the polarization function of a non-interacting 2D massless Dirac fermion system at a finite temperature and carrier density (*29*). More details can be found, for example, in Refs. (*22,23*).

In our calculations we have also estimated the impact of the 'environment' such as i) nearby metal gates (by modeling them as perfect conductors), ii) the uniaxial anisotropy of dielectric hBN, and iii) thin-film effects. The bare Coulomb potential $2\pi e^2/q$ is strongly modified by these three factors. The effective Coulomb interaction v_q can be written in the form $2\pi e^2\mathcal{G}(qd,qd')/q$ where the explicit functional dependence of the form factor $\mathcal{G}(x,y)$ on its variables x and y is rather cumbersome and will be reported elsewhere. The form factor depends on the thickness d and d' of the hBN slab below and above graphene, respectively. It also depends on the static values of the in-plane $\epsilon_x(\omega)$ and out-of-plane $\epsilon_z(\omega)$ components of the hBN permittivity tensor: see, for example, Ref. (*30*). Numerical results for ℓ_{ee} in encapsulated SLG are shown in *fig. S3*.

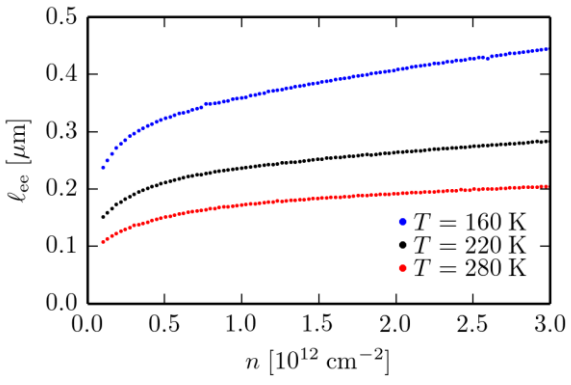

Fig. S3. Numerical results for the e-e mean free path ℓ_{ee} in our encapsulated SLG devices. Results are shown as a function of carrier density n and for three T. For this particular calculation, we used $d = 80$ nm and $d' = 70$ nm and took into account the top metal gate simulating the device shown in *fig. S1A*. We have also checked that metal gates at such distances play little role (the presence of

the gate changed ℓ_{ee} typically by less than 5% with respect to the ungated case), in agreement with the fact that the SLG devices with and without top gates exhibited the R_V behavior indistinguishable within variations between different contacts.

Besides determining the region of parameter space where the hydrodynamics theory can be applied, the frequency of electron-electron collisions also determines the numerical value of the electron liquid viscosity. The usual estimate for the value of the kinematic viscosity of a classical liquid is $\nu \sim v\ell_{coll}$ (*31*), where v is a characteristic velocity (e.g. the thermal velocity for classical liquids) of particles and ℓ_{coll} is the mean free path for inter-particle collisions.

Microscopic calculations for SLG yield (*25*):

$$\nu = \frac{1}{4} v_F \tilde{\ell}_{ee} \qquad (S1).$$

where $\tilde{\ell}_{ee}$ is a characteristic length associated with electron-electron scattering, which is of the same order of magnitude as ℓ_{ee} in the explored range of parameters. Their ratio $\tilde{\ell}_{ee}/\ell_{ee}$ is shown in *fig. S4*. Eq. (*S1*) is consistent with the above estimate for classical fluids. From Eq. (*S1*) we also find that the viscosity diffusion length $D_\nu = \sqrt{\nu\tau}$, which determines the size of electron whirlpools, is equal to $D_\nu = \sqrt{\tilde{\ell}_{ee}\ell}/2$ and, therefore, depends on both electron-electron collisions and momentum-non-conserving collisions.

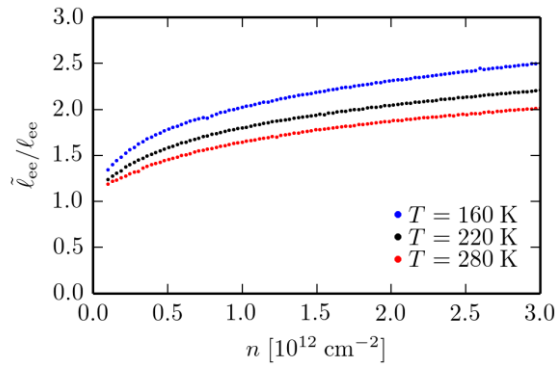

Fig. S4. Comparison between ℓ_{ee} and $\tilde{\ell}_{ee}$. Numerical results for the ratio $\tilde{\ell}_{ee}/\ell_{ee}$ in the same range of densities and for the same temperatures as in *fig. S3*.

#4 On pseudo-relativistic and pressure terms in the Navier-Stokes equation

Because of the pseudo-relativistic nature of transport in SLG, the Navier-Stokes equation for the two-dimensional electron liquid in SLG contains a number of pseudo-relativistic terms (*32*). Such terms have not been considered in Eq. (2) of the main text. It is possible to demonstrate that, if one considers only linear deviations from a situation of uniform and static equilibrium ($n(\boldsymbol{r},t) = n$ and $\boldsymbol{v}(\boldsymbol{r},t) = \boldsymbol{0}$), the only pseudo-relativistic correction that survives is the appearance of the effective

(cyclotron) mass $m = \hbar k_{\mathrm{F}}/v_{\mathrm{D}}$ in the definition of the Drude-like conductivity σ_0 for the case of SLG.

In deriving Eq. (2) of the main text we have also neglected a term arising from the pressure P of the electron liquid, i.e. $-\nabla P(\boldsymbol{r},t)$. Here we show that, for a gated structure like the one used in our experiments, this term is simply proportional to the electric field and its only effect is to give a small correction to the capacitance between the graphene sheet and the top and bottom gates. In a gated structure, the electric potential and carrier density can be related by the so-called local capacitance approximation (LCA) (*32*), i.e. $\phi(\boldsymbol{r},t) = -en(\boldsymbol{r},t)/C$ where C is the capacitance per unit area. For a double gated device, $C = \epsilon(d+d')/(4\pi d\, d')$ where d and d' are the distances between graphene and the bottom and top gates, respectively, and $\epsilon = \sqrt{\epsilon_x(0)\epsilon_z(0)} \approx 4.4$ is the static dielectric constant of bulk hBN (we neglect the thin-film effects discussed in the previous Section). The quantities $\epsilon_x(\omega)$ and $\epsilon_z(\omega)$ have been introduced in the previous Section.

Using the LCA and the local density approximation $\nabla P(\boldsymbol{r},t) \approx (\partial P_{\mathrm{hom}}/\partial n)\nabla n(\boldsymbol{r},t)$, we can estimate the sum of the electric force and the force due to pressure as following

$$-\left(\frac{e^2 n}{C} + \frac{\partial P_{\mathrm{hom}}}{\partial n}\right)\nabla n(\boldsymbol{r},t) \qquad (S2)$$

where P_{hom} is the pressure of the homogeneous 2D electron liquid in SLG or BLG. Evaluating the two terms inside the round brackets at the equilibrium density n and approximating $\partial P_{\mathrm{hom}}/\partial n$ with its zero-temperature non-interacting value, i.e., $\partial P_{\mathrm{hom}}/\partial n \approx \xi E_{\mathrm{F}}$ where $\xi = 1/2$ ($\xi = 1$) for SLG (BLG), we can show that the ratio between the pressure term and the potential term is

$$\frac{\partial P_{\mathrm{hom}}/\partial n}{e^2 n/C} \approx \frac{d+d'}{4dd'\ \xi k_{\mathrm{TF}}} \qquad (S3)$$

where k_{TF} is the Thomas-Fermi screening wave number. For encapsulated SLG, $k_{\mathrm{TF}} = 4\,\alpha_{\mathrm{ee}} k_{\mathrm{F}} \approx (2.9\ \mathrm{nm})^{-1}$, where $\alpha_{\mathrm{ee}} = e^2/(\hbar v_{\mathrm{D}}\epsilon) \approx 0.5$ is the so-called graphene fine structure constant (*29*). Using a carrier density of $10^{12}\ \mathrm{cm}^{-2}$, $d = 80\ \mathrm{nm}$ and $d' = 80\ \mathrm{nm}$, we find that the ratio in Eq. (*S3*) is much smaller than unity. The pressure term can be safely neglected. For an encapsulated BLG sheet $k_{\mathrm{TF}} = 2e^2 m/(\hbar^2\epsilon) \approx (3.8\ \mathrm{nm})^{-1}$, irrespective of density (*14*). Therefore, the ratio (*S3*) is also negligible in this case.

#5 Smallness of the Reynolds number

The validity of the linearized Navier-Stokes equation (Eq. (2) of the main text) relies on the smallness of the Reynolds number (*1*), a dimensionless parameter that depends on the sample geometry and controls the smallness of the nonlinear term $[\boldsymbol{v}(\boldsymbol{r},t)\cdot\nabla]\boldsymbol{v}(\boldsymbol{r},t)$ in the convective derivative in the full Navier-Stokes equation with respect to the viscous term. In our case

$$\left|\frac{[\boldsymbol{v}(\boldsymbol{r},t)\cdot\nabla]\boldsymbol{v}(\boldsymbol{r},t)}{\nu\nabla^2\boldsymbol{v}(\boldsymbol{r},t)}\right| \approx \frac{|\boldsymbol{v}|W}{\nu} = \frac{I}{en\nu} \equiv \mathcal{R} \qquad (S4).$$

For a typical probing current $I = 10^{-7}$ A, $W = 1$ μm and $n = 10^{12}$ cm^{-2}, we estimate $|\boldsymbol{v}| \sim I/(enW) \approx 10^4$ cm/s. The corresponding value of the Reynolds number is $\mathcal{R} \sim 10^{-3} \ll 1$ if using $\nu \sim 10^3$ cm^2/s found theoretically (*25*) and in the experiment (Fig. 4 of the main text). Our linearized approximation is therefore fully justified.

#6 On the boundary conditions for solid-state hydrodynamic equations

The hydrodynamic equations need to be accompanied by appropriate boundary conditions (BCs). If viscosity is negligible, the current is proportional to the gradient of the potential. In this case it is sufficient to solve the Laplace equation for the potential to obtain both potential and current spatial patterns. The BCs that the potential must obey at the boundaries of the sample are of two types. In regions of the boundary where no electrical contacts are present, the normal component of the current (that is the normal derivative of the potential in the non-viscous regime) must be zero. In the regions of the boundaries where an electrical contact is present, the potential immediately inside the sample must be equal to the electric potential of the contact. Since the sample is current biased, we fix the total current flowing from each contact instead of fixing the value of the potential at each contact. It can be shown using standard theorems on the Laplace equation that these BCs (Neumann outside the contacts and Dirichlet at the contacts) uniquely determine the solution of the problem.

In the general case of a viscous flow, Eq. (2) of the main text requires additional BCs on the tangential component of the current. Generally, edges exert friction on the 2D electron liquid. The corresponding force (per unit length) is given by (*1*)

$$F_t = \epsilon_{ij}\hat{n}_i\sigma'_{jk}\hat{n}_k \qquad (S5).$$

In Eq. (*S5*), σ'_{jk} is the 2D viscous stress tensor, i.e. $\sigma'_{jk} = \eta\left(\partial_j v_k + \partial_k v_j - \delta_{ij}\partial_l v_l\right)$. In writing the previous expression for σ'_{jk} we have set to zero the diagonal contribution that is proportional to the so-called bulk viscosity and negligible (*25*).

The frictional force is in general a function of the tangential velocity $v_t = \epsilon_{ij}\hat{n}_i v_j$. For small velocities the force is simply proportional to the velocity leading to the BC

$$\epsilon_{ij}\hat{n}_i\hat{n}_k(\partial_j v_k + \partial_k v_j) = \epsilon_{ij}\hat{n}_i v_j / l_{\mathrm{b}} \qquad (S6)$$

where l_{b} is a characteristic length scale associated with boundary scattering. If this length is very small, Eq. (*S6*) reduces to the standard "no-slip" boundary condition commonly used in the description of classical liquids (*1*).

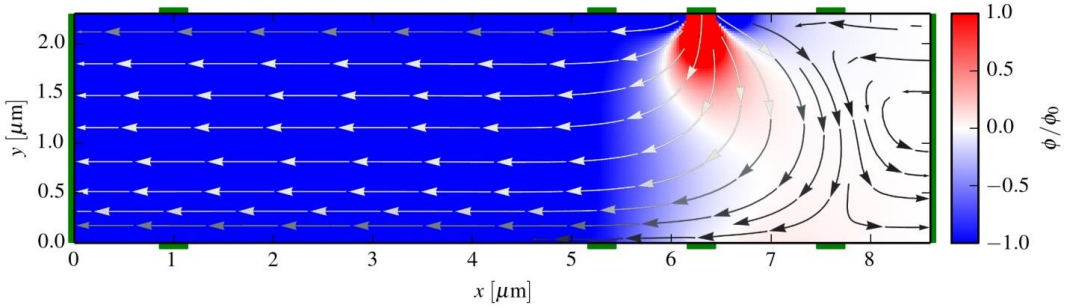

Fig. S5. Influence of boundary conditions. Calculated current density $\boldsymbol{J}(\boldsymbol{r})$ and electric potential $\phi(\boldsymbol{r})$ for the same geometry and the same $D_v = 0.7$ μm as in Fig. 3B of the main text. The difference is no-slip boundary conditions (l_{b}=0) used in this figure whereas l_{b}= ∞ in the main text.

We do not know precisely the value of l_{b} but we know that the combined effect of friction and viscosity arising at the boundaries can lead to an anomalous temperature dependence of the longitudinal resistivity ρ_{xx} which is known as the Gurzhi effect (*7*). As discussed in one of the following Sections, our experimental data for ρ_{xx} exhibit a monotonic behavior as a function of T, up to our highest temperature and for all carrier densities. This behavior suggests that the Gurzhi effect is small. For this reason, we can use to a good approximation the following BCs (*12*)

$$\epsilon_{ij}\hat{n}_i\hat{n}_k(\partial_j v_k + \partial_k v_j) = 0 \qquad (S7)$$

which assumes that l_{b} is larger than the characteristics length scales of the problem, D_v (vorticity diffusion length) and W (width of our multiterminal devices). Physically, Eq. (*S7*) corresponds to a vanishing tangential force acting on a moving liquid (*1*). At high current densities, however, the friction from the boundaries can be enhanced with respect to the simple linear model in Eq. (*S6*). In this case the Gurzhi effect can be observed in the differential resistance (see below).

In *fig. S5* we show that different values of l_{b} have little impact on the formation of whirlpools near current injecting contacts. The reader is urged to compare *fig. S5* (no-slip boundary conditions) with Fig. 3B in the main text, which was obtained using the free-surface BCs (Eq. *S7*)

#7 Applicability limits for hydrodynamic description of electron transport in doped graphene

The focus of our report is on the doped regime because the situation near the CNP is severely complicated by the presence of thermally excited quasiparticles, electron-hole puddles (*33*) and the large electron wavelength. In addition, thermoelectric effects (energy flow) are also expected to play a significant role near the CNP, although they appear only in the second order with respect to applied current I in zero magnetic field (see, for example, ref. *34*).

Under realistic experimental conditions, one important limit is set by charge inhomogeneity that impacts the viscosity analysis presented in Fig. 4 of the main text. Indeed, Eq. (4) assumes that $\sigma_0 = 1/\rho_{xx}$ is constant whereas the inhomogeneity locally modifies conductivity and stray currents. The electron-hole asymmetry seen in the experimental plots for R_V and the associated asymmetry in Fig. 4 of the main text are not expected in theory, and this provides a qualitative indication of the best accuracy one can expect for the extracted values of ν.

Our hydrodynamic theory suggests no high-T cutoff, at least up to temperatures at which optical phonon scattering starts playing a role. In fact, the theory smoothly converges with the standard Drude theory as viscosity tends to zero upon increasing T. However, there is a clear high-T cutoff on R_V being negative. It is simply dictated by the two competing terms in Eq. (4) of the main text, which are due to stray currents and viscous flow. After subtracting the stray-current contribution from the measured vicinity resistance (see below), we find that the hydrodynamic term smoothly extend to high *T* over the entire temperature range without any sign of cutoff.

On the other hand, the essential condition of electron hydrodynamics ($\ell_\mathrm{ee} \ll \ell$) certainly fails at temperatures below 50 K where the phase breaking length in graphene (which is smaller than ℓ_ee) is known to reach a micrometer scale (see, e.g., ref. *35*) and electron transport can be described in terms of single-particle ballistics (billiard-ball model). Our hydrodynamic theory does not capture the crossover ($\ell_\mathrm{ee} \sim \ell$) into this single-particle regime, and it remains to be investigated how strong the above inequality condition should be to allow the hydrodynamic description.

#8 Absence of the Gurzhi effect in longitudinal resistivity

Resistivity of an electron liquid is determined by interplay between bulk scattering (charged impurities, lattice vibrations, crystal defects, etc.), collisions at sample boundaries and e-e scattering (*7,15*). Bulk scattering normally increases with T. On the other hand, a combined effect of boundary and electron-electron scattering results in a contribution to ρ_{xx} which increases with T if

$\ell_{ee} \gg W$ (Knudsen regime) but decreases if the electron system enters the viscous flow regime, $\ell_{ee} \ll W$. The transition between the two limits may result in a non-monotonic temperature dependence of ρ_{xx}. This phenomenon is referred to as the Gurzhi effect (*7,15*). In reality, this effect is severely obscured by various bulk scattering mechanisms and expected to be weak (*15*).

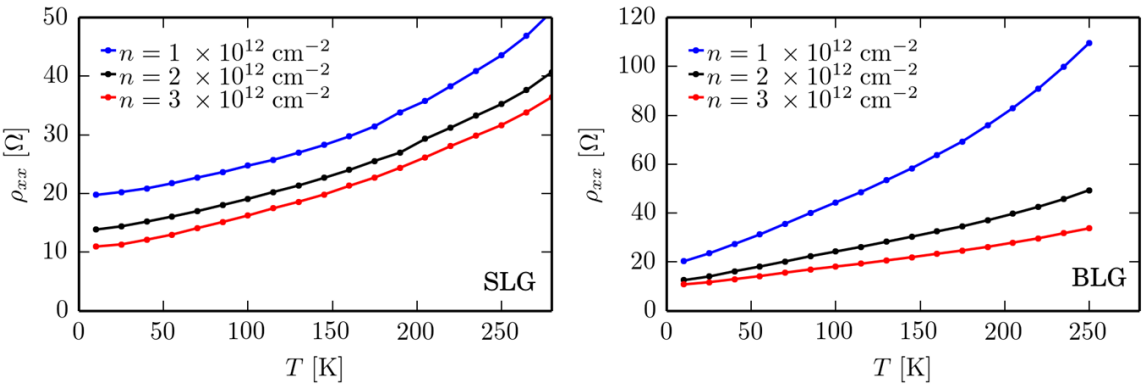

Fig. S6. Temperature dependence of longitudinal resistivity. Left and right panels are for SLG and BLG devices, respectively. The *T* dependences are monotonic, although one can notice that the curves slightly bulge around 100 K, which we attribute to a small hydrodynamics contribution related to the Gurzhi effect, as discussed in the next section.

In *fig. S6*, we show typical measurements of ρ_{xx} as a function of T for our SLG and BLG devices at different carrier concentrations. The behavior of $\rho_{xx}(T)$ is monotonic (no Gurzhi effect) even in the region of parameter space where electron-electron scattering is strong enough to cause the observed sign change in the vicinity geometry. This can be attributed to relative insensitivity of electron flow to boundary scattering in this simplest geometry of measurements as discussed in the preceding section. Neglecting more subtle effects observed in the differential resistance (see the next section), the absence of the Gurzhi effect in $\rho_{xx}(T)$ justifies our choice of (free-surface) BCs described by Eq. (*S7*), in which the force exerted by the boundary on the electron fluid flow is neglected.

Using the BC of Eq. (*S7*), we have solved numerically the linearized steady-state hydrodynamic equations for the longitudinal geometry and the results are plotted in *fig. S7* for SLG and BLG. This figure shows that ρ_{xx} depends only on the phenomenological scattering time τ in the Navier-Stokes equation (Eq. (2) in the main text) and exhibits little dependence on D_ν and, hence, the electron viscosity ν. This is the reason why we can use $\rho_{xx}(n,T)$ to find $\tau(n,T)$ and, more generally, why the previous literature on electron transport in graphene, which completely

neglected high electron viscosity, does not require revision if the measurements were carried out in the standard longitudinal geometry.

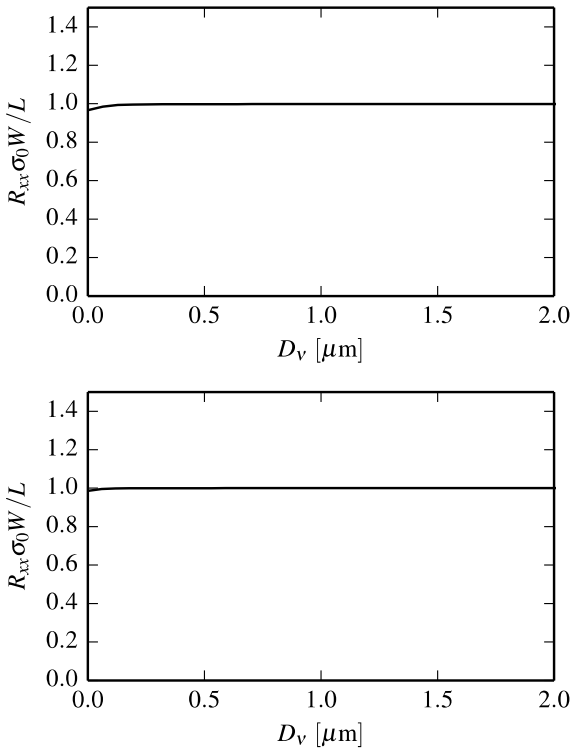

Fig. S7. Numerical solutions of the linearized hydrodynamic equations in the longitudinal geometry. In these plots we show the calculated longitudinal resistivity ρ_{xx} as a function of D_v (in μm) for SLG (left) and BLG (right). In solving the hydrodynamic equations we have utilized the free-surface BCs of Eq. (*S7*). From these numerical results, we infer that ρ_{xx} is simply equal to the inverse of the Drude-like conductivity $\sigma_0 \equiv ne^2\tau/m$.

#9 Gurzhi effect with increasing the electron temperature

Despite the absence of notable deviations in $\rho_{xx}(T)$ from a monotonic behavior, evidence for the Gurzhi effect could clearly be observed in the longitudinal differential resistance dV/dI measured as a function of a large applied current I. The current increased the temperature of the electron system well above the graphene lattice temperature and cryostat's temperature, T. Accordingly, these measurements enhanced electron-electron scattering whereas electron-phonon scattering remained relatively weak. Therefore, the dV/dI curves can qualitatively be viewed as changes in ρ_{xx} induced by increasing the electron temperature. Examples of the observed dV/dI as a function of I are shown in *fig. S8*.

At carrier concentrations $|n| > 1 \times 10^{12}$ cm^{-2} we observed rather featureless dV/dI curves up to our highest $I \approx 300$ μA (*fig. S8A*). For smaller $|n|$, the behavior of dV/dI became strongly nonmonotonic, which can be attributed to the Gurzhi effect (*7,15*). We interpret the observed nonlinearity as follows (*15*). At low T and low I, electron-electron scattering is weak ($\ell_{ee} \gtrsim W$), and we are in the Knudsen-like regime where the viscosity is determined by scattering at the channel edges. In this regime, resistivity grows with increasing the electron temperature (increasing I), similar to the case of classical dilute gases. At higher I (> 50 μA), the further increase in the electron temperature pushes the system into the Navier-Stokes regime with ℓ_{ee} becoming shorter than W. In this case, the flow starts being ruled by internal electron viscosity. The transition between the two regimes is known to lead to a drop in flow resistivity, as first observed by Knudsen for classical gases and, more recently (*15*), reported as the Gurzhi effect for electrons, also using the dV/dI measurements. The T dependence in *fig. S8B* shows that $I \sim 100$ μA heats up the electron system to ~ 200 K, which leads to the transition into the Navier-Stokes regime. This is in good agreement with the T range where our hydrodynamic effects were found strongest. Also, note that the Gurzhi effect appeared within the same range of carrier concentrations in which we observed largest negative R_V (compare *fig. S8* with Fig. 2A of the main text and *fig. S9*).

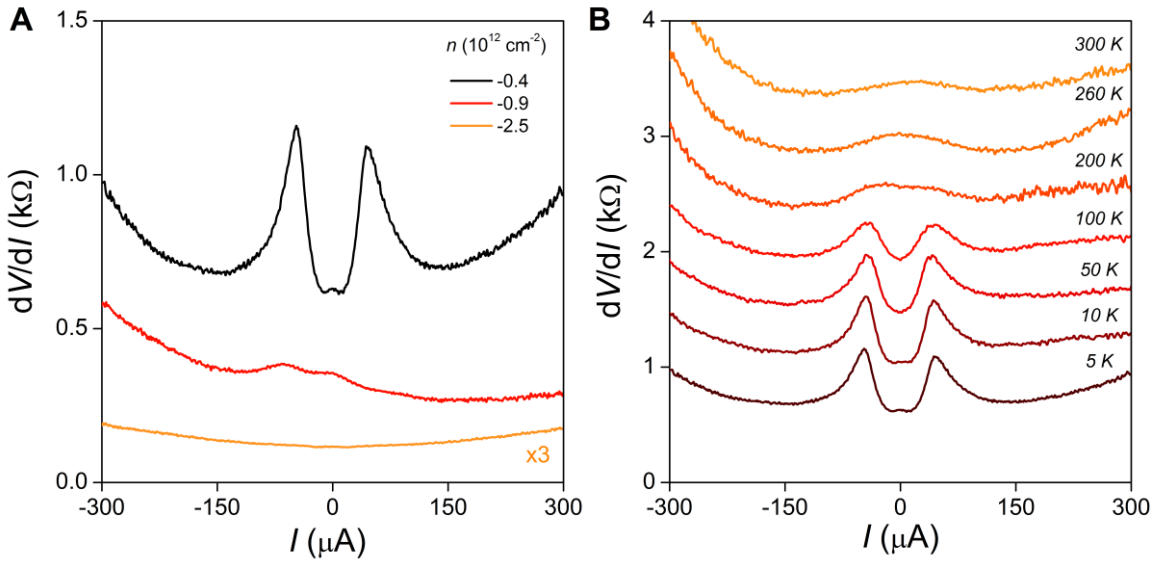

Fig. S8. Longitudinal differential resistance. (**A**) Examples of dV/dI as a function of applied current for a SLG device. To measure dV/dI, we applied an oscillating current $I + I_{ac}\cos(\omega t)$ along the main channel where I_{ac} is the low-frequency current, much smaller than I. The ac voltage drop that appeared at side contacts yielded dV/dI. The main channel was 2.5 μm wide, and voltage probes were separated by 8 μm. $T = 5$ K; $I_{ac} = 50$ nA. (**B**) Temperature dependence

of the differential resistance in (A) for hole doping with $n = -0.4 \times 10^{12}$ cm^{-2}. The curves in (B) are offset for clarity by 300 Ohms each.

#10 Reproducibility of negative vicinity response

To illustrate that the observed whirlpool effects were reproducible for different devices and using different contacts, *fig. S9* shows two more examples of R_V maps. They are for SLG devices with low-T μ of ≈ 50 m^2 V^{-1} s^{-1} and the distance L to the nearest vicinity probe of ≈ 1 μm. These maps are rather similar to those shown in Fig. 2 of the main text. Again, we observed large negative vicinity resistance away from the CNP and over a large range of T and n.

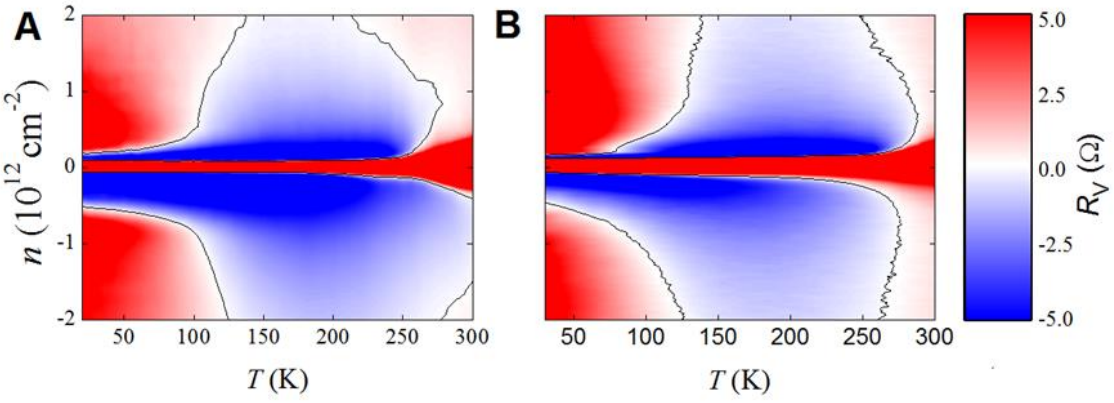

Fig. S9. **Further examples of negative vicinity resistance.** (**A**) and (**B**) are $R_V(n,T)$ maps for two different high-quality SLG devices and the distance between the injection and vicinity contacts of 1 μm.

#11 Changes from normal flow to backflow induced by electron heating

Negative vicinity voltage V_V is attributed to electron whirlpools and expected only in the viscous-flow regime. This requires ℓ_{ee} to be smaller than the characteristic scale in the problem, that is, the distance L between the injector and voltage contacts. In addition, to be detectable in transport experiments whirlpools should be sufficiently large in size (large D_v) to reach from the injection region to voltage probes. Because ℓ_{ee} depends on the electron temperature, the nature of electron flow can be controlled not only by changing the lattice temperature as in the experiments described in the main text but also by heating up the electron system using large dc currents I as discussed in the above section on the Gurzhi effect. We have carried out such measurements of V_V as a function of the electron temperature, and examples of the observed negative vicinity response are shown *fig. S10A*. It plots typical behavior of V_V as a function of I for three characteristic temperatures of the cryostat, *T*. For the case of low T, the I-V curve exhibits a positive slope at

small I which corresponds to the same linear-response $R_V = V_V/I$ as in the maps of Fig. 2 of the main text and *fig. S9*. This is the Knudsen flow regime. At higher currents ($I > 50$ μA), the voltage response becomes nonlinear reaching first a maximum and then changing the sign to negative. This is because the current heats up the electron system and drives it into the Navier-Stokes regime such that whirlpools appear near the injection point. At even higher currents, V_V changes its sign again, from negative to conventional positive, indicating that the electron temperature becomes high enough (> 300 K) and the system approaches the high-T regime of small D_v. If we increased the cryostat temperature to 100 K (*fig. S8A*), the electron system entered the viscous-flow regime even at vanishingly small probing currents, and the I-V curves – linear over a large range of I – yield negative R_V, in agreement with the results presented in the main text. At sufficiently high currents, the system again exhibits positive V_V, which corresponds to dominating stray currents. Further increase in T in *fig. S10A*, changes the character of I-V characteristics once again because the system is already close to the transport regime of small D_v, even without being heated by current. Note that these changes are closely connected with the Gurzhi effect reported in *fig. S8*. However, because the vicinity geometry is much more sensitive to a viscous flow contribution, voltage rather than its derivative changes the sign as a function of I in *fig. S10*.

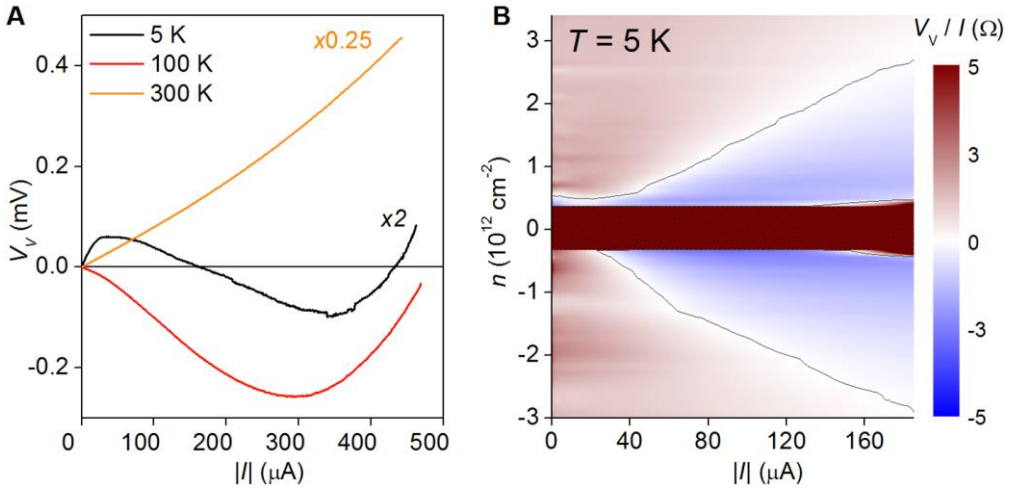

Fig. S10. Vicinity voltage as a function of applied current. (**A**) I-V characteristics at three characteristic T for a BLG device at hole doping $n = -2.5 \times 10^{12}$ cm^{-2}. (**B**) Map of the normalized nonlinear vicinity resistance V_V/I measured at $T = 5$ K. It is important to note that large I can lead to temperature gradients between different contacts and, as a result, spurious thermoelectric signals may appear in such measurements. Because the thermopower contribution depends only on the absolute value of I and not on its sign, the contribution can easily be eliminated by symmetrizing V_V with respect to the direction of dc current. This procedure was applied for the

shown plots and, accordingly, they are presented as a function of $|I|$. The brown rectangle in (B) is the region around the CNP with no collected data to avoid overheating and switching between different mesoscopic states

For further comparison between effects of electron heating and cryostat's T, *fig. S10B* shows a map of V_V/I, the nonlinear vicinity response normalized by the applied current. This map closely resembles the $R_V(T,n)$ maps in Fig. 2 of the main text and *fig. S9* and also shows a clear transition from normal electron flow at low *T* to backflow at intermediate electron temperatures. Note that in *fig. S10B* we had to limit our measurements to relatively small $I < 200$ μA so that the transport regime dominated by stray currents (approached above 400 μA in *fig. S10A*) could not be reached. This is because such high currents occasionally switched our devices between different mesoscopic states whereas the V_V maps required a few days of continuous measurements. For the same reason, we avoided measurements of $V_V(I)$ around the charge neutrality point in *fig. S10B* where high resistivity of graphene resulted in significant Joule heating even for relatively small currents.

The observed strong enhancement of the negative vicinity signal with increasing the electron temperature is in good agreement with the expected behavior of local whirlpools inside graphene's electron liquid and, also, rules out a contribution from single-particle ballistic effects. Indeed, we found experimentally that the latter phenomena such as negative transfer resistance and magnetic focusing (*19,21*) are rapidly and monotonically suppressed with increasing I.

#12 Dependence of electron backflow on distance to the injection contact

We have investigated how negative vicinity resistance decays with increasing the distance L between the injection and voltage contacts (see the sketch in *fig. S11*). This figure shows examples of the temperature dependence of R_V in the linear I-V regime for different $L = 1,\ 1.3$ and 2.3 μm, which were measured for the same BLG device at a fixed carrier concentration of 1.5×10^{12} cm^{-2}. All the plotted curves exhibit negative R_V but the temperature range in which the backflow occurs rapidly narrows with increasing L, and we could not detect any backflow for $L > 2.5$ μm in any of our devices. The magnitude of the negative signal is found to decay rapidly (practically exponentially) with L (top inset of *fig. S11*), yielding a characteristic scale of ≈ 0.5 μm. This provides a qualitative estimate for the size of electron whirlpools, in agreement with our theoretical estimates for D_v. Indeed, for the particular device in *fig. S11*, we can estimate $D_v \approx 0.4$ μm using our independent measurements of $\nu \approx 0.1$ m^{2}s^{-1} and $\tau \approx 1.5$ ps (see the main text and above).

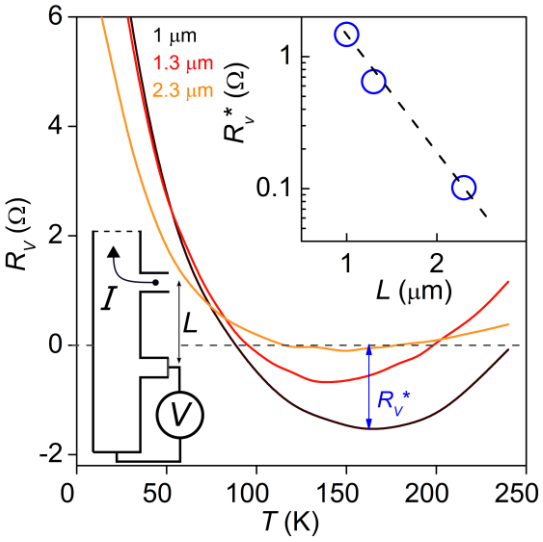

Fig. S11. Vicinity resistance measured at different distances from the injection contact. All the contacts were ≈ 0.3 μm in width. Top inset: Maximum value of negative R_V as a function of L. The dashed curve is the best fit with $D_v \approx 0.5$ μm. The probing current was 0.3 μA.

#13 Stray-current contribution to the vicinity resistance

In the vicinity geometry, stray currents near the voltage probe are not negligible. Their contribution to the measured vicinity resistance is given by the first term $b\sigma_0^{-1}$ in Eq. (4) of the main text where *b* is the geometrical factor dependent on *L*, *W* and width of the contact regions (*36*). Fig. 1E of the main text and *fig. S1D* clearly show that the classical contribution was rather significant and competed with the viscous term in R_V over a range of *T* and n. In this report, we have deliberately focused on the sign change in R_V because the negative resistance is an exceptional qualitative effect, which in our case cannot be explained without taking into account a finite viscosity of the electron liquid. However, to elucidate the hydrodynamic behavior in more detail, we can go a step further and analyze the anomalous part of R_V, which comes on top of the contribution from stray currents. To this end, we write $\Delta R_V \equiv R_V - b/\sigma_0$ to isolate the second part of Eq. (4) which depends on D_v and arises exclusively due to a finite viscosity. *Fig. S12* shows a typical example of ΔR_V observed in our devices. It is clear that at *T* > 50 K the negative ΔR_V extends over the entire range of carrier concentrations away from the CNP (*fig. S12A*). *Figure S12B* suggests that electron whirlpools persist well above room T.

It is important to note that the above subtraction analysis is based on the assumption of spatially uniform σ_0 whereas the experimental devices exhibit a certain level of charge inhomogeneity, especially close to the CNP. Qualitatively, one can gauge the influence of charge inhomogeneity from

the pronounced electron-hole asymmetry in the R_V maps, which in theory should be symmetric. The asymmetry was found to be contact dependent and arises due to non-uniform charge distribution near the vicinity contacts. Furthermore, the subtraction analysis is not applicable in the low-T regime because it ignores single-particle ballistic effects that modify stray currents on a distance of the order of the mean free path. Notwithstanding these limitations, the subtraction procedure in *fig. S12* provides a qualitatively accurate picture, especially at high T where single-particle phenomena can be neglected and for $n \gtrsim 1 \times 10^{12}$ cm^{-2} where the electron system become more uniform.

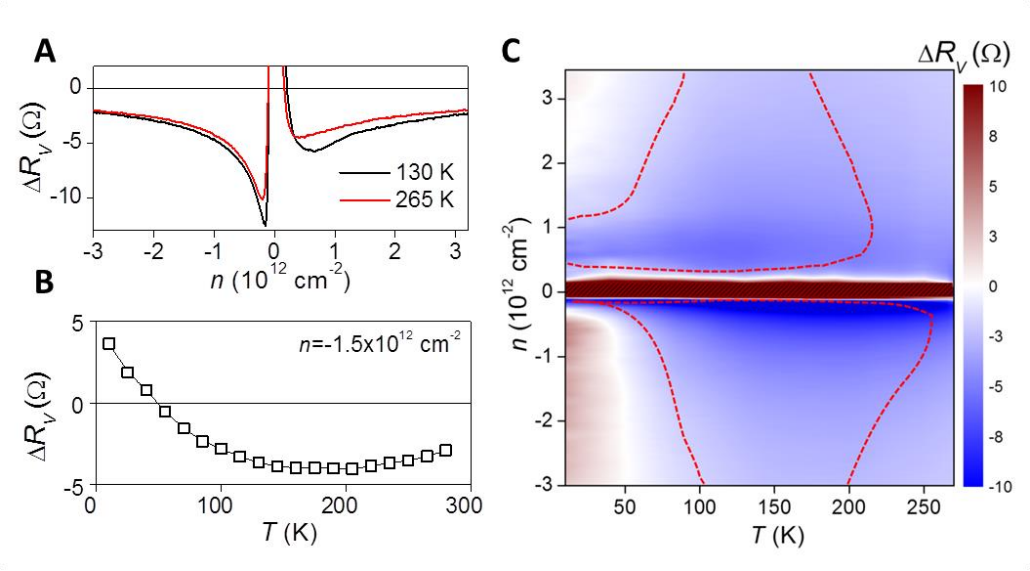

Fig. S12. Hydrodynamic part of vicinity resistance after subtracting a calculated contribution from stray currents. (**A**) $\Delta R_V(n)$ at two characteristic temperatures and (**B**) $\Delta R_V\ (T)$ for a typical carrier density away from the neutrality point. (**C**) Map $\Delta R_V(n,T)$ covering the entire range of measured temperatures and concentrations. Data are for the same device as in Fig. 2B of the main text. The red traces outline the region of negative R_V in Fig. 2B. The brown rectangle indicates the region with ΔR_V > +10 Ohm around the CNP where our hydrodynamic analysis is not expected to be applicable.

#14 Ballistic contribution due to reflection from device boundaries

Charge carriers reflected from the boundary opposite to the current-injecting contact can reach the vicinity probe if ℓ is comparable with the travel distance of $\approx 2W$. In this case, one can speculate that reflected electrons can give rise to a contribution similar to the negative bend resistance usually observed for ballistic Hall crosses (*19*). To this end, we have performed numerical simulations using the Landauer-Büttiker formalism and diffusive scattering at graphene edges. The analysis is standard and, therefore, not reported here for the sake of brevity. The simulations yielded the negative bend

resistance for the Hall bar geometry, as expected, but we could find only positive contributions for the vicinity geometry. Therefore, the standard theory of ballistic transport cannot explain negative R_V. More importantly, our experimental observations also disagree with the above scenario involving ballistic reflection from device boundaries. First, negative R_V is observed for W up to 4 μm and typical $\ell < 2$ μm $< 2W$ so that the number of electrons coming back to the boundary of origin is exponentially small, $\exp(-2W/\ell)$. Second, we have not observed any dependence of the amplitude of negative R_V on W, beyond usual variations for different contacts and devices. All our devices showed similar behavior, independent of their size and features such as contacts present at the opposite edge. Third, ℓ increases with decreasing T and, therefore, any ballistic contribution is expected to be most pronounced at low T. In contrast, R_V is always found positive in the regime of longest ℓ (that is, at low T and high n), in agreement with our numerical analysis.

Despite the overwhelming evidence described above, let us present an additional set of experiments that further prove little contribution from reflected electrons into R_V and confirm its positive sign. We fabricated devices similar to those described above but submicron slits were added between injecting and vicinity contacts (see *fig. S13*). The basic idea is that such obstacles should stop viscous backflow from reaching the vicinity probe (effective distance L increases significantly). *Fig. S13A* shows that, if no slit is present between the contacts, we observed the standard behavior for R_V. It is positive at long ℓ at low T but changes sign at higher T becoming most negative around $150 - 200$ K, in agreement with measurements for the other devices (cf. Fig. 2 of the main text and *fig. S9*). On the other hand, if a slit is added next to a vicinity probe, R_V does not change its sign remaining positive (*fig. S13B*). At low T, this positive signal is attributed to reflected ballistic electrons reaching the voltage probes for $\ell > W$. Note that R_V in *fig. S13B* is notably smaller than that in *fig. S13A*, in agreement with our numerical simulations and general expectations due to the shadow provided by the slit. As T increases, R_V decreases to zero because for $\ell \ll W$ the geometry gradually becomes nonlocal (*24*).

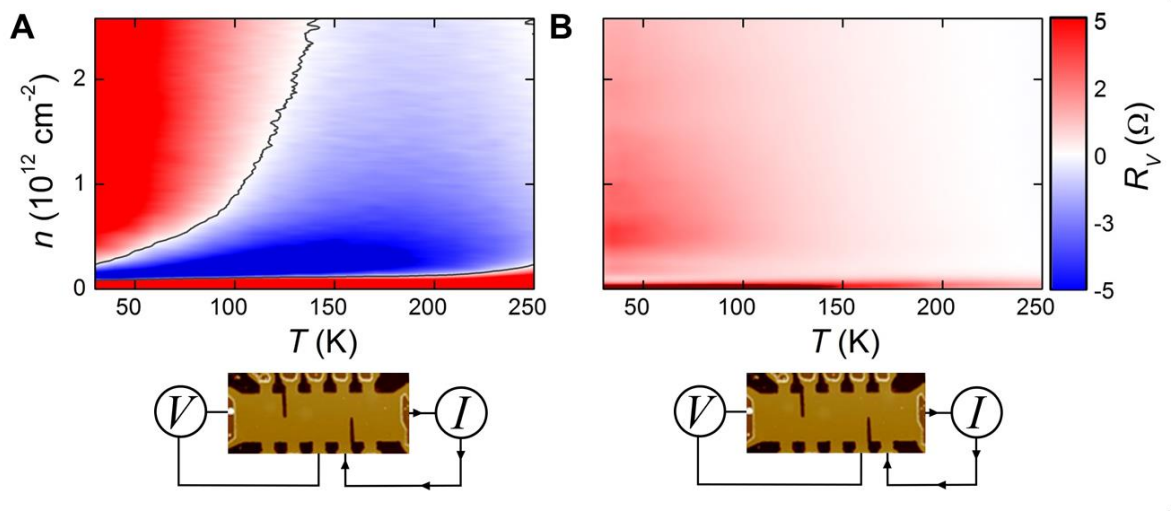

Fig. S13. Placing an obstacle to shade the vicinity probe. (**A**) $\mathrm{R_V(n,T)}$ for the 'standard'' vicinity geometry as shown schematically in the panel below. The panel utilizes an atomic-force micrograph of a device with two narrow notches etched through encapsulated SLG; $\mathrm{W} = 2$ μm. (**B**) Similar measurements but in the geometry where the slit separates vicinity and injector contacts. The schematic is shown in the panel below.

#15 Numerical simulations of hydrodynamic equations

To solve the linearized steady-state Navier-Stokes equation we discretized the differential operators on a square mesh and solve the corresponding sparse linear system. To improve the discretization of the differential operators, the values of the potential and the two components of the velocity are sampled on three different staggered meshes (*37*). The meshes were chosen in such a way that, at the boundary, the velocity component orthogonal to the boundary was sampled.

Different BCs were used to represent the sample edge, an open contact and a current-carrying contact:

(i) the velocity component orthogonal to the edges vanished;

(ii) the total current flowing through an open contact vanished;

(iii) the total current flowing through a current contact was fixed by the experimental conditions.

At the sample boundary (both sample edge and contacts) either no-slip or free-surface boundary conditions were implemented to fix the velocity component parallel to the boundary. We reiterate that the velocity component parallel to the boundary was sampled at a finite distance from the boundary due to the choice of the staggered meshes. An auxiliary set of velocity variables, parallel to the boundary, was introduced just outside of the sample area to implement the desired BCs. More specifically, no-slip boundary conditions were implemented by requiring that the velocity

components parallel to the boundary, just inside and outside the sample, were opposite. The free-surface BCs were implemented by discretizing the differential relation of Eq. (*S7*) and making use of the auxiliary set of velocity variables. We used a few hundred mesh nodes in each direction for a typical sample. The solution of the sparse linear system typically takes a few seconds on a desktop computer and its output is the full potential and velocity profile with the desired BC.

Finally, we comment on the dependence of Eq. (4) of the main text on the BCs. We remind the reader that Eq. (4), coupled with a longitudinal four-probe transport measurement of the phenomenological parameter τ, is needed to extract the kinematic viscosity ν of the electron liquid in graphene. Below we will refer to Eq. (4) of the main text as the 'calibration' curve because it relates the vicinity resistance to the two fundamental parameters of the theory, ν and τ. Eq. (4) in the main text was derived analytically by assuming free-surface BCs and neglecting a) finite-size effects in the longitudinal Hall bar direction and b) BCs at metal contacts. *Fig. S14* illustrates the dependence of the 'calibration' curve on different BCs, calculated numerically by relaxing constraints a) and b): no-slip (red squares) versus free-surface (filled circles). We also show, for the sake of generality, the analytical result for free-surface BCs, i.e. Eq. (4) of the main text.

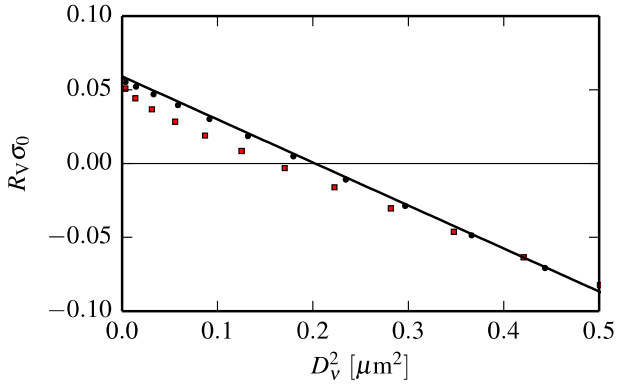

Fig. S14. 'Calibration' curve for our all-electrical viscometer. Calculated vicinity resistance R_V (in units of $1/\sigma_0$) as a function of D_ν^2 (in μm^2). For $D_\nu^2 \approx 0.2$ μm^2 the vicinity resistance becomes positive. Filled circles denote fully numerical results for the finite-size BLG device with ten electrodes (obtained by utilizing free-surface BCs). The solid line represents the approximate analytical result of Eq. (4) of the main text, which was obtained with free-surface BCs whereas red squares are the results of numerical calculations obtained by utilizing no-slip BCs ($l_b = 0$).

Full list of references

1. L. D. Landau, E. M. Lifshitz. *Fluid Mechanics.* Pergamon, New York, 1987.

2. G. K. Batchelor. *An Introduction to Fluid Dynamics*. Cambridge University Press, Cambridge, 1967.

3. B. V. Jacak, B. Müller. The exploration of hot nuclear matter. *Science* **337**, 310-314 (2012).

4. C. Cao *et al*. Universal quantum viscosity in a unitary Fermi gas. *Science* **331**, 58-61 (2011).

5. E. Elliott, J. A. Joseph, J. E. Thomas. Anomalous minimum in the shear viscosity of a Fermi gas. *Phys. Rev. Lett.* **113**, 020406 (2014).

6. T. Schäfer, D. Teaney. Nearly perfect fluidity: from cold atomic gases to hot quark gluon plasmas. *Rep. Prog. Phys.* **72**, 126001 (2009).

7. R. N. Gurzhi. Hydrodynamic effects in solids at low temperature. *Sov. Phys. Uspekhi* **11**, 255-270 (1968).

8. A. O. Govorov, J. J. Heremans. Hydrodynamic effects in interacting Fermi electron jets. *Phys. Rev. Lett.* **92**, 026803 (2004).

9. R. Bistritzer, A. H. MacDonald. Hydrodynamic theory of transport in doped graphene. *Phys. Rev. B* **80**, 085109 (2009).

10. M. Müller, J. Schmalian, L. Fritz. Graphene: a nearly perfect fluid. *Phys. Rev. Lett.* **103**, 025301 (2009).

11. A. V. Andreev, S. A. Kivelson, B. Spivak. Hydrodynamic description of transport in strongly correlated electron systems. *Phys. Rev. Lett.* **106**, 256804 (2011).

12. A. Tomadin, G. Vignale, M. Polini. Corbino disk viscometer for 2D quantum electron liquids. *Phys. Rev. Lett.* **113**, 235901 (2014).

13. B. N. Narozhny, I. V. Gornyi, M. Titov, M. Schütt, A. D. Mirlin. Hydrodynamics in graphene: linear-response transport. *Phys. Rev. B* **91**, 035414 (2015).

14. G. F. Giuliani, G. Vignale. *Quantum Theory of the Electron Liquid*. Cambridge University Press, Cambridge, 2005.

15. M. J. M. de Jong, L. W. Molenkamp. Hydrodynamic electron flow in high-mobility wires. *Phys. Rev. B* **51**, 13389 (1995).

16. J. C. W. Song, L. S. Levitov. Energy-driven drag at charge neutrality in graphene. *Phys. Rev. Lett.* **109**, 236602 (2012).

17. R. V. Gorbachev *et al*. Strong Coulomb drag and broken symmetry in double-layer graphene. *Nature Phys.* **8**, 896-901 (2012).

18. See supporting material on *Science* Online.

19. A. S. Mayorov *et al*. Micrometer-scale ballistic transport in encapsulated graphene at room temperature. *Nano Lett.* **11**, 2396-2399 (2011).

20. L. Wang *et al*. One-dimensional electrical contact to a two-dimensional material. *Science* **342**, 614-617 (2013).

21. T. Taychatanapat, K. Watanabe, T. Taniguchi, P. Jarillo-Herrero. Electrically tunable transverse magnetic focusing in graphene. *Nature Phys.* **9**, 225-229 (2013).

22. Q. Li, S. Das Sarma. Finite temperature inelastic mean free path and quasiparticle lifetime in graphene. *Phys. Rev. B* **87**, 085406 (2013).

23. M. Polini, G. Vignale. The quasiparticle lifetime in a doped graphene sheet. *arXiv:1404.5728* (2014).

24. D. A. Abanin *et al*. Giant nonlocality near the Dirac point in graphene. *Science* **332**, 328-330 (2011).

25. A. Principi, G. Vignale, M. Carrega, M. Polini. Bulk and shear viscosities of the 2D electron liquid in a doped graphene sheet. *arXiv:1506.06030* (2015).

26. V. A. Kretinin *et al.* Electronic properties of graphene encapsulated with different 2D atomic crystals.

Nano Lett. **14**, 3270-3276 (2014).

27. M. Ben Shalom *et al*. Proximity superconductivity in ballistic graphene, from Fabry-Perot oscillations

to random Andreev states in magnetic field. *arXiv:1504.03286* (2015).

28. S. Haigh *et al*. Cross-sectional imaging of individual layers and buried interfaces of graphene-based heterostructures and superlattices. *Nature Mater.* **11**, 764-767 (2012).

29. V. N. Kotov, B. Uchoa, V. M. Pereira, F. Guinea, A. H. Castro Neto. Electron-electron interactions in graphene: current status and perspectives. *Rev. Mod. Phys.* **84**, 1067 (2012).

30. A. Tomadin, A. Principi, J. C. W. Song, L. S. Levitov, M. Polini, Accessing phonon polaritons in hyperbolic crystals by angle-resolved photoemission spectroscopy. *Phys. Rev. Lett.* **115**, 087401 (2015).

31. L. D. Landau, E. M. Lifshitz. *Physical Kinetics.* Pergamon, New York, 1981.

32. A. Tomadin, M. Polini. Theory of the plasma-wave photoresponse of a gated graphene sheet. *Phys. Rev. B* **88**, 205426 (2013).

33. S. Adam, E. H. Hwang, V. M. Galitski, S. Das Sarma. A self-consistent theory for graphene transport. *PNAS* **104**, 18392-18397 (2007).

34. J. Renard, M. Studer, J. A. Folk. Origins of nonlocality near the Dirac point in graphene. *Phys. Rev. Lett.* **112**, 116601 (2014).

35. D. K. Ki *et al*. Inelastic scattering in a monolayer graphene sheet: A weak-localization study. *Phys. Rev. B* **78**, 125409 (2008).

36. I. Torre, A. Tomadin, A. K. Geim, M. Polini. Non-local transport and the hydrodynamic shear viscosity in graphene. *arXiv:1508.00363* (2015).

37. F. H. Harlow, J. E. Welch. Numerical calculation of time-dependent viscous incompressible flow of fluid with free surface. *The Physics of Fluids* **8**, 2182 (1965).

Chapter 7 – Super ballistic flow in viscous electron fluids

Paper title: Superballistic flow of viscous electron fluid through graphene constrictions

Journal Reference: Nature Physics (August 2017 advance online)

DOI: 10.1038/nphys4240

My Contribution: I designed the experiment, performed transport measurements and analysed all the experimental data measured in this work. I also supervised the project and wrote (in conjunction with my co-authors) the manuscript.

Full Author List: **R. Krishna Kumar,** D. A. Bandurin, F. M. D. Pellegrino , Y. Cao, A. Principi, H. Guo, G. H. Auton, M. Ben Shalom, L. A. Ponomarenko, G. Falkovich, K. Watanabe, T. Taniguchi, I. V. Grigorieva, L. S. Levitov, M. Polini and A. K. Geim

Author contributions: A.K.G., L.S.L. and M.P. designed and supervised the project. Y.C., G.H.A. and M.B.S. fabricated the studied devices. T.T. and K.W. provided quality boron-nitride crystals. Transport measurements and data analysis were carried out by R.K.K. and D.A.B. Theory analysis was done by F.M.D.P., A.P., H.G., G.F., L.S.L. and M.P. R.K.K., D.A.B., L.S.L., M.P. and A.K.G. wrote the manuscript. L.A.P. and I.V.G. provided experimental support and contributed to writing the manuscript. All authors contributed to discussions.

Abstract: This experiment continues with the themes of the previous chapter. We study viscous electron flow, but this time through graphene constrictions. We essentially probe Poiseulle type flow of the electron fluid by measuring anomalous temperature dependence of the resistance across the constrictions. We observe a drop in resistance upon increasing temperature due to a decrease in electron viscosity. The effect was first postulated by Gurzhi in 1963 but until now has not been observed experimentally. In addition to this, we find that the conductance through constrictions is larger in the viscous regime than the ballistic regime, that is, in the absence of electron-electron collisions at T = 0 K. The constrictions allow us to define maximum conductance in the ballistic regime, known as the Sharvin limit. Remarkably, the conductance in the viscous regime exceeds this limit. By analysing our data we were able to extract the one-body electron-electron mean free path, which showed remarkable agreement with independent many-body calculations.

nature physics

LETTERS

PUBLISHED ONLINE: 21 AUGUST 2017 | DOI: 10.1038/NPHYS4240

Superballistic flow of viscous electron fluid through graphene constrictions

R. Krishna Kumar[1,2,3], D. A. Bandurin[1,2], F. M. D. Pellegrino[4], Y. Cao[2], A. Principi[5], H. Guo[6], G. H. Auton[2], M. Ben Shalom[1,2], L. A. Ponomarenko[3], G. Falkovich[7,8], K. Watanabe[9], T. Taniguchi[9], I. V. Grigorieva[1], L. S. Levitov[6], M. Polini[1,10] and A. K. Geim[1,2]*

Electron–electron (e–e) collisions can impact transport in a variety of surprising and sometimes counterintuitive ways[1–6]. Despite strong interest, experiments on the subject proved challenging because of the simultaneous presence of different scattering mechanisms that suppress or obscure consequences of e–e scattering[7–11]. Only recently, sufficiently clean electron systems with transport dominated by e–e collisions have become available, showing behaviour characteristic of highly viscous fluids[12–14]. Here we study electron transport through graphene constrictions and show that their conductance below 150 K increases with increasing temperature, in stark contrast to the metallic character of doped graphene[15]. Notably, the measured conductance exceeds the maximum conductance possible for free electrons[16,17]. This anomalous behaviour is attributed to collective movement of interacting electrons, which 'shields' individual carriers from momentum loss at sample boundaries[18,19]. The measurements allow us to identify the conductance contribution arising due to electron viscosity and determine its temperature dependence. Besides fundamental interest, our work shows that viscous effects can facilitate high-mobility transport at elevated temperatures, a potentially useful behaviour for designing graphene-based devices.

Graphene hosts a high-quality electron system with weak phonon coupling[20,21] such that e–e collisions can become the dominant scattering process at elevated temperatures, T. In addition, the electronic structure of graphene inhibits Umklapp processes[15], which ensures that e–e scattering is momentum conserving. These features lead to a fluid-like behaviour of charge carriers, with the momentum taking on the role of a collective variable that governs local equilibrium. Previous studies of the electron hydrodynamics in graphene were carried out using the vicinity geometry and Hall bar devices of a uniform width. Anomalous (negative) voltages were observed, indicating a highly viscous flow, more viscous than that of honey[12,22,23]. In this report, we employ a narrow constriction geometry (Fig. 1a) which offers unique insight into the behaviour of viscous electron fluids. In particular, the hydrodynamic conductance through such constrictions becomes 'superballistic', exceeding the fundamental upper bound allowed in the ballistic limit, which is given by the Sharvin formula[16,17]. This is in agreement with theoretical predictions[18,19] and is attributed to a peculiar behaviour of viscous flows that self-organize into streams with different velocities, with 'sheaths' of a slow-moving fluid near the constriction edges (Fig. 1b). The cooperative behaviour helps charge carriers to circumnavigate the edges, the only place where the electron flow can lose its net momentum. The physics behind is fairly similar to that involved in the transition from the Knudsen to Poiseuille regimes, well understood in gas dynamics, where the hydrodynamic pressure can rapidly drop upon increasing the gas density and the rate of collisions between molecules[24].

Our devices are made of monolayer graphene encapsulated between hexagonal boron-nitride crystals, as described in Supplementary Section 1. The device design resembles a multi-terminal Hall bar, endowed with constrictions positioned between adjacent voltage probes (Fig. 1c). Below we refer to them as (classical) point contacts (PCs). Five such Hall bars were investigated, each having PCs of various widths w and a reference region without a constriction. The latter allowed standard characterization of graphene, including measurements of its longitudinal resistivity ρ_{xx}. All our devices exhibited mobilities exceeding 10 $m^2\,V^{-1}\,s^{-1}$ at liquid-helium T, which translates into a mean free path exceeding 1 μm with respect to momentum-non-conserving collisions (Supplementary Section 2).

Examples of the measured PC conductance G_{pc} at 2 K are given in Fig. 1d. In the low-T regime, all scattering lengths exceed w and transport is ballistic, which allows G_{pc} to be described by the Sharvin formula[16]

$$G_b = \frac{4e^2}{h} w \frac{\sqrt{\pi|n|}}{\pi} \quad (1)$$

where n is the carrier concentration (positive and negative n denote electron and hole doping, respectively). The expression is derived by summing the contributions of individual electron modes that propagate through the constriction, with each of them contributing the conductance quantum, e^2/h, towards the total conductance. The dashed curves in Fig. 1d show the PC conductance calculated using equation (1) and assuming the width values, w_{AFM}, as determined by atomic force microscopy (AFM). The observed agreement between the experiment and equation (1) does not rely on any fitting parameters. Alternatively, we could fit our experimental curves using equation (1) and extract the effective width w for each PC (Supplementary Section 3). The results are plotted in the inset of

[1]School of Physics and Astronomy, University of Manchester, Manchester M13 9PL, UK. [2]National Graphene Institute, University of Manchester, Manchester M13 9PL, UK. [3]Department of Physics, University of Lancaster, Lancaster LA1 4YW, UK. [4]NEST, Istituto Nanoscienze-CNR and Scuola Normale Superiore, 56126 Pisa, Italy. [5]Radboud University, Institute for Molecules and Materials, 6525 AJ Nijmegen, the Netherlands. [6]Massachusetts Institute of Technology, Cambridge, Massachusetts 02139, USA. [7]Department of Physics, Weizmann Institute of Science, Rehovot 76100, Israel. [8]Institute for Information Transmission Problems, Moscow 127994, Russia. [9]National Institute for Materials Science, 1-1 Namiki, Tsukuba 305-0044, Japan. [10]Istituto Italiano di Tecnologia, Graphene Labs, Via Morego 30, 16163 Genova, Italy. *e-mail: geim@manchester.ac.uk

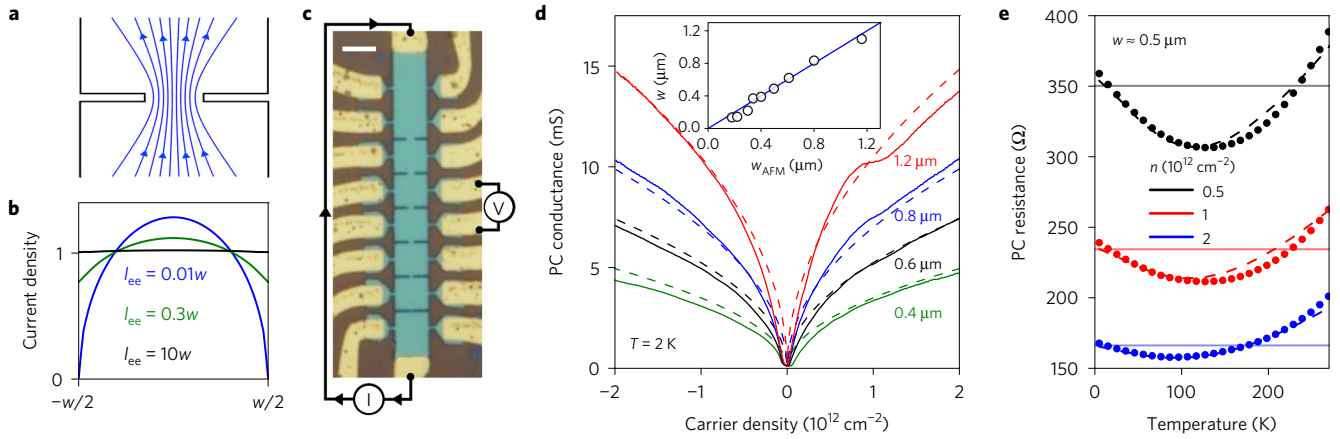

Figure 1 | Electron flow through graphene constrictions. a, Schematic of viscous flow in a PC. **b**, Distribution of the electric current across the PC, normalized by the total current. In the hydrodynamic regime (e–e scattering length $l_{ee} \ll w$), there is little flow near the edges (blue curve), which reduces the loss of net momentum. Black curve: ballistic regime $l_{ee} \gg w$. **c**, Optical micrograph of one of our devices and schematic of our four-probe measurements. Scale bar, 5 μm. The PCs vary in width from 0.1 to 1.2 μm. **d**, Measurements of the low-T conductance for PCs of different w (solid curves). Dashed curves: ballistic conductance given by equation (1). Inset: PC width w found as the best fit to experimental $G_{pc}(n)$ is plotted as a function of w_{AFM}. Solid line: $w \equiv w_{AFM}$. **e**, PC resistance, $1/G_{pc}$, for a 0.5-μm constriction at representative carrier densities. Dots: experimental data. Horizontal lines: ballistic resistance given by equation (1). Dashed curves: theoretical predictions for a viscous electron fluid, using simplified expressions for the T dependence of e–e and electron–phonon scattering ($\propto T^2$ and T, respectively). Details are given in Supplementary Section 4.

Fig. 1d as a function of w_{AFM}. For $w \geq 0.4$ μm, the agreement between w and w_{AFM} is within ∼5%. Deviations become larger for our smallest constrictions, suggesting that they are effectively narrower, possibly because of edge defects. Although we focus here on classical PCs with a large number of transmitting modes, we note that our devices with $w < 0.2$ μm exhibit certain signs of conductance quantization, fairly similar to those reported previously[25,26], but they are rapidly washed out upon raising T above 30 K.

The central result of our study is presented in Fig. 1e. It shows that the resistance of graphene PCs, $R_{pc} \equiv 1/G_{pc}$, is a non-monotonic function of T, first decreasing as temperature increases. Such T dependence, typical for insulators, is unexpected for our metallic system. It is also in contrast to the T dependence of ρ_{xx} observed in our Hall bar devices. They exhibit ρ_{xx} monotonically increasing with T, the standard behaviour in doped graphene (Supplementary Section 2). All our PCs with $w < 1$ μm exhibited this anomalous, insulating-like T dependence up to 100–150 K (Fig. 2a). As a consequence, R_{pc} in its minimum corresponds to conductance values that could exceed the ballistic limit by >15% (Fig. 1e). At higher T, R_{pc} starts growing monotonically and follows the same trend as ρ_{xx}. The minima in $R_{pc}(T)$ were more pronounced for narrower constrictions (Fig. 2a), corroborating the importance of the geometry. Figure 2b,c elaborates on the non-metallic behaviour of graphene PCs by plotting maps of the derivative dR_{pc}/dT as a function of both n and T. The anomalous insulating-like T dependence shows up as the blue regions whereas the metallic behaviour appears in red. For narrow constrictions, the anomalous behaviour was observed for all accessible n below 100 K, becoming most pronounced at low densities but away from the neutrality point (Figs 1e and 2b). For wide PCs (Fig. 2c), the non-metallic region becomes tiny, in agreement with the expected crossover from the PC to standard Hall bar geometry.

To describe the non-metallic behaviour in our PCs, we first invoke the recent theory[18] that predicts that e–e scattering modifies equation (1) as

$$G = G_b + G_\nu \quad \text{where} \quad G_\nu = \frac{\sqrt{\pi|n|}e^2 w^2 \nu_F}{32\hbar\nu} \tag{2}$$

v_F is the Fermi velocity and e–e collisions are parameterized through the kinematic viscosity $\nu = v_F l_{ee}/4$. The quantity G_ν is calculated for the Stokes flow through a PC in the extreme hydrodynamic regime (that is, for the e–e scattering length $l_{ee} \ll w$). The additive form of equation (2) is valid[18,19] for all values of l_{ee}/w, even close to the ballistic regime $l_{ee} \gg w$. This implies that G should increase with T (in the first approximation[15,27], as $\propto 1/l_{ee} \propto T^2$), which leads to the initial drop in resistance (Fig. 1e). Equation (2) also suggests that the viscous effects should be more pronounced at low n, where electron viscosity is smaller, in agreement with the experiment (Figs 1e and 2b). The description by equation (2) is valid until phonon scattering becomes significant at higher T. To describe both low-T and high-T regimes on an equal footing, we extended the transport model of ref. 18 to account for acoustic-phonon scattering using an additional term $\propto T$ in the kinetic equation (Supplementary Section 4). The results are plotted in Fig. 1e, showing good agreement with the experiment.

For further analysis, we used our experimental data to extract G_ν, which in turn enabled us to determine ν and l_{ee}. To this end, we first followed the standard approach in analysis of transport data for quantum PCs, which takes into account the contact resistance R_C arising from the wide regions leading to constrictions[17,28]. Accordingly, the total resistance of PCs can be represented as

$$R_{pc} = (G_b + G_\nu)^{-1} + R_C \tag{3}$$

To avoid fitting parameters, we model the contact resistance as $R_C = b\rho_{xx}$, where b is a numerical coefficient calculated by solving the Poisson equation for each specific PC geometry and ρ_{xx} is taken as measured from the reference regions. For our devices, b ranged between 2 and 5 (Supplementary Section 5). Examples of the resulting $\Delta R = R_{pc} - b\rho_{xx} = (G_b + G_\nu)^{-1}$ are plotted in Fig. 3a. The figure shows that, after the phonon contribution is accounted for through R_C, the resistance ΔR (attributable to the narrowing itself) monotonically decreases with increasing T over the entire T range, in agreement with equation (2). The validity of this analysis is further confirmed by the fact that the extracted values of ΔR were found to be independent of b (that is, insensitive to voltage probes positions relative to PCs; see Supplementary Fig. 1). As a next step, we use the conductance G_b found in the limit of low T for each PC and subtract this value from $1/\Delta R = G_b + G_\nu$ to obtain the viscous conductance G_ν. The results are shown in Fig. 3b for several PCs. Remarkably, if G_ν is normalized by w^2, all the

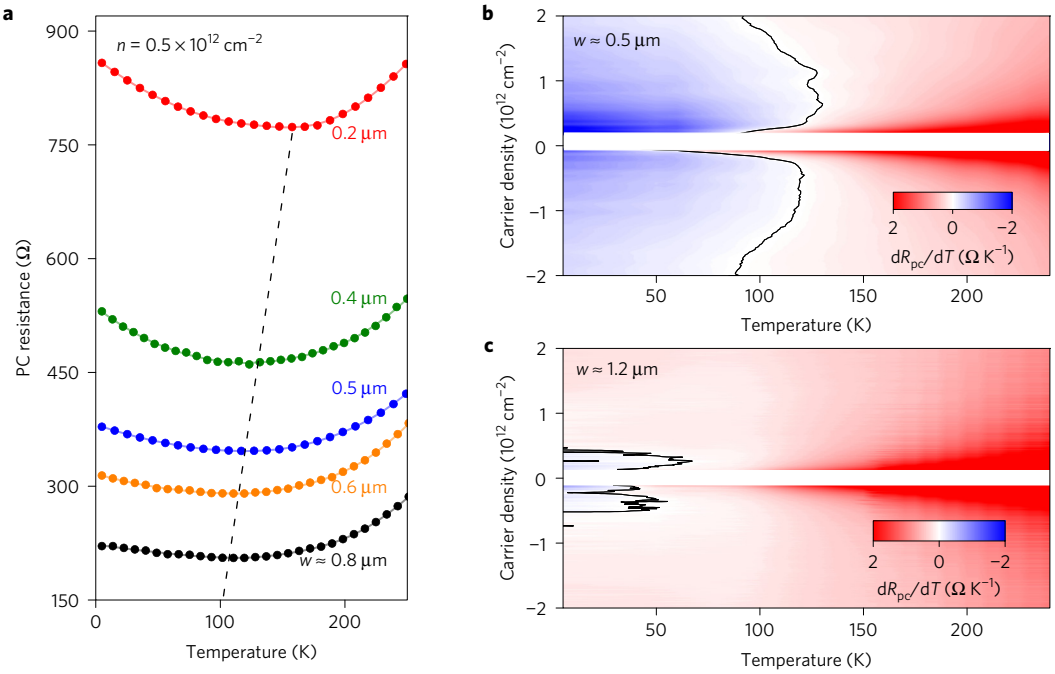

Figure 2 | Transition from metallic to insulating behaviour in constrictions of different widths. a, Temperature dependence for PCs with different w at a given n. The dashed line indicates that the minima shift to higher T and become deeper for narrower constrictions. **b**,**c**, Colour map $dR_{pc}/dT(T,n)$ for $w \approx 0.5$ and 1.2 μm. The black contours mark a transition from the insulating to metallic T dependence. The white stripes near zero n cover regions near the neutrality point, in which charge disorder becomes important and transport involves thermal broadening and other interaction effects[12,13] beyond the scope of this work.

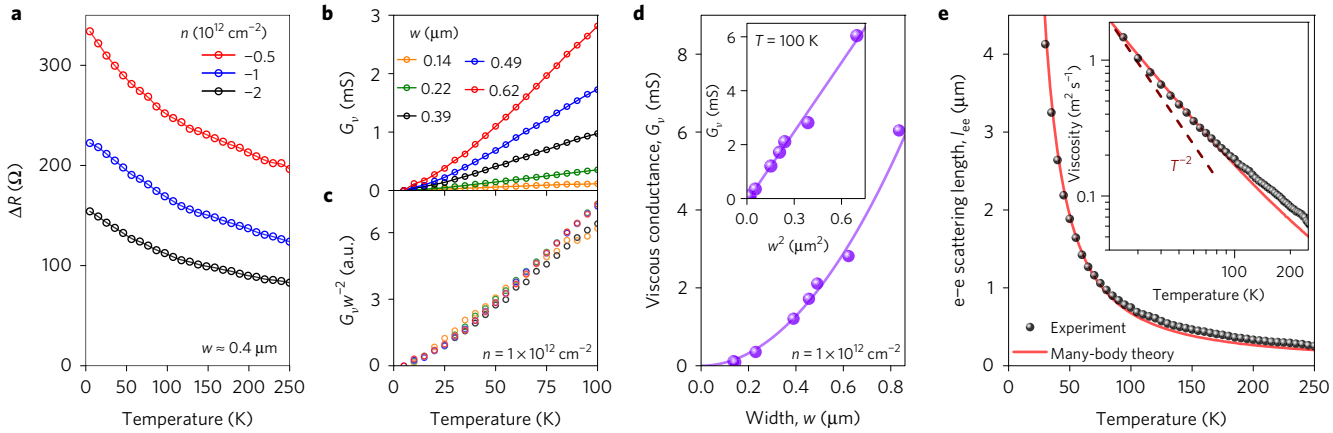

Figure 3 | Quantifying e–e interactions in graphene. a, T dependence of the PC resistance after subtracting the contribution from contact regions. **b**, Viscous conductance G_ν at a given n for PCs with w ranging between 0.1 and 0.6 μm. **c**, Data from **b** normalized by w^2. **d**, G_ν as a function of w for given $T = 100$ K and $n = 10^{12}$ cm^{-2}. Solid curve: best fit to equation (2) yields $\nu \approx 0.16$ m^2 s^{-1}, a value five orders of magnitude larger than the kinematic viscosity of water. Inset: same data as a function of w^2. **e**, T dependence of the e–e scattering length found as $l_{ee} = 4\nu/v_F$ (symbols) for $n = 10^{12}$ cm^{-2} and $w \approx 0.5$ μm. Red curve: microscopic calculations of l_{ee} (Supplementary Section 6). Inset: $\nu(T)$ on a log–log scale. The data are from the main panel and colour-coded accordingly. The dashed line indicates the $1/T^2$ dependence.

experimental data collapse onto a single curve (Fig. 3c). This scaling is starkly different from the Sharvin dependence $G_b \propto w$ observed in the ballistic regime (Fig. 1d) and, more generally, from any known behaviour of electrical conductance that always varies linearly with the sample width. However, our result is in excellent agreement with equation (2) that suggests $G_\nu \propto w^2$. The w^2 scaling behaviour is further validated in Fig. 3d, lending strong support to our analysis.

The measured dependence $G_\nu(T)$ allows us to determine $\nu(T)$ and $l_{ee}(T)$ using equation (2). The results are shown in Fig. 3e and compared with the calculations[29] detailed in Supplementary Section 6. The agreement is surprisingly good (especially taking into account that neither experiment nor calculations use any fitting parameters) and holds for different PC devices and different carrier densities (Supplementary Section 7). We also note that the agreement is markedly better than the one achieved previously using measurements of ν in the vicinity geometry[12], and even accommodates the fact that both experimental and theoretical curves in Fig. 3e (inset) deviate from the $1/T^2$ dependence expected for the normal Fermi liquid[6,30]. The deviations arise because temperatures ~50–100 K are not insignificant with respect to the Fermi energy. Furthermore, our calculations in Fig. 3e stray slightly off the experimental curve above 100 K. In fact, this is expected because, in the hydrodynamic regime $l_{ee} \ll w$, the kinematic viscosity can no longer be expressed in terms of l_{ee} (as above) and

requires a more accurate theoretical description using the two-body stress–stress response function[29]. Although the strong inequality $l_{ee} \ll w$ is not reached in our experiments, the experimental data in Fig. 3e do tend in the expected direction (Supplementary Section 8).

To conclude, graphene constrictions provide a unique insight into the impact of e–e interactions on electron transport. The observed negative T dependence of the point contact resistance, its superballistic values and the unusual w^2 scaling are clear indicators of the important role of e–e collisions in clean metals at elevated temperatures. Our analysis also offers a guide for unravelling intricate interaction effects contributing at the crossover between the ballistic and hydrodynamic transport regimes.

Methods

Methods, including statements of data availability and any associated accession codes and references, are available in the online version of this paper.

Received 12 March 2017; accepted 14 July 2017; published online 21 August 2017

References

1. Gurzhi, R. N. Minimum of resistance in impurity-fee conductors. *Sov. Phys. JETP* **17,** 521–522 (1963).
2. Gurzhi, R. N. Hydrodynamic effects in solids at low temperature. *Sov. Phys. Usp.* **11,** 255–270 (1968).
3. Govorov, A. O. & Heremans, J. J. Hydrodynamic effects in interacting Fermi electron jets. *Phys. Rev. Lett.* **92,** 026803 (2004).
4. Müller, M., Schmalian, J. & Fritz, L. Graphene: a nearly perfect fluid. *Phys. Rev. Lett.* **103,** 025301 (2009).
5. Mendoza, M., Herrmann, H. J. & Succi, S. Preturbulent regimes in graphene flow. *Phys. Rev. Lett.* **106,** 156601 (2011).
6. Forcella, D., Zaanen, J., Valentinis, D. & van der Marel, D. Electromagnetic properties of viscous charged fluids. *Phys. Rev. B* **90,** 035143 (2014).
7. Yu, Z. Z. *et al*. Negative temperature derivative of resistivity in thin potassium samples: the Gurzhi Effect? *Phys. Rev. Lett.* **52,** 368–371 (1984).
8. de Jong, M. J. M. & Molenkamp, L. W. Hydrodynamic electron flow in high-mobility wires. *Phys. Rev. B* **51,** 13389–13402 (1995).
9. Renard, V. *et al*. Boundary-mediated electron–electron interactions in quantum point contacts. *Phys. Rev. Lett.* **100,** 186801 (2008).
10. Nagaev, K. E. & Kostyuchenko, T. V. Electron–electron scattering and magnetoresistance of ballistic microcontacts. *Phys. Rev. B* **81,** 125316 (2010).
11. Melnikov, M. Y. *et al*. Influence of e–e scattering on the temperature dependence of the resistance of a classical ballistic point contact in a two-dimensional electron system. *Phys. Rev. B* **86,** 075425 (2012).
12. Bandurin, D. A. *et al*. Negative local resistance caused by viscous electron backflow in graphene. *Science* **351,** 1055–1058 (2016).
13. Crossno, J. *et al*. Observation of the Dirac fluid and the breakdown of the Wiedemann–Franz law in graphene. *Science* **351,** 1058–1061 (2016).
14. Moll, P. J. W., Kushwaha, P., Nandi, N., Schmidt, B. & Mackenzie, A. P. Evidence for hydrodynamic electron flow in $PdCoO_2$. *Science* **351,** 1061–1064 (2016).
15. Castro Neto, A. H., Guinea, F., Peres, N. M. R., Novoselov, K. S. & Geim, A. K. The electronic properties of graphene. *Rev. Mod. Phys.* **81,** 109–162 (2009).
16. Sharvin, Y. V. A possible method for studying Fermi surfaces. *Sov. Phys. JETP* **21,** 655–656 (1965).
17. Beenakker, C. W. J. & van Houten, H. Quantum transport in semiconductor nanostructures. *Solid State Phys.* **44,** 1–228 (1991).
18. Guo, H., Ilseven, E., Falkovich, G. & Levitov, L. Higher-than-ballistic conduction of viscous electron flows. *Proc. Natl Acad. Sci. USA* **114,** 3068–3073 (2017).
19. Guo, H., Ilseven, E., Falkovich, G. & Levitov, L. Stokes paradox, back reflections and interaction-enhanced conduction. Preprint at http://arxiv.org/abs/1612.09239 (2016).
20. Mayorov, A. S. *et al*. Micrometer-scale ballistic transport in encapsulated graphene at room temperature. *Nano Lett.* **11,** 2396–2399 (2011).
21. Wang, L. *et al*. One-dimensional electrical contact to a two-dimensional material. *Science* **342,** 614–617 (2013).
22. Torre, I., Tomadin, A., Geim, A. K. & Polini, M. Nonlocal transport and the hydrodynamic shear viscosity in graphene. *Phys. Rev. B* **92,** 165433 (2015).
23. Levitov, L. & Falkovich, G. Electron viscosity, current vortices and negative nonlocal resistance in graphene. *Nat. Phys.* **12,** 672–676 (2016).
24. Knudsen, M. Die Gesetze der Molekularströmung und der inneren Reibungsströmung der Gase durch Röhren (The laws of molecular flow and of inner frictional flow of gases through tubes). *Ann. Phys.* **28,** 75–130 (1909).
25. Tombros, N. *et al*. Quantized conductance of a suspended graphene nanoconstriction. *Nat. Phys.* **7,** 697–700 (2011).
26. Terrés, B. *et al*. Size quantization of Dirac fermions in graphene constrictions. *Nat. Commun.* **7,** 11528 (2016).
27. Kotov, V. N., Uchoa, B., Pereira, V. M., Guinea, F. & Castro Neto, A. H. Electron–electron interactions in graphene: Current status and perspectives. *Rev. Mod. Phys.* **84,** 1067–1125 (2012).
28. de Jong, M. J. M. Transition from Sharvin to Drude resistance in high-mobility wires. *Phys. Rev. B* **49,** 7778–7781 (1994).
29. Principi, A., Vignale, G., Carrega, M. & Polini, M. Bulk and shear viscosities of the 2D electron liquid in a doped graphene sheet. *Phys. Rev. B* **93,** 125410 (2016).
30. Polini, M. & Vignale, G. The quasiparticle lifetime in a doped graphene sheet. Preprint at http://arxiv.org/abs/1404.5728 (2014).

Acknowledgements

This work was supported by Engineering and Physical Sciences Research Council, Graphene Flagship, the Royal Society and Lloyd's Register Foundation. L.S.L. acknowledges support from the Center for Integrated Quantum Materials under NSF award 1231319, the Center for Excitonics, an Energy Frontier Research Center funded by the US Department of Energy, Office of Science, Basic Energy Sciences, under award DESC0001088, and MIT-Israel Seed Fund. G.F. acknowledges ISF grant 882 and RSF grant 14-22-00259. A.P. was supported by ERC Advanced Grant FEMTO/NANO and Spinoza Prize. M.P. acknowledges Fondazione Istituto Italiano di Tecnologia and the European Union's Horizon 2020 programme under grant 696656 'GrapheneCore1'. D.A.B. and I.V.G. thank the Marie Curie programme SPINOGRAPH. G.H.A. was supported by EPSRC grant EP/M507969. R.K.K. acknowledges support from Doctoral Training Centre NOWNANO. The authors would like to thank E. Khestanova for the help with AFM measurements.

Author contributions

A.K.G., L.S.L. and M.P. designed and supervised the project. Y.C., G.H.A. and M.B.S. fabricated the studied devices. T.T. and K.W. provided quality boron-nitride crystals. Transport measurements and data analysis were carried out by R.K.K. and D.A.B. Theory analysis was done by F.M.D.P., A.P., H.G., G.F., L.S.L. and M.P. R.K.K., D.A.B., L.S.L., M.P. and A.K.G. wrote the manuscript. L.S.L. wrote Supplementary Section 4. A.P. and M.P. wrote Supplementary Sections 6 and 8. L.A.P. and I.V.G. provided experimental support and contributed to writing the manuscript. All authors contributed to discussions.

Additional information

Supplementary information is available in the online version of the paper. Reprints and permissions information is available online at www.nature.com/reprints. Publisher's note: Springer Nature remains neutral with regard to jurisdictional claims in published maps and institutional affiliations. Correspondence and requests for materials should be addressed to A.K.G.

Competing financial interests

The authors declare no competing financial interests.

Methods

Our devices were made from encapsulated graphene heterostructures using electron-beam lithography and standard microfabrication procedures (Supplementary Section 1). The constriction widths were determined using Bruker's FastScan atomic force microscope. The electrical measurements were carried out in a variable temperature insert employing lock-in techniques at low frequencies (10–30 Hz) and with excitation currents of 0.1–1 μA.

Data availability. The data that support the plots within this paper and other findings of this study are available from the corresponding author upon reasonable request.

Supplementary Information

Super-ballistic flow of viscous electron fluid through graphene constrictions

R. Krishna Kumar, D. A. Bandurin, F. M. D. Pellegrino, Y. Cao, A. Principi, H. Guo, G. H. Auton, M. Ben Shalom, L. A. Ponomarenko, G. Falkovich, K. Watanabe, T. Taniguchi, I. V. Grigorieva, L. S. Levitov, M. Polini, A. K. Geim

S1. Device fabrication

Our encapsulated-graphene devices were made following a recipe similar to that used in the previous reports[1,2,3]. First, an hBN-graphene-hBN stack was assembled using the dry peel technique[2]. This involved mechanical cleavage to obtain monolayer graphene and hBN crystals less than 50 nm thick. The selected crystallites were stacked on top of each other using a polymer membrane attached to a micromanipulator[2]. The resulting heterostructure was transferred on top of an oxidized silicon wafer (290 nm of SiO_2) which served in our experiments as a back gate. After this, the heterostructure was patterned by electron beam lithography to first define contact regions. Reactive ion etching (RIE) was employed to selectively remove the heterostructure areas unprotected by the lithographic mask, which resulted in trenches for depositing long electrical leads and metal contacts to graphene (Fig. S1a). 3 nm of chromium followed by 80 nm of gold were evaporated into the trenches. This fabrication sequence allowed us to prevent contamination of the narrow graphene edges that were exposed by RIE, which reduced the contact resistance[3].

Next, the same lithography and etching procedures were employed again to define the final device geometry. Figure S1a shows another device used in our experiments (in addition to that shown in Fig. 1c of the main text). The two Hall bars host four constrictions and accompanying reference regions. Note that we could probe point contacts (PCs) using voltage probes placed at different distances. To determine PCs' width, the devices were imaged by atomic force microscopy (AFM). An example of the obtained AFM images is provided in Fig. S1b, and a line trace in Fig. S1b shows a typical height profile $h(x)$ across the constriction. Because of much quicker etching of hBN in comparison with graphene, a step-like feature develops in the etched slope[3] as indicated by the arrow in Fig. S1b. This feature allows us to accurately determine the vertical position of the graphene channel. To calculate its width w_{AFM}, we took into account both graphene's vertical position (Fig. S1c) and a finite opening angle of our AFM tips (~20°).

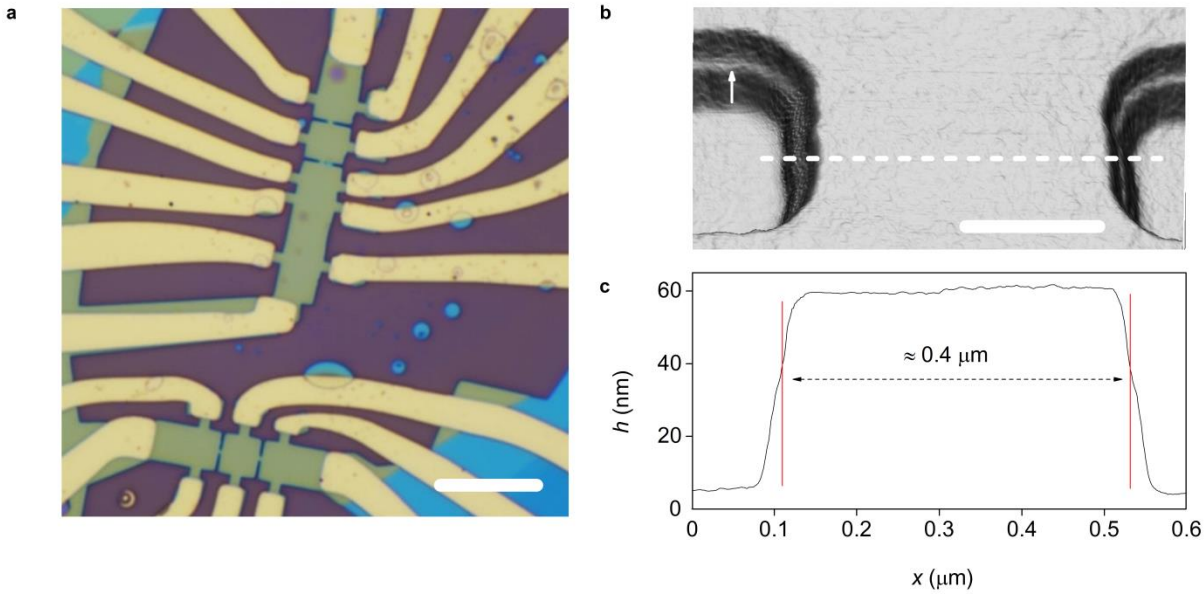

Figure S1|Graphene point contacts. a, Optical image of a device with PCs varying in width from 0.2 to 0.6 μm. Scale bar: 10 μm. **b,** Three dimensional AFM image of one of the point contacts. Scale bar: 0.2 μm. **c,** Height profile along the white dashed line in (b). Red lines indicate the width w_{AFM} for this particular constriction; graphene is buried 20 nm under the hBN layer.

S2. Mobility and mean free path

We characterized quality of our graphene devices using their reference regions. The longitudinal and Hall resistivities (ρ_{xx} and ρ_{xy}, respectively) were measured in the standard four-probe geometry as a function of back gate voltage. Figure S2a shows $\rho_{xx}(n)$ at different T, where carrier density n was determined from ρ_{xy}. One can see a typical behavior for high quality graphene. At low T, ρ_{xx} exhibits a peak at the charge neutrality point (NP) with a sharp decrease down to 20-50 Ω for $|n| > 0.5\times10^{12}$ cm^{-2}. Away from the NP, ρ_{xx} grows monotonically with T (inset of Fig. S2a) as expected for phonon-limited transport in doped graphene[4].

The mobility was calculated using the Drude formula, $\mu = 1/ne\rho_{xx}$ where e is the electron charge. For typical $n \sim 1\times10^{12}$ cm^{-2}, μ exceeded 15 $m^2V^{-1}s^{-1}$ at 5 K and was around 5 $m^2V^{-1}s^{-1}$ at room temperature. These values translate into the elastic mean free path $l = \mu\hbar/e(n\pi)^{0.5}$ of about 1 to a few microns at all T (Fig. S2b) which exceeds the dimensions of our constrictions and implies ballistic transport through them with respect to momentum-non-conserving collisions. To illustrate that such ballistic transport occurs not only inside reference regions but also for the sections of our devices with PCs, we carried out measurements in the bend geometry[5,6] (micrograph in Fig. S2c). This figure shows an example of the bend resistance $R_B(n)$ measured from a region located between two PCs.

For n away from the NP and at liquid-helium T, R_B becomes negative, which indicates direct, ballistic transmission of charge carriers from, for example, current contact (1) into voltage contact (4) (refs. 5,6). The negative bend resistance was found for all the regions of our devices, proving their high homogeneity and, also, implying that l at low T was comparable to the Hall bars' width, in agreement with the above estimates based on the Drude model (inset of Fig. S2b). The ballistic transmission was rapidly suppressed with increasing temperature and disappeared at around 100 K (inset of Fig. S2c).

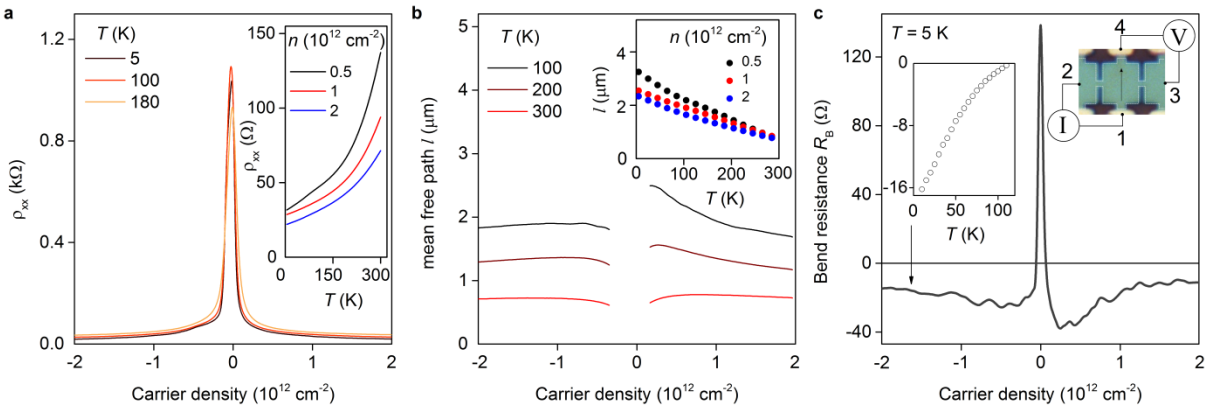

Figure S2| Characterization of encapsulated graphene. a, ρ_{xx} as a function of n at different temperatures. Inset: $\rho_{xx}(T)$ for a few n. **b**, Elastic mean free path as a function of n at high $T \geq 100$ K. Inset: Complete T dependence for various n. **d**, Bend resistance $R_B(n)$ at low T. The micrograph shows schematics of the bend geometry used in the experiment where $R_B = R_{12,34}$ (for details see refs. 5,6). Inset: Temperature dependence of R_B at the density indicated by the black arrow, $n = -1.7\times10^{12}$ cm^{-2}.

S3. Finding the width of point contacts

In a conventional two-dimensional electron gas (e.g., in GaAlAs heterostructures), local gates are used to deplete charge carriers in specific areas, creating insulating regions that inhibit current pathways. This allows constrictions with smooth edges. In graphene devices, constrictions are made by milling away the material. Accordingly, our PCs are defined by actual graphene edges. Figures S3a-b show two more examples of AFM images of our PCs with $w_{AFM} \approx 0.2$ and 0.5 μm. Due to limitations of electron-beam lithography, the edge profiles are unavoidably rough on a sub-100-nm scale. The destructive nature of RIE may also introduce microscopic cracks[7] that cannot be visualized being buried under the top hBN layer. Such edge disorder may be responsible for the lowering of the

PC conductance below the Sharvin limit[7] and is expected to contribute more in our narrowest devices (Fig. 1d of the main text).

To gain further information about our narrowest PCs, we compared their measured conductance with that expected from the Sharvin formula. Figure S3d mirrors the presentation in Fig. 1d of the main text, showing the PC conductance as a function of density n, for the constrictions presented in Figs. S3a-c. The theory curves are again plotted using the width measured by AFM. In the case of $w_{AFM} \approx 0.2$ μm, G_{pc} was found to be notably lower than that expected from eq. (1) of the main text. As discussed above, this can be attributed to the edge roughness playing a relatively more prominent role for narrower constrictions[7]. However, even for the narrowest PC, its $G_{pc}(n)$ still scales linearly with the Fermi wave vector k_F, following the Sharvin formula (inset of Fig. S3d). This allows us to find the constriction's effective width w. We used such linear fits to determine effective widths for all our PC devices. Figure S3e shows examples of the fitting procedure for five PCs, plotting G_{pc} as a function of k_F. In all our devices, the dependences $G_{pc}(k_F)$ were clearly linear which shows that the effective width w is a good approximation for describing graphene constrictions. Such an approach was also used previously for suspended graphene constrictions[8].

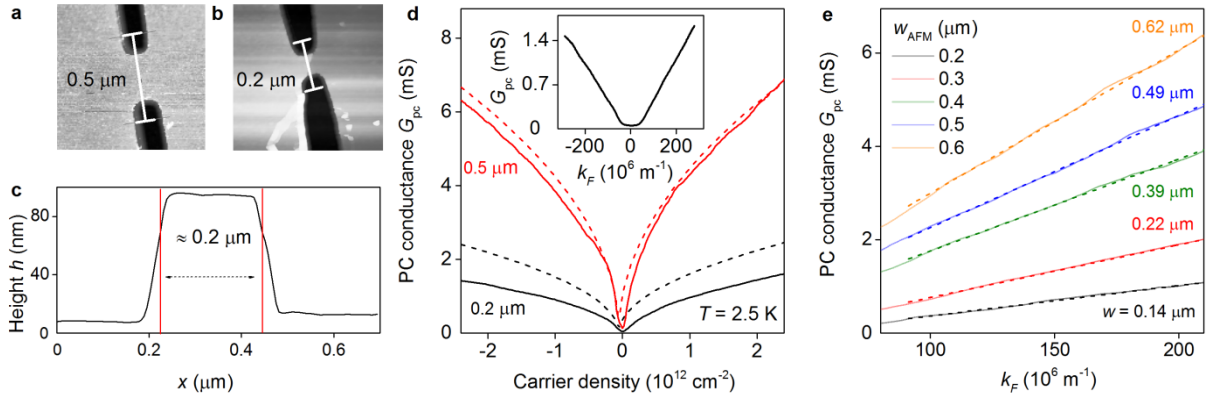

Figure S3| Point contact widths. a-b, AFM images of our constrictions. Grey scale: black - 0 nm; white - 95 nm. **c**, Height profile across the narrowest constriction, similar to the presentation in Fig. S1. **d**, Low-T conductance for the devices in (a) and (b). Solid curves: Experimental data. Dashed: Sharvin expression using the width determined by AFM. Inset: G_{pc} for the 0.2 μm PC is re-plotted as a function of k_F. **e,** G_{pc} as a function of k_F for several PCs measured at 2 K (electron doping). The dashed lines are linear fits to our experimental data (solid curves). The effective width w, extracted from the best fits to eq. (1) of the main text, is color-coded for each constriction.

S4. Modelling the ballistic-to-viscous crossover

Transport measurements reported in the main text were carried out using constrictions with w ranging from 0.2 to 1.2 μm and carrier densities of the order of 10^{12} cm^{-2}. The observed 'super-ballistic' behavior (that is, the suppression of the PC resistance below the ballistic Sharvin-Landauer value) was found to be most prominent at temperatures below 100 K. Under these conditions the e-e scattering mean free path l_{ee}, which depends on T and n, is comparable to the constriction width w. Therefore, modelling electron transport in our experimental system requires a method that can operate at the crossover between the ballistic and hydrodynamic regimes. To this end, we have used an approach developed in ref. 9, which is based on a kinetic equation with the collision operator describing momentum-conserving e-e collisions. In the absence of momentum-relaxing processes, such as electron-phonon scattering, this approach predicts the conductance G_{pc} that attains a ballistic value at zero T and increases monotonically with increasing temperature. In the present work, to account for the non-monotonic temperature dependence of the measured resistance R_{pc}, first growing and then decreasing, we have extended the model of ref. 9 by adding to the kinetic equation a momentum-relaxing term that describes electron-phonon scattering. In notations of ref. 9 our model reads

$$(\partial_t + v\nabla_x)f(\theta,x) = -\gamma_{ee}(1-P)f(\theta,x) - \gamma_{ep}(1-P_0)f(\theta,x). \qquad \text{(S1)}$$

where $f(\vartheta,\mathbf{x})$ is the non-equilibrium carrier distribution at the 2D Fermi surface parameterized by the angle ϑ. The rates γ_{ee} and γ_{ep} describe the e-e scattering and electron-phonon scattering processes, the quantities P and P_0 are projectors on the angular harmonics with m = 0, ±1 and m = 0, respectively, and 1 stands for the identity operator. As in ref. 9, this model assumes that all harmonics of the distribution function, which are not conserved, should relax at equal rates. The relaxation rates are equal to $\gamma_{ee} + \gamma_{ep}$ for m = ±2, ±3,… and γ_{ee} for m = ±1. The single-rate assumption allows us to reduce the integral-differential kinetic equation to a closed-form self-consistency relation for quasi-hydrodynamic variables (i.e., the m = 0,±1 angular harmonics), providing a means for solving it in the constriction geometry.

Incorporating the electron-phonon scattering term in the approach of ref. 9 significantly changes the algebra but conceptually proves to be uneventful. Given the scattering rate values γ_{ee} and γ_{ep}, we first find the current profile in the constriction cross-section. This is done considering non-slip boundary conditions, which we modelled by adding to the right-hand side of eq. (S1) a delta function term of the form $-b\delta(y)\delta(w/2 - |x|)P_{\pm} f(\theta,x)$ where the operator $P_{\pm}$ projects $f(\theta,x)$ on the m = 0,±1 angular harmonics. The parameter b is taken to the limit $b \to \infty$ to model an impenetrable boundary

at the half-lines $y = 0$, $|x|>w/2$. We then derive a self-consistent relation for current density in the constriction, solve it numerically and use the solution to determine the potential distribution in the regions adjacent to the constriction. The potential difference, obtained for the unit total current, yields the resistance.

As a simple model, we use the temperature dependences for the rates γ_{ee} and γ_{ep} in the following form

$$\gamma_{ee} = \frac{aT^2}{n^{1/2}} \times \frac{v_F}{w}, \qquad \gamma_{ep} = cT \times \frac{v_F}{w} \tag{S2}$$

where $v_F = 10^6$ m/s is the graphene Fermi velocity. These dependences correspond to the prediction of the Fermi liquid theory at weak coupling and the electron-phonon scattering rate due to acoustic phonons. The fits to the experimental dependences $R_{pc}(T)$ shown in Fig. 1e of the main text were obtained with the best-fit values of $a = 8.6\times10^3$ K^{-2} m^{-1} and $c = 2\times10^{-3}$ K^{-1}, which were taken to be identical for all densities n. To test the robustness of our model, we also explored other power-law and polynomial temperature dependences, and found that modest deviations from the T^2 and T scaling do not impact quality of the fits and may even lead to slight improvement. The agreement between the fits and the experimental data in Fig. 1e, impressive as it is, should therefore not be taken as evidence for the T^2 and T scaling for the rates γ_{ee} and γ_{ep}. Indeed, the analysis presented in the final part of the main text effectively uses a faster T dependence for phonon scattering and γ_{ee} somewhat slower than T^2, which provides a surprisingly good quantitative agreement with the experimental data. Let us also note that, if the different contributions described above were simply summed up using eq. (3) of the main text rather than the full model based on eq. (S1), we obtained practically the same theoretical dependences (within a few %). This further validates our analysis of the experimental data using eq. (3).

S5. Ohmic contribution to point contact resistance

Narrow constrictions that define PCs are connected to broader regions in which current and voltage contacts are located (see the above images of our experimental devices). In the presence of elastic scattering, these regions are responsible for an additional Ohmic contribution R_C that depends on details of device's geometry and the distance to voltage probes. This contribution is significant even at low T where transport is ballistic over a few μm distances and collisions with device edges become a dominant scattering process. The Ohmic contribution grows with increasing temperature (that is, with increasing electron-phonon scattering) and can obscure the viscous-flow behavior. Therefore,

we subtracted R_C from the measured resistance R_{pc} to extract the conductance that comes exclusively from PCs, as described in the main text. Such a procedure is standard in analysis of electron transport through quantum PCs[10].

To account for different geometries of contact regions, we calculated R_C numerically. To this end, we computed $R_C = V_{12}/I_{56}$ (see Fig. S4a as an example) by solving the following set of equations

$$\nabla . J(r) = 0 , \qquad \frac{\sigma_0}{e} \nabla\phi(r) - J(r) = 0 \tag{S3}$$

where $J(r)$ is the current density, $\phi(r)$ is the electric potential in the two-dimensional plane, $\sigma_0 = ne^2\tau/m$ the Drude-like conductivity with m and e being the effective mass and the electron charge, respectively, and τ is the phenomenological scattering time that accounts for all possible momentum-non-conserving collisions, including those at graphene edges. To solve the above differential equations, we followed the procedure used in ref. 10. In brief, by discretizing the differential operators on a square mesh, we obtained a set of sparse linear equations that could readily be solved. Our method involved three different staggered meshes that sampled values of the potential and, independently, the two components of the current density[10]. This was required to ensure that the velocity component orthogonal to the boundary was sampled, too. Finally, we used the following boundary conditions to simulate device's edges and contacts: (i) the current orthogonal to the edges was zero, (ii) the current was also zero through voltage contacts, (iii) the total current through source and drain contacts was fixed, as in the experiment.

Exploiting the linearity of the problem, we can write the Ohmic contribution as $R_C = b\rho_{xx}$, where b is a dimensionless function of the ratios w/W and L/W. The calculated coefficient b is plotted in Fig. S4b as a function of w/W for the geometry used in our experiments with $L/W = 1$.

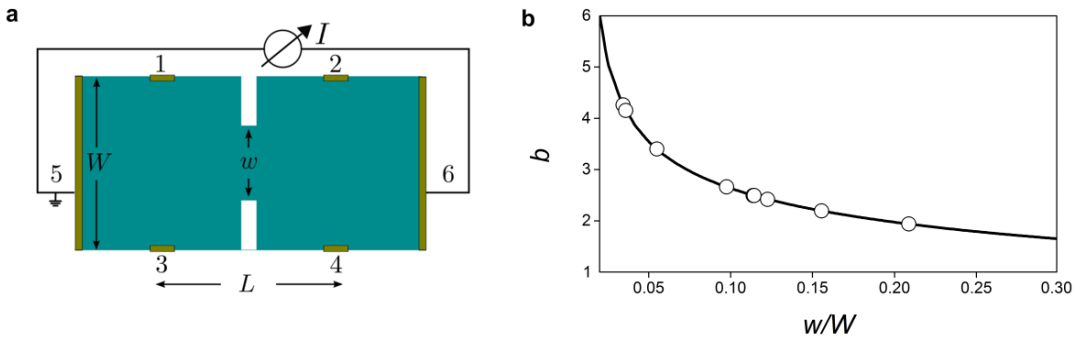

Figure S4| Ohmic contribution. **a**, Schematic of the device geometry. Electrical current I is passed between contacts 5 and 6. Voltage drop is measured between pairs of contacts 1 and 2 or 3 and 4. **b**, Coefficient b as a function of w/W for the given $L/W = 1$. The solid curve shows our numerical results. The open circles correspond to the geometry of PC devices measured in this work

S6. Microscopic calculations of electron-electron scattering

In this section, we provide details of microscopic calculations of l_{ee} which were presented in Fig. 3e of the main text. We have determined l_{ee} from the imaginary part of the retarded quasiparticle self-energy $\Sigma_\lambda(k, \omega)$ averaged over the Fermi surface[11]. The conduction and valence bands are marked with $\lambda = +$ and $-$, respectively. For an electron-doped system, we use

$$l_{ee}^{-1} \equiv \frac{2}{v_F} \int d\omega \left(\frac{\partial n_F(\omega)}{\partial \omega} \right) \Im m[\Sigma_+(k_F, \omega)] \tag{S4}$$

where k_F is the Fermi wave vector and $n_F(\omega)$ is the Fermi distribution. Below we use $\hbar \equiv 1$ and $k_B \equiv 1$ for the Planck and Boltzmann constants, respectively. In the spirit of the large-N approximation (where $N = 4$ is the number of fermion flavors in graphene), the quasiparticle self-energy $\Sigma_\lambda(k, \omega)$ can be calculated within the G_0W approximation. For monolayer graphene[12,13]

$$\Im m[\Sigma_\lambda(k_F, \omega)] = \int \frac{d^2\boldsymbol{q}}{(2\pi)^2} \sum_{\lambda'} \Im m\left[W\left(q, \omega - \xi_{\boldsymbol{k}-\boldsymbol{q},\lambda'}\right)\right] \mathcal{F}_{\lambda\lambda'}\left(\theta_{\boldsymbol{k},\boldsymbol{k}-\boldsymbol{q}}\right) \left[n_B\left(\omega - \xi_{\boldsymbol{k}-\boldsymbol{q},\lambda'}\right) + n_F\left(-\xi_{\boldsymbol{k}-\boldsymbol{q},\lambda'}\right)\right] \tag{S5}$$

where $n_{F/B}(\varepsilon) = (e^{\varepsilon/T} \pm 1)^{-1}$ are the usual Fermi and Bose distribution factors, respectively, and $W(q,\omega) = V(q,\omega)/\varepsilon(q,\omega)$ is the screened Coulomb interaction. The Fourier transform of the bare Coulomb interaction, $V(q,\omega) = 2\pi e^2 \mathcal{G}(qd,qd')/q$, contains the form-factor $\mathcal{G}(qd,qd')$, which encodes all the information about the dielectric environment surrounding the graphene. It depends on the thickness d and d' of hBN above and below the graphene plane, as well as on the in-plane ϵ_x and out-of-plane ϵ_z components of the dielectric tensor of hBN. The full expression for $\mathcal{G}$ is given, for example, in the Supplementary Material of ref. 14. Finally, $\xi_{\boldsymbol{k},\lambda} = \lambda v_F k - \mu(T)$ is the band energy measured from the chemical potential $\mu(T)$ and $\varepsilon(q,\omega) = 1 - V(q,\omega)\chi_{nn}(q,\omega)$ is the RPA dynamical dielectric function. Here, $\chi_{nn}(q,\omega)$ is the density-density response function of graphene, which can be found in refs. 15–19. $\mathcal{F}_{\lambda\lambda'}(\theta_{\boldsymbol{k},\boldsymbol{k}-\boldsymbol{q}}) = [1 + \lambda\lambda'\cos(\theta_{\boldsymbol{k},\boldsymbol{k}-\boldsymbol{q}})]/2$ is the square of the matrix element of the density operator, with $\theta_{\boldsymbol{k},\boldsymbol{k}-\boldsymbol{q}} = \theta_{\boldsymbol{k}} - \theta_{\boldsymbol{k}-\boldsymbol{q}}$ being the angle between the vectors $\boldsymbol{k}$ and $\boldsymbol{k} - \boldsymbol{q}$.

For completeness, we note that in the Fermi liquid regime[12] eq. (S4) can be simplified to

$$l_{ee}^{-1} = \frac{\pi k_F}{N} \left(\frac{T}{\varepsilon_F}\right)^2 \ln\left(\frac{2\varepsilon_F}{T}\right) \tag{S6}$$

where $\varepsilon_F = v_F k_F$ is the Fermi energy.

S7. Sample and density dependences of e-e scattering length

In monolayer graphene, where charge carriers are massless Dirac fermions, e-e scattering is dominated by processes that transfer a small amount of the momentum[13]. Such events, usually referred to as collinear collisions, are weakly sensitive to the dielectric enviroment[17]. Therefore, our devices with different thicknesses of top and bottom hBN layers are not expected[13] to exhibit drastically different l_{ee}. Indeed, Fig. S5a plots $l_{ee}(T)$ for several PCs in two of our devices with different d and d'. For these devices, the e-e scattering lengths calculated as described in Section 6 are indistinguishable on the scale of Fig. S5a, yielding the same curve. As for the experiment, l_{ee} found for all our PCs closely follow the same functional dependence (see Fig. S5a) and exhibit quantitative agreement with the calculations. This substantiates the robustness of the experimental and analytical methods used in this report.

Until now, we presented $l_{ee}(T)$ only for fixed carrier densities. For completeness, Fig. S5b shows the density dependence of l_{ee} at fixed T. To find $l_{ee}(n)$, we followed the same analytical procedure as explained in the main text, which allowed us to extract the viscous conductance G_v and, consequently, obtain l_{ee} without using any fitting parameters. Comparison in Fig. S5b between our experiment and calculations again shows good agreement. Perhaps unsurprisingly, it holds best for intermediate T around 100 K, where our PCs are sufficiently away from the purely ballistic regime while the electron-phonon contribution to R_{pc} remains relatively small. Let us note that, in this experiment, l_{ee} slowly increases with n, which is in contrast to the trend reported for the vicinity geometry (see Ref. 12 of the main text) but in agreement with the theory that expects l_{ee} to be approximately proportional to $n^{0.5}$.

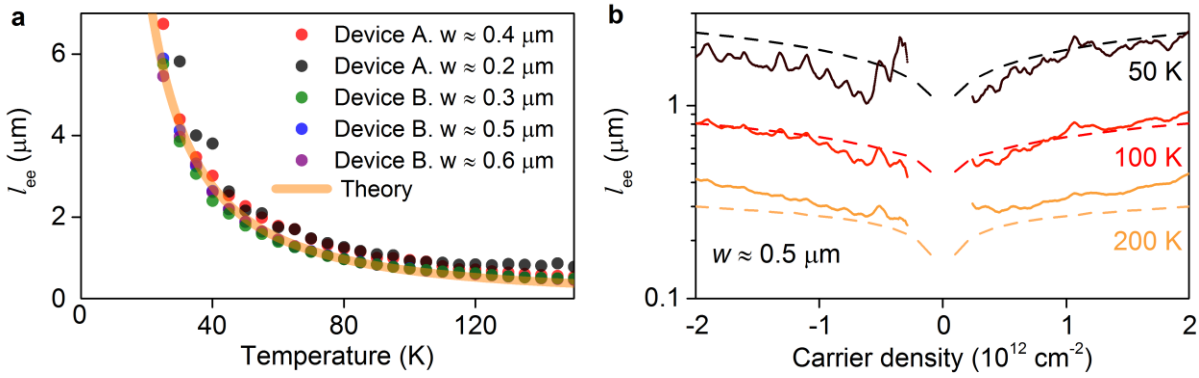

Figure S5|Electron-electron scattering for different devices and carrier densities. a, l_{ee} as a function of T measured using devices A and B with several PCs; $n = 1\times10^{12}$ cm^{-2}. Device A is made of graphene encapsulated between hBN crystals off approximately equal thickness ($d \approx d' \sim 40$ nm). In device B, top hBN is ~20 nm whereas the bottom one ~30 nm. Orange curve: Microscopic calculations of $l_{ee}(T)$ for both A and B. **b,** l_{ee} as a function of n at different T in a constriction with $w \approx 0.5$ μm (solid curves). Dashed curves: Calculations of $l_{ee}(n)$.

S8. Different length scales for electron viscosity

Our experimental data allow us to determine the characteristic length for e-e collisions responsible for the super-ballistic flow. As discussed above and in the main text, we find that these lengths agree extremely well with the e-e mean free path l_{ee}, associated with the quasiparticle lifetime $\tau_{ee} = l_{ee}/v_F$. However, at high temperatures, deep in the hydrodynamic regime, the quasiparticle lifetime is expected to be no longer the relevant length scale governing the viscous electron flow. In this regime, the kinematic viscosity ν is better described by the 'viscous' mean free path l_V, which is of the same order but not identical to l_{ee}.

The kinematic viscosity ν is related to l_V by the standard expression $\nu = v_F l_V/4$ and can be calculated from the stress-stress linear response function $\chi_{ij,kl}(\mathbf{q}, \omega)$ as

$$\nu = -\lim_{\omega\to 0}\frac{1}{4\,n\,m_c\omega}\sum_{i,j=x,y}\Im m\left[\chi_{ij,ij}(\mathbf{0},\omega)-\frac{1}{2}\chi_{ii,jj}(\mathbf{0},\omega)\right], \qquad \text{(S7)}$$

where $m_c = k_F/v_F$ is the effective mass for monolayer graphene. After rather lengthy calculations (see ref. 20 for technical details), the viscosity length is found to be given by

$$\ell_\nu^{-1} = \frac{2}{v_F}\int d\omega\left(\frac{\partial n_F(\omega)}{\partial\omega}\right)\Im m\left[\Sigma_+^{(\nu)}(k_F,\omega)\right], \qquad \text{(S8)}$$

where

$$\Im m\left[\Sigma_{\lambda}^{(v)}(k_{\mathrm{F}},\omega)\right]$$
$$= \int \frac{d^2\boldsymbol{q}}{(2\pi)^2} \sum_{\lambda'} \Im m\left[W(q,\omega-\xi_{\boldsymbol{k}-\boldsymbol{q},\lambda'})\right]\mathcal{F}_{\lambda\lambda'}\left(\theta_{\boldsymbol{k},\boldsymbol{k}-\boldsymbol{q}}\right)\left[n_{\mathrm{B}}(\omega-\xi_{\boldsymbol{k}-\boldsymbol{q},\lambda'})\right.$$
$$\left. + n_{\mathrm{F}}(-\xi_{\boldsymbol{k}-\boldsymbol{q},\lambda'})\right]\sin^2(\theta_{\boldsymbol{k},\boldsymbol{k}-\boldsymbol{q}}) \qquad \text{(S9)}.$$

In the Fermi liquid regime[12] the viscosity length behaves as

$$\ell_v^{-1} = \mathcal{N}\alpha_{ee}^2 k_{\mathrm{F}}\left(\frac{T}{\varepsilon_{\mathrm{F}}}\right)^2, \qquad \text{(S10)}$$

where $\alpha_{ee} = 2.2$ is the e-e coupling constant of graphene, and the coefficient $\mathcal{N}\sim 0.1$ has a rather cumbersome expression, depending on microscopic details (see ref. 20).

Figure S6 compares our experimental data (same as in Fig. 3e in the main text) with microscopic calculations for both lengths l_{ee} and l_v. As shown in the main text, the experimental data follows l_{ee} closely until about 100 K. Beyond this *T*, the extracted length deviates slightly upwards from l_{ee} and tends towards l_v as expected in the extreme hydrodynamic regime $l_{ee} << w$. Proper validation of this transition from l_{ee} to l_v would require measurements at much higher *T*, inaccessible for our experimental devices. Accordingly, Fig. S6 is used here only to point out similarities and differences between our experimental data and e-e scattering length scales, whilst better theoretical understanding is required to make any further conclusions.

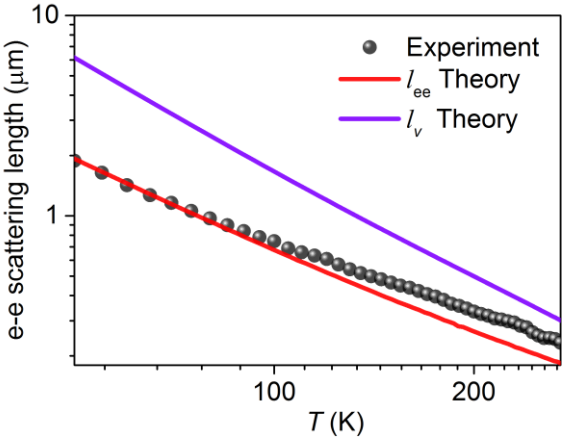

Figure S6| Different viscous length. Black symbols: Electron-electron scattering length determined experimentally for a graphene constriction with $w \approx 0.5$ um; $n = 10^{12}$ cm^{-2}. Red and purple curves: Microscopic calculations of l_{ee} and l_V as a function of *T* for the given *n*.

Supplementary References

1. Wang, L. *et al.* One-dimensional electrical contact to a two-dimensional material. *Science* **342,** 614–617 (2013).
2. Kretinin, A. V. *et al.* Electronic properties of graphene encapsulated with different two-dimensional atomic crystals. *Nano Lett.* **14,** 3270–3276 (2014).
3. Ben Shalom, M. *et al.* Quantum oscillations of the critical current and high-field superconducting proximity in ballistic graphene. *Nat. Phys.* **12,** 318–322 (2015).
4. Hwang, E. H. & Das Sarma, S. Acoustic phonon scattering limited carrier mobility in two-dimensional extrinsic graphene. *Phys. Rev. B* **77,** 115449 (2008).
5. Mayorov, A. S. *et al.* Micrometer-scale ballistic transport in encapsulated graphene at room temperature. *Nano Lett.* **11,** 2396–2399 (2011).
6. Beconcini, M. *et al.* Scaling approach to tight-binding transport in realistic graphene devices: The case of transverse magnetic focusing. *Phys. Rev. B* **94,** 115441 (2016).
7. Terrés, B. *et al.* Size quantization of Dirac fermions in graphene constrictions. *Nat. Commun.* **7,** 11528 (2016).
8. Tombros, N. *et al.* Quantized conductance of a suspended graphene nanoconstriction. *Nat. Phys.* **7,** 697–700 (2011).
9. Guo, H., Ilseven, E., Falkovich, G. & Levitov, L. Higher-Than-Ballistic Conduction of Viscous Electron Flows. *arXiv:1607.07269v2* (2017).
10. Harlow, F. H. & Welch, J. E. Numerical calculation of time-dependent viscous incompressible flow of fluid with free surface. *Phys. Fluids* **8,** 2182–2189 (1965).
11. Principi, A. & Vignale, G. Intrinsic charge and spin conductivities of doped graphene in the Fermi-liquid regime. *Phys. Rev. B* **91,** 205423 (2015).
12. Giuliani, G. & Vignale, G. *Quantum Theory of the Electron Liquid*. (Cambridge University Press, 2005).
13. Polini, M. & Vignale, G. The quasiparticle lifetime in a doped graphene sheet. *arXiv:1404.5728v1* (2014).
14. Alonso-González, P. *et al.* Acoustic terahertz graphene plasmons revealed by photocurrent nanoscopy. *Nat. Nanotechnol.* (2016). doi:10.1038/nnano.2016.185
15. Shung, K. W. K. Dielectric function and plasmon structure of stage-1 intercalated graphite. *Phys. Rev. B* **34,** 979–993 (1986).
16. Wunsch, B., Stauber, T., Sols, F. & Guinea, F. Dynamical polarization of graphene at finite doping. *New J. Phys.* **8,** 318–1367 (2006).
17. Hwang, E. H. & Das Sarma, S. Dielectric function, screening, and plasmons in two-dimensional

graphene. *Phys. Rev. B* **75,** 205418 (2007).

18. Polini, M. *et al.* Plasmons and the spectral function of graphene. *Phys. Rev. B* **77,** 81411 (2008).
19. Principi, A., Polini, M. & Vignale, G. Linear response of doped graphene sheets to vector potentials. *Phys. Rev. B* **80,** 75418 (2009).
20. Principi, A., Vignale, G., Carrega, M. & Polini, M. Bulk and shear viscosities of the 2D electron liquid in a doped graphene sheet. *Phys. Rev. B* **93,** 125410 (2016).

Chapter 8 – Brown-Zak oscillations

Paper title: High temperature quantum oscillations caused by recurring Bloch states in graphene superlattices

Journal Reference: Science 357, 181-184 (2017)

DOI: 10.1038/nphys4240

My contribution: I discovered the new quantum oscillations described in this work. I also built a specialist high-temperature measurement insert and developed a technique for measuring graphene samples at 400 K without degradation. I performed transport measurements, analysed the data and contributed to writing the manuscript. I wrote most of the Supplementary Section.

Full Author List: **R. Krishna Kumar**, X. Chen, G. H. Auton, A. Mischenko, D. A. Bandurin, S. V. Morozov, Y. Cao, E. Khestanova, M. Ben Shalom, A. V. Kretinin, K. S. Novoselov, L. Eaves, I. V. Grigorieva, L. A. Ponomarenko, V. I. Fal'ko, A. K. Geim

Author contributions: R.K.K, S.V and L.A.P performed transport experiments/analysed data. A. M made capacitance measurements. G.H.A, Y.C, M.B.S and A.V.K fabricated the devices. X.C and V.I.F provided theoretical support. L.A.P, A.K.G and V.I.F supervised the project. A.K.G, V.F.I, R.K.K and L.A.P wrote the manuscript. L.E, I.V.G and K.S.N provided useful discussions and contributed to writing the manuscript.

Abstract: magneto-oscillatory phenomena take on many different forms in Condensed Matter physics. However, the different effects tend to have the same fundamental origin of which there is only a handful. Quantum oscillations for one instance, originate due to the coherence of electron trajectories and/or preservation in of phase in the electron wave function. This restricts the phenomena to liquid helium temperatures. Here, we present a completely novel type of quantum oscillation which we called Brown-Zak oscillations. The underlying physics is due to the magnetic translation group which was described in chapter 3.5, where electron motion change periodically between straight and curved trajectories as the magnetic field is increased. This results in strong oscillations in the conductivity upon increasing magnetic field. These oscillations show novel behaviour not found in any other type of magneto-oscillation. The most outstanding is the fact that they are extremely robust with respect to temperature. For example, we could observe the Brown-Zak oscillations still at 373 K, the boiling point of water.

REPORT

GRAPHENE

High-temperature quantum oscillations caused by recurring Bloch states in graphene superlattices

R. Krishna Kumar,[1,2,3] X. Chen,[2] G. H. Auton,[2] A. Mishchenko,[1] D. A. Bandurin,[1] S. V. Morozov,[4,5] Y. Cao,[2] E. Khestanova,[1] M. Ben Shalom,[1] A. V. Kretinin,[2,6] K. S. Novoselov,[2] L. Eaves,[2,7] I. V. Grigorieva,[1] L. A. Ponomarenko,[3] V. I. Fal'ko,[1,2]* A. K. Geim[1,2]*

Cyclotron motion of charge carriers in metals and semiconductors leads to Landau quantization and magneto-oscillatory behavior in their properties. Cryogenic temperatures are usually required to observe these oscillations. We show that graphene superlattices support a different type of quantum oscillation that does not rely on Landau quantization. The oscillations are extremely robust and persist well above room temperature in magnetic fields of only a few tesla. We attribute this phenomenon to repetitive changes in the electronic structure of superlattices such that charge carriers experience effectively no magnetic field at simple fractions of the flux quantum per superlattice unit cell. Our work hints at unexplored physics in Hofstadter butterfly systems at high temperatures.

Oscillations of physical properties of materials with magnetic field are a well known and important phenomenon in condensed matter physics. Despite having a variety of experimental manifestations, there are only a few basic types of oscillations: those of either quantum or semiclassical origin (*1*–*5*). Semiclassical size effects, such as Gantmakher and Weiss oscillations, appear owing to commensurability between the cyclotron orbit and a certain length in an experimental system (*1*–*4*). Quantum magneto-oscillations are different in that they arise from periodic changes in the interference along closed electron trajectories (*1*–*5*). Most commonly, quantum oscillations involve cyclotron trajectories. This leads to Landau quantization and, consequently, Shubnikov–de Haas (SdH) oscillations in magnetoresistance and the associated oscillatory behavior in many other properties (*1*–*3*). In addition, quantum oscillations may arise from interference on trajectories imposed by sample geometry, leading to Aharonov-Bohm oscillations in mesoscopic rings, for instance (*3*, *5*). Whatever their exact origin, the observation of such oscillatory effects normally requires low temperatures (T), and this requirement is particularly severe in the case of quantum oscillations that rely on the monochromaticity of interfering electron waves. Even in graphene, with its massless Dirac spectrum and exceptionally large cyclotron gaps, SdH oscillations rarely survive above 100 K. At room T, high magnetic fields (B) of ~30 T are needed to observe the last two SdH oscillations arising from the maximal gaps between the zeroth and first Landau levels (LLs) of graphene (*6*). In all other materials, quantum oscillations disappear at much lower T.

Electronic systems with superlattices can also exhibit magneto-oscillations. In this case, the interference of electrons diffracting at a superlattice potential in a magnetic field results in fractal, self-similar spectra that are often referred to as Hofstadter butterflies (HBs) (*7*–*12*). Their fractal structure reflects the fact that charge carriers effectively experience no magnetic field if magnetic flux ϕ through the superlattice unit cell is commensurate with the magnetic flux quantum, ϕ_0 (*7*–*9*). This topic has attracted interest for decades (*11*–*16*) but received a particular boost thanks to the recent observation of clear self-similar features in transport characteristics and in the density of states (DOS) of graphene superlattices (*17*–*25*). Because the HB depicts quantum states developed from partial admixing of graphene's original LLs (*12*), superlattice-related gaps already become smeared at relatively low T, well below those at which signatures of quantization in the main spectrum disappear. Therefore, it is perhaps not surprising that investigations of Hofstadter systems were confined mostly to low T. As shown below, this has resulted in a failure to notice some unusual physics: Superlattices exhibit robust high-T oscillations in their transport characteristics, which are different in origin from the known oscillatory effects.

We used multiterminal Hall bar devices (Fig. 1A, inset, and fig. S1) made from graphene superlattices (*26*) to carry out our transport measurements. Monolayer graphene was placed on top of a hexagonal boron nitride (hBN) crystal, and their crystallographic axes were aligned with an accuracy of better than 2° (*17*, *24*). The resulting moiré pattern gives rise to a periodic potential that is known to affect the electronic spectrum of graphene (*23*–*25*). To ensure that the charge carriers have high mobility, the graphene was encapsulated using a second hBN crystal, which was intentionally misaligned by ~15° with respect to graphene's axes. Although the second hBN layer also leads to a moiré pattern, it has a short periodicity and, accordingly, any superlattice effects may appear only at high carrier concentrations n or ultrahigh B, beyond those accessible in transport experiments (*17*–*25*). Therefore, the second hBN effectively serves as an inert, atomically-flat cover protecting graphene from the environment. Six superlattice devices were investigated and showed consistent behavior, which is described below. As a reference, we also studied devices made according to the same procedures but with the graphene misaligned with respect to both top and bottom hBN layers.

Figure 1A shows typical behavior of the longitudinal resistivity ρ_{xx} for graphene superlattices as a function of B at various T. For comparison, Fig. 1B plots similar measurements for the reference device. In the latter case, ρ_{xx} exhibits pronounced SdH oscillations at liquid-helium T, which develop into the quantum Hall effect above a few tesla. The SdH oscillations are rapidly suppressed with increasing T and completely vanish above liquid-nitrogen T, the standard behavior for graphene in these relatively weak fields (*27*, *28*). In stark contrast, graphene superlattices exhibit prominent oscillations over the entire T range (Fig. 1A and fig. S2). At both high and low T, the oscillations are periodic in $1/B$ (figs. S3 and S4). The oscillations in Fig. 1A change their frequency at ~50 K. This is the same T range in which SdH oscillations disappear in the reference device of Fig. 1B. For certain ranges of n and B, we observed that SdH oscillations vanished first, before new oscillations emerged at higher T. An example of such nonmonotonic T dependence is shown in fig. S2. To emphasize the robustness of the high-T oscillations, we show that they remain well developed even at boiling-water T in moderate B (Fig. 1C). The oscillations were observed even at higher T, but above 400 K our devices (both superlattice and reference devices) showed rapid deterioration in quality and strong hysteresis as a function of gate voltage.

The high-T and SdH oscillations differ not only in their periodicity and thermal stability but also because they have distinctly different n dependences. Figure 2, A and B, shows Landau fan diagrams for the longitudinal conductivity σ_{xx} of

[1]School of Physics and Astronomy, University of Manchester, Manchester M13 9PL, UK. [2]National Graphene Institute, University of Manchester, Manchester M13 9PL, UK. [3]Department of Physics, University of Lancaster, Lancaster LA1 4YW, UK. [4]Institute of Microelectronics Technology and High Purity Materials, Russian Academy of Sciences, Chernogolovka 142432, Russia. [5]National University of Science and Technology (MISiS), Moscow 119049, Russia. [6]School of Materials, University of Manchester, Manchester M13 9PL, UK. [7]School of Physics and Astronomy, University of Nottingham, Nottingham NG7 2RD, UK.
*Corresponding author. Email: vladimir.falko@manchester.ac.uk (V.I.F.); geim@manchester.ac.uk (A.K.G.)

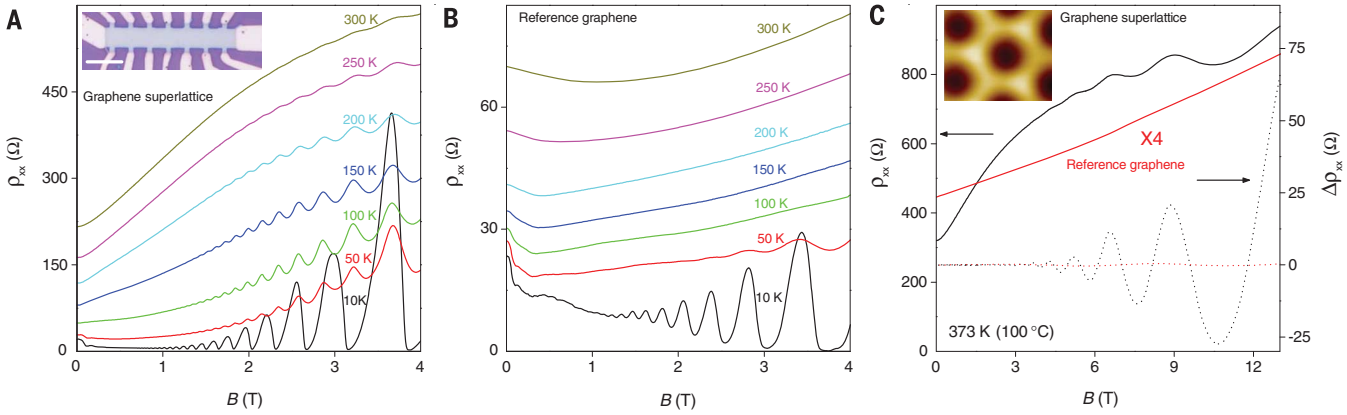

Fig. 1. High-temperature oscillations in graphene superlattices. (**A**) ρ_{xx} at relatively small B for a superlattice device with a moiré periodicity of ≈13.6 nm. The electron density is $n \approx 1.7 \times 10^{12}$ cm^{-2} and is induced by a back-gate voltage. (Inset) Optical micrograph of one of our Hall bar devices. Scale bar, 5 μm. Ω, ohms. (**B**) Same as (A) but using the reference device at the same n. (**C**) Magnetoresistance curves for the devices in (A) and (B) at 100°C (solid curves). ρ_{xx} for the reference device is multiplied by a factor of 4. Dotted curves: Oscillatory behavior is emphasized by subtracting a smooth background, using fourth-order polynomials as best fits to the original ρ_{xx} curves (*26*). At 100°C, graphene superlattices exhibit oscillations starting below 4 T, whereas no sign of oscillatory behavior could be discerned at this T in our reference devices at any B. (Inset) Scanning tunneling image illustrates typical moiré patterns found in our devices [for details, see (*30*)].

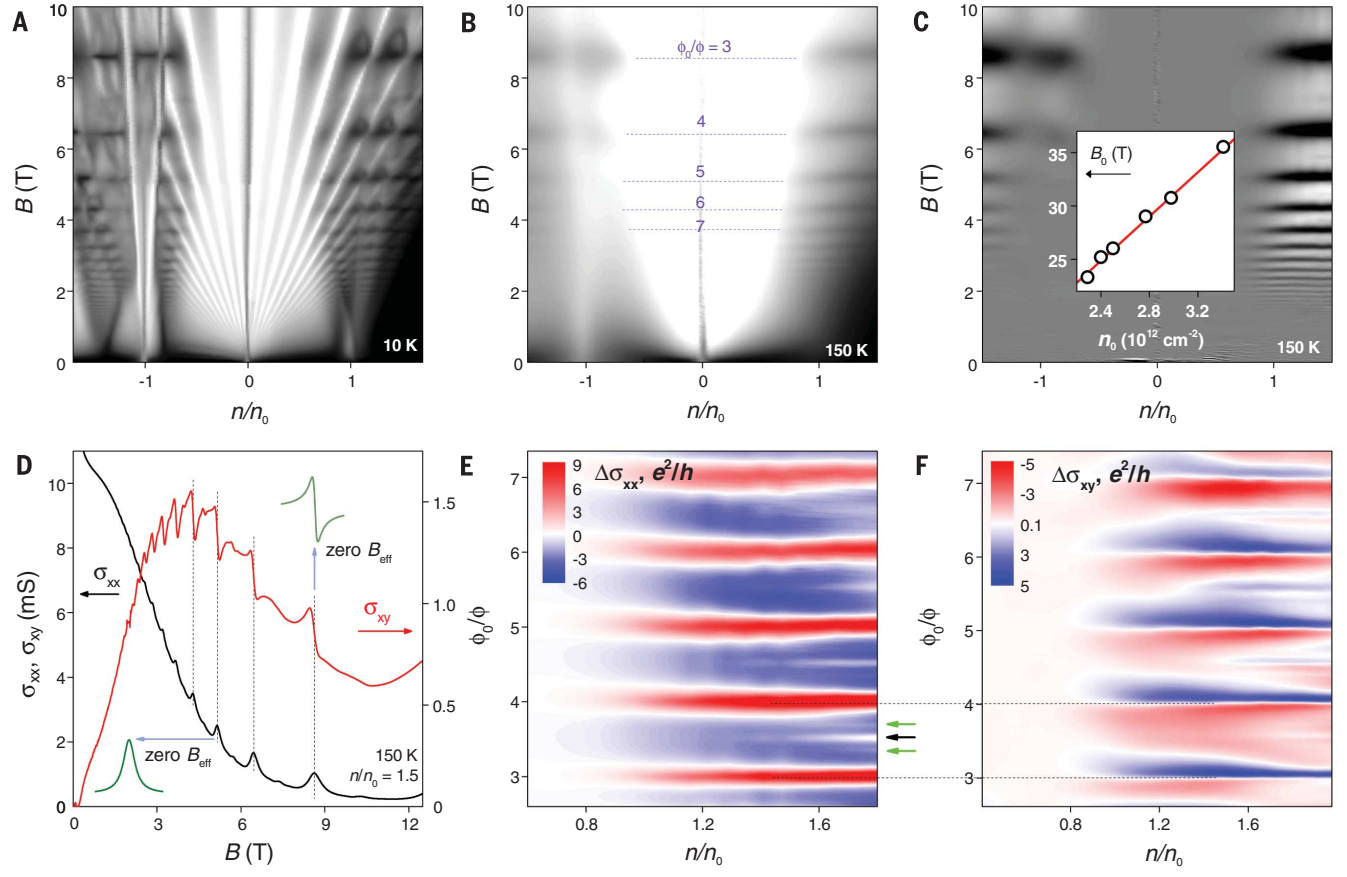

Fig. 2. Concentration and field dependence of Brown-Zak (BZ) oscillations. (**A**) Low-T fan diagram $\sigma_{xx}(n, B)$ for a superlattice device with $a \approx$ 13.9 nm. The gray scale is logarithmic: white, 0.015 mS; black, 15 mS. (**B**) Same device as (A) but at 150 K. Logarithmic gray scale: white, 0.1 mS; black, 10 mS. The dotted lines denote $B = \phi_0/qS$. (**C**) Same as (B) but for $\Delta\sigma_{xx}$ obtained by subtracting a smooth best-fit background (*26*). Linear gray scale: ±0.3 mS. (Inset) Fundamental frequency B_0 of BZ oscillations found in our different devices as a function of $n_0 = 8/\sqrt{3}a^2$. (**D**) Near $B = \phi_0/qS$ (dashed lines are for q = 3 to 6), local changes in σ_{xx} and σ_{xy} resemble magnetotransport in metals near zero field, as illustrated by the green inset curves. (**E**) Part of (C) near the second-generation NP for electron doping is magnified and plotted as a function of ϕ_0/ϕ. The main maxima in $\Delta\sigma_{xx}$ occur at $\phi_0/\phi = q$. A few extra maxima for p = 2 and 3 are indicated by black and green arrows, respectively (see fig. S6 for details). (**F**) Corresponding behavior of $\Delta\sigma_{xy}$ (smooth background subtracted). Its zeros align with the red maxima in $\Delta\sigma_{xx}$.

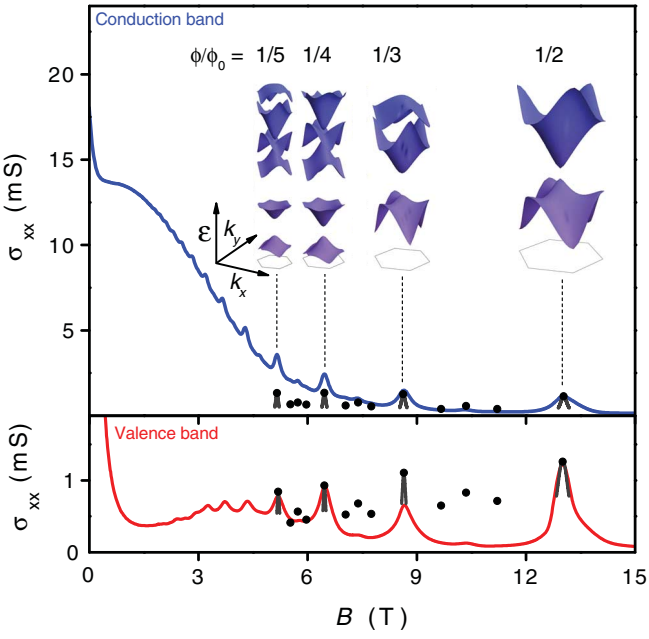

Fig. 3. BZ oscillations as recurring Bloch states in small effective fields. Solid curves: σ_{xx} at 100 K for electron and hole doping (n/n_0 = ±1.6) (top and bottom panels, respectively) in a superlattice device with $a \approx$ 13.6 nm. Black dots and curves: σ_{xx} calculated in the constant-τ approximation for different p and q. Inset image: BZ minibands $\varepsilon(\vec{\mathbf{k}})$ inside the first Brillouin zones indicated by the gray hexagons (their size decreases with increasing q). The minibands were calculated for a generic graphene-on-hBN superlattice (*29*) and correspond to broadened LLs (for example, LLs are 2 and 3 for q = 2 and range from 3 to 8 for q = 5). Only those minibands at energies relevant to the doping level on the experimental curves are shown.

graphene superlattices as a function of B and n (we plot σ_{xx} rather than ρ_{xx} to facilitate the explanation given below for the origin of the high-T oscillations). At low T (Fig. 2A), we observe the same behavior as reported previously (*17*–*22*): Numerous LLs fan out from the main (n = 0) and second-generation neutrality points (NPs) that are found at $n = \pm n_0$, where $n_0 = 4/S$ corresponds to four charge carriers per superlattice unit cell with the area $S = \sqrt{3}a^2/2$ and the superlattice period a (*17*–*22*). The LL intersections result in third-generation NPs at finite B (*19*). Minima in σ_{xx} evolve linearly in B and originate from first-, second-, and third-generation NPs (*17*–*22*). This reflects the fact that the DOS for all LLs (including those caused by fractal gaps) is the same and proportional to B (*11*). At T > 100 K, the Landau quantization dominating the low-T diagrams wanes and, instead, oscillations with a periodicity independent of n emerge (Fig. 2, B and C). This independence of n clearly distinguishes the high-T oscillations from all of the known magneto-oscillatory effects arising from either Landau quantization or commensurability (*1*–*5*). For the reasons that become clear below, we refer to the observed high-T phenomenon as Brown-Zak (BZ) oscillations (*7*, *8*).

The BZ oscillations become stronger with increased doping (Fig. 2C), in agreement with the fact that the superlattice spectrum is modified more strongly at energies away from the main Dirac point (*17*–*22*). The maxima in σ_{xx} are found at $B = \phi_0/qS$, which corresponds to unit fractions of ϕ_0 piercing a superlattice unit cell (q is an integer). The relation between the superlattice period and the periodicity of the high-T oscillations holds accurately for all of our devices (Fig. 2C, inset; for details, see fig. S3). This is the same periodicity that underlines the Hofstadter spectrum and describes the recurrence of third-generation NPs (*17*, *18*). However, BZ oscillations emerge most profoundly at high T, in the absence of any remaining signs of the Hofstadter spectrum or Landau quantization (fig. S5). Our capacitance measurements (fig. S5A) reveal no sign of behavior similar to BZ oscillations in the DOS, even at liquid-helium T that allow the clearest view of the HB (*20*, *25*). These observations prove that BZ oscillations are a transport phenomenon, unrelated to the spectral gaps that make up the Hofstadter spectrum. BZ oscillations do not disappear at low T and, retrospectively, can be recognized as horizontal streaks connecting third-generation NPs on the transport Landau fan diagrams (*17*–*19*) (Fig. 2A). However, the streaks are heavily crisscrossed by LLs, which makes them easy to overlook or wrongly associate with the quantized Hofstadter spectrum (*17*).

The HB spectrum is expected to exhibit a fractal periodicity associated with not only unit fractions but all of the simple fractions, p/q, corresponding to p flux quanta per q cells. No signatures of such higher-order states were found in the previous experiments (*17*–*22*) nor can they be resolved in our present fan diagrams at low T. However, the fractions with p = 2 and 3 become evident in BZ oscillations (Fig. 2E) and are most prominent at high n (fig. S6). This again indicates that the BZ oscillations are governed by the same underlying periodicity as is the HB spectrum. We also find that BZ oscillations are stronger for electrons than for holes (Fig. 2B and fig. S7). This is in contrast to the relative strengths of all other features reported previously for graphene-on-hBN superlattices (*17*–*25*). The electron-hole asymmetry is probably connected to the observed stronger electron-phonon scattering for hole doping (fig. S7).

To explain BZ oscillations, we recall that at $B = \phi_0 p/Sq$, the electronic spectrum of superlattices can be reduced to the case of zero magnetic field by introducing new Bloch states and the associated magnetic minibands, different for each p/q. This concept was put forward by Brown (*7*) and Zak (*8*) and predates the work by Hofstadter (*10*). Examples of BZ minibands for several unit fractions of ϕ_0 are shown in Fig. 3 and fig. S8, using a generic graphene-on-hBN potential (*26*). Each miniband can be viewed as a superlattice-broadened LL, such that its energy dispersion $\varepsilon(\vec{\mathbf{k}})$ disappears in the limit of vanishing superlattice modulation (*12*). If the Fermi energy ε_F lies within these superlattice-broadened LLs, the system should exhibit a metallic behavior (*25*). The Hofstadter spectrum can then be understood as Landau quantization of BZ minibands in the effective field $B_{eff} = B - \phi_0 p/qS$ (*20*, *29*). With this concept in mind, let us take a closer look at the experimental behavior of σ_{xx} and the Hall conductivity σ_{xy} at high T and small B_{eff}—that is, in the absence of Landau quantization in BZ minibands (Fig. 2, D to F, and fig. S6). One can see that every time BZ minibands are formed, σ_{xx} exhibits a local maximum and σ_{xy} shows a $B_{eff}/(1 + B_{eff}^2)$–like feature on top of a smoothly varying background. This local behavior resembles changes in σ_{xx} and σ_{xy} expected for any metallic system near zero B and approximated by the functional forms $1/(1 + B^2)$ and $B/(1 + B^2)$, respectively (*1*–*3*). The latter are sketched in the insets of Fig. 2D and match well the shape of local changes in σ_{xx} and σ_{xy} near fractional fluxes $\phi = \phi_0 p/q$, which correspond to B_{eff} = 0 (Figs. 2D and 3 and fig. S6).

The described analogy between magnetotransport in normal metals and in BZ minibands can be elaborated using the approximation of a constant scattering time τ (*1*–*3*). We assume τ to be the same for all minibands and magnetic fields. In this approximation, $\sigma_{xx} \propto v^2\tau$ and is determined by the group velocity of charge carriers, v (*26*). Each BZ miniband effectively represents a different two-dimensional system with a different k-dependent velocity. If T is larger than the cyclotron gaps, as in our case, the Fermi step becomes smeared over several minibands, which all contribute to σ_{xx}. In this regime, one can define $\langle v^2 \rangle$ averaged over an interval of $\pm T$ around ε_F. We calculate $\langle v^2 \rangle$ using a representative miniband spectrum for a graphene-on-hBN superlattice, which was computed with the model developed in (*29*). The resulting conductivity is evaluated as (*26*)

$$\sigma_{xx} = \frac{4e^2}{h} \frac{\pi\varepsilon_F\tau}{h} \frac{\langle v^2 \rangle}{v_F^2}$$

where e is the electron charge, v_F is the Fermi-Dirac velocity, and h is Planck's constant (*26*). The only fitting parameter is τ, which we choose so that σ_{xx} fits the experimental values for $\phi = \phi_0/2$ (Fig. 3). For other p/q, the calculated σ_{xx} are shown by black dots. Furthermore, according to the classical magnetotransport theory (*1*–*3*), σ_{xx} near zero B_{eff} should vary as $\sigma_{xx}(B_{eff}) = \sigma_{xx}(0)/(1 + \alpha B_{eff}^2)$, where α is a p- and q-dependent

coefficient. It can be evaluated (*26*) without extra fitting parameters (narrow black parabolas in Fig. 3). One can see that the theory provides qualitative agreement for the observed experimental peaks. The derived values of τ yield $\sigma_{xx}(B = 0) \approx 20$ mS, again in qualitative agreement with experiment. It would be unreasonable to expect any better agreement because of the limited knowledge about the graphene-on-hBN superlattice potential (*20*, *29*) and the used τ approximation. The observed exponential T dependence of BZ oscillations (detailed in fig. S4) can also be understood qualitatively as arising from scattering on acoustic phonons such that the scattering length $(\propto 1/T)$ becomes shorter than the characteristic size, aq, of supercells responsible for the q-peak in conductivity (*26*).

To conclude, graphene superlattices exhibit a distinct quantum oscillatory phenomenon that can be understood as repetitive formation of different metallic systems, the BZ minibands. At simple fractions of ϕ_0, charge carriers effectively experience zero magnetic field, which results in straight rather than curved (cyclotron) trajectories. Straighter trajectories lead to weaker Hall effect and higher conductivity. The smooth background (varying over many q) is attributed to trajectories that involve transitions between different minibands and effectively become curved. The reported oscillations do not require monochromaticity, which allows them to persist up to exceptionally high T, beyond the existence of LLs. The extrapolation of the observed T dependences (fig. S4B) suggests that the quantum oscillations may be observable even at 1000 K. Further theory is required to understand details of temperature, field, and concentration dependences of BZ oscillations; the origin of the electron-hole asymmetry of phonon scattering; the behavior of higher-order fractions; and the effect of interminiband scattering, which is responsible for the non-oscillating background.

REFERENCES AND NOTES

1. N. W. Ashcroft, N. D. Mermin, *Solid State Physics* (Holt, Rinehart and Winston, 1976).
2. M. Springford, *Electrons at the Fermi Surface* (Cambridge Univ. Press, 1980).
3. C. W. J. Beenakker, H. van Houten, *Solid State Phys.* **44**, 1–228 (1991).
4. R. R. Gerhardts, D. Weiss, Kv. Klitzing, *Phys. Rev. Lett.* **62**, 1173–1176 (1989).
5. R. A. Webb, S. Washburn, C. P. Umbach, R. B. Laibowitz, *Phys. Rev. Lett.* **54**, 2696–2699 (1985).
6. K. S. Novoselov *et al*., *Science* **315**, 1379 (2007).
7. E. Brown, *Phys. Rev.* **133**, A1038–A1044 (1964).
8. J. Zak, *Phys. Rev.* **134**, A1602–A1606 (1964).
9. P. G. Harper, *Proc. Phys. Soc. A* **68**, 879–892 (1955).
10. D. R. Hofstadter, *Phys. Rev. B* **14**, 2239–2249 (1976).
11. G. H. Wannier, *Phys. Stat. Sol. B* **88**, 757–765 (1978).
12. D. Thouless, M. Kohmoto, M. Nightingale, M. den Nijs, *Phys. Rev. Lett.* **49**, 405–408 (1982).
13. A. H. MacDonald, *Phys. Rev. B* **28**, 6713–6717 (1983).
14. C. Albrecht *et al*., *Phys. Rev. Lett.* **86**, 147–150 (2001).
15. M. C. Geisler *et al*., *Physica E* **25**, 227–232 (2004).
16. S. Melinte *et al*., *Phys. Rev. Lett.* **92**, 036802 (2004).
17. L. A. Ponomarenko *et al*., *Nature* **497**, 594–597 (2013).
18. C. R. Dean *et al*., *Nature* **497**, 598–602 (2013).
19. B. Hunt *et al*., *Science* **340**, 1427–1430 (2013).
20. G. L. Yu *et al*., *Nat. Phys.* **10**, 525–529 (2014).
21. L. Wang *et al*., *Science* **350**, 1231–1234 (2015).
22. W. Yang *et al*., *Nano Lett.* **16**, 2387–2392 (2016).
23. M. Yankowitz *et al*., *Nat. Phys.* **8**, 382–386 (2012).
24. C. R. Woods *et al*., *Nat. Phys.* **10**, 451–456 (2014).
25. Z. G. Chen *et al*., *Nat. Commun.* **5**, 4461 (2014).
26. See supplementary materials.
27. K. S. Novoselov *et al*., *Nature* **438**, 197–200 (2005).
28. Y. Zhang, Y. W. Tan, H. L. Stormer, P. Kim, *Nature* **438**, 201–204 (2005).
29. X. Chen *et al*., *Phys. Rev. B* **89**, 075401 (2014).
30. N. M. Freitag *et al*., *Nano Lett.* **16**, 5798–5805 (2016).

ACKNOWLEDGMENTS

This work was supported by the European Research Council, Lloyd's Register Foundation, the Graphene Flagship, and the Royal Society. R.K.K. and E.K. acknowledge support from the Engineering and Physical Sciences Research Council, D.A.B. and I.V.G. from the Marie Curie program SPINOGRAPH, and S.V.M. from the Russian Science Foundation and National University of Science and Technology (MISiS).

SUPPLEMENTARY MATERIALS

www.sciencemag.org/content/357/6347/181/suppl/DC1
Supplementary Text
Figs. S1 to S10
References (*31*–*45*)

3 November 2016; accepted 9 June 2017
10.1126/science.aal3357

Science

High-temperature quantum oscillations caused by recurring Bloch states in graphene superlattices

R. Krishna Kumar, X. Chen, G. H. Auton, A. Mishchenko, D. A. Bandurin, S. V. Morozov, Y. Cao, E. Khestanova, M. Ben Shalom, A. V. Kretinin, K. S. Novoselov, L. Eaves, I. V. Grigorieva, L. A. Ponomarenko, V. I. Fal'ko and A. K. Geim

Science **357** (6347), 181-184.
DOI: 10.1126/science.aal3357

Heat-loving quantum oscillations

The shape of the Fermi surface in a conductor can be gleaned through quantum oscillations—periodic changes in transport properties as an external magnetic field is varied. Like most quantum properties, the phenomenon can usually be observed only at very low temperatures. Krishna Kumar *et al.* report quantum oscillations in graphene that do not go away even at the temperature of boiling water. Although "ordinary," low-temperature quantum oscillations die away, another oscillatory behavior sets in that is extremely robust to heating. These resilient oscillations appear only in samples in which graphene is nearly aligned with its hexagonal boron nitride substrate, indicating that they are caused by the potential of the moiré superlattice that forms in such circumstances.

Science, this issue p. 181

Supplementary Materials for

High-temperature quantum oscillations due to recurring Bloch states in graphene superlattices

R. Krishna Kumar, X. Chen, G. H. Auton, A. Mishchenko, S. V. Morozov, Y. Cao, E. Khestanova, D. A. Bandurin, M. Ben Shalom, A. V. Kretinin, K. S. Novoselov, L. Eaves, I. V. Grigorieva, L. A. Ponomarenko, V. I. Fal'ko, A. K. Geim

correspondence to: geim@manchester.ac.uk; v.falko@manchester.ac.uk

This PDF file includes:

Device fabrication

Our devices were made following procedures similar to those described previously (*31*). First, an hBN/graphene/hBN stack was assembled using the dry-peel technique (*32*). This involved mechanical cleavage of graphite and hBN on top of an oxidized silicon wafer, after which graphene monolayers and relatively thick (30-70 nm) hBN crystallites were identified using an optical microscope. The crystals were picked up from the substrate using a polymer membrane attached to the tip of a micromanipulator to assemble a three-layer stack such that graphene was encapsulated between two hBN crystals. Both graphene and hBN cleave preferentially along their main in-plane crystallographic axes, which often results in crystallites having relatively long and straight edges. Such edges were used to align graphene with respect to the bottom hBN using a rotational stage and by controlling the procedure under an optical microscope. The resulting accuracy of alignment was ≈ 1.5° (*33*). The top hBN crystal was misaligned intentionally to avoid possible contribution from a competing moiré potential (*18, 20*). The resulting heterostructure was placed on top of an oxidized silicon wafer (*n*-doped Si with SiO_2 thickness of either 90 or 290 nm) which served as a back gate. The next step involved electron beam lithography to make windows in a polymer mask, which defined contact regions to graphene. Reactive ion etching was employed to mill trenches in the heterostructure using these windows, which exposed the graphene monolayer. Metallic contacts (3 nm Cr/ 80 nm Au) were evaporated into the trenches, which was followed by lift-off of the polymer mask. This procedure prevented contamination of exposed graphene edges with polymer residues, resulting in high-quality contacts (*31*). Finally, another round of lithography and ion etching was used to define a device in the multiterminal Hall bar geometry (fig. S1). The Hall bars had typical widths of 1–4 μm and lengths 10–20 μm.

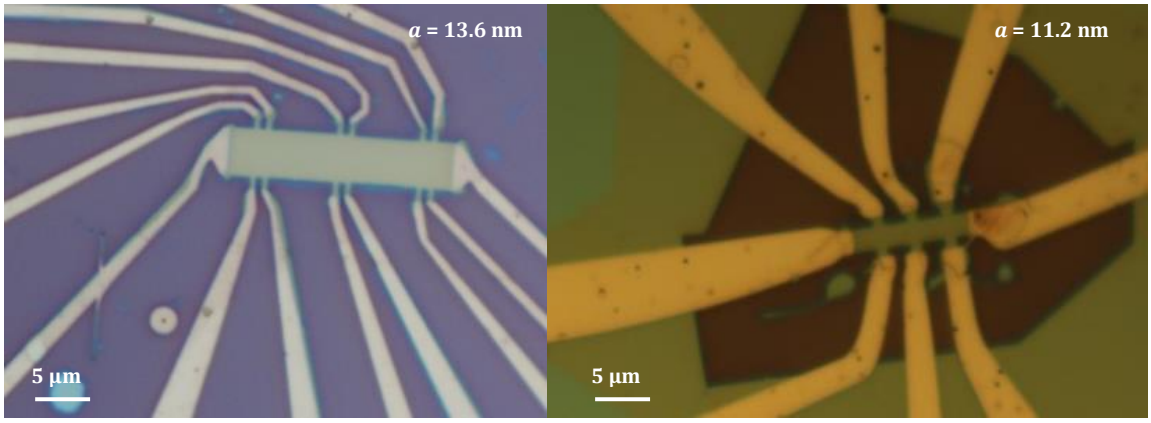

Fig. S1. Experimental devices. Optical images of two of our devices. Their superlattices had periodicities a specified on the photos, as evaluated from the position n_0 of the second-generation NPs.

Further examples of Brown-Zak oscillations

BZ oscillations are found to be a universal feature of graphene superlattices. To show this, fig. S2 mirrors the presentation of Figs. 1A-B but uses a different superlattice device with a shorter a (that is, larger n_0). Again, one can see that, in the reference device, quantum oscillations become rapidly suppressed and practically disappear already at 50 K. In contrast, the graphene superlattice exhibits oscillations that remain clearly visible at room T in fields as low as 2.5 T. For this particular carrier concentration $n \approx 0.6n_0$, the amplitude of oscillations varies non-monotonically with increasing temperature. Below 3 T, the SdH oscillations are completely washed out at 50 K whereas the BZ oscillations emerge only at 100 K, seemingly growing with increasing T. We attribute this nonmonotonic dependence to beatings between the SdH and BZ oscillations. On the Landau fan diagrams this corresponds to fields and concentrations where minima in σ_{xx} due to Landau quantization cross the conductivity maxima due to the formation of BZ minibands (see Fig. 2).

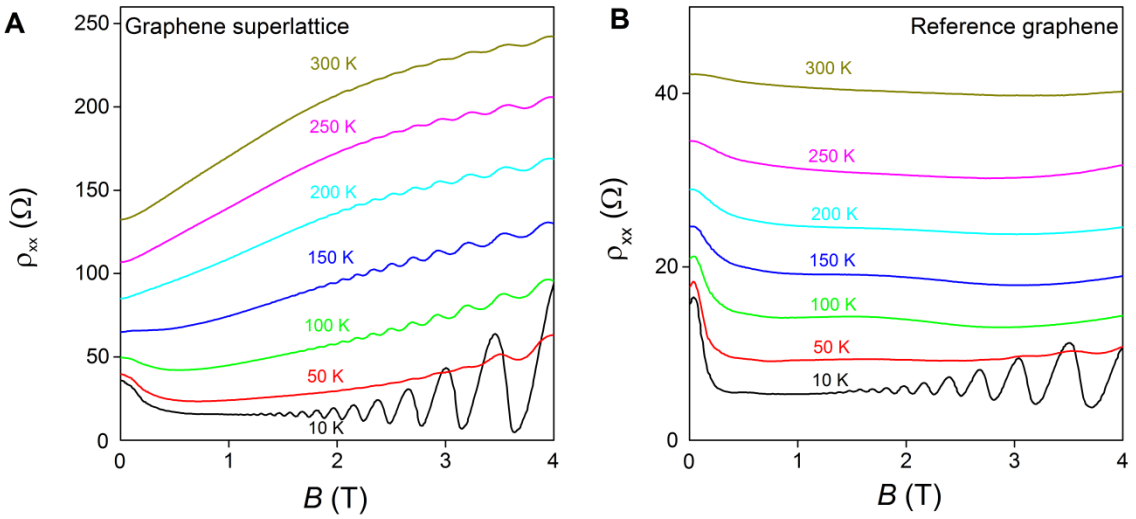

Fig. S2

Emergence of Brown-Zak oscillations with increasing temperature. (**A**) $\rho_{xx}(B)$ for a graphene superlattice with $a \approx 11.2$ nm ($n_0 \approx 3.5\times10^{12}$ cm^{-2}) at various T. (**B**) Same for the reference graphene device. For both plots, $n \approx 2.2\times10^{12}$ cm^{-2}.

Frequency of Brown-Zak oscillations

BZ oscillations are periodic in $1/B$ (Figs. 2E-F & figs. S3-S4), so that at small amplitudes they can be described by $\cos(2\pi B_0/B)$. Their frequency B_0 was found to be independent of n but varied from sample to sample (fig. S3B). This is attributed to different periodicities a of the moiré pattern in different devices, which is caused by random, slightly different alignment between the crystallographic axes of the graphene and bottom hBN lattices (*17-25*). For our devices, a varied between ≈11.2 and 14.2 nm and could readily be evaluated from the carrier concentration n_0 at which second-generation NPs occurred. Indeed, the NPs occur if the lowest electron or highest hole minibands are fully occupied, which correspond to 4 charge carriers per superlattice unit cell with area S (*17-25,30,34*). This leads to the equation $n_0 = 4/S = 8/\sqrt{3}a^2$, which relates n_0 and a.

Examples of BZ oscillations with different frequencies are shown in fig. S3. One can see that the oscillations are fastest (largest B_0) for the device with the shortest period a (largest n_0). The inset of fig. S3B summarizes the observed behavior $B_0(n_0)$ using data for all the studied devices. These are the same data set as in Fig. 2C of the main text but the specific devices from figs. S3A-B are now indicated by arrows. The experimental dependence is accurately described by the equation $B_0 = \phi_0/S$ or, equivalently, $B_0 = \phi_0 n_0/4$. This means that maxima of BZ oscillations in σ_{xx} occur exactly at $B = \phi_0/qS$.

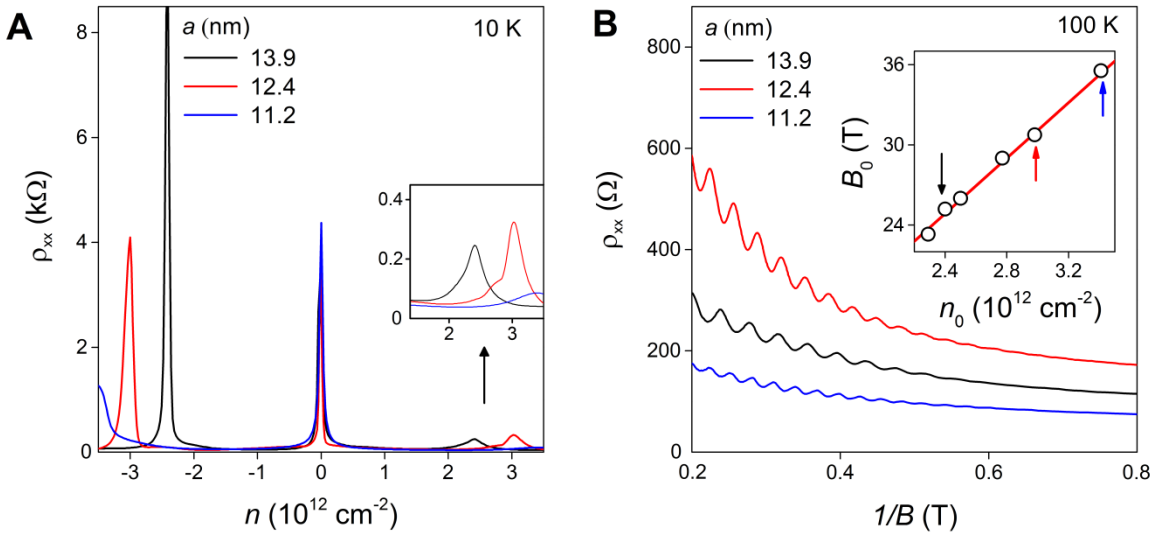

Fig. S3

Frequency of Brown-Zak oscillations for different graphene superlattices. (**A**) Examples of characterization of our superlattice devices. The second-generation NPs are found at $\pm n_0$ which can be translated into the values of a and S for the superlattices (*17-25*). Inset: Behavior near the electron NPs is magnified. (**B**) BZ oscillations for the three devices in (A) at approximately the same normalized density $n/n_0 \approx 0.75$. Inset: Frequency B_0 of the BZ oscillations for all our superlattice devices as a function of the position of their NPs (symbols). This includes the devices in (A,B) as indicated by the color-coded arrows. Red line: Expected dependence $B_0 = \phi_0 n_0/4$. B_0 corresponds to the last maximum in σ_{xx} that should appear at one ϕ_0 per superlattice unit cell.

Amplitude of BZ oscillations

At low T and high B, BZ and SdH oscillations coexist, which not only makes it difficult to find out a functional dependence for BZ oscillations but also leads to such abnormalities as the nonmonotonic T dependence of the overall amplitude of quantum oscillations, as discussed for the case of fig. S2. Therefore, to examine behavior of BZ oscillations quantitatively, we have focused on high T and relatively low B where the contribution of SdH oscillations is small. In addition, SdH oscillations in graphene are suppressed with increasing n because cyclotron gaps become smaller with increasing ε_F (*28,29*). Accordingly, we studied functional dependences of BZ oscillations at n above the second-generation NP. In this regime, BZ oscillations also become stronger (Fig. 2C, fig. S6) so that we could accurately measure their amplitude over a wide range of T. Examples of the observed T and B dependences are shown in fig. S4. The measured amplitude of the BZ oscillations, $\Delta\sigma_{xx}$, is plotted in fig. S4B as a function of T for different B up to 5 T. This covers a range of rational fluxes described by

q from 5 up to 37. One can see that $\Delta\sigma_{xx}$ changes exponentially over two orders of magnitude, suggesting the functional dependence $\Delta\sigma_{xx} \propto \exp(-T/T^*)$ where T^* is a constant.

With regard to the field dependence, fig. S4B shows that the BZ oscillations decay slower with *T* for higher *B*. For *T* > 200 K where the effect of cyclotron gaps is negligible, the BZ oscillations became small enough and practically sinusoidal. In this regime, we find that their amplitude $\Delta\sigma_{xx}$ can be described accurately as an exponential dependence on 1/*B* (fig. S4C). Therefore, the experiments suggest that the amplitude of BZ oscillations has the functional form $\ln(\Delta\sigma_{xx}) \propto -T/B$.

Qualitatively, this dependence can be understood as follows. BZ oscillations arise due to spatial quantization at the length scale $L \approx aq \equiv aB_0/B$, which involves *q* unit cells in the makeup of the magnetic miniband arising for $B = \phi_0/qS$ (*7,8,30,34*). As long as Bloch wavefunctions of this miniband are not completely randomized by scattering, the miniband electronic structure is expected to affect transport properties of a graphene superlattice. Over the *T* range of our experiments, electron collisions on acoustic phonons are known to be the dominant scattering mechanism. It is described by a mean free path $\ell \propto 1/T$. For small amplitude of oscillations, it is reasonable to assume that $\Delta\sigma_{xx}$ is an exponential function of the dimensionless parameter, L/ℓ, which translates into $\ln(\Delta\sigma_{xx}) \propto -aTB_0/B \propto -T/B$, in agreement with the experiment. Further theoretical analysis and modeling are required to explain the observed *T* and *B* dependence quantitatively.

As discussed in the main text, we had to limit the *T* range in our experiments in order to avoid irreversible damage of our devices. Nonetheless, let us note that, by extrapolating the dependences of fig. S4B to higher *T* (for example, consider the 5T curve in this figure), one can find that BZ oscillations should in principle be observable up to 500 K ($\Delta\sigma_{xx}$ extrapolates to >0.01 mS). This consideration agrees well with Fig. 1C, where the oscillations are clearly seen at 373 K below 4 T. Moreover, in the latter case, $n < n_0$ and, therefore, BZ oscillations are weaker than those for *n* above the second-generation NP (Fig. 2C). The observed *T*/*B* functional form for the oscillation amplitude suggests that increasing *B* to 10 T (by a factor of 2) should result in the same $\Delta\sigma_{xx}$ > 0.01 mS at 1,000 K. However, electron-electron scattering increases with temperature as T^2 and, for graphene, the corresponding mean free path is expected to reach a 10-nm scale close 1,000 K, too. Therefore, we conservatively estimate that the widely available magnets with *B* = 16 T should allow the observation of BZ oscillations at approximately 1,000 K, assuming that no additional scattering mechanism is unexpectedly activated above 400 K.

Density of states in graphene superlattices

Graphene devices are known to exhibit strong dependence of their differential capacitance *C* on gate voltage, which is due to both graphene's low DOS and the use of nanometer thin dielectric layers between graphene and the gate (*20,35,36*). The latter minimizes a contribution from the classical (geometric) capacitance making it easier to measure the quantum capacitance due to the varying DoS. Capacitance measurements were previously employed to study the DoS in pristine graphene (*35,36*) and, more recently, in graphene superlattices at low *T* (*20*). Using the same technique and experimental procedures as those described in (*20*), we studied the DoS for several superlattice devices. Examples of the measured Landau fan capacitance diagrams *C*(*B,n*) are shown in fig. S5. Cyclotron gaps appear in the diagrams as black stripes (minima in *C*). At low *T*, LLs are seen fanning out from the main and second-generation NPs. The latter cyclotron gaps are more pronounced for holes than electrons. Intersections of main and second-generation LLs result in third-generation NPs, near which the replica quantum Hall ferromagnetism was reported (*20*). The low-*T* behavior of the DoS in graphene superlattices (fig. S5A) agrees well with that reported previously (revealing the Hofstadter butterfly spectrum) and, therefore, we refer to (*20*) for further explanations.

Taking into account that, in transport experiments, BZ oscillations become better resolved at elevated *T*, we have extended the capacitance measurements into the high-*T* regime. As expected, cyclotron gaps in the DoS become smeared with increasing *T*. Only the largest gaps for the main spectrum plus the DoS minima originating from the second-generation NP for hole doping could be observed at 100 K (fig. S5B). Importantly, no sign of horizontal streaks can be discerned in fig. S5, not only at high but also at low *T*. This is in stark contrast to transport measurements where such streaks that correspond to BZ oscillations are always present on Landau fan diagrams (Fig. 2, fig. S7A).

In more detail, fig. S5C shows *C*(*B*) curves at several *T* for fixed *n* near the second-generation NP for electrons, where BZ oscillations are strongest in transport experiments. No oscillatory behavior is noticeable in the capacitance measurements above 100 K. At 200 K, there is no sign left of the LL minimum even at 15 T. For comparison, fig. S5D plots ρ_{xx} measured at the same *T*: BZ oscillations appear already at $B < 3$ T. To summarize, no signatures of *n*-independent oscillations were found in the DoS at any *T* and *B*, which strongly suggests that the high-*T* oscillations observed in transport characteristics are not due to any extra gaps in the electronic spectra of graphene superlattices.

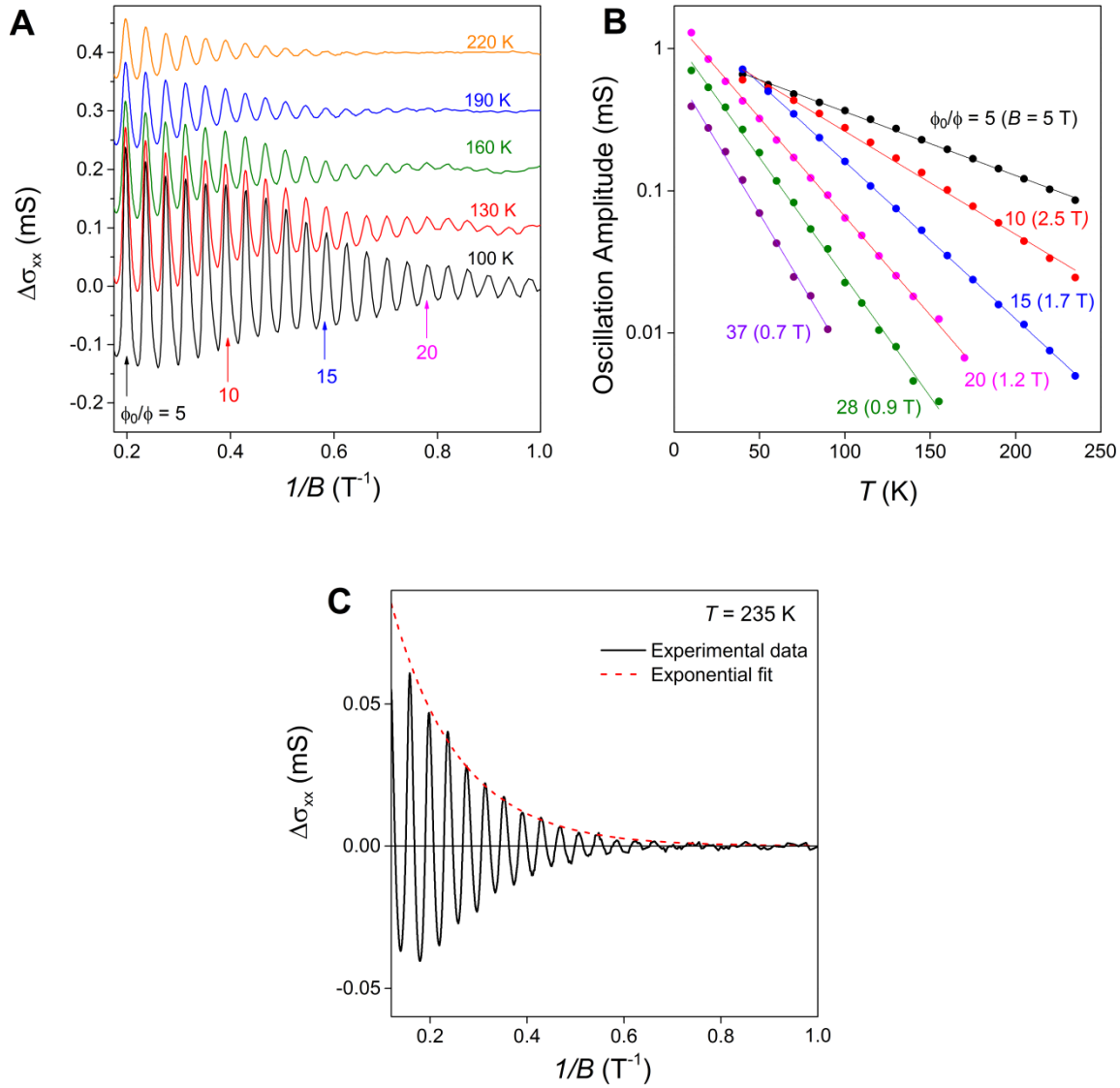

Fig. S4

Temperature and field dependence of Brown-Zak oscillations. (**A**) Examples of $\Delta\sigma_{xx}$ as a function of $1/B$ at different T for our superlattice device with $a \approx 13.6$ nm ($n_0 \approx 2.5\times10^{12}$ cm^{-2}). The presented curves are for $n \approx 2.9\times10^{12}$ cm^{-2}. For clarity, the curves are shifted vertically by 0.1 mS. (**B**) Detailed T dependence of the oscillation amplitude. Some of the maxima are marked by their q and color-coded in (A). (**C**) At high T, BZ oscillations decay exponentially as a function of $1/B$.

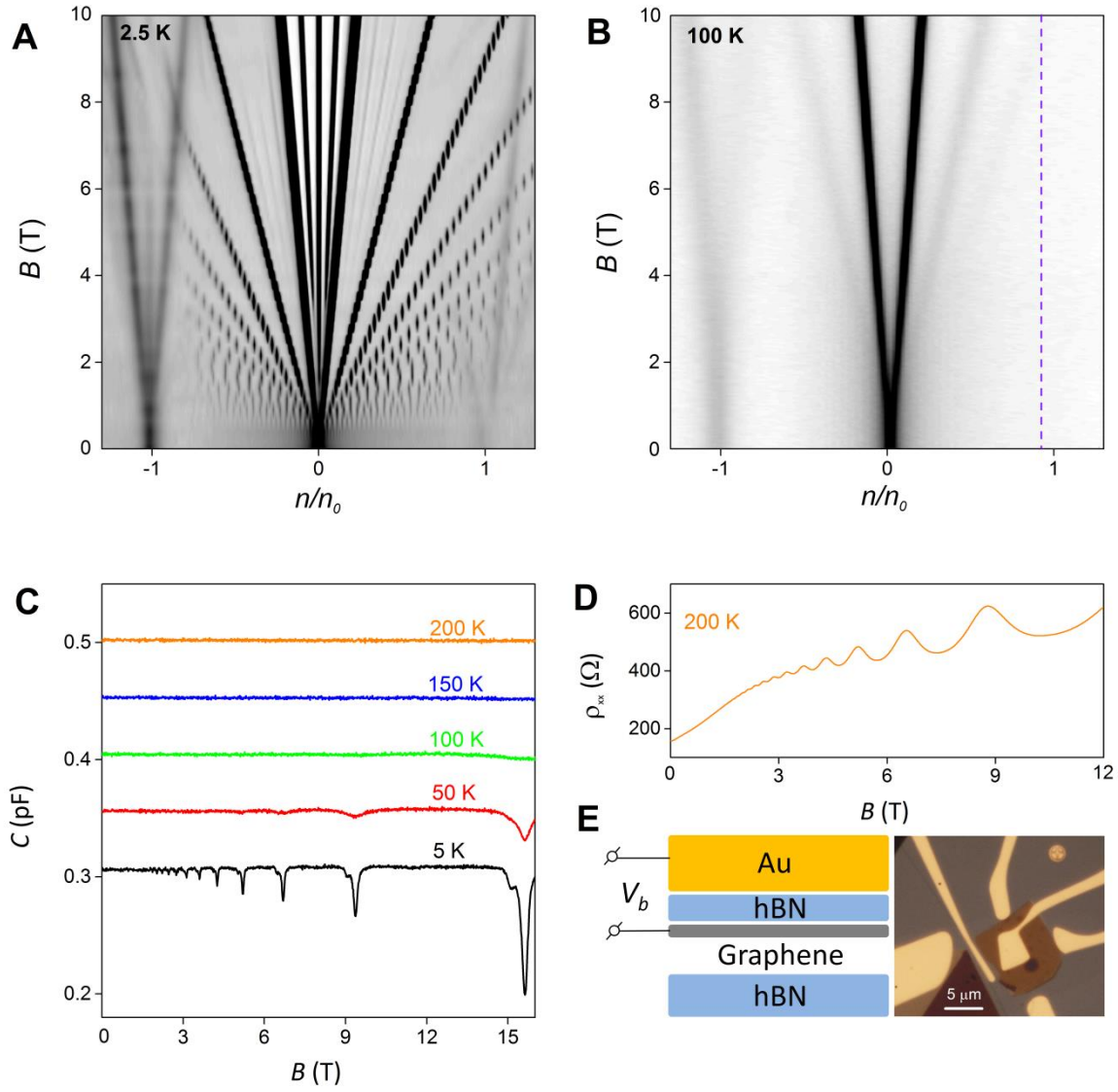

Fig. S5

Differential capacitance for graphene superlattices. (**A**) Low-*T* Landau fan diagram $C(n,B)$ for a capacitor with $a \approx 13.5$ nm. Grey linear scale: black 0.266 pF; white 0.293 pF. (**B**) Same as in (A) but at 100 K. Scale: black 0.328 pF; white 0.357 pF. (**C**) Examples of $C(B)$ for the fixed $n \approx 2.3\times10^{12}$ cm^{-2} ($n/n_0 \approx 0.9$) which corresponds to the purple dashed line in (B). The curves are shifted vertically for clarity. (**D**) $\rho_{xx}(B)$ for a Hall bar device with $a \approx 13.9$ nm and measured at the same n and T as the orange curve in (C). (**E**) Schematic and optical image of one of our capacitance devices. For details, see (*20*).

Higher-order BZ oscillations

At electron concentrations beyond the second-generation NP, additional features were found in the transport properties of graphene superlattices at elevated *T*. Extra maxima could be discerned in Fig. 2E (arrows) but they are even better resolved in fig. S6A where *n* was increased to $\approx 2n_0$, close to the highest concentration accessible for our devices. In addition, fig. S6B plots both σ_{xx} and σ_{xy} in this regime at a slightly lower *T* of 100 K to enhance the extra features. The maxima in σ_{xx} align with smeared step-like features in σ_{xy}. Their positions correspond to $B = p\phi_0/qS$ where p = 2 and 3, as indicated by the dotted curves and blue arrows, respectively. We attribute these transport anomalies to the formation of Brown-Zak minibands for the case where *p* flux quanta penetrate through *q* unit cells (*7,8,30,34*). The features are weaker than those for unit fractions ϕ_0/q in the same range of *B* because *p* times larger areas are involved in their formation (*7,8*). This is in agreement with the above discussion of the amplitude of BZ oscillations, which decays exponentially with the involved length scale $L \approx apq$.

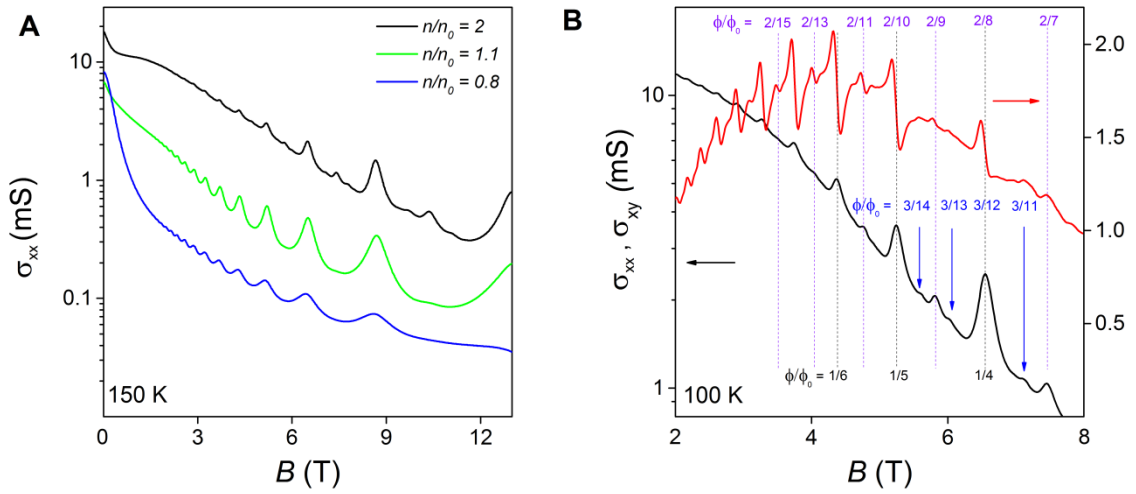

Fig. S6

Fractal BZ oscillations. (**A**) High-*T* conductivity in graphene superlattices with increasing *n* beyond the second-generation NP for electrons. The same device as in Fig. 2 ($a \approx$13.9 nm). New features are seen to appear on the curve with $n = 2n_0$. The logarithmic scale is used to amplify the additional maxima in σ_{xx} against the background. (**B**) Comparison of the extra features in σ_{xx} with those in σ_{xy}. The electron density is $2n_0$.

BZ oscillations for hole doping

It is well established that the DoS in graphene-on-hBN superlattices is modified stronger for the valence than conduction band (*17,25,34*). The resulting electron-hole asymmetry is also clearly seen in our present devices where cyclotron gaps in the DoS (figs. S5A-B), the second-generation NPs (fig. S3A) and LLs in σ_{xx} at low *T* (Fig. 2A) are most pronounced for hole doping. In contrast, BZ oscillations are more visible for electrons rather than holes (Fig. 2B) and, accordingly, the main text focused on the results obtained for electron doping (positive *n*). To emphasize the generality of this 'reversed' electron-hole asymmetry, figs. S7A-B show data similar to those of Fig. 2 but for another superlattice device ($a \approx 13.6$nm).

From the experimental point of view, the origin of the unexpected asymmetry becomes clear if we look closer at the *T*-dependence of scattering in graphene-on-hBN superlattices. To this end, fig. S7C plots ρ_{xx} as a function of electron and hole doping at different *T*. The resistivity grows faster with increasing *T* for the valence band compared to the conduction band. The behavior is quantified in fig. S7D using the fixed concentrations $n/n_0 \approx \pm 0.7$ for electrons and holes. One can see that electron-phonon scattering evolves linearly with *T* and is approximately 4 times stronger for holes than electrons. It is also clear from fig. S7D, that superlattice effects strongly enhance phonon scattering with respect to pristine graphene. Indeed, the reference devices (encapsulated but non-aligned graphene) exhibit one-to-two orders of magnitude weaker phonon scattering. Because the amplitude of BZ oscillations depends exponentially on the mean free path ℓ (fig. S4), it is hardly surprising that, at elevated *T*, the oscillations are more strongly suppressed for hole doping. The asymmetry of electron-phonon scattering is apparently caused by the moiré pattern and has not been noted previously (*17-25*). The asymmetry's origin is likely to be specific to graphene-on-hBN superlattices and remains to be understood.

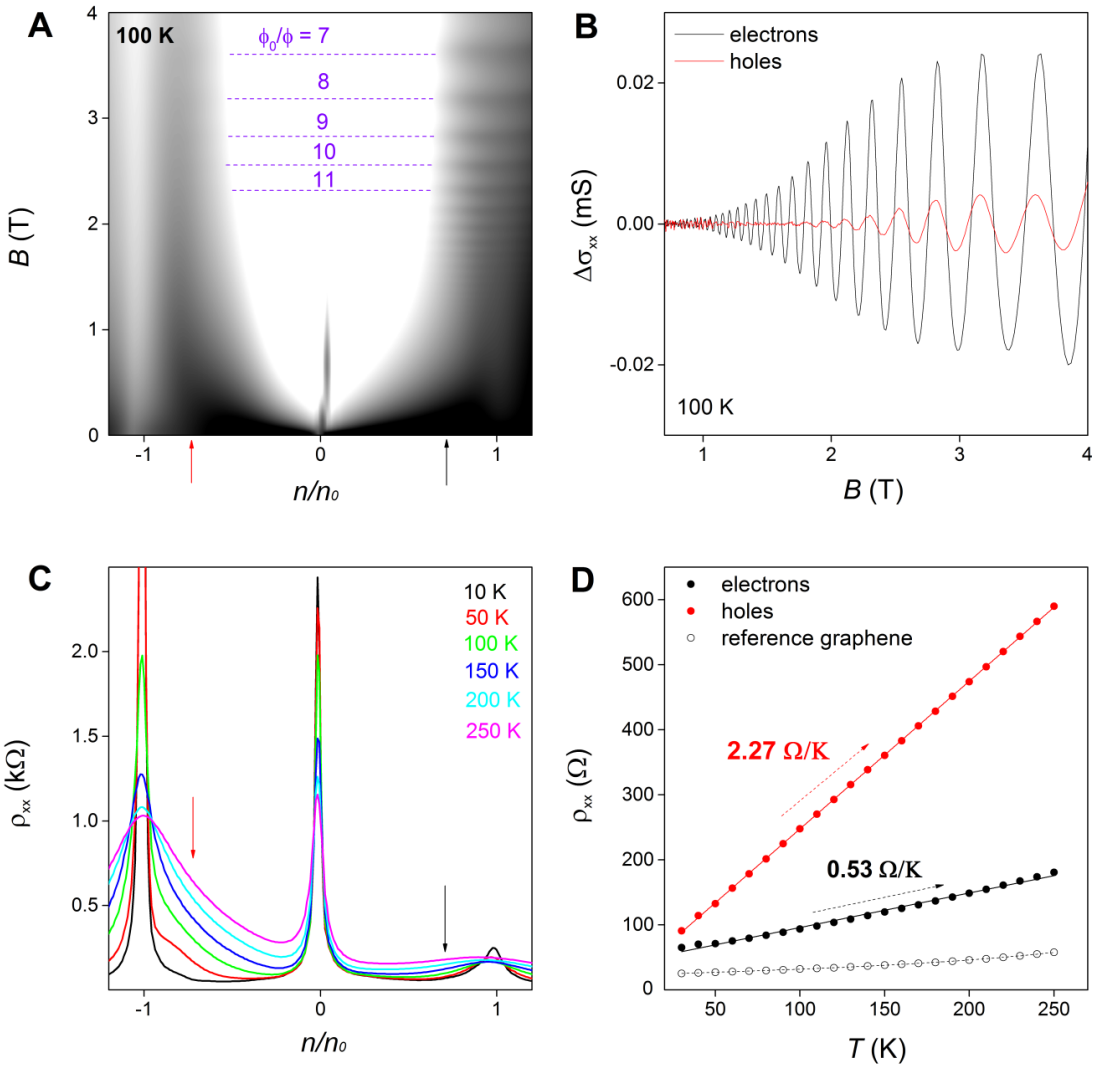

Fig. S7

Electron-hole asymmetry of Brown-Zak oscillations. (**A**) σ_{xx} as a function of n and B, similar to Fig. 2B but for a superlattice device with a ≈13.6 nm. The grey scale is logarithmic: white 0.09mS; black 5mS. (**B**) After subtracting a smooth background, $\Delta\sigma_{xx}(B)$ is plotted for the fixed $n \approx \pm 1.7\times10^{12}$ cm^{-2} [$n/n_0 \approx \pm 0.7$]. These electron and hole concentrations are marked by the black and red arrows in (A), respectively. (**C**) ρ_{xx} for the same device as a function of n at various T in zero B (the curves are color coded). The resistivity increases with T faster for holes than electrons and much faster than in reference devices. (**D**) Detailed T-dependence for electrons and holes at the same n as in (B). Dots – experiment; lines – best linear fits. Values for the linear slopes are shown next to the curves. For comparison, T-dependence found in the reference device is plotted for the same concentration (open circles). In non-aligned devices, electrons and holes exhibit similar T-dependences (*28,29*).

Brown-Zak magnetic minibands

Let us consider graphene's spectrum modified by the presence of a moiré potential induced by the hBN substrate. We use a hexagonal Bravais lattice $n_1\vec{a}_1 + n_2\vec{a}_2$ with the superlattice period $a = a_1 = a_2$. In magnetic fields, $B = B_{p/q} = p\phi_0/qS$, magnetic minibands are formed (*7,8*). To describe these minibands, we employ the phenomenological model developed in (*30,34*) and based on the Hamiltonian

$$\hat{H} = v_F\vec{p}\cdot\vec{\sigma} + u_0^+ f_+ + \xi\sigma_3 u_3^+ f_- + \frac{\xi}{b}u_1^+\vec{\sigma}\cdot[\vec{\ell}_z\times\nabla f_-],$$
$$f_\pm = \sum\nolimits_{m=1\ldots6}(\pm1)^{m+\frac{1}{2}}e^{i\vec{b}_m\cdot\vec{r}} \quad , \qquad \text{(S1)}$$

where σ_i are the Pauli matrices acting on the sublattice Bloch states $(\phi_{\mathrm{AK}}, \phi_{\mathrm{BK}})^T$ in the K valley ($\xi = 1$) and $(\phi_{\mathrm{BK'}}, -\phi_{\mathrm{AK'}})^T$ in the K' valley ($\xi = -1$). $f_\pm$ are six Bragg vectors $\vec{b}_m$ ($b_{1,2,3,4,5,6} = b = \frac{4\pi}{\sqrt{3}a}$) of the superlattice. The effect of magnetic field is incorporated in (S1) as $\vec{p} = -i\hbar\nabla + e\vec{A}$ where the vector potential $\vec{A} = \frac{Bx_1}{a\sqrt{3}}(2\vec{a}_2 - \vec{a}_1)$ is written in the hexagonal (non-orthogonal) coordinate system (x_1, x_2) such that $\vec{r} = x_1\vec{a}_1 + x_2\vec{a}_2$, which was adapted for the case of hexagonal superlattices (*34*).

The miniband spectrum plotted in fig. S8 was obtained using the computational procedure developed in (*34*). In our modelling, we chose $u_0^+ = 21.7$ meV, $u_1^+ = -30.6$ meV and $u_3^+ = -22.2$ meV, which are to be compared with $v_g b_m = 357$ meV, the case of perfectly matching graphene and hBN lattices. The resulting spectrum displays the same features as discussed earlier (*34,37-42*) using various models for graphene-hBN coupling:

i. At $\phi \ll \phi_0$, minibands converge into LLs separated by the cyclotron gaps $\sim\hbar\omega_c$ which are large for massless Dirac fermions in graphene.

ii. Individual minibands are systematically wider at unit fractions $\phi = \phi_0/q$ compared to nearby rational flux values. Minibands are q-fold degenerate and dispersed over a Brillouin zone with the area, $S_{\mathrm{BmZ}} = \frac{8\pi^2}{3\sqrt{3}}(qa)^{-2}$.

iii. If intervals $\frac{1}{q+1}\phi_0 < \phi < \frac{1}{q}\phi_0$ for different q are compared, the sparsity of the spectrum increases upon increasing q. Minibands for unit fractions $1/q$ are widest, followed by the sequence $2/q$ that exhibits somewhat narrower bands and, then, by the $3/q$ sequence.

iv. Away from the unit fractions, minibands bunch so that they can be described as LLs for third-generation Dirac fermions (*20,34*). These LLs are effectively the response of the BZ minibands to the effective magnetic field $B_{\mathrm{eff}} = B - B_{1/q}$, with the gaps set by the corresponding effective cyclotron energies $\sim\hbar\omega_c^{eff}(B_{eff})$.

The spectrum in fig. S8 is generic (*30,34*), and we use it below to explain only the qualitative features expected for electron transport in graphene superlattices.

Magnetotransport in Brown-Zak minibands

At low temperatures, $kT \ll \hbar\omega_c, \hbar\omega_c^{eff}$, the hierarchy of gaps in the Hofstadter spectrum manifests itself in a sequence of incompressible quantum Hall states, which were studied earlier using magnetotransport and magnetocapacitance measurements (*17-22*). High temperatures, $kT \gg \hbar\omega_c$, smear the Fermi step over several minibands, and this makes measurements insensitive to the presence of even large spectral gaps, leaving aside extra gaps due to the superlattice potential. In the high-*T* regime, magnetotransport reflects the hierarchy of the width of magnetic minibands. Indeed, elastic diffusion of electrons in wider minibands should generate larger σ_{xx} than in narrower minibands, resulting in magneto-oscillations periodic in 1/*B* where maxima in σ_{xx} occur at $B = B_{\frac{1}{q}}$, the fields with widest minibands. Additional weaker maxima appear for $p > 1$, where minibands exhibit weaker broadening. The resulting oscillations can sustain higher *T*, compared to SdH oscillations, and be less sensitive to charge carrier inhomogeneity because they rely not on cyclotron gaps but, importantly, on the stability of the magnetic miniband structure and Bloch wavefunctions.

To describe the high-*T* oscillations, we use the τ-approximation with a single τ and analyse the Boltzmann equation

$$\frac{\partial f}{\partial t} + e(\vec{E} + B\vec{l}_z \times \vec{v}) \cdot \nabla_p f + \vec{v} \cdot \nabla f = -\frac{1}{\tau}[f - f_F] \qquad \text{(S2)}$$

where the occupancy for the plane-wave states $\vec{p}$ across Brillouin minizones with each '*n*-th' BZ miniband for a particular fraction *p/q* is described by the distribution function $f(\vec{p}, n)$. In the linear response regime such that $f - f_F \propto E$ (where f_F is the Fermi function at the base *T*), analysis can be performed using the Taylor expansion in powers of the effective magnetic field $B_{eff} = B - B_{\frac{1}{q}}$. Therefore, we write $f - f_F = f_1^{(0)} + B_{eff} f_1^{(1)} + B_{eff}^2 f_1^{(2)}$. By solving eq. (S2) using iterations in powers of B_{eff}, we find that

$$f - f_F = -\tau e\vec{E} \cdot \vec{v}\partial_\epsilon f_F + e^2 B\tau\left(\vec{l}_z \times \vec{v}\right) \cdot \nabla_p \left(\tau e\vec{E} \cdot \vec{v}\partial_\epsilon f_F\right)$$

$$-e^3 B^2 \tau(\hat{l}_z \times \vec{v}) \cdot \nabla_p(\tau(\hat{l}_z \times \vec{v}) \cdot \nabla_p(\tau e\vec{E} \cdot \vec{v}\partial_\epsilon f_F)).$$

Using the relation between dissipative conductivity $\sigma \equiv \sigma_{xx} = \sigma_{yy}$ (as prescribed by the hexagonal symmetry) and the Joule heating, we obtain

$$E^2\sigma = \vec{E} \cdot \vec{j} = 4e\sum_n \int_{\mathrm{BmZ}} \vec{E} \cdot \vec{v} f(\vec{p}, n) \frac{d^2p}{(2\pi\hbar)^2}, \qquad \text{(S3)}$$

and express it in terms of the band structure parameters computed for a group of *N* minibands in Brown-Zak spectrum at each $\phi = \frac{p}{q}\phi_0$

$$\langle F \rangle = \frac{1}{NS_{\mathrm{BmZ}}} \sum_n \int_{\mathrm{BmZ}} F(\vec{p}, n) \frac{d^2p}{(2\pi\hbar)^2}. \quad \text{(S4)}$$

We then use average values of the relevant band parameters that emerge from the iterative solution of eq. (S2) and are evaluated for the numerically computed miniband spectra for the model in eq. (S1). Eq. (S4) can be further simplified using the relation

$$\sum_n \int_{\mathrm{BmZ}} F(\vec{p}, n) \frac{d^2p}{(2\pi\hbar)^2} \to \langle F \rangle \int \gamma(\varepsilon) \partial_\varepsilon f_F d\varepsilon = \langle F \rangle \gamma(\varepsilon_F) \,,$$

which is based on the fact that, at the energy scale extended over several minibands, the DoS for the 'smeared' spectrum can be approximated by the DoS in the unperturbed graphene, $\gamma(\varepsilon_\mathrm{F}) = \frac{2\varepsilon_\mathrm{F}}{\pi\hbar^2 v_\mathrm{F}^2}$. This leads to

$$\sigma = \frac{2e^2}{h} \frac{\varepsilon_\mathrm{F}\tau}{\hbar} \left[\frac{\langle v^2 \rangle}{v_\mathrm{F}^2} + e^2 B^2 \tau^2 \frac{\langle \sum_{i=x,y} \left([\vec{v} \times \nabla_p]_z v_i \right)^2 \rangle}{v_\mathrm{F}^2} \right] \quad \text{(S5)}$$

which takes into account all valley and spin states. We evaluate mean values, $\langle v^2 \rangle$ and $\langle \sum_{i=x,y} \left([\vec{v} \times \nabla_p]_z v_i \right)^2 \rangle$, by averaging the computed values over several minibands as illustrated in the inset of Fig. 3 and in fig. S8.

It is interesting to note that BZ oscillations can also be expected in diamagnetic response of superlattices, not only in their electron transport. Indeed, each BZ miniband effectively represents a distinct metallic system and, therefore, should exhibit specific diamagnetism. By changing magnetic field, one can sample these different states and is expected to observe a varying diamagnetic response with the periodicity $B = p\phi_0/qS$. This would be a de Haas – van Alphen -like effect but without Landau quantization. Such an analogue of BZ oscillations in magnetization seems to have been observed in recent tight-binding calculations (*43*), reflecting the recurring formation of different Bloch states.

Why have Brown-Zak oscillations remained unnoticed until now?

There have been a number of experimental reports studying magnetotransport properties in aligned graphene-on-hBN devices (*17-22,25*). These included measurements at elevated *T*. We believe that the reason why these high-*T* oscillations have not been noticed earlier is partly due to the way in which Landau fan diagrams and *B* dependences are usually measured for graphene devices. This involves sweeping gate voltage whereas other variables such as *B* and *T* are fixed. From the experimental point of view, this approach is most convenient. However, in such measurements, it is also easy to miss even very strong BZ oscillations, as illustrated in fig. S9. At low *T*, ρ_{xx} for both

superlattice and reference devices in fig. S9 exhibits multiple minima (SdH oscillations). In contrast, only peaks at the NPs survive at high *T*. Otherwise, ρ_{xx} curves are featureless for both devices, with no sign of BZ oscillations even though they are quite pronounced if *B,* rather than *n,* is swept at a given *T* (cf. fig. S5D). This is because BZ minibands appear and disappear as a function of flux per superlattice unit cell and, unlike SdH oscillations, do not vary with *n*.

We expect that BZ oscillations are not unique to graphene-on-hBN and can be observed for other moiré superlattices. A particularly promising candidate is twisted bilayer graphene that was reported to exhibit clear superlattice effects (see, e.g., refs. *44-45*).

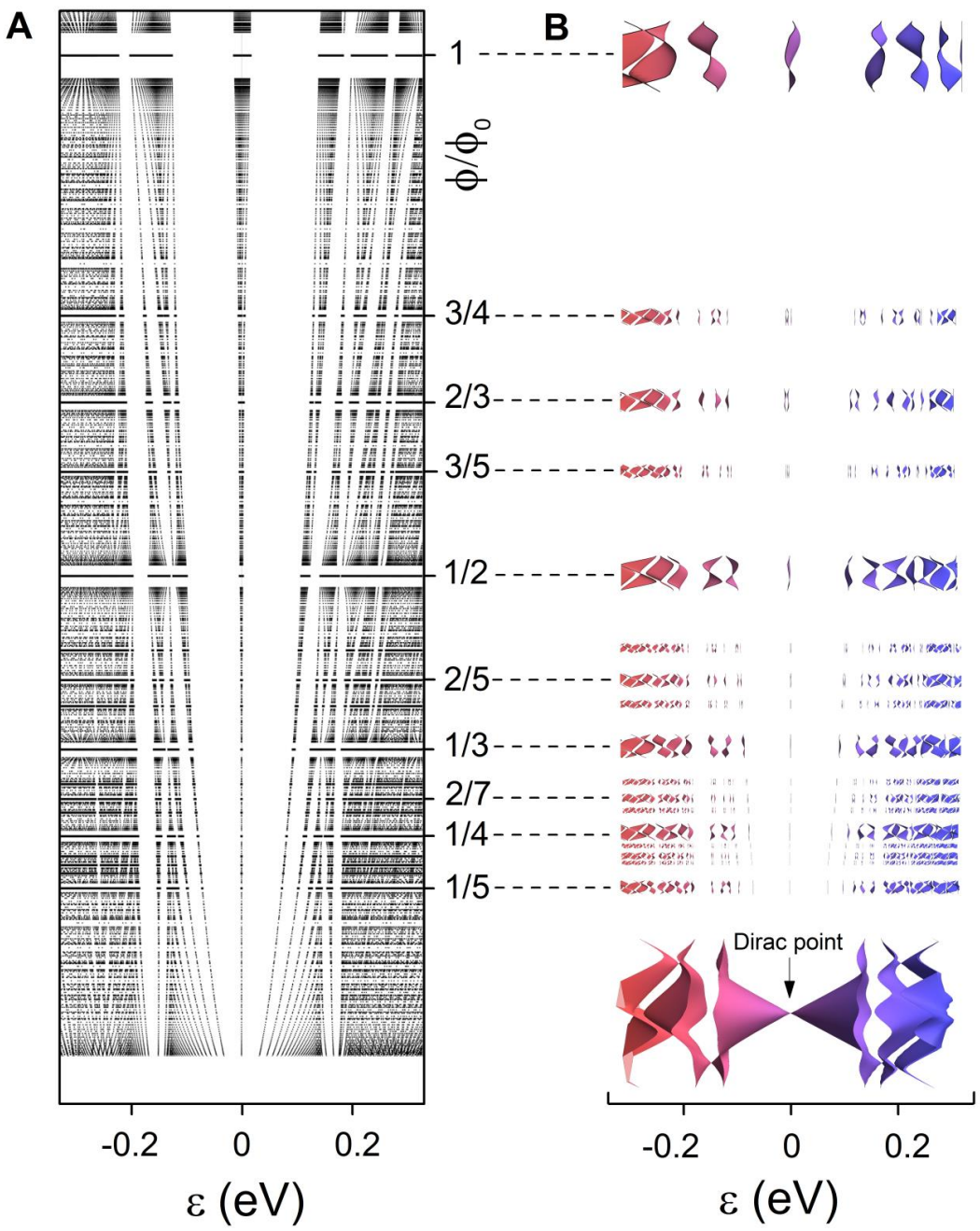

Fig. S8

Spectra of graphene superlattices in magnetic field. (**A**) Bands and gaps in the Hofstadter spectrum. Black dots: States calculated for numerous simple fractions p/q. The horizontal white stripes correspond to missing data because of computational limitations [for details, see (*30,34*)]. (**B**) Dispersions $\varepsilon(\vec{k})$ in magnetic mini-bands that appear exactly at $\phi/\phi_0 = p/q$ for some q = 1 to 5 and p = 1 to 3. The electronic spectra are aligned vertically against the corresponding values of ϕ/ϕ_0 in (A) but show the dispersion against k_x and k_y within the first Brillouin minizones (similar to the case of the inset in Fig. 3). The lowest inset to the right is the superlattice's modified Dirac spectrum in zero B (*30*).

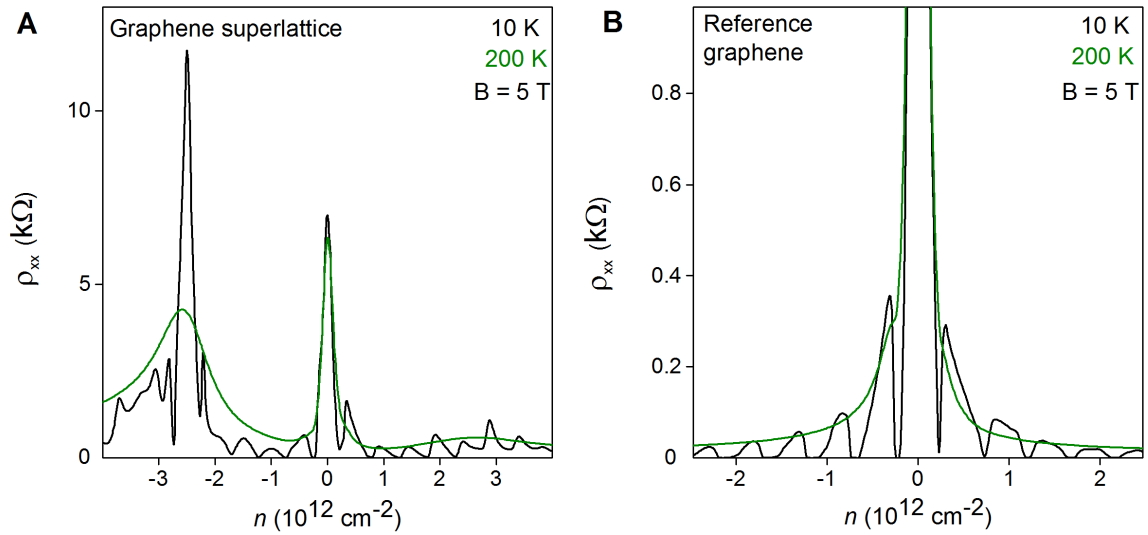

Fig. S9

Standard approach to measuring resistivity for graphene devices. (**A** and **B**) Superlattice and reference devices, respectively. Landau quantization is clearly visible at 10 K but the curves become featureless at 200 K, except for the peaks at the NPs. BZ oscillations are quite strong in the superlattice device at 200 K for this range of *B* but do not show up at all in the measurements in (A) using charge-density sweeps.

Magnetotransport in low fields

Fig. 2D shows that σ_{xx} and σ_{xy} exhibited rapid changes near zero *B*. These low-*B* features are irrelevant for the scope of the current report that focuses on BZ oscillations. Nonetheless, for completeness we show these features in more detail in fig. S10. It plots the experimentally measured ρ_{xx} and ρ_{xy} over the entire range of *B* in Fig. 2D and magnifies the behavior around zero *B*. The sharp dip in ρ_{xx} and sign-changing ρ_{xy} can be attributed to a complex electronic band structure of graphene superlattices at the energies above the second-generation NP (see the lowest panel in fig. S8B). The particular behavior (shown for $n/n_0 \approx 1.5$) was found to change with changing *n* only by a fraction of n_0. At high doping, several Brillouin minizones with opposite charge carriers are likely to contribute to the transport characteristics (*20,30,34*). In addition, minibands can become depopulated with increasing *B*. Although the features in the inset of fig. S10 are relatively small, when translated into σ_{xy}, they lead to the notable nonmonotonic behavior at low *B* in Fig. 2D. This regime lies beyond the experimental range in which BZ oscillations are observable and requires separate investigation.

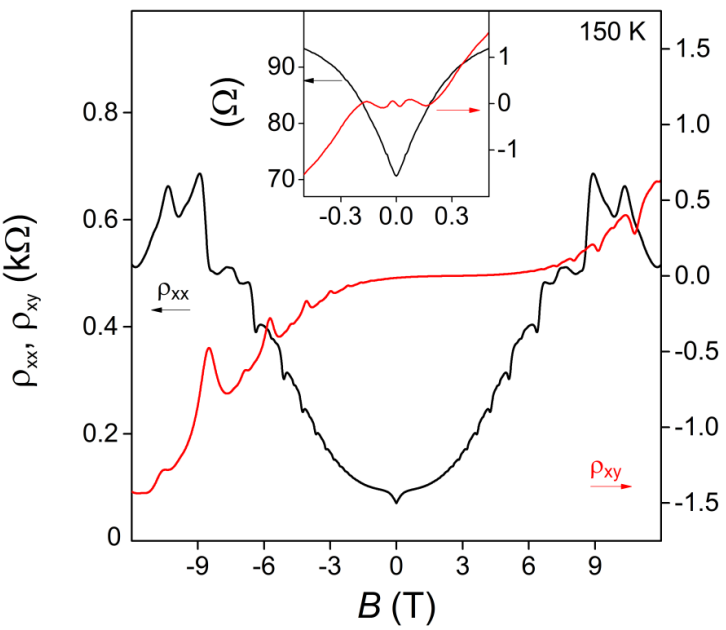

Fig. S10

Low-field transport at high doping. ρ_{xx} and ρ_{xy} for the superlattice device in Fig. 2 of the main text. Both characteristics exhibit anomalous behavior in low *B* such that the Hall effect changes its sign twice, and ρ_{xx} shows a sharp dip. This is attributed to a complex miniband structure at energies beyond the second-generation NP. Inset: Low-*B* region is magnified.

Full list of references

1. N. W. Ashcroft & N. D. Mermin, *Solid State Physics* (Holt, Rinehart and Winston, New York, 1976).

2. M. Springford, *Electrons at the Fermi Surface* (Cambridge University Press, 1980).

3. C. W. J. Beenakker & H. van Houten. Quantum transport in semiconductor nanostructures. *Solid State Phys.* **44**, 1-228 (1991).

4. R. R. Gerhardts, D. Weiss, K. V. Klitzing. Novel magnetoresistance oscillations in a periodically modulated two-dimensional electron gas. *Phys. Rev. Lett.* **62**, 1173-1176 (1989).

5. R. Webb, S. Washburn, C. P. Umbach , R. B. Laibowitz. Observation of h/e Aharonov-Bohm oscillations in normal-metal rings. *Phys. Rev. Lett.* **54**, 2696-2699 (1985).

6. K. S. Novoselov *et al*. Room-temperature quantum Hall effect in graphene. *Science* **315**, 1379 (2007)

7. E. Brown. Bloch electrons in a uniform magnetic field. *Phys. Rev.* **133,** A1038-A1044 (1964).

8. J. Zak. Magnetic translation group. *Phys. Rev.* **134,** A1602-A1611 (1964).

9. P. G. Harper. The general motion of conduction electrons in a uniform magnetic field, with application to the diamagnetism of metals. *Proc. Phys. Soc. London A* **68**, 879-892 (1955).

10. D. R. Hofstadter. Energy levels and wave functions of Bloch electrons in rational and irrational magnetic fields. *Phys. Rev. B* **14**, 2239–2249 (1976).

11. G. H. Wannier. A result not dependent on rationality for Bloch electrons in a magnetic field. *Phys. Status Solidi B* **88**, 757–765 (1978).

12. D. Thouless, M. Kohmoto, M. Nightingale & M. den Nijs. Quantized Hall conductance in a two-dimensional periodic potential. *Phys. Rev. Lett.* **49**, 405–408 (1982)

13. A. H. MacDonald. Landau-level subband structure of electrons on a square lattice. *Phys. Rev. B* **28**, 6713–6717 (1983).

14. C. Albrecht *et al.* Evidence of Hofstadter's fractal energy spectrum in the quantized Hall conductance. *Phys. Rev. Lett.* **86**, 147–150 (2001).

15. M. C. Geisler *et al.* Detection of Landau band coupling induced rearrangement of the Hofstadter butterfly. *Physica E* **25**, 227–232 (2004).

16. S. Melinte *et al.* Laterally modulated 2D electron system in the extreme quantum limit. *Phys. Rev. Lett.* **92**, 036802 (2004).

17. L. A. Ponomarenko *et al*. Cloning of Dirac fermions in graphene superlattices. *Nature* **497,** 594-597 (2013).

18. C. R. Dean *et al*. Hofstadter's butterfly and the fractal quantum Hall effect in moiré superlattices. *Nature* **497,** 598-602 (2013).

19. B. Hunt *et al*. Massive Dirac fermions and Hofstadter butterfly in a van der Waals heterostructure. *Science* **340,** 1427-1430 (2013).
20. G. L. Yu *et al*. Hierarchy of Hofstadter states and replica quantum Hall ferromagnetism in graphene superlattices. *Nature Phys.* **10**, 525-529 (2014).
21. L. Wang *et al*. Evidence for a fractional fractal quantum Hall effect in graphene superlattices. *Science* **350**, 1231-1234 (2015).
22. W. Yang *et al*. Hofstadter butterfly and many-body effects in epitaxial graphene superlattice. *Nano Lett.* **16**, 2387-2392 (2016).
23. M. Yankowitz *et al*. Emergence of superlattice Dirac points in graphene on hexagonal boron nitride. *Nature Phys.* **8,** 382-386 (2012).
24. C. R. Woods *et al.* Commensurate-incommensurate transition for graphene on hexagonal boron nitride. *Nature Phys.* **10**, 451-456 (2014).
25. Z. G. Chen *et al*. Observation of an intrinsic bandgap and Landau level renormalization in graphene/boron-nitride heterostructures. *Nature Commun.* **5**, 4461 (2014).
26. See supplementary materials on *Science* Online.
27. N. M. Freitag *et al*. Electrostatically confined monolayer graphene quantum dots with orbital and valley splittings. *Nano Lett.* **16**, 5798-5805 (2016).
28. K. S. Novoselov *et al.* Two-dimensional gas of massless Dirac fermions in graphene. *Nature* **438**, 197-200 (2005).
29. Y. Zhang, J. W. Tan, H. L. Stormer, P. Kim. Experimental observation of the quantum Hall effect and Berry's phase in graphene. *Nature* **438**, 201-204 (2005).
30. X. Chen, J. Wallbank, A. Patel, M. Mucha-Kruczynski, E. McCann, V. I. Fal'ko. Dirac edges of fractal magnetic minibands in graphene with hexagonal moiré superlattices. *Phys. Rev. B* **89**, 075401 (2014)
31. M. Ben Shalom *et al*. Quantum oscillations of the critical current and high-field superconducting proximity in ballistic graphene. *Nature Phys.* **12**, 318–322 (2016).
32. A. V. Kretinin *et al*. Electronic properties of graphene encapsulated with different two-dimensional atomic crystals. *Nano Lett.* **14**, 3270–3276 (2014).
33. R. V. Gorbachev *et al*. Detecting topological currents in graphene superlattices. *Science* **346**, 448-451 (2014).
34. J. Wallbank, A. Patel, M. Mucha-Kruczyński, A. Geim, V. I. Fal'ko. Generic miniband structure of graphene on a hexagonal substrate. *Phys. Rev. B* **87**, 245408 (2013).
35. J. Xia, F. Chen, J. Li, N. Tao. Measurement of the quantum capacitance of graphene. *Nature Nano.* **4**, 505-509 (2009).

36. G. L. Yu *et al*. Interaction phenomena in graphene seen through quantum capacitance. *PNAS* **110**, 3282-3286 (2013).
37. C. Ortix, L. Yang, J. van den Brink. Graphene on incommensurate substrates: Trigonal warping and emerging Dirac cone replicas with halved group velocity. *Phys. Rev. B* **86**, 081405 (2012).
38. M. Kindermann, B. Uchoa, D. L. Miller. Zero-energy modes and gate-tunable gap in graphene on hexagonal boron nitride. *Phys. Rev. B* **86**, 115415 (2012).
39. M. Diez, J. P. Dahlhaus, M. Wimmer, C. W. J. Beenakker. Emergence of massless Dirac fermions in graphene's Hofstadter butterfly at switches of the quantum Hall phase connectivity. *Phys. Rev. Lett.* **112**, 196602 (2014).
40. P. Moon & M. Koshino. Electronic properties of graphene/hexagonal-boron-nitride moiré superlattice. *Phys. Rev. B* **90**, 155406 (2014).
41. L. A. Chizhova, F. Libisch, J. Burgdorfer. Graphene quantum dot on boron nitride: Dirac cone replica and Hofstadter butterfly. *Phys. Rev. B* **90**, 165404 (2014).
42. G. J. Slotman, M. M. van Wijk, P. L. Zhao, A. Fasolino, M. I. Katsnelson, S. Yuan. Effect of structural relaxation on the electronic structure of graphene on hexagonal boron nitride. *Phys. Rev. Lett.* **115**, 186801 (2015).
43. K. Kishigi & Y. Hasegawa. Quantum oscillations of magnetization in tight-binding electrons on a honeycomb lattice. *Phys. Rev. B* **90**, 085427 (2014).
44. Y. Cao *et al*. Superlattice-induced insulating states and valley-protected orbits in twisted bilayer graphene. *Phys. Rev. Lett*. **117**, 116804 (2016).
45. Y. Hasegawa & M. Kohmoto. Periodic Landau gauge and quantum Hall effect in twisted bilayer graphene. *Phys. Rev. B* **88**, 125426 (2013).

Chapter 9 – Summary & Outlook

In the preceding chapters, we demonstrated a number of novel transport phenomena unique to graphene. The results emphasise the significance of electron transport in graphene from the point of view of fundamental physics. Even now, fifteen years on since discovery, we have found new physics. This is because of two reasons. The first is the availability of ultra-high quality samples, which allow us to truly study the intrinsic properties of graphene. Second, we focused our experiments in the regime of moderate-high temperatures, that is, 100 – 300 K. Typically quantum transport phenomena are dominant at liquid helium temperatures (< 5 K), where scattering is minimal and the fermi-level is well defined. Indeed, in current high-quality graphene heterostructures, new exotic electron phases are being studied for the first time in Condensed matter physics[62,63]. At the same time, restricting experiments to these temperatures has resulted in missed opportunities. For example, in 2013 graphene/hBN superlattices became a popular system for studying transport because of its high-mobility and large super lattice periodicity[48,55,64]. Since then, experiments in Moiré superlattices have revolved around the Hofstader butterfly physics[65,66,67]. Since the Hofstader butterfly originates from Landau quantisation, it is logical to perform experiments as low a temperature as possible to resolve the spectral gaps. However, despite numerous experimental efforts, the Brown-Zak oscillations went un-noticed until this year, because not enough attention was paid to the high temperature regime. This Thesis shows the importance of performing non-conventional experiments and poking around in an un-familiar parameter space.

9.1 Viscous Electron flow in graphene

The work presented in Chapter. 5 and 6 are amongst the first experiments which seek to uncover viscous flow of the electron liquid. We note however, that we were not the only group studying hydrodynamics. Last year, two further works on electron hydrodynamics (one in graphene)[68] featured in the same issue as the paper presented in Chapter. 6. Although graphene is an ideal system for studying viscous flows, the work by Mackenzie[69] raises questions as to what other materials might host a viscous electron liquid. Since these works, there has been a recent surge in electron hydrodynamics, with many more theoretical papers appearing over the past year[70,71,72,73]. As for experiment, viscous electrons have already demonstrated their significance in transport; current which flows against the applied electric field[74], viscous flows conducting beyond the ballistic limit[75], and the violation of the Wiedemann-Franz law in graphene[68].

In Chapter 5, we presented the first measurement of electron viscosity in graphene devices by studying electron whirlpools. Whilst the theoretical model could accurately describe many aspects of the experiment, it was only applicable when transport was deep in the hydrodynamic regime at temperatures 150 – 300 K. It failed to explain the behaviour of electrons at low temperature's where electron-electron collisions are infrequent. For example, single particle effects like magnetic focussing are not expected in the viscous regime. Instead, we had to employ the Landauer-Buttiker formalism and approach the problem in terms of transmission coefficients. We could describe both the ballistic and hydrodynamic regime in their extreme limits but could not interpolate smoothly between them. A different theoretical approach was required to describe the transition from ballistic to viscous flow.

In Chapter 6, we did just this. Equipped with a suitable theory, we studied electron transport through graphene point contacts. The theory (Guo PNAS 2017)[76] started with the Boltzman transport equation, allowing one to continuously tune electron-electron scattering through a collision integral. Remarkably, our collaborators found that the transition between ballistic and viscous transport regimes is dictated by a simple interpolation formula (see equation (2) in Chapter 7). Our analysis of experimental data with this formula validated its significance. First, we could observe the peculiar scaling behaviour expected for the viscous conductance ($G_v \sim w^2$). Second, we were able to measure the electron-electron mean free path at all experimentally accessible temperatures, whether in the ballistic regime at T = 5 K, or in the hydrodynamic regime at 200 K. The result was quite astonishing when it was compared to independent many-body calculations performed by our collaborators. To emphasise the significance here, let us note that this result came from two independent theoretical groups. The interpolation formula from Professor Leonid Levitov's group at MIT was used to extract the electron-electron mean free path, which showed unprecedented agreement with many-body calculations performed by Italian researchers led by Professor Marco Polini and Professor Giovanni Vignale. The work presented in Chapter. 7 showed that we have already gained significant understanding in to the cross-over regime between ballistic and viscous electron transport.

As for future work, there still exists an open question. In Chapter. 6, we start to see electron whirlpools at around 150 – 200 K suggesting the system transitions to a viscous regime. Notably, in the same geometry, we can also observe magnetic focussing. In fact, magnetic focussing has been shown to persist even up to room temperature[29]. This suggests that viscous electron whirlpools and magnetic focussing somehow co-exist. Currently there is not a clear picture how ballistic phenomena persist even in the hydrodynamic regime. Of course, one can speculate, but a proper understanding

is required and future work in this direction is likely to uncover the properties of these viscous electron beams.

9.2 Electron transport in Brown-Zak mini-bands

The newly discovered Brown-Zak oscillations have proven themselves the most robust type of quantum oscillation in condensed matter physics. The fact that we could observe oscillations even at 373 K, demonstrates the stability of Brown-Zak mini-bands in graphene. More importantly, it has shown the significance of the magnetic translation group derived by Zak[52] over 50 years ago. Furthermore, its persistence to high temperatures show that the concepts like zero magnetic field have nothing to do with Landau quantisation; something which was not clear in the early experimental works on the Hofstadter Butterfly[55].

Brown-Zak oscillations host rather unique properties. The most intriguing is their strict frequency dependence, which depends only on the area of the super lattice unit cell and, in contrast to other oscillatory phenomena, is independent on carrier density. Therefore, the oscillations provide a tool for directly measuring the structural properties of the crystal. This is especially useful for the case of novel superlattice systems in their infancy, where Brown-Zak oscillations could be used as a characterisation technique.

In our experiments performed in Chapter 7, we provide an experimental signature of the Brown-Zak mini-band structure. The Brown-Zak mini-bands essentially represent different metallic systems. An interesting experiment then would be to study electron transport of these new metallic systems, where the current distribution might look rather different than the case of graphene in zero magnetic fields. With this in mind, we would go to those special values of magnetic field when $\phi/\phi_0 = 1/q$, and perform different transport experiments. For example, we could perform non-local measurements and use the valley hall effect as a tool to probe berry curvature[57] in the Brown-Zak mini-bands.

The zero effective magnetic fields arising from the magnetic translation group is extremely persistent with respect to temperature smearing. In Chapter. 7, we probed zero effective magnetic field by measuring σ_{xx} and σ_{xy}, where we found peaks in σ_{xx} accompanied by zeros in σ_{xy} for those special values of magnetic field when $\phi/\phi_0 = 1/q$. The question remains to what extent this is truly zero effective magnetic field and whether the electrons are really moving straight. To understand this, we could study ballistic transport, which is extremely sensitive to weak magnetic fields, in the Brown-Zak mini-bands. For example, bend resistance experiments which were summarised in Chapter 2.3 could be performed in a superlattice device, where measurement of a negative bend resistance would serve as a tool for probing straight trajectories. Although this is the simplest, there

are a number of other transport experiments which could be used to study the zero effective magnetic fields.

9.3 Closing remarks

The experiments performed in this Thesis demonstrate the importance of graphene research in the solid-state physics community. Indeed, it has gained the most attention out of all the two-dimensional materials. This is not because it was discovered first, but because it is still the highest quality two-dimensional monolayer around. In general, new systems of high-quality are likely to host new physics. In this sense, graphene has certainly proven itself a unique platform for performing transport experiments and we can only hope other two-dimensional materials will deliver a rich variety of novel physics.

Bibliography

1. Seeger, K. *Semiconductor Physics: An Introduction*. (Springer, 2013).

2. von Klitzing, K. The quantized Hall effect. *Rev. Mod. Phys.* **58,** 519–531 (1986).

3. Solomon, P. M., Price, P. J., Frank, D. J. & La Tulipe, D. C. New phenomena in coupled transport between 2D and 3D electron-gas layers. *Phys. Rev. Lett.* **63,** 2508–2511 (1989).

4. Gramila, T. J., Eisenstein, J. P., MacDonald, A. H., Pfeiffer, L. N. & West, K. W. Mutual friction between parallel two-dimensional electron systems. *Phys. Rev. Lett.* **66,** 1216–1219 (1991).

5. Novoselov, K. S. *et al.* Two-dimensional gas of massless Dirac fermions in graphene. *Nature* **438,** 197–200 (2005).

6. Mak, K. F., Lee, C., Hone, J., Shan, J. & Heinz, T. F. Atomically Thin MoS2: A New Direct-Gap Semiconductor. *Phys. Rev. Lett.* **105,** 136805 (2010).

7. Pakdel, A., Bando, Y. & Golberg, D. Nano boron nitride flatland. *Chem. Soc. Rev.* **43,** 934–959 (2014).

8. Ugeda, M. M. *et al.* Characterization of collective ground states in single-layer NbSe2. *Nat Phys* **12,** 92–97 (2016).

9. Castro Neto, A. H., Guinea, F., Peres, N. M. R., Novoselov, K. S. & Geim, A. K. The electronic properties of graphene. *Rev. Mod. Phys.* **81,** 109–162 (2009).

10. Geim, A. K. & Grigorieva, I. V. Van der Waals heterostructures. *Nature* **499,** 419–425 (2013).

11. Britnell, L. *et al.* Field-Effect Tunneling Transistor Based on Vertical Graphene Heterostructures. *Science.* **335,** 947 LP-950 (2012).

12. Abanin, D. A. *et al.* Dissipative Quantum Hall Effect in Graphene near the Dirac Point. *Phys. Rev. Lett.* **98,** 196806 (2007).

13. Ponomarenko, L. A. *et al.* Density of States and Zero Landau Level Probed through Capacitance of Graphene. *Phys. Rev. Lett.* **105,** 136801 (2010).

14. Katsnelson, M. I., Novoselov, K. S. & Geim, A. K. Chiral tunnelling and the Klein paradox in graphene. *Nat Phys* **2,** 620–625 (2006).

15. Wallace, P. R. The Band Theory of Graphite. *Phys. Rev.* **71,** 622–634 (1947).

16. Zhang, Y., Tan, Y.-W., Stormer, H. L. & Kim, P. Experimental observation of the quantum Hall effect and Berry's phase in graphene. *Nature* **438,** 201–204 (2005).

17. Fratini, S. & Guinea, F. Substrate-limited electron dynamics in graphene. *Phys. Rev. B* **77,** 195415 (2008).

18. Chen, J.-H., Jang, C., Xiao, S., Ishigami, M. & Fuhrer, M. S. Intrinsic and extrinsic performance limits of graphene devices on SiO2. *Nat Nano* **3,** 206–209 (2008).

19. C R., D. *et al.* Boron nitride substrates for high-quality graphene electronics. *Nat Nano* **5,** 722–726 (2010).

20. Mayorov, A. S. *et al.* Micrometer-Scale Ballistic Transport in Encapsulated Graphene at Room Temperature. *Nano Lett.* **11,** 2396–2399 (2011).

21. R., D. *et al.* Boron nitride substrates for high-quality graphene electronics. *Nat Nano* **5,** 722–726 (2010).

22. Viktor Ariel, A. N. Electron effective mass in graphene. *arXiv* **1206,** (2012).

23. Landauer, R. Spatial variation of currents and fields due to localized scatterers in metallic conduction. *IBM J. Res. Dev.* **1,** 223–231 (1957).

24. Ouisse, T. *Electron Transport in Nanostructures and Mesoscopic Devices: An Introduction*. (John Wiley & Sons, 2013).

25. Sharvin, Y. V. A possible method for studying Fermi surfaces. *J. Exp. Theor. Phys.* **21,** 655–656 (1965).

26. Terrés, B. *et al.* Size quantization of Dirac fermions in graphene constrictions. *Nat. Commun.* **7,** 11528 (2016).

27. Tombros, N. *et al.* Quantized conductance of a suspended graphene nanoconstriction. *Nat Phys* **7,** 697–700 (2011).

28. van Wees, B. J. *et al.* Quantized conductance of point contacts in a two-dimensional electron gas. *Phys. Rev. Lett.* **60,** 848–850 (1988).

29. Taychatanapat, T., Watanabe, K., Taniguchi, T. & Jarillo-Herrero, P. Electrically tunable transverse magnetic focusing in graphene. *Nat Phys* **9,** 225–229 (2013).

30. Lee, M. *et al.* Ballistic miniband conduction in a graphene superlattice. *Science.* **353,** 1526 LP-1529 (2016).

31. Pfeiffer, L., West, K. W., Stormer, H. L. & Baldwin, K. W. Electron mobilities exceeding 10^7 cm^2/V s in modulation-doped GaAs. *Appl. Phys. Lett.* **55,** 1888–1890 (1989).

32. Kawamura, T. & Das Sarma, S. Phonon-scattering-limited electron mobilities in $Al_xGa_{1-x}As$/GaAs heterojunctions. *Phys. Rev. B* **45,** 3612–3627 (1992).

33. Hwang, E. H. & Das Sarma, S. Acoustic phonon scattering limited carrier mobility in two-dimensional extrinsic graphene. *Phys. Rev. B* **77,** 115449 (2008).

34. L. D. Landau, E. M. Lifshitz. *Fluid Mechanics (Pergamon Press, 1987).*

35. Teaney, T. S. and D. Nearly perfect fluidity: from cold atomic gases to hot quark gluon plasmas. *Reports Prog. Phys.* **72,** 126001 (2009).

36. Cao, C. *et al.* Universal Quantum Viscosity in a Unitary Fermi Gas. *Science.* **331,** 58 LP-61 (2011).

37. Jacak, B. V & Müller, B. The Exploration of Hot Nuclear Matter. *Science.* **337,** 310 LP-314 (2012).

38. Tomadin, A., Vignale, G. & Polini, M. Corbino Disk Viscometer for 2D Quantum Electron Liquids. *Phys. Rev. Lett.* **113,** 235901 (2014).

39. Gurzhi, R. N. Minimum of resistance in impurity-free conductors. *Sov. Phys. JETP, 44, 771.* (1963).

40. Gurzhi, R. N. HYDRODYNAMIC EFFECTS IN SOLIDS AT LOW TEMPERATURE. *Sov. Phys. Uspekhi* **11,** 255 (1968).

41. Giuliani, G. F. & Quinn, J. J. Lifetime of a quasiparticle in a two-dimensional electron gas. *Phys. Rev. B* **26,** 4421–4428 (1982).

42. de Jong, M. J. M. & Molenkamp, L. W. Hydrodynamic electron flow in high-mobility wires. *Phys. Rev. B* **51,** 13389–13402 (1995).

43. Gurzhi, R. N., Kalinenko, A. N. & Kopeliovich, A. I. Electron-Electron Collisions and a New Hydrodynamic Effect in Two-Dimensional Electron Gas. *Phys. Rev. Lett.* **74,** 3872–3875 (1995).

44. Principi, A., Vignale, G., Carrega, M. & Polini, M. Bulk and shear viscosities of the two-dimensional electron liquid in a doped graphene sheet. *Phys. Rev. B* **93,** 125410 (2016).

45. Torre, I., Tomadin, A., Geim, A. K. & Polini, M. Nonlocal transport and the hydrodynamic shear viscosity in graphene. *Phys. Rev. B* **92,** 165433 (2015).

46. Levitov, L. & Falkovich, G. Electron viscosity, current vortices and negative nonlocal resistance in graphene. *Nat Phys* **12,** 672–676 (2016).

47. Schubnikow, L. & De Haas, W. J. A New Phenomenon in the Change of Resistance in a Magnetic Field of Single Crystals of Bismuth. *Nature* **126,** 500–500 (1930).

48. Ponomarenko, L. A. *et al.* Cloning of Dirac fermions in graphene superlattices. *Nature* **497,** 594–597 (2013).

49. Jeno Soloym. *Fundamentals of the Physics of Solids: Volume 2 Electronic Properties*. (2007).

50. Wang, S. X. and Z. W. and H. L. and Y. H. and G. L. and X. C. and T. H. and W. Y. and Y. W. and J. L. and J. S. and Y. C. and Y. H. and F. Z. and R. L. and C. C. and N. Universal low-temperature Ohmic contacts for quantum transport in transition metal dichalcogenides. *2D Mater.* **3,** 21007 (2016).

51. Harper, P. G. Single Band Motion of Conduction Electrons in a Uniform Magnetic Field. *Proc. Phys. Soc. Sect. A* **68,** 874 (1955).

52. Zak, J. Magnetic Translation Group. *Phys. Rev.* **134,** A1602–A1606 (1964).

53. Hofstadter, D. R. Energy levels and wave functions of Bloch electrons in rational and irrational magnetic fields. *Phys. Rev. B* **14,** 2239–2249 (1976).

54. Yankowitz, M. *et al.* Emergence of superlattice Dirac points in graphene on hexagonal boron nitride. *Nat Phys* **8,** 382–386 (2012).

55. Dean, C. R. *et al.* Hofstadter's butterfly and the fractal quantum Hall effect in moire superlattices. *Nature* **497,** 598–602 (2013).

56. Wallbank, J. R., Patel, A. A., Mucha-Kruczyński, M., Geim, A. K. & Fal'ko, V. I. Generic miniband structure of graphene on a hexagonal substrate. *Phys. Rev. B* **87,** 245408 (2013).

57. Gorbachev, R. V *et al.* Detecting topological currents in graphene superlattices. *Science.* **346,** 448 LP-451 (2014).

58. Novoselov, K. S. *et al.* Electric Field Effect in Atomically Thin Carbon Films. *Science.* **306,** 666 LP-669 (2004).

59. Ferrari, A. C. *et al.* Raman Spectrum of Graphene and Graphene Layers. *Phys. Rev. Lett.* **97,** 187401 (2006).

60. Yi, M. & Shen, Z. A review on mechanical exfoliation for the scalable production of graphene. *J. Mater. Chem. A* **3,** 11700–11715 (2015).

61. Wang, L. *et al.* One-Dimensional Electrical Contact to a Two-Dimensional Material. *Science.* **342,** 614 LP-617 (2013).

62. Li, J. I. A., Taniguchi, T., Watanabe, K., Hone, J. & Dean, C. R. Excitonic superfluid phase in double bilayer graphene. *Nat Phys* **13,** 751–755 (2017).

63. Liu, X., Watanabe, K., Taniguchi, T., Halperin, B. I. & Kim, P. Quantum Hall drag of exciton condensate in graphene. *Nat Phys* **13,** 746–750 (2017).

64. Hunt, B. *et al.* Massive Dirac Fermions and Hofstadter Butterfly in a van der Waals Heterostructure. *Science.* **340,** 1427 LP-1430 (2013).

65. Yu, G. L. *et al.* Hierarchy of Hofstadter states and replica quantum Hall ferromagnetism in graphene superlattices. *Nat Phys* **10,** 525–529 (2014).

66. Wang, L. *et al.* Evidence for a fractional fractal quantum Hall effect in graphene superlattices. *Science.* **350,** 1231 LP-1234 (2015).

67. Yang, W. *et al.* Hofstadter Butterfly and Many-Body Effects in Epitaxial Graphene Superlattice. *Nano Lett.* **16,** 2387–2392 (2016).

68. Crossno, J. *et al.* Observation of the Dirac fluid and the breakdown of the Wiedemann-Franz law in graphene. *Science.* **351,** 1058 LP-1061 (2016).

69. Moll, P. J. W., Kushwaha, P., Nandi, N., Schmidt, B. & Mackenzie, A. P. Evidence for hydrodynamic electron flow in PdCoO2. *Science.* **351,** 1061–1064 (2016).

70. Scaffidi, T., Nandi, N., Schmidt, B., Mackenzie, A. P. & Moore, J. E. Hydrodynamic Electron Flow and Hall Viscosity. *Phys. Rev. Lett.* **118,** 226601 (2017).

71. Gregory Falkovich, L. L. Linking spatial distributions of potential and current in viscous electronics. *arXiv* **1607,** (2016).

72. Guo, H., Ilseven, E., Falkovich, G. & Levitov, L. Stokes paradox, back reflections and interaction-enhanced conduction. *arXiv* **1612,** (2017).

73. Pellegrino, F. M. D., Torre, I. & Polini, M. Non-local transport and the Hall viscosity of 2D hydrodynamic electron liquids. *arXiv* **1706,** (2017).

74. Bandurin, D. A. *et al.* Negative local resistance caused by viscous electron backflow in graphene. *Science* **351**, 1055-1058. (2016).

75. Krishna Kumar, R. *et al.* Superballistic flow of viscous electron fluid through graphene constrictions. *Nat Phys* **advance on,** (2017).

76. Guo, H., Ilseven, E., Falkovich, G. & Levitov, L. S. Higher-than-ballistic conduction of viscous electron flows. *Proc. Natl. Acad. Sci.* **114,** 3068–3073 (2017).